BOUNDARY LAYER ANALYSIS OF NON-NEWTONIAN NANOFLUID FLOWS WITH HEAT AND MASS TRANSFER OVER STRETCHING SURFACES

Endale Ersino Bafe

A Dissertation Submitted to the Department of Applied Mathematics College of Applied Natural Science

Presented in Partial Fulfillment of the Requirement for the Degree of Doctor of Philosophy in Applied Mathematics (Computational Fluid Dynamics)

Office of Graduate Studies
Adama Science and Technology University

June, 2025
Adama, Ethiopia

BOUNDARY LAYER ANALYSIS OF NON-NEWTONIAN NANOFLUID FLOWS WITH HEAT AND MASS TRANSFER OVER STRETCHING SURFACES

Endale Ersino Bafe

Main Supervisor: Mitiku Daba Firdi (Associate Professor)

Co-Supervisor: Lemi Guta Enyadene (Associate Professor)

A Dissertation Submitted to the Department of Applied Mathematics College of Applied Natural Science

Presented in Partial Fulfillment of the Requirement for the Degree of Doctor of Philosophy in Applied Mathematics (Computational Fluid Dynamics)

Office of Graduate Studies

Adama Science and Technology University

June, 2025

Adama, Ethiopia

Declaration

I, hereby declare that this dissertation entitled **"Boundary Layer Analysis of Non-Newtonian Nanofluid Flows with Heat and Mass Transfer over Stretching Surfaces"** is my own, original work. Thus, it has not been submitted to any university for analogous purpose. The references used in this dissertation have been properly recognized through appropriate and correct citations.

Mr. Endale Ersino Bafe	____________________	____________________
Name of Student	Signature	Date

Recommendation

We, the supervisors of this dissertation work, hereby certify that we have read and revised the dissertation entitled **"Boundary Layer Analysis of Non-Newtonian Nanofluid Flows with Heat and Mass Transfer over Stretching Surfaces"** prepared under our guidance by Endale Ersino submitted in fulfillment of the requirements for the degree of Doctor of Philosophy in Applied Mathematics. Therefore, we recommend the submission of dissertation to the department for further review and defense.

Dr. Mitiku Daba Firdi	____________________	____________________
Major Supervisor	Signature	Date
Dr. Lemi Guta Enyadene	____________________	____________________
Co-Supervisor	Signature	Date

Approval Page

We, hereby certify that the recommendations and suggestions made by the board of examiners are appropriately incorporated into the final version of the dissertation entitled **"Boundary Layer Analysis of Non-Newtonian Nanofluid Flows with Heat and Mass Transfer over Stretching Surfaces"** by Endale Ersino.

Dr. Mitiku Daba Firdi	____________________	______________
Major Supervisor	Signature	Date
Dr. Lemi Guta Enyadene	____________________	______________
Co-Spervisor	Signature	Date

We, the undersigned, members of the Board of Examiners for this dissertation open defense by Endale Ersino have read and evaluated the dissertation entitled **"Boundary Layer Analysis of Non-Newtonian Nanofluid Flows with Heat and Mass Transfer over Stretching Surfaces"** and examined the candidate during open defense. This is, therefore, to certify that the dissertation is accepted for fulfillment of the requirement of the degree of Doctor of Philosophy in Applied Mathematics.

Chairperson	Signature	Date
Internal Examiner 1	Signature	Date
Internal Examiner 2	Signature	Date
External Examiner 1	Signature	Date
External Examiner 2	Signature	Date

Finally, approval and acceptance of the dissertation is contingent upon submission of its final copy to the Office of Postgraduate Studies (OPGS) through the candidate's Department Graduate Council (DGC) and School Graduate Committee (SGC).

Department Head	Signature	Date
School Dean	Signature	Date
Office of Postgraduate Studies, Dean	Signature	Date

ACKNOWLEDGMENTS

First and foremost, I give all thanks and glory to God for His abundant provisions, wisdom, and strength throughout this journey. His grace has been my sustenance, guiding me through every challenge and milestone in the completion of this dissertation.

I am profoundly grateful to my main supervisor, Dr. Mitiku Daba, whose unwavering guidance, enthusiasm, and patience have been instrumental throughout the course of this dissertation. His exceptional support and insightful mentorship have been invaluable, and this work would not have reached its current state without his contributions. Dr. Mitiku has taught several critical courses that have greatly enriched my understanding and enabled the successful completion of this dissertation. His knowledge and advice have been a cornerstone of my academic journey, and I cannot thank him enough for his dedication and encouragement.

I would also like to extend my sincere gratitude to my co-supervisor, Dr. Lemi Guta, for providing technical and theoretical guidance that has significantly shaped the research.

My appreciation further goes to Adama Science and Technology University (ASTU) for their financial support (Grant No. ASTU/SP-R/284/24) and to Hawassa University for sponsoring my PhD studies at ASTU. I am equally thankful to the applied Mathematics department head, instructors, and all members of the applied natural sciences college at ASTU for their valuable support and clear communication during my time at the university.

I am deeply indebted to my family members and classmates, whose financial and emotional support have been a source of strength throughout this journey.

Finally, I express my heartfelt gratitude to my beloved wife, Likelesh Gona Assefa, my daughter, Selome Endale, and my sons, Kaleb Endale, Sophonias Endale, and Amen Endale, for their unwavering love, encouragement, and sacrifices. To my extended family, your constant support and belief in me have played a pivotal role in my success.

Dedication

This dissertation work is dedicated to all my family members.

List of Publications

This PhD dissertation contributed the following original papers which were published in peer reviewed international journals indexed in Scopus, Web of Science, UGC CARE, and DOAJ.

1. E.E. Bafe, M.D. Firdi, & L.G. Enyadene, (2023). Numerical investigation of MHD Carreau nanofluid flow with nonlinear thermal radiation and joule heating by employing Darcy-Forchheimer effect over a stretching porous medium. *Int. J. Differ. Equ. 2023 (2023) 83-92,* http://dx.doi.org/10.1155/2023/5495140.

2. E.E. Bafe, M.D. Firdi, & L.G. Enyadene, (2024). Magnetohydrodynamic thermo-bioconvective flow of 3D rotating Williamson nanofluid with Arrhenius activation energy in a Darcy-Forchheimer medium over an exponentially stretching Surface, *International Journal of Thermofluids 21 (2024) 100585*, https://doi.org/10.1016/j.ijtf.2024.100585.

3. E.E. Bafe, M.D. Firdi, & L.G. Enyadene, (2024). Entropy generation and Cattaneo-Christov heat flux analysis of binary and ternary hybrid Maxwell nanofluid flows with slip and convective conditions. *Case Studies in Thermal Engineering 61 (2024) 104986* https://doi.org/10.1016/j.csite.2024.104986

4. E.E. Bafe, M.D. Firdi, & L.G. Enyadene, (2024). The non-Fourier-Fick's heat and mass flux effect in a bioconvective nanofluid flow over a stretching cylinder with suction/injection and convective conditions. *Results in physics 68 (2024) 104986* https://doi.org/10.1016/j.rinp.2024.108068

5. E.E. Bafe, M.D. Firdi, & L.G. Enyadene, (2025). Unsteady Williamson nanofluid flow over a rotating cone: Effects of variable properties, thermal radiation, and chemical reactions, *International Journal of Thermofluids 27 (2025) 101211*, https://doi.org/10.1016/j.ijft.2025.101211.

TABLE OF CONTENTS

List of Tables

List of Figures

List of Acronyms and Abbreviations

	Acronyms
b	Chemotaxis constant
Be	Bejan number
Br	Brinkman number
$\mathrm{B_0}$	Magnetic field strength[$Kg/K.s$]
C	Nanoparticle concentration[kg/$\mathrm{m^3}$]
$\mathrm{c_F}$	Forchheimer coefficient
$\mathrm{C_f}$	Skin friction (tangential)
$\mathrm{C_g}$	Skin friction (azimuthal)
$\mathrm{c_p}$	Specific heat coefficient[$J/Kg.K$]
C_s	Concentration susceptibility
$\mathrm{C_w}$	Wall concentration[$\mathrm{kg/m^3}$]
$\mathrm{C_\infty}$	Ambient concentration[kg/m^3]
$\mathrm{D_b}$	Nanoparticle diffusivity[m^2/s]
$\mathrm{D_m}$	Microbes diffusivity[m^2/s]
$\mathrm{D_M}$	Mass diffusivity[m^2/s]
$\mathrm{D_T}$	Thermophoresis coefficient[m^2/s]
E	Local Activation energy
$\mathrm{E_a}$	Activation energy[$\mathrm{kg.m^2/s^2.mol}$]
Ec	Eckert number
g	Acceleration due to gravity [m/s^2]
Gr	Grashof number
$\mathrm{h_m}$	Mass transfer coefficient[m/s]
$\mathrm{h_t}$	Heat transfer coefficient[$\mathrm{W/K.m^2}$]
k	Thermal conductivity[$W/m.K$]
$k^\star$	Permeability factor
$\mathrm{k_b^\star}$	Reaction rate(microbe) [$\mathrm{m^3/s.cell}$]
$\mathrm{k_e}$	Mean absorption coefficient[1/m]
$\mathrm{k_p^\star}$	Reaction rate(nanoparticle) [$\mathrm{m^3/s.mol}$]
L	Characteristic length scale[m]
$\mathrm{Le_1}$	Lewis number(nanoparticle)
$\mathrm{Le_2}$	Lewis number(microbe)
M	Magnetic parameter
N	Microbe concentration [cell/$\mathrm{m^3}$]
Nb	Brownian motion parameter
Nm	Brownian motion (microbial)
Nr	Buoyancy ratio number
Nt	Thermophoresis parameter
$\mathrm{Nu_x}$	Local Nusselt number
$\mathrm{N_w}$	Wall concentration(microbes)[cell/$\mathrm{m^3}$]
$\mathrm{N_\infty}$	Microbe ambient concentration[cell/$\mathrm{m^3}$]
P	Fluid pressure[$\mathrm{kg/m.s^2}$]
$\mathrm{p_b}$	Bioconvective Peclet number
Pr	Prandtl number
$\mathrm{q_r}$	Radiation flux[W/m^2]

$\mathrm{Q_0}$	Local heat source/sink
$\mathrm{R_b}$	Bioconvective Rayleigh number
$\mathrm{R_d}$	Radiation parameter
$\mathrm{Re_x}$	Local Reynolds number
$\mathrm{Sc_b}$	Schmidt number(nanoparticle)
$\mathrm{Sc_p}$	Schmidt number(microbe)
Sh_x	Local Sherwood number
T	Fluid temperature [K]
$\mathrm{T_w}$	Wall temperature[K]
$\mathrm{T_\infty}$	Ambient temperature[K]
u, v, w	Velocity components[m/s]
$\mathrm{W_c}$	Cell swimming speed[m/s]
We	Weissenberg number
x, y, z	Space coordinates(rectangular)[m]
$\mathrm{x_w}$	Microbe density ratio
	Greek Symbols
α	Local inertia coefficient
α_1	Angular velocity ration
β_2	Local velocity slip
β_3	Local thermal slip
β_{i1}	Biot number(thermal)
β_C	Solutal expansion coefficient[$\mathrm{m^3/kg}$]
β_m	Microbe expansion coefficient[$\mathrm{m^3/kg}$]
β_T	Thermal expansion coefficient[1/K]
β_w	Suction/injection
γ_2	Biot number (solutal)
γ_3	Biot number (microbial)
γ_b	Chemical reaction (microbial)
γ_c	Chemical reaction rate
Γ	Carreau/Williamson time material
δ	Dummy parameter
ϵ_2	Variable solutal diffusivity
ϵ_1	Variable thermal conductivity
η	Similarity variable
θ	Dimensionless temperature
θ_0	Variable viscosity parameter
θ_w	Temperature ratio number
κ	Heat diffusivity constant
λ	Porosity parameter
λ_1	Maxwell number
$\lambda_1^\star$	Maxwell relaxation factor
λ_2	Thermal relaxation number
$\lambda_2^\star$	Thermal relaxation factor
λ_3	Solutal relaxation number

$\lambda_3^\star$	Concentration relaxation factor		**Abbreviations**
λ_m	Mixed convection parameter	2D/3D	2/3 dimension
μ	Dynamic viscosity$[\mathrm{kg/m.s}]$	CC	Cattaneo-Christov
ν	Kinematic viscosity$[m^2/s]$	MHD	Magnetohydrodynamics
ξ	Porous medium porosity	ODEs	Ordinary differential equations
ρ_f	Fluid density$[Kg/m^3]$	PDEs	Partial differential equations
σ_0	Electrical conductivity$[\mathrm{A}^2.\mathrm{s}^3/\mathrm{kg.m}^3]$	SLLM	Spectral local linearization method
σ^*	Stefan-Boltzmann constant$[W/m^2.K^4]$	SQLM	Spectral quasilinearization method
χ	Dimensionless microbe density	SRM	Spectral relaxation method
$\boldsymbol{\tau}$	Stress tensor$[\mathrm{kg/m.s}^2]$	SWTC	Specified wall temperature/concentration
ϕ	Dimensionless concentration	STSF	Specified thermo-solutal flux
	Subscripts	RTT	Reynolds transport theorem
f	Base fluid	DT	Divergence theorem
p	Nanoparticle		
nf	Nanofluid		
bhf	Binary hybrid nanofluid		
thnf	Ternary hybrid nanofluid		
w	Surface condition		
∞	Ambient condition		

Abstract

The growing energy demand calls for advanced heat and mass transfer technologies in industrial and engineering applications. Conventional fluids with traditional enhancement methods often fall short in meeting these requirements. Nanofluids have shown promise in improving thermal performance. Considering the prevalence of non-Newtonian characteristics in practical systems, this dissertation investigates the heat and mass transfer behavior of non-Newtonian nanofluids flow under a range of physical influences, including MHD, thermal radiation, chemical reactions, Brownian motion, thermophoresis and porous media effects. Special attention is given to the influence of bioconvection, variable thermophysical properties, viscous dissipation, mixed convection, and heat source/sink. The governing PDEs are reduced into ODEs using similarity transformations and solved via spectral methods and MATLAB's bvp4c solver. Validation against existing benchmarks and residual norm analyses confirm the accuracy of the numerical approaches. The study focuses on Carreau and Williamson nanofluids, as well as binary and ternary hybrid Maxwell nanofluids. Results indicate that shear-thickening Carreau fluids exhibit superior heat and mass transfer performance compared to their shear-thinning counterparts. In Williamson nanofluids, the inclusion of bioconvective microorganisms and Arrhenius activation energy elevate temperature and concentration distributions, respectively. Moreover, thermal Biot numbers and non-Fickian fluxes substantially modulated the heat and mass transfer rates. Hybrid nanofluids flow analysis over rotating disk reveals that ternary hybrid nanofluid exhibits greater resistance to Lorentz and porous medium drag forces compared to binary hybrid nanofluid. Additionally, unsteady flow over a rotating cone reveals that variable thermal conductivity and solutal diffusivity enhance temperature and concentration under specified wall temperature and concentration conditions, but lead to reductions under specified thermosolutal flux conditions. This study advances the understanding of heat and mass transfer behavior in non-Newtonian nanofluids with practical relevance to diverse engineering and biomedical systems. Finally, based on the findings, recommendations for future research are proposed.

Key words: Non-Newtonian nanofluids; Thermal radiation; Bioconvection; Hybrid nanofluids; Variable thermophysical properties; Spectral methods.

CHAPTER ONE

Introduction

1.1 Background of the Study

1.1.1 Brief Historical Background

The study of fluid mechanics-concerned with the behavior of fluids at rest and in motion-has evolved over centuries. From empirical uses in ancient engineering to the modern theoretical and computational frameworks, fluid mechanics has remained central to both scientific inquiry and technological development (Batchelor (2000)).

(a) Ancient applications of fluid mechanics

Early civilizations, including those in Mesopotamia, Egypt, China, and Greece, applied rudimentary principles of fluid mechanics in agriculture, water management, and infrastructure. The construction of irrigation systems along the Nile and the Euphrates, and the development of aqueducts and canals, are prime examples of how ancient societies manipulated fluid flow to sustain agriculture and urbanization (Oppenheim (2013), Needham (1974)). In classical Greece, Archimedes (287-212 BCE) introduced the principle of buoyancy, establishing the theoretical basis of hydrostatics and setting a precedent for the mathematical treatment of fluid behavior (Heath (2002)).

(b) Foundational theories and mathematical formalization

The renaissance and enlightenment periods saw significant theoretical advancements. Leonardo da Vinci's qualitative observations of fluid motion, turbulence, and wave dynamics laid a visual and conceptual foundation (Capra (2008)). Later, Isaac Newton (1687) introduced the concept of viscosity, marking the early formalization of fluid resistance (Darrigol (2005)). Blaise Pascal's work on pressure in static fluids led to Pascal's Law, while Daniel Bernoulli's 'Hydrodynamica (1738)' connected energy conservation principles to fluid flow, resulting in the well-known Bernoulli's principle (Chalmers and Chalmers (2017), Truesdell (2012)).

The 19th century witnessed the mathematical codification of viscous fluid motion. The Navier–Stokes equations, developed by Claude-Louis Navier and George Gabriel Stokes, became the cornerstone of modern fluid dynamics. Concurrently, Henri Darcy's empirical studies of flow in porous media and Lord Kelvin's thermodynamic contributions expanded the applicability of fluid mechanics to natural and industrial systems (Darcy (1856), Crowther et al. (1948)).

(c) Experimental and boundary layer developments

A key experimental advancement was Reynolds' pipe flow experiment (1883), which distinguished laminar and turbulent regimes and introduced the Reynolds number as a fundamental flow parameter. This laid the groundwork for modern studies of flow stability and transition. Building on such insights, Prandtl's boundary layer theory (1904) revolutionized the analysis of viscous flows near solid surfaces (Prandtl (1905)). Blasius later provided analytical solutions for laminar boundary layers over flat plates (Blasius (1908)), while Sakiadis extended the theory to moving surfaces, enabling applications in polymer processing and coating flows (Sakiadis (1961)).

(d) Computational advancements and modern applications

The latter half of the 20th century witnessed the emergence of computational fluid dynamics (CFD), revolutionizing the ability to simulate complex, nonlinear flows across a wide range of applications. CFD enabled breakthroughs in aerospace, automotive, biomedical, and environmental engineering, transforming how fluid behavior is analyzed and optimized (Ferziger and Perić (2002)).

Contemporary relevance and research motivation

These historical developments have collectively laid the groundwork for modern explorations into complex fluid systems, including non-Newtonian fluids and nanofluids as described in Fagbenle et al. (2020). The foundational understanding of boundary layers, viscous effects, and porous media flows has been extended to incorporate nanoscale physics, thermophoresis, Brownian motion, and magnetohydrodynamics. Today, the modeling and control of such flows are crucial in cutting-edge applications such as energy systems, bioconvection, advanced cooling technologies, and chemical reactors. Motivated by this legacy, the present study aims to contribute to the evolving body of knowledge by investigating the thermo-hydrodynamic behavior of non-Newtonian nanofluids under diverse physical effects.

1.1.2 Theoretical background

1.1.2.1 Boundary layer flow

The boundary layer theory, developed by Ludwig Prandtl in 1904, forms a fundamental aspect of modern fluid dynamics. It describes the behavior of fluid flow close to a solid boundary where the effects of viscosity are significant. When a fluid flows past a solid surface, the velocity of the fluid particles adjacent to the surface equals the velocity of the surface (no-slip condition), while the velocity increases gradually as we move away from the surface, eventually matching the free-stream velocity outside the boundary layer (Schlichting and Gersten, 2016). The boundary layer, therefore, is the area in the neighborhood of the interfaces (solid/fluid or fluid/fluid), where the fluid variables evolve from the interface to the free-stream values. Boundary layer theory simplifies the analysis of complex fluid flows by dividing the flow domain into two regions: the boundary layer, where viscous effects are predominant, and the outer flow region, where the effects of viscosity can be neglected, and inviscid flow equations apply.

The flow inside the boundary layer may be laminar or turbulent. As shown in Fig. 1.1.1, the boundary layer is laminar in a short distance downstream from the leading edge of flat plate; transition occurs over a short region of the plate. The transition region extends downstream to the locations where the boundary-layer flow becomes completely turbulent. A

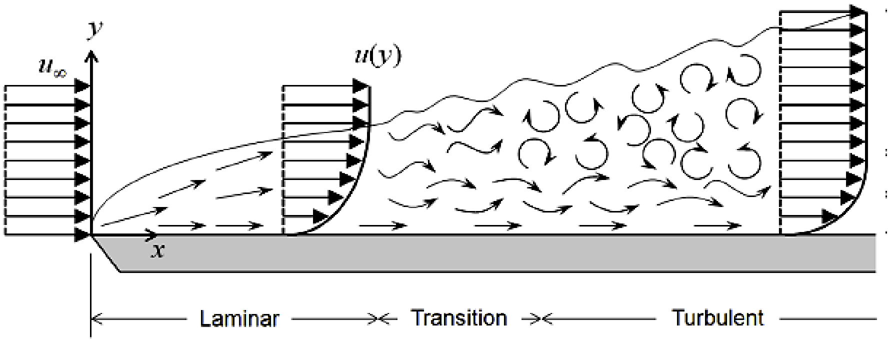

Figure 1.1.1: Velocity boundary layer development on a flat plate
doi:10.5120/ijca2018916374

key assumption in boundary layer theory is that within the thin layer near the wall, viscous forces are comparable to inertial forces along the flow direction. This assumption allows for the derivation of the boundary layer equations, which significantly simplify the governing Navier-Stokes equations in this region. The theory is fundamental in predicting skin friction, drag forces, heat transfer rates, and fluid resistance over surfaces.

There are three primary boundary layers: momentum, thermal, and concentration boundary layers. The momentum boundary layer, as depicted in Figure 1.1.1, develops due to viscosity, while the thermal boundary layer forms in response to a temperature gradient, with its thickness governed by the relative importance of thermal and momentum diffusivities (Cengel and Ghajar, 2020). Similarly, the concentration boundary layer controls species transport within a fluid through molecular diffusion, with its thickness determined by the ratio of momentum to mass diffusivity. These boundary layers interact in various engineering applications, including heat exchangers, aerodynamic flow control, and multiphase flow systems, where coupled heat and mass transfer significantly affect system performance.

1.1.2.2 Heat transfer process

Heat transfer in fluid mechanics is a critical aspect in many engineering applications such as cooling systems, heat exchangers, heat energy production, and materials processing. It involves the study of how thermal energy is transferred between fluids and solid boundaries or within the fluid itself due to temperature differences. The driving potential or the force which causes the transfer of energy as heat is the difference in temperature between systems. There are three modes of energy transfer: conduction, convection, and radiation.

a. Heat Conduction

Heat conduction is a mode of thermal energy transfer arising from the microscopic interactions of molecules or atoms, where particles with higher kinetic energy transfer energy to neighboring particles with lower kinetic energy. In fluid dynamics, conduction plays a significant role in stationary or slowly moving fluids, where molecular collisions govern the thermal transport.

The classical formulation of heat conduction was introduced by Joseph Fourier in 1822 (Baron Fourier et al., 2003), expressed mathematically as:

$$\boldsymbol{q}_h = -k\nabla T, \tag{1.1.1}$$

where $\boldsymbol{q}_h$ denotes the heat flux vector (W/m^2), k is the thermal conductivity of the medium $(\mathrm{W/mK})$, and ∇T represents the temperature gradient. This relation assumes that the thermal response is instantaneous, implying an infinite speed of heat propagation–a fundamental limitation of the Fourier model.

To address this physical inconsistency, the concept of finite thermal propagation speed was introduced by Cattaneo (1948). He proposed a modification to Fourier's law by incorporating a thermal relaxation time, leading to the Maxwell–Cattaneo model. This formulation accounts for the lag between the applied temperature gradient and the resultant heat flux.

Subsequently, Christov extended this model by incorporating frame-invariant (objective) derivatives, specifically using the Oldroyd upper-convected derivative, resulting in the Cattaneo–Christov heat flux model. This refined model ensures compatibility with the principles of continuum mechanics, particularly under time-dependent and deformable flow fields.

The Cattaneo–Christov heat flux model is given by:

$$\boldsymbol{q}_h + \lambda_1^\star \left(\frac{\partial \boldsymbol{q}_h}{\partial t} + \boldsymbol{v} \cdot \nabla \boldsymbol{q}_h - \boldsymbol{q}_h \cdot \nabla \boldsymbol{v} + (\nabla \cdot \boldsymbol{v}) \boldsymbol{q}_h \right) = -k\nabla T, \tag{1.1.2}$$

where $\boldsymbol{q}_h$ is the modified heat flux vector, $\lambda_1^\star$ is the thermal relaxation time, and $\boldsymbol{v}$ is the velocity field. This formulation leads to a hyperbolic-type energy equation, enabling the modeling of thermal wave phenomena–an essential feature in high-speed or microscale heat transfer processes.

b. Convection

This mode of heat transfer is by combined molecular diffusion and bulk flow. It plays a major role in fluid dynamics, especially in systems involving moving fluids or temperature gradients between solid surfaces and the fluid. Convection can occur in three forms. Natural (free) convection: when fluid movement is driven by buoyancy forces due to temperature-induced density changes, forced convection: when external forces (such as pumps or fans) drive fluid motion, and mixed convection: when both natural and forced convection contribute significantly to the fluid motion and heat transfer. It happens when buoyancy-driven and externally-driven forces act together. The rate equation for convective heat transfer was first expressed by Newton in 1701, and is referred to as Newton's law of cooling.

$$q = h(T_w - T_f), \tag{1.1.3}$$

where, q is the heat flux, h is the convective heat transfer coefficient $(\mathrm{W/m^2.K})$, T_w is the surface temperature and T_f is a characteristic fluid temperature.

c. Radiation

Radiation is the transfer of heat through electromagnetic waves without the need for a medium. Energy radiates from all types of matter under all conditions and at all times. The emission of thermal radiation arises from random fluctuations in the quantized internal energy states of the emitting matter (Howell et al. (2020)). In fluid dynamics problems, radiation is significant when the system involves high temperatures. Thermal radiation is an electromagnetic mechanism, which allows energy transport with the speed of light through regions of space that are devoid of any matter. Radiant energy exchange between surfaces or between a region and its surroundings is described by the Stefan-Boltzmann law, which states that the radiant energy transmitted is proportional to the difference of the fourth power of the temperatures of the surfaces. The heat flux (q) emitted by a real surface is given by:

$$q = \epsilon\sigma^{\star}T_w^4, \tag{1.1.4}$$

where, ϵ denotes the emissivity of the surface, $\sigma^{\star}$ is proportionality parameter known as the Stefan-Boltzmann parameter, T_w is the surface temperature.

In actual situations all heat-transfer processes involve combination of these mechanisms and the analysis of heat transfer is closely intertwined with the governing laws of fluid motion, including the Navier-Stokes equations, and is often considered alongside conservation laws of mass and momentum.

1.1.2.3 Mass transfer processes

Mass transfer is a fundamental process in fluid dynamics that describes the movement of mass from one point to another within a fluid system. It plays a crucial role in various engineering and scientific applications, including chemical processes, chemical reactors, heat exchangers, separation processes, environmental systems, and biological transport. Mass transfer can occur in single-phase or multiphase systems and is typically driven by concentration, temperature, or pressure gradients. Mass transfer in fluids occurs primarily through two mechanisms:

a. Diffusion Mass Transfer

Diffusion is the transport phenomenon by which molecular species move from regions of higher concentration to regions of lower concentration, primarily due to random thermal motion. In classical theory, this process is governed by Fick's law, which asserts that the diffusive mass flux is proportional to the negative gradient of concentration:

$$\boldsymbol{q}_m = -D\nabla C, \tag{1.1.5}$$

where $\boldsymbol{q}_m$ represents the mass diffusion flux $(\mathrm{kg/m^2 s})$, D is the mass diffusivity $(\mathrm{m^2/s})$, and C is the concentration of the species $(\mathrm{kg/m^3})$ (Kumar et al. (2023)). Like Fourier's law in heat conduction, Fick's law yields a parabolic partial differential equation, which inherently assumes an infinite speed of disturbance propagation. This assumption becomes physically unrealistic in certain contexts such as high-frequency oscillations, fast chemical reactions, or microscale and nanoscale transport systems.

To address this shortcoming and incorporate the finite speed of mass transport, the classical Fickian framework can be generalized by introducing a solutal relaxation time. This results in the Maxwell–Cattaneo model for mass diffusion. Analogous to the heat conduction case, Christov (2009) extended this model by replacing the time derivative with an objective (frame-invariant) Oldroyd upper-convected derivative, yielding the Cattaneo–Christov mass flux model.

The generalized non-Fickian mass flux model is given by:

$$\boldsymbol{q}_m + \lambda_2^\star \left(\frac{\partial \boldsymbol{q}_m}{\partial t} + \boldsymbol{v} \cdot \nabla \boldsymbol{q}_m - \boldsymbol{q}_m \cdot \nabla \boldsymbol{v} + (\nabla \cdot \boldsymbol{v}) \boldsymbol{q}_m \right) = -D\nabla C, \tag{1.1.6}$$

where $\boldsymbol{q}_m$ is the modified mass flux vector, $\lambda_2^\star$ denotes the solutal relaxation time, $\boldsymbol{v}$ is the velocity field, and D is the diffusion coefficient. This formulation leads to a hyperbolic-type species transport equation, enabling the modeling of finite-speed diffusion waves. It is particularly relevant for describing non-equilibrium mass transport in dynamically evolving or high-gradient environments.

b. Convective mass transfer

Convective mass transfer involves the bulk movement of a fluid carrying mass from one location to another. It occurs due to fluid motion and can be classified into:

- **Natural (Free) convection**: Caused by density differences due to concentration or temperature variations.
- **Forced convection**: Induced by external means such as a pump or fan.

The mass transfer rate in convection is often described using the convective mass transfer coefficient (h_m) and follows the relation:

$$q_m = h_m(C_s - C_\infty), \tag{1.1.7}$$

where C_s is the species concentration at the surface, and C_∞ is the concentration in the bulk fluid (Aboulhasanzadeh et al. (2012)).

1.1.2.4 Non-Newtonian fluids

Fluids can be classified into various categories based on their physical properties. Compressible and incompressible fluids are distinguished by their response to pressure changes. Incompressible fluids, like water, exhibit negligible changes in density under pressure, while compressible fluids, like gases, experience significant density variations.

Another classification is viscous and inviscid fluids. Viscous fluids have resistance to flow due to internal friction (viscosity), whereas inviscid fluids are idealized with no viscosity, simplifying fluid dynamics calculations.

Fluids are also classified as Newtonian and non-Newtonian based on how they respond to applied stress. Newtonian fluids, such as water and oil, follow Newton's law of viscosity, where the shear stress is directly proportional to the rate of strain.

$$\boldsymbol{\tau} = -\mu \dot{\boldsymbol{\gamma}}, \tag{1.1.8}$$

where, $\boldsymbol{\tau}$ is shear stress tensor, μ is proportionality constant fluid viscosity, and $\dot{\boldsymbol{\gamma}} = \nabla \boldsymbol{v} + (\nabla \boldsymbol{v})^t$ is rate of strain tensor. Eq. (1.1.8) can be extended to the more generalized version of Newton's viscosity relation in the vector-tensor notation as:

$$\boldsymbol{\tau} = -\mu\Big(\nabla \boldsymbol{v} + (\nabla \boldsymbol{v})^t\Big) + \Big(\frac{2}{3}\mu - \boldsymbol{\kappa}\Big)\Big(\nabla . \boldsymbol{v}\Big)\boldsymbol{\delta}, \tag{1.1.9}$$

here, $\boldsymbol{\delta}$ represents the Kronecker delta tensor and $\boldsymbol{\kappa}$, the dilatational viscosity, is identically zero for monatomic gases at low density. Moreover, for incompressible liquids $(\nabla.\boldsymbol{v}) = 0$, and therefore the second term is discarded anyway.

In contrast, non-Newtonian fluids are fluids with a stress that can have a nonlinear and/or temporal dependence on the rate of deformation. As described in (Guedda (2007)), the physical origin of a non-Newtonian behavior mainly relates to the microstructure of the material. For example, polymeric materials, including solutions and melts, consist of molecules with extremely high molecular weights, often in the range of hundreds of millions. In a quiescent state, these long-chain molecules typically adopt a coiled configuration and may become entangled with one another. The resulting flow phenomena depend on this interaction, and in general will produce viscoelastic behavior.

Non-Newtonian fluids do not have a constant viscosity. Their viscosity can change under stress, time, or deformation history. These fluids are classified into several types:

- Shear-thinning (pseudoplastic) fluids, like paint or blood, where viscosity decreases with increasing shear rate.
- Shear-thickening (dilatant) fluids, such as cornstarch in water, where viscosity increases with shear rate.
- Viscoelastic (memory) fluids, like lubricants and Silly Putty, where the stress depends in a well-defined way on the history of the deformation.
- Thixotropic fluids, like ketchup, where the shear stress (or apparent viscosity) decreases with increasing time of application of a constant shear rate.
- Rheopetic fluids, wherein the shear stress (or the apparent viscosity) increases with increasing time of application of a constant shear rate.
- Bingham plastics, like toothpaste, require a yield stress to flow, behaving as solids under low stress. For Bingham plastic fluid, the shear stress beyond the yield stress is linearly proportional to the shear rate. If the yield stress approaches zero, the Bingham plastic fluid can be approximately treated as a Newtonian fluid.

These types of non-Newtonian fluids discussed above are presented in Figure 1.1.2.

Non-Newtonian fluids are crucial in many industries, from pharmaceuticals to food processing and polymer manufacturing. Understanding their behavior is essential for designing equipment and optimizing processes involving complex flow conditions, such as in biological systems, chemical reactors, and material science. Nonetheless, a major challenge in analyzing non-Newtonian fluids arises from the absence of a universally applicable equation of state

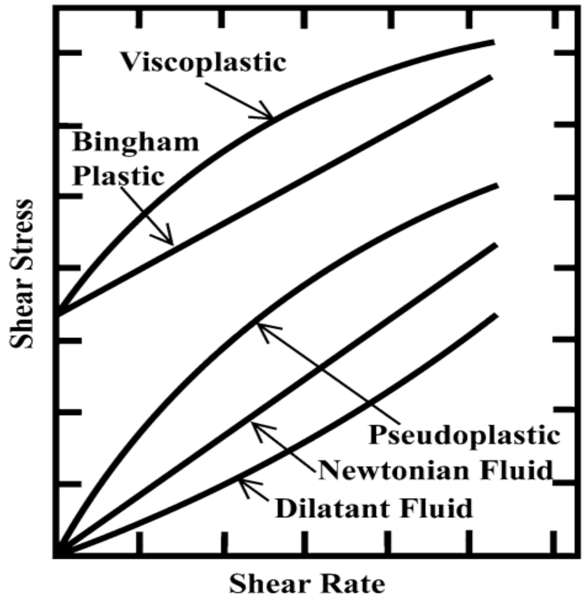

Figure 1.1.2: The different types of non-Newtonian fluids
Fagbenle et al. (2020)

relating the stress tensor to the flow conditions, due to the diverse classifications of these fluids. Some attempts designed to arrive at a generalized formulation to describe the rheological properties of these fluids as discerned by Byron et al. (2002) are:

a. **The generalized Newtonian models**

These models primarily describe steady-state shear flows, capturing non-Newtonian viscosity effects but not normal stress, time-dependent, or elastic effects. For incompressible generalized Newtonian fluids, the stress tensor is expressed as:

$$\boldsymbol{\tau} = -\eta(\dot{\gamma})\left[\nabla \boldsymbol{v} + (\nabla \boldsymbol{v})^t\right] = -\eta(\dot{\gamma})\mathbf{D}_1, \tag{1.1.10}$$

where $\mathbf{D}_1 = \nabla \boldsymbol{v} + (\nabla \boldsymbol{v})^t$ is the rate-of-strain tensor, and $\dot{\gamma} = \sqrt{\frac{1}{2}\mathrm{tr}(\mathbf{D}_1^2)}$ is the shear rate magnitude. The non-Newtonian viscosity $\eta(\dot{\gamma})$ has several empirical expressions:

i. **Power-law model**:

$$\eta = m\dot{\gamma}^{n-1}, \tag{1.1.11}$$

ii. **Carreau fluid model**:

$$\eta = \eta_\infty + (\eta_0 - \eta_\infty)\left[1 + (\Gamma_1\dot{\gamma})^2\right]^{\frac{n-1}{2}}, \tag{1.1.12}$$

iii. **Williamson fluid model**:

$$\eta = \eta_\infty + \frac{\eta_0 - \eta_\infty}{1 - \Gamma_1\dot{\gamma}}, \tag{1.1.13}$$

where η_0 and η_∞ are the zero and infinite shear rate viscosities respectively, Γ_1 is a relaxation time, and m, n are fluid parameters.

b. Elasticity and the linear viscoelastic model

This model introduces time dependence into Newton's law of viscosity while preserving linearity. It is derived by combining Newton's law for viscous fluids and Hooke's law for elastic solids. Two common linear viscoelastic models are:

i. **Maxwell model**:

$$\boldsymbol{\tau} + \lambda_1 \frac{\partial \boldsymbol{\tau}}{\partial t} = -\eta_0 \dot{\boldsymbol{\gamma}}, \tag{1.1.14}$$

ii. **Jeffrey model**:

$$\boldsymbol{\tau} + \lambda_1 \frac{\partial \boldsymbol{\tau}}{\partial t} = -\eta_0 \left(1 + \lambda_2 \frac{\partial}{\partial t}\right) \dot{\boldsymbol{\gamma}}, \tag{1.1.15}$$

where λ_1 is the relaxation time and λ_2 is the retardation time.

c. Nonlinear viscoelastic models

These models generalize the linear models and are capable of describing all types of flow. They assume that the constitutive relation between the stress and kinematic tensors should be invariant under the instantaneous orientation of the fluid particle. A typical nonlinear viscoelastic constitutive equation is:

$$\boldsymbol{\tau} + \lambda_1 \frac{\partial \boldsymbol{\tau}}{\partial t} + \frac{1}{2}\mu_0 \mathrm{tr}(\boldsymbol{\tau})\dot{\boldsymbol{\gamma}} - \frac{\mu_1}{2}(\dot{\boldsymbol{\gamma}} \cdot \boldsymbol{\tau} + \boldsymbol{\tau} \cdot \dot{\boldsymbol{\gamma}}) = -\eta_0 \left(\dot{\boldsymbol{\gamma}} + \lambda_2 \frac{\partial \dot{\boldsymbol{\gamma}}}{\partial t} - \mu_2 \dot{\boldsymbol{\gamma}} \cdot \dot{\boldsymbol{\gamma}}\right), \tag{1.1.16}$$

where λ_1, λ_2, μ_0, μ_1, and μ_2 are time-related parameters. The stress and strain-rate tensors are considered in a corotating frame.

In this dissertation, the Carreau and Williamson models are selected from the generalized Newtonian category, while the Maxwell model represents the linear viscoelastic class. The nonlinear viscoelastic model is recommended for future research due to its comprehensive capability in modeling complex flow behaviors.

1.1.2.5 Nanofluids flow models and their applications

Nanofluids, a recent innovation in thermal sciences, have garnered substantial attention due to their enhanced thermophysical properties and potential for improving heat transfer processes. These fluids are engineered by dispersing nanometer-sized particles into base fluids, resulting in significantly improved heat transfer characteristics compared to conventional fluids. Traditional heat transfer media such as water, ethylene glycol, and oil exhibit low thermal conductivity, which limits their effectiveness in thermal management systems. Conversely, solid particles possess higher thermal conductivities; however, early attempts to enhance heat transfer by dispersing micrometer-sized particles introduced challenges, including sedimentation, channel clogging, and elevated viscosity.

In 1995, Choi and Eastman (Choi and Eastman (1995)) at Argonne national laboratory introduced the concept of nanofluids-suspensions of nanoparticles (e.g., metals, metal oxides, and carbides) with sizes below 100 nm in conventional base fluids. This innovation addresses the limitations associated with larger particles and significantly enhances the thermal performance of the base fluids. The growing demand for improved heat transfer media has driven researchers to explore such advanced alternatives.

Nanofluids exhibit markedly improved thermal properties, including increased thermal conductivity, altered thermal expansion coefficients, modified viscosity, and enhanced specific heat, all of which contribute to superior heat transfer performance.

In the progression of nanofluid research, two primary modeling approaches have been developed: the single-phase and two-phase models. The two-phase model, pioneered by Buongiorno (2006), accounts for a non-zero relative velocity between the nanoparticles and the base fluid. It incorporates the effects of Brownian motion and thermophoretic diffusion, enabling a more accurate representation of the heat and mass transfer processes involving both the dispersed and continuous phases.

According to Buongiorno, the nanoparticle mass flux resulting from Brownian diffusion and thermophoresis is expressed as

$$\boldsymbol{j}_p = \boldsymbol{j}_b + \boldsymbol{j}_t = -\rho_p D_b \nabla\phi - \rho_p D_T \frac{\nabla T}{T_\infty}, \tag{1.1.17}$$

where ρ_p denotes the nanoparticle density, ϕ represents the nanoparticle volume fraction (concentration), T is the local fluid temperature, and T_∞ is the reference temperature. D_b is Brownian motion and D_T is thermophoresis diffusion given respectively as:

$$D_b = \frac{k_b T}{3\pi\mu_f d_p}; \ \ D_T = \left(\frac{\mu_f}{\rho_f}\right)\left(\frac{0.26k_f}{2k_f + k_p}\right), \tag{1.1.18}$$

where, k_b stands for Boltzmann's constant, μ_f represents the viscosity of the base fluid, d_p signifies the nanoparticle diameter, ρ_f denotes the density of the base fluid, and k_f and k_p correspond to the thermal conductivity of the base fluid and nanoparticles, respectively.

The equation for mass transfer in the absence of chemical reaction is generally presented as:

$$\frac{D\phi}{Dt} = -\frac{1}{\rho_p}\nabla.\boldsymbol{j}_p. \tag{1.1.19}$$

Therefore, equation of nanoparticles mass transport turns into:

$$\frac{\partial \phi}{\partial t} + \boldsymbol{v}.\nabla \phi = \nabla.\left(D_b \nabla \phi + D_T \frac{\nabla T}{T_\infty} \right), \tag{1.1.20}$$

where $\boldsymbol{v}$ is the nanofluid velocity. Recently, Khan et al. (2024) examined the Buongiorno model and melting heat transfer in nonlinear mixed convective flow.

In contrast to the two-phase approach, the single-phase model, initially proposed by Tiwari and Das (2007), assumes thermal equilibrium between the base fluid and the suspended nanoparticles. This model neglects interphase heat transfer and interaction forces, treating the nanofluid as a homogeneous medium. The governing equations are therefore formulated for an effective continuous phase. A comprehensive comparison of single- and two-phase nanofluid models for laminar flow over a stretching sheet was recently conducted by Rehman et al. (2024), offering insights into their respective capabilities and limitations.

Nanofluids find application across diverse fields such as engineering, energy systems, biomedicine, and environmental science. Their unique thermal, mechanical, and rheological properties enhance performance in various systems, including solar collectors, heat exchangers, automotive cooling systems, and seawater desalination units, as illustrated in Figure 1.1.3.

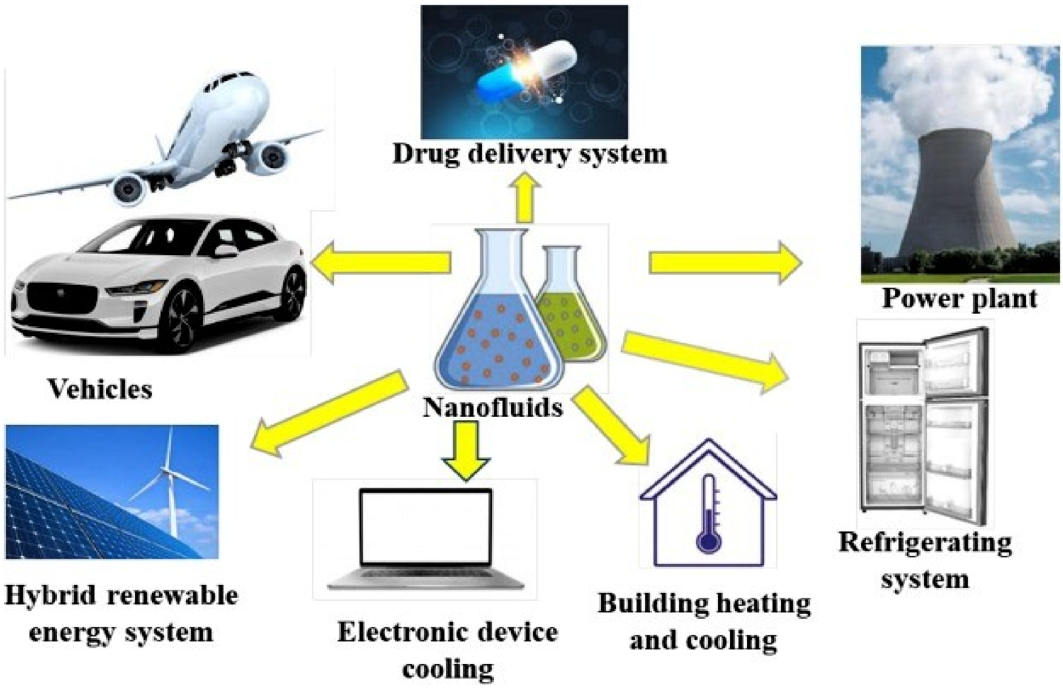

Figure 1.1.3: Applications of nanofluids: https://doi.org/10.1016/j.enconman.2022.115790

In electronic cooling, for example, the use of nanofluids improves the heat transfer coefficient by significantly increasing the coolant's thermal conductivity. In biomedical applications, magnetic nanofluids are employed in imaging techniques, targeted drug delivery, cancer therapy, and cell separation.

1.1.2.6 Flows in porous media

A porous medium is a fixed solid matrix with a connected void space through which a fluid can flow. The fraction of void space to total volume is called the porosity. These media are ubiquitous in both natural and engineered systems, including soil, biological tissues, insulation materials, ceramic engineering, packed bed reactors, food technology, and fibrous composites. The transport of fluids through porous media is fundamentally governed by the interactions between the fluid and the solid matrix, and is characterized by complex momentum and energy exchange mechanisms. As such, understanding fluid flow behavior in porous substrates is essential in numerous disciplines such as geophysics, petroleum engineering, chemical processing, and biomedical engineering. Figure 1.1.4 illustrates a high-resolution image of the velocity field within an isotropic porous medium. The velocity distribution reveals a relatively uniform profile at low flow rates, transitioning into a more dispersed pattern in the advective, non-diffusive regime.

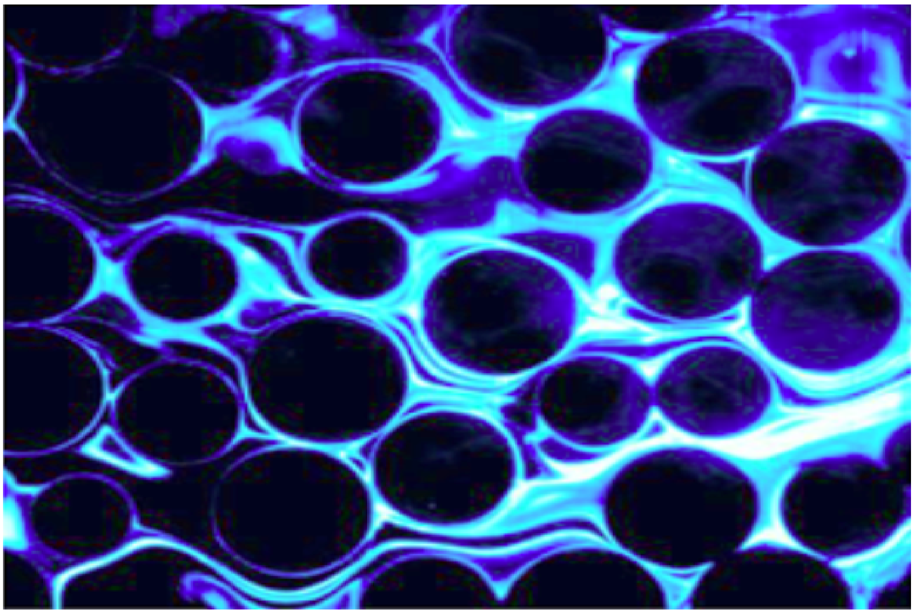

Figure 1.1.4: Flow in porous media
https://doi.org/10.1017/jfm.2020.113

The classical foundation for modeling fluid flow in porous media is Darcy's law, proposed by Henry Darcy in 1856. Darcy's law, which in its refined modern form can be expressed as follows:

$$\frac{\partial p}{\partial x} = -\frac{\mu \xi}{K^\star}\boldsymbol{v}, \tag{1.1.21}$$

where $\dfrac{\partial p}{\partial x}$ is the pressure gradient, $\boldsymbol{v}$ is Darcy velocity, μ is the fluid viscosity and $K^\star$ is the permeability of porous medium [m^2], and ξ is porosity of the medium. Darcy's law holds under the assumption of slow, laminar, and viscous-dominated flow conditions typically associated with low Reynolds numbers.

However, Darcy's law becomes insufficient for describing flows at higher velocities where inertial effects become non-negligible. To address this limitation, Forchheimer, (1901) introduced a nonlinear correction by incorporating an additional inertial term into Darcy's equation, leading to the Darcy–Forchheimer model:

$$\frac{\partial p}{\partial x} = -\frac{\mu \xi}{K^{\star}}\boldsymbol{v} - \frac{c_F \xi \rho}{K^{\star 1/2}} v \boldsymbol{v}, \tag{1.1.22}$$

where c_F is the Forchheimer coefficient, and ρ is the fluid density. This model provides a more accurate description of flow in porous media at moderate to high velocities and has been widely applied in simulations of filtration, enhanced oil recovery, and groundwater hydrology.

For incompressible flow, the momentum equation incorporating porous media total drag force per unit volume in the absence of gravitational and Lorentz forces is (Hsu and Cheng (1990); Anwar and Rasheed (2017)), given by:

$$\boldsymbol{B} = -\Big[\frac{\mu_f \xi \boldsymbol{v}}{K^{\star}} + \frac{\rho c_F \xi \boldsymbol{v}|\boldsymbol{v}|}{\sqrt{K^{\star}}}\Big]$$

leading to the modified momentum equation:

$$\rho\left[\frac{\partial \boldsymbol{v}}{\partial t} + \boldsymbol{v}\cdot(\nabla \boldsymbol{v})\right] = \nabla\cdot\boldsymbol{\tau} - \left[\frac{\mu_f \xi \boldsymbol{v}}{K^{\star}} + \frac{\rho c_F \xi \boldsymbol{v}|\boldsymbol{v}|}{\sqrt{K^{\star}}}\right]. \tag{1.1.23}$$

In recent years, the study of non-Newtonian nanofluid flows through porous media has gained significant attention due to the combined complexity and rich physics arising from non-Newtonian rheology, nanoscale thermal effects, and porous confinement.

The intersection of non-Newtonian nanofluid dynamics and porous media flow is particularly relevant in bioengineering, thermal insulation, drug delivery, chemical reactors, and microfluidic systems, where controlling flow resistance and heat/mass transport is critical. For instance, Al-Chlaihawi et al. (2022) studied Newtonian and non-Newtonian hybrid nanofluid flow in porous media under conjugate natural convection, demonstrating that the high surface area and complex pore structure of porous media can significantly enhance convective heat transfer in various applications. Recently, Jubair et al. (2025) examined the influence of pollutant discharge concentration on the flow behavior of non-Newtonian nanofluids over a permeable Riga surface under the effects of thermal radiation.

Despite the progress, several challenges and open questions remain. The coupling between complex rheological models and porous media flow resistance, in non-Newtonian nanofluids demand further investigation. Moreover, the interaction between stretching or rotating boundaries and porous substrates introduces additional flow complexities that are not fully addressed in existing models.

Therefore, the current study is motivated by the need to advance understanding of boundary layer flows involving non-Newtonian nanofluids over stretchable and rotating surfaces embedded in porous media. Such analyses can contribute to the design of more efficient thermal management systems, filtration devices, and advanced manufacturing processes.

1.1.2.7 Motile microorganisms induced bioconvective flows

Bioconvection refers to the spontaneous, collective fluid motion that arises in suspensions of self-propelled, motile microorganisms–typically denser than the surrounding fluid medium. These microorganisms, such as Chlamydomonas nivalis and Euglena, often exhibit upward swimming behavior due to external stimuli like gravity, light, or chemical gradients. As they accumulate near the upper regions of the fluid column, localized increases in density lead to gravitational instabilities that initiate convective motion and generate organized bioconvective patterns.

Mandal et al. (2023) elaborated that the motility of microorganisms is governed by two principal mechanisms: taxis and kinesis. Taxis refers to directed movement in response to environmental cues. For instance, phototactic organisms swim toward (positive phototaxis) or away from (negative phototaxis) light sources, while chemotactic and oxytactic responses are driven by gradients in chemical substances or oxygen, respectively. Euglena demonstrates positive phototaxis by orienting toward light, whereas mosquitoes exhibit negative phototaxis by avoiding it. In contrast, kinesis describes random, undirected motion that varies with stimulus intensity but not direction.

Among the various forms of taxis, gyrotaxis and oxytaxis are particularly relevant to bioconvection. Bottom-heavy algae, such as Chlamydomonas, exhibit gyrotactic behavior due to their asymmetric mass distribution. In quiescent fluid, they swim upward, while in shear flows, their orientation results from a balance between gravitational torque and viscous drag, often aligning them with downwelling fluid. Oxytactic bacteria respond to oxygen gradients by migrating toward regions of higher oxygen concentration, forming dense microbial layers and enhancing oxygen uptake from the environment. These motility behaviors, especially when coupled with the presence of nanoparticles in nanofluids, can influence the transport properties of the system (Sadiq et al. (2024)). The resulting bioconvection enhances mixing, alters heat and mass transfer, and plays a critical role in applications involving bioreactors, biosensors, and environmental processes.

There exist three major mechanisms responsible for the transport of microorganisms:

macroscopic convection, random motion, and self-propelled swimming. The conservation of microorganism population is mathematically described by (Kuznetsov (2010)):

$$\frac{\partial n}{\partial t} = -\nabla \cdot \Xi_1, \tag{1.1.24}$$

where

$$\Xi_1 = n\boldsymbol{v} + nW_c\hat{\boldsymbol{p}} - D_m \nabla n, \tag{1.1.25}$$

is the total flux of microbes due to fluid convection, microorganism self-propulsion, and diffusion. Here, $n\boldsymbol{v}$ represents the flux due to advection, n is the motile microorganism density, $W_c\hat{\boldsymbol{p}}$ denotes the average relative swimming velocity, W_c is assumed constant, $\hat{\boldsymbol{p}}$ is a unit vector representing the average orientation of cells, and D_m is the microbial diffusivity.

In recent years, bioconvection has attracted considerable interest due to its relevance in various biological and engineering systems. It plays a critical role in the mixing and transport processes in microbial bioreactors, wastewater treatment systems, biosensors, and microfluidic devices. The integration of nanofluids into bioconvective flow systems presents an exciting area of research, especially in the context of thermal management and biomedical applications. When combined with bioconvective effects induced by motile microorganisms, such hybrid systems can significantly influence heat and mass transfer characteristics. This synergy is particularly relevant in microscale and nanoscale devices where passive cooling methods are inefficient.

1.1.2.8 Magnetohydrodynamics

MHD is the branch of continuum mechanics which deals with the motion of an electrically conducting fluid in the presence of a magnetic field. The subject is also sometimes called 'hydromagnetics' or 'magneto-fluid dynamics'. This field combines principles of fluid dynamics and electromagnetism, governing the interaction between the flow of the conducting fluid (such as plasmas, liquid metals, and some nanofluids) and the applied magnetic field. The fluid in question must be electrically conducting and non-magnetic. The motion of conducting material across the magnetic lines of force cause electric currents to flow. The magnetic fields associated with these currents modify the magnetic field which creates them. On the other hand, the flow of electric current across a magnetic field is associated with a body force, the so-called Lorentz force, which influences the fluid flow. It is this intimate interdependence of hydrodynamics and electrodynamics which really defines and characterizes magnetohydrodynamics. There are four fundamental equations of electromagnetism known as Maxwell's equations which can be written in differential forms.

$$\nabla.\boldsymbol{B} = 0 \qquad \text{(Gauss law in magnetostatics)}, \tag{1.1.26}$$

$$\nabla.\boldsymbol{E} = \frac{\rho_e}{\epsilon_0} \qquad \text{(Gauss law in electrostatics)}, \tag{1.1.27}$$

$$\nabla \times \boldsymbol{B} = \mu_0\Big(\boldsymbol{J} + \epsilon_0\frac{\partial \boldsymbol{E}}{\partial t}\Big) \qquad \text{(Ampere-Maxwell equation)}, \tag{1.1.28}$$

$$\nabla \times \boldsymbol{E} = -\frac{\partial \boldsymbol{B}}{\partial t} \qquad \text{(Faraday's Law)}, \tag{1.1.29}$$

where,

$$\boldsymbol{J} = \sigma_0\Big(\boldsymbol{E} + \boldsymbol{v} \times \boldsymbol{B}\Big). \tag{1.1.30}$$

In the above description, $\boldsymbol{J}$ is the current density, μ_0 is the magnetic permeability, $\boldsymbol{E}$ is the electric field, ρ_e is the charge density, $\boldsymbol{B}$ is the magnetic field, ϵ_0 is the permittivity of free space, and σ_0 is the fluid's electrical conductivity. Since in MHD the electric force is minute by comparison with the Lorentz force, the electromagnetic force **F** is expressed as

$$\boldsymbol{F} = \boldsymbol{J} \times \boldsymbol{B} = \sigma_0\Big(\boldsymbol{v} \times \boldsymbol{B}\Big) \times \boldsymbol{B}. \tag{1.1.31}$$

It is noticed that when the density of an electrically conducting fluid is low and/or applied magnetic field is strong, the Hall and ion slip effects become significant. The Hall effect refers to the generation of a secondary electric field perpendicular to both the flow and the applied magnetic field due to the Lorentz force. The ion slip effect accounts for the drift of ions relative to neutral particles in a weakly ionized fluid, resulting in altered electrical conductivity. When the Hall and ion slip effects are included, the current density, $\boldsymbol{J}$ is modified. The modified Ohm's law incorporating Hall and ion slip effects (Ghara et al. (2012)) is:

$$\boldsymbol{J} = \sigma_0\Bigg(\boldsymbol{E} + \boldsymbol{v} \times \boldsymbol{B}\Bigg) - \frac{\omega_e\tau_e}{B_0}\Bigg(\boldsymbol{J} \times \boldsymbol{B}\Bigg) - \frac{\omega_e\tau_e\beta_i}{B_0^2}\Bigg[\Bigg(\boldsymbol{J} \times \boldsymbol{B}\Bigg) \times \boldsymbol{B}\Bigg], \tag{1.1.32}$$

where, $\omega_e\tau_e = \beta_e$ is Hall parameter, ω_e is the electron cyclotron frequency and τ_e is the electron collision time, β_i is ion slip parameter, and B_0 is the magnitude of the magnetic field.

In MHD, the fluid flow equations are modified to account for the Lorentz force, which arises due to the interaction between the fluid's velocity field and the magnetic field.

1.1.2.9 Thermodynamic basis of entropy and irreversibility

The second law of thermodynamics is a fundamental principle governing the direction of thermodynamic processes and the quality of energy transformations. It introduces the concept of entropy, a measure of energy dispersion or disorder, and provides criteria for the irreversibility of natural processes. At its core, the second law asserts that natural processes tend to move towards a state of greater entropy, indicating a progression toward thermodynamic equilibrium. It places limitations on the efficiency of energy conversion systems, such as engines, refrigerators, and heat exchangers, and underpins the theoretical maximum performance of thermal devices.

Entropy generation analysis provides enormous importance in real-world engineering systems such as for efficiency studies, cost accounting, and economic analyses (Magagula et al. (2020)). For example, sustainability objectives and initiatives across the world towards a more sustainable environment demand an optimal use of resources whereby entropy generation assessments play a significant role. In engineering systems, especially those involving nanofluids and biological mechanisms such as bioconvection, the second law provides a framework for assessing entropy generation and thermodynamic irreversibility, both critical in optimizing heat and mass transfer processes.

The second law of thermodynamics states:

$$\Delta S_{\text{total}} = \Delta S_{\text{system}} + \Delta S_{\text{surrounding}} \equiv S_{\text{gen}} > 0, \tag{1.1.33}$$

where ΔS_{total} is the total entropy changes, and S_{gen} is the rate of entropy generation due to irreversibilities. For a process to take place or for a device to function $S_{\text{gen}} > 0$. The greater the value of S_{gen}, the lower the efficiency of the device, process, or system.

Entropy generation in boundary layer flows has become a major focus of current research. The boundary layer, an open thermodynamic system, experiences energy losses to the environment primarily due to irreversibility. Irreversibility is the destruction of useful energy or entropy generation. Since entropy generation measures inefficiencies in engineering systems, minimizing it is essential for enhancing the performance of thermal and fluid processes. Irreversible processes include drag (friction), heat addition, diffusion of species, chemical reactions, Joule heating, fluid viscosity in a flow, heat diffusion, and many more. This energy loss reduces the efficiency of the several cycles, making the assessment of entropy generation in convective boundary layers crucial for optimization. In particular, research on entropy generation in laminar boundary layers can inform the optimal design of bodies to enhance heat, mass, and momentum transfer.

The governing equation for local entropy generation due to flow and heat transfer, according to Fagbenle et al. (2020), is given by:

$$S_{\text{gen}} = S_{\text{gen}}(\text{friction}) + S_{\text{gen}}(\text{thermal}) + S_{\text{gen}}(\text{other effects}), \tag{1.1.34}$$

where "other effects" may include entropy generation due to viscous dissipation, fluid damping

(Darcy and non-Darcy), electromagnetic fields, and chemical reactions.

1.2 Statement of the Problem

The analysis of heat and mass transfer in boundary layer fluid flow plays a vital role in various scientific and engineering applications. In particular, non-Newtonian fluids–characterized by diverse rheological behaviors such as shear thinning, shear thickening, viscoelastic, and yield stress–have gained considerable attention since the mid-20$^{\text{th}}$ century. These fluids are found in numerous industrial processes involving food products, polymers, biomedical substances, and slurries (Subhas and Veena (1998), Khan and Khan (2014)). Their complex flow behavior challenges classical models, necessitating advanced formulations to accurately capture transport phenomena. The integration of nanotechnology into non-Newtonian fluid system has further enriched the field. Nanofluids exhibit enhanced thermal conductivity and heat transfer performance. While both simple and hybrid nanofluids have been extensively studied (Masuda et al. (1993), Ramesh et al. (2012), Bouslimi et al. (2021), Gamachu and Ibrahim (2023)), the combined behavior of nanoparticles within non-Newtonian fluids remains an evolving area of research.

Magnetohydrodynamics plays significant role in regulating flow behaviour and is crucial in applications such as polymer extrusion, cooling systems, and MHD generators. Although studies have examined the effects of Joule heating, Hall currents, and ion slip (Sheikholeslami and Ganji (2015), Ibrahim and Anbessa (2020), Jalili et al. (2023c), Mahmood et al. (2023)), their collective influence on non-Newtonian nanofluids requires further characterization, particularly in hybrid nanofluid and unsteady flow configurations. Furthermore, bioconvection introduces additional non-linearities to the transport equations. When coupled with chemical reactions, this phenomenon significantly alters flow dynamics. Recent works (Gangadhar et al. (2024), Bilal et al. (2024)) suggest that bioconvection can enhance or suppress transport rates in nanofluids, but its role in conjunction with MHD effects and non-Newtonian behavior is not yet fully understood.

Thermal radiation becomes significant in high-temperature environments, where radiative heat flux may rival conductive and convective modes. Yet, its incorporation into non-Newtonian nanofluid models–especially within complex geometries–remains limited (Howell et al. (2020)). Similarly, mixed convection, resulting from the interaction of buoyancy-driven and forced convection, introduces additional coupling between thermal and hydrodynamic fields. In porous media, such interactions are influenced by Darcy–Forchheimer drag and permeability effects. Suction and injection at the boundary further alter boundary layer thickness and stability, making them relevant for modern applications such as chemical vapor deposition and filtration (Nazari et al. (2020), Li et al. (2024)).

Moreover, many thermophysical properties-such as viscosity, thermal conductivity, and solutal diffusivity-are temperature or concentration dependent (Prasad et al. (2024)). These variations, along with transport phenomena such as Soret and Dufour diffusion, further complicate modeling efforts. Non-Fourier and non-Fick flux theories, which account for finite relaxation times in heat and mass diffusion, also demand deeper investigation to better reflect nanoscale transport behavior.

Despite notable progress, gaps remain in understanding the heat and mass transfer mechanism of non-Newtonian nanofluid systems with the combined effects of Lorentz and porous medium drag forces, nonlinear radiation, Ohmic heating, chemical reactions, variable thermophysical properties, mixed and microorganism-induced convection. Additionally, entropy generation, a crucial measure of thermodynamic irreversibility, is often overlooked in studies involving hybrid nanofluids.

1.3 Objectives of the study

1.3.1 General objective

The general objective of this dissertation is to analyze the boundary layer heat and mass transfer in non-Newtonian nanofluids flow over stretching surfaces

1.3.2 Specific objectives

The specific objectives of the dissertation are to:

1. examine the effects of key governing parameters on velocity, temperature and concentration fields.

2. investigate the influence of nonlinear radiation, Joule heating, and chemical reactions on MHD Carreau nanofluid flow through a porous medium.

3. examine MHD thermobioconvective flow of 3D rotating Williamson nanofluid in an exponentially stretching porous surface considering various flow phenomena using `SLLM`.

4. compare entropy generation and Cattaneo–Christov heat flux mechanisms in binary and ternary hybrid Maxwell nanofluid flows.

5. examine the effects of non-Fourier heat flux and non-Fick's mass flux in bioconvective nanofluid flow over a stretching cylinder.

6. investigate the impact of variable thermophysical properties, thermal radiation, and chemical reactions on unsteady Williamson nanofluid flow over a rotating cone.

1.4 Significance of the study

According to the literature, researchers have been interested in the transport properties of non-Newtonian nanofluids since the 1950s due to increasing global demand for efficient energy transport and utilization, as well as the production of persistent heat-transferring equipment used in various human activities such as process industries (e.g., food, polymers, emulsions), petroleum industry, lubrication, surface coating, biomedical, environmental remediation, and anaerobic digestion. To this end, this study has the following significance.

1. It gives mathematical model representing boundary layer heat and mass transfer characteristic in the regime of non-Newtonian nanofluid flows that can have a potential benefits in the fields of engineering, biotechnology, process and petroleum industries, medical and pharmaceutical activities.

2. It advances the understanding of heat and mass transfer behavior in non-Newtonian nanofluids subject to various physical factors.

3. It provides an efficient computational technique for simulating similar flow problems.

4. It can be used by other researchers as a reference for further advances in the field of MHD thermobioconvective flow of non-Newtonian nanofluids.

1.5 Scope of the study

This dissertation focuses on the theoretical and numerical analysis of boundary layer heat and mass transfer in non-Newtonian nanofluids over stretching and rotating surfaces. The study is confined to laminar, incompressible boundary layer flow, with the governing equations derived from the conservation of mass, momentum, and energy. Similarity transformations are employed to reduce the coupled partial differential equations to a system of ordinary differential equations, which are solved using the MATLAB `bvp4c` solver and spectral methods. The analysis focuses on the influence of key physical parameters on the velocity, temperature, and concentration fields, as well as on the surface heat and mass transfer rates.

1.6 Organization of the dissertation

This dissertation is structured to systematically address the challenges associated with boundary layer heat and mass transport phenomena in non-Newtonian nanofluids. It begins with an introduction to the fundamental principles of fluid mechanics, providing the necessary background for understanding the study. Following this, chapter two provides a comprehensive literature review to examine existing research, highlight key findings, and identify gaps in the study of boundary layer heat and mass transfer in non-Newtonian nanofluid flows.

Chapter three discusses the numerical methods used to solve the nondimensionalized and transformed system of ordinary differential equations of the study. With this foundation established, chapter four explores the flow, heat, and mass transport characteristics of MHD Carreau nanofluid flows in porous media over a stretching sheet, considering various modulating factors. Chapter five focuses on the thermo-bioconvective flow of MHD Williamson nanofluid, incorporating nonlinear thermal radiation, double diffusion, mixed convection, and heat generation or absorption over an exponentially extending vertical sheet.

Chapter six extends the analysis to entropy generation and Cattaneo-Christov heat flux in binary and ternary hybrid Maxwell nanofluids within a porous medium over radially stretching and rotating horizontal disks. Additionally, the effects of non-Fourier-Fick's heat and mass flux in bioconvective Carreau nanofluid flows over a stretching cylinder, incorporating suction/injection and convective boundary conditions is examined in chapter seven. In chapter eight, the dissertation also investigates the unsteady Williamson nanofluid flow over a rotating cone under the influence of variable transport properties, thermal radiation, and chemical reactions. Finally, the study concludes by summarizing the key findings and providing recommendations for future research directions.

CHAPTER TWO

Review of the Literature

This chapter provides an in-depth review of the scientific studies conducted on the boundary layer heat and mass transfer properties of non-Newtonian nanofluids. The review systematically addresses the influence of various flow modulators, including drag forces arising from the application of magnetic field and porous media, mixed convection, thermal radiation, bioconvection, Brownian and thermophoretic diffusion, chemical reactions, viscous dissipation, suction/injection, CC heat and mass flux, convective boundary conditions, heat generation/absorption, and variable thermo-solutal properties. Through this analysis, existing research gaps and challenges in the field have been critically identified, forming the basis for the current study.

2.1 Heat and Mass Transfer in non-Newtonian Nanofluid Regime

In recent years, non-Newtonian nanofluids have garnered substantial attention within the scientific community due to their complex rheological behavior, characterized by a nonlinear relationship between stress and deformation rate. These fluids play a pivotal role in diverse applications, including the chemical and nuclear industries, bioengineering, arterial blood flow, mud drilling, polymeric fluid dynamics, oil reservoir design, and material processing. Examples of non-Newtonian fluids include paint, butter, honey, ketchup, toothpaste, detergents, liquid crystals, pulps, synovial fluid, blood at low shear rates, and shaving creams. Consequently, researchers have proposed various constitutive models tailored to specific rheological properties, such as the Eyring–Powell, Carreau, Maxwell, Oldroyd-B, power-law, Casson, and Williamson fluid models. Several researches including those in (Xu and Liao (2009), Krishnamurthy et al. (2016), Khan et al. (2020a), Aljuaydi et al. (2023)) have been done to determine the stability of these fluid dynamics in order to accurately predict their rheological behavior.

Carreau fluids, a subclass of generalized Newtonian fluids, exhibit shear-dependent viscosity characterized by three distinct regimes: Newtonian behavior ($n = 1$), shear-thickening or dilatant behavior ($n > 1$), and shear-thinning or pseudoplastic behavior ($0 < n < 1$), where n denotes the power-law index. This model was initially introduced by Carreau (1972), based on the assumptions of molecular network theory. Several investigations have leveraged Carreau fluid models to study boundary layer flows under various boundary conditions, taking consideration of shear thinning and thickening cases. For instance, Rudraswamy et al. (2017), Muntazir et al. (2021), and Khan et al. (2017) employed such models to elucidate boundary layer flow mechanisms. Furthermore, Ghani and Siri (2018), applied the Haar wavelet quasi-linearization approach to analyze MHD Carreau nanofluid flows, accounting for velocity slip and suction/injection effects over an expanding surface. Babu et al. (2021) investigated non-linear MHD convective flows of Carreau nanofluids, incorporating the influences of viscous dissipation and Arrhenius activation energy above an exponentially expanding surface.

The Williamson fluid model is notable for its shear-thinning feature (Shawky et al. (2019)), making it relevant for applications such as blood flow studies in cardiovascular disease treatment and food mixing through chime motion in the intestine, as elaborated by Chandel and Sood (2022). An intriguing characteristic of the Williamson model is its ability to describe the variation in apparent viscosity across the spectrum of shear rates, ranging from zero-shear-rate viscosity to infinite-shear-rate viscosity. Conversely, viscoelastic non-Newtonian fluids with memory effects are effectively modeled using the Maxwell fluid model, which incorporates fluid relaxation time to account for these memory effects. These fluids are critical in various manufactured liquids, including plastics, polymers, pulps, toothpaste, and fossil fluids (Zhou et al. (2021); Mustafa et al. (2017)). The Maxwell model accurately captures both the elastic and viscous properties of these fluids, offering valuable insights into their intricate flow behaviors.

One of the primary concern in engineering, industrial, electronics, and biomedical endeavors is to improve the heat and mass transfer mechanism of various systems. Regarding this, nanofluids play a remarkable role. Nanofluids have emerged as promising candidates in this regard. These fluids consist of a base liquid–such as water, blood, ethylene glycol, vegetable oils, or sodium alginate–with uniformly dispersed nanoparticles typically smaller than 100 nm. The suspended nanoparticles may be metals (e.g., Cu, Al, Ag, Ti), metal oxides (e.g., $\mathrm{Al_2O_3}$, $\mathrm{MoS_2}$, $\mathrm{Fe_3O_4}$, $\mathrm{TiO_2}$), carbides (e.g., TiC, SiC), or carbon-based nanostructures such as single- and multi-walled carbon nanotubes (SWCNTs, MWCNTs).

Compared to traditional base fluids, nanofluids exhibit enhanced thermophysical properties including improved thermal conductivity, higher heat transfer coefficients, and tunable viscosity. They also offer advantages over conventional slurries used for thermal enhancement (Serrano et al. (2009); Saidur et al. (2011); Pordanjani et al. (2021)):

- They exhibit a high specific surface area, providing an increased heat transfer interface between particles and the surrounding fluid.

- Their dispersion stability is enhanced due to the dominant influence of Brownian motion.

- They require less pumping power than pure liquids to achieve comparable levels of heat transfer enhancement.

- They minimize particle clogging compared to conventional slurries, facilitating system miniaturization.

- Thermal properties can be tailored by adjusting particle type and concentration, offering flexibility across applications.

These characteristics make nanofluids suitable for diverse applications, including hyperthermia treatment, cooling in electronics and automotive systems, solar thermal collectors, safety systems in nuclear reactors, and defense or aerospace technologies. However, research into nanofluids is ongoing, particularly regarding the optimization of nanoparticle dispersion techniques and the mechanisms governing thermal conductivity enhancement.

The initial concept of using nanoparticles to improve thermal conductivity in base fluids was introduced by Choi and Eastman (1995). Building on this, Xuan and Li (2000) proposed a systematic approach for nanofluid preparation and used the hot-wire method to measure thermal conductivity, observing substantial improvements with increasing nanoparticle volume fraction. Subsequently, Eastman et al. (2001) reported a 40% increase in thermal conductivity for copper nanoparticle-ethylene glycol mixtures at only 0.3% volume fraction. Buongiorno (2006) identified key slip mechanisms in nanofluid transport, concluding that Brownian motion and thermophoresis are dominant in laminar flow regimes. Haddad et al. (2012) investigated Rayleigh-Bènard convection of CuO-water nanofluid, revealing that both effects become more significant at lower nanoparticle concentrations.

Further investigations by Irfan (2021) addressed their roles in Carreau nanofluid mixed convection flows, while Bouslimi et al. (2021) applied a Runge-Kutta-based shooting technique to study nanofluid heat and mass transfer behavior under Soret diffusion and nonlinear surface heating. Biomedical applications of nanofluids are also gaining attentions. For instance, Jalili et al. (2023b) examined hybrid nanofluid behavior in stenosed arteries–a condition marked by narrowing due to plaque accumulation. Their study demonstrated that increasing the volume fraction of $\mathrm{Al_2O_3}$ nanoparticles lowers the temperature profile in the constricted region, offering insights into the use of nanofluids in vascular thermal therapies.

Majeed et al. (2021) explored how thermophoretic diffusion and Brownian motion influence magnetohydrodynamic nanofluid flow past a stretching circular cylinder, taking into account the effects of variable magnetic fields, non-uniform free stream velocity, and various slip boundary conditions. Jalili et al. (2023c) conducted a thermal analysis of micropolar nanofluids, focusing on thermophoresis, Brownian motion, and Hall currents. Hamid et al. (2019) studied transient convective heat transport in MHD Williamson nanofluids, revealing that an increase in convective heat transport and viscosity ratio parameters led to higher temperature profiles and skin friction coefficients, respectively. Furthermore, Idrees et al. (2022)

examined the heat transfer dynamics of three-dimensional rotational flow in Williamson nanofluids. Their results indicated that increasing the Williamson parameter reduces the primary velocity while enhancing the secondary velocity of the hybrid nanofluid.

2.1.1 Hybrid nanofluid

Researchers seeking to achieve maximum thermal enhancement with minimal nanoparticle concentrations (less than 1% by volume) have investigated dispersing nanocomposite materials into carrier fluids. This approach includes combining two dissimilar nanoparticles with conventional fluids to create binary hybrid nanofluids or adding three different nanoparticles to the base fluids to create ternary hybrid nanofluids. These hybrid nanofluids have demonstrated enhanced thermophysical properties compared to simple nanofluids. The concept is to combine the strengths of dissimilar nanoparticles to form a nanocomposite mixture, thereby optimizing their collective thermal performance. Haider et al. (2024b) provided a comparative model for blood flow through arteries involving MDH and hybrid nanofluids. Using a thermochemical synthesis technique, Suresh et al. (2012) conducted an experimental study on convective heat transfer performance of Al_2O_3–Cu/water binary hybrid nanofluid flowing through a uniformly heated circular tube. Their findings revealed that the Nusselt number increased by up to 13.56% at a Reynolds number of 1730 compared to that of pure water. By Saeed et al. (2021), a bihybrid nanofluid flow of Al_2O_3 and TiO_2 nanoparticles in water as a base fluid over a spinning disk in Darcy–Forchheimer porous space was investigated. Incorporating the effect of non-uniform heat source/sink, Ragupathi et al. (2019) analyzed the heat transfer behavior of three dimensional flow of $H_2O/NaC_6H_9O_7$ based nanofluids with Fe_3O_4/Al_2O_3 nanoparticle over a Riga plate.

Hybrid nanofluids have demonstrated a wide range of applications, including but not limited to medical diagnostics and disease treatment as explored in Haider et al. (2024a), biosensors, aerospace technology, chemical engineering, biotechnology, metal coatings, and cooling systems such as computer chips. In comparison to binary hybrid nanofluids, ternary hybrid nanofluids offer better heat transfer rates, mechanical resistance, and aspect ratios due to their higher thermal conductivities. The MHD ternary hybrid nanofluid flow composed of $Al_2O_3 - Cu - TiO_2$ nanoparticles in water base fluid over a rotating disk was contemplated by Rafique et al. (2023). Their findings indicate that compared to regular fluids, the Nusselt number improved by about 8.4% for nanofluids, 16.8% for hybrid nanofluids, and 38.05% for ternary hybrid nanofluids when the mass suction parameter was increased from 2.0 to 2.4. In the attendance of Cattaneo–Christov heat flux and non-linear thermal radiation, Alqawasmi et al. (2023) examined the ternary hybrid nanofluid flow formed by dispersing Ag, $MnZnFe_2O_4$, and Cu nanoparticles in pure water over a spinning disk. Singh et al. (2023)

conducted a comparative study on ternary hybrid nanofluid ($SiO_2 - MoS_2 - TiO_2$/kerosene oil) and hybrid nanofluid ($SiO_2 - TiO_2$/kerosene oil) under quadratic thermal radiation. Farooq et al. (2024) recently explored the impact of nonlinear mixed convection on ternary hybrid nanofluids' stagnation point flow towards a vertical Riga plate. Their findings indicate that ternary hybrid nanofluids achieve higher velocity profiles compared to binary hybrid nanofluids when the mixed convection parameter is increased. Recent noteworthy studies on hybrid and trihybrid nanofluids are documented in (Thakur et al. (2023); Ali et al. (2023); Arshad et al. (2023); Dey et al. (2024)).

2.1.2 Stability of nanofluids

The stability of hybrid nanofluids is fundamental for their practical applications and effectiveness. Stability is influenced by various factors, including nanoparticle concentration, size, shape, magnetic field, temperature, base fluid properties such as viscosity, and preparation methods (Timofeeva et al. (2011); Chakraborty and Panigrahi (2020); Borode et al. (2023)). Ensuring optimal concentration, small and uniform particle size, and adding magnetic nanoparticles can prevent agglomeration, thus enhancing long-term thermal performance. Researchers, including those in (Shahsavar et al. (2015); Almanassra et al. (2020); Tahmasebi-Boldaji et al. (2023)), have used methods like two-step processes, ultrasonication, surfactants, and surface modifications to improve hybrid nanofluid stability. Optimizing these factors is crucial for exploiting the full potential of hybrid nanofluids in advanced technological applications.

Considerable advancements have been made in hybrid nanofluid research, particularly in dispersing solid nanomaterials within Newtonian base fluids such as water, vegetable oil, ethylene glycol, gasoline, engine oil, kerosene, alcohol, water-ethylene glycol mixtures, and paraffin oil. In contrast, investigations involving non-Newtonian base fluids, such as blood and sodium alginate, remain limited. Nevertheless, the unique rheological characteristics of non-Newtonian fluids significantly enhance the stability of hybrid nanofluids.

2.2 Radiative MHD Convection

The magnetic field is indispensable in controlling fluid flow and thermal transport. As such, it is applicable in biological, chemical, mechanical, and medical activities. MHD studies the dynamic interactions between magnetic fields and conducting fluids. The motion of liquid generates electric current, which changes the mechanical properties of the liquid. This interaction results in a Lorentz force which regulates the fluid motion and thermal transport.

Magnetohydrodynamic analysis is widely applicable to various natural and engineering systems, including astrophysical and geophysical processes, MHD pumps and generators, flow meters, magnetic separation, and filtration technologies. Ishak et al. (2008) examined the behavior of hydromagnetic flow and thermal energy transport over a vertically stretching surface under a spatially varying magnetic field. Their results indicated that increasing the magnetic field intensity reduces both heat energy loss and local skin friction. Additionally, Bouslimi et al. (2021) explored the heat and mass transfer characteristics of Williamson nanofluid flow across a porous medium subject to magnetic effects, Joule heating, nonlinear thermal radiation, and chemical reactions over a stretching surface. Waqas (2021) conducted the thermally radiative, magnetized non-Newtonian Casson liquid flow driven by a stretchable cylinder, accounting for the effects of thermosolutal stratification and buoyancy forces. In a recent study, Gupta et al. (2024) examined the behavior of radiative MHD flow of Carreau nanofluid past an inclined stretching cylindrical surface. Their analysis incorporated the effects of convective heating, second-order velocity slip, and chemical reactions influenced by activation energy.

The implementation of strong magnetic field represents a contemporary approach in MHD applications to harness the benefits of electromagnetic forces. The interaction of an applied magnetic field with the moving charge carriers (electrons) within a conductor induces a deflection of these carriers due to the Lorentz force. This deflection results in charge accumulation along one side of the conductor, generating an opposing electric field that leads to a voltage difference known as the Hall voltage. In fluid dynamics, the Hall effect is characterized by the transverse voltage differential (TVD) that arises across a conductor when subjected to a magnetic field perpendicular to the direction of fluid flow (Akram et al. (2024)). The combined Hall and ion-slip effects significantly influence the current density in conducting fluids, making them vital for applications in power generation, MHD accelerators, semiconductor characterization, magnetic field sensing, and refrigeration systems.

The Hall effect has practical relevance beyond traditional engineering applications, extending to biomedical fields such as magnetic resonance angiography (MRA). For instance, Ramzan et al. (2020) investigated the effects of Hall and ion-slip currents on bioconvective tangent hyperbolic nanofluid flow, demonstrating that increased values of the ion-slip and Hall parameters enhance fluid velocity. Hamid et al. (2021) studied the impact of Hall currents and chemical reactions on the MHD flow of hybrid nanoparticles suspended in hybrid base fluids. Shah et al. (2019) examined Hall current effects between two parallel plates in a rotating system of Casson nanofluid flow, employing both numerical and optimal methods. Their findings revealed that Hall currents reduce conductivity, which subsequently increases fluid velocity and temperature. Utilizing the spectral relaxation method, Ibrahim and Anbessa (2021) examined the influence of Hall and ion slip currents, along with variable thermal conductivity, on the mixed convective flow of Williamson nanofluid over a nonlinear porous stretching surface.

Thermal radiation plays a crucial role in MHD convective heat transfer processes characterized by steep temperature gradients. Its impact is particularly important in high-temperature systems such as nuclear reactors, electric power generation units, solar energy collectors, glass manufacturing, aerospace propulsion, biofuel processing, and the production of polymer sheets. To explore energy generation in confined geometries, Jalili et al. (2023a) analyzed the unsteady squeezing flow of MHD Casson fluid between two circular plates under thermal radiation. Their findings indicated a 20% increase in the temperature of the non-Newtonian fluid as the squeezing parameter intensified. Investigating thermal and flow transport in both 2D and 3D cavities, Zhang et al. (2017) studied the combined effects of magnetic fields and thermal radiation on MHD convection. The results highlighted that significant differences in flow structure and heat transfer emerge under strong thermal radiation and weak magnetic fields when comparing two- and three-dimensional configurations.

Shaw et al. (2022) explored the behavior of MHD hybrid nanofluids under quadratic and nonlinear thermal radiation conditions. Additionally, Irfan et al. (2022) incorporated radiative heat transfer and convective mechanisms to study the influence of Joule heating on magnetically influenced Carreau nanofluids. In a more recent study, Jalili et al. (2022) applied a combination of analytical and numerical methods to investigate heat and mass transport in an axisymmetric micropolar fluid subjected to a magnetic field within a cylindrical polar coordinate framework. Their analysis revealed that increasing the radiation parameter from 0 to 8% alters the shape of the temperature distribution, although the maximum and minimum temperature levels remain unchanged.

2.3 Convective Transport in Porous Medium

Convective heat and mass transfer through porous media is prevalent across a broad range of natural, industrial, and engineering systems. The presence of porous structures enhances convective processes by offering a larger interfacial area and facilitating improved fluid mixing. Particularly, the transport of non-Newtonian fluids through porous media has gained attention due to its relevance in applications such as soil mechanics, gel chromatography, paper drying, packed bed reactors, oil extraction, and geothermal reservoirs. The foundational theory describing fluid motion in porous materials was developed by Darcy in 1856, which effectively models low-velocity flows in such media Sobieski and Trykozko (2014). Building on this framework, Hayat et al. (2011) explored mixed convection of power-law fluids in saturated porous spaces. Similarly, Sedki (2022) investigated nanofluid transport over a nonlinear stretching surface embedded in a Darcy-type porous medium, incorporating the effects of thermal radiation and chemical reactions. Additionally, Verma et al. (2021) focused on the forced convection of Eyring–Powell nanofluid flow over a stretching sheet under the influence of a free-stream, showing that increasing the permeability resistance past a critical point suppresses dual solutions and promotes uniqueness.

Progress in this field has led to the extension of Darcy's law to include inertial effects through the Darcy–Forchheimer model, which introduces a nonlinear inertial drag term to better characterize high-velocity flows. For instance, Rasool and Zhang (2019) examined nanofluid motion subject to convective boundary conditions in a Darcy–Forchheimer porous medium, finding that stronger resistance due to porosity elevates the temperature distribution, while nanoparticle concentration diminishes with increased inertial resistance. The potential of various hybrid nanofluids as solar thermal absorbers in Darcy–Forchheimer environments was studied by Alzahrani et al. (2021), highlighting their application in solar energy systems. Furthermore, Siddiq et al. (2021) analyzed the influence of non-Darcy–Forchheimer flow in the context of MHD Carreau nanofluid dynamics over a stretching sheet, considering the combined impacts of thermal radiation and internal heat generation or absorption.

Investigators provided an extensive review on the heat transfer characteristics under the concurrent application of nanofluids and porous media. Rasool et al. (2021) reported the Darcy-Forchheimer porosity relation in a convectively heated MHD nanofluid flow over nonlinear stretching surface. The study assumed a viscoelastic nanofluid flow with the convective thermal and solutal boundary conditions. The skin friction rise and both the heat and mass flux number thinning is observed for increase in porosity and Forchheimer numbers. The authors in Shahid et al. (2022) analyzed the bi-convection MHD flow of Carreau nanofluids past an upper paraboloid porous surface, considering the effects of activation energy and chemical reactions. Further studies on convective heat and mass transport of nanofluid in porous medium can be seen in (Mahdi et al. (2015), Zeeshan et al. (2018), Rasool et al. (2022), Singh et al. (2024)).

2.4 Bioconvective Heat Transfer

Among the various techniques used to improve the thermal efficiency of energy systems, one approach involves dispersing microorganisms in commonly used nanofluids. The cells are denser than the working fluid, swim towards the surface of the fluid. The clustering of microbes at the surface of the fluid induces instability and the microbes start to fall downward. The upward swimming and the downward diffusion of the motile microorganisms in a quiescent fluid results bioconvection. Pedley and Kessler (1992) conducted an in-depth studies in this field. Afterward, the onset of bioconvection in suspensions of microorganisms has been extensively investigated. In particular, the studies referenced in (Bahloul et al. (2005), Kuznetsov (2005), and Sheremet and Pop (2014)) examined this phenomenon in populations of gravitactic, gyrotactic, and oxytactic microorganisms, respectively. In oxytaxis, the motility of microorganisms is directed by gradients in oxygen concentration, allowing them to move towards areas with optimal oxygen levels. Gravitaxis describes the movement guided by gravitational forces, where microorganisms orient themselves in response to gravity. Gyrotaxis, on the other hand, involves a complex orientation driven by the balance between physical torques created by gravitational pull and viscous drag.

Bioconvection with motile microorganisms has captured researchers' interest due to its extensive applications in engineering, biotechnology, microbial-enhanced oil recovery, biofuels, cancer treatment, bio-polymer synthesis, bio-fertilization, and other fields. Taking into account varying thermal conductivity and second-order slip, Abdelmalek et al. (2021) investigated the bioconvection flow of Williamson nanofluid over a stretched cylinder. The findings indicated a decline in the distribution of gyrotactic microorganism density as Peclet and bioconvection Lewis numbers increased. In their study on the bioconvective phenomena of Eyring–Powell nanofluid flow in the presence of a heat source/sink, nonlinear thermal radiation, and activation energy, Khan et al. (2022b) observed a decrease in the density of motile microorganisms corresponding to an increase in bioconvection Lewis number, buoyancy ratio, and Peclet number. Another study by Habibishandiz et al. (2023), considered a constant and periodic wall temperature inside a square porous cavity for heat transfer analysis of nanofluids containing oxytactic microorganisms. In this study, microbes enhanced the heat transfer rate when a periodic wall temperature was applied and had a reverse effect when a constant temperature was considered.

The existence of microorganisms effectively stabilize the nanofluid suspension by preventing the agglomeration of nanoparticles and enhances microscale mixing and mass transport. The mixed convection nanofluid flow of gyrotactic microorganisms past a horizontal circular cylinder subjected to convective boundary conditions was scrutinized by Rashad and Nabwey (2019). Bilal et al. (2024) examined the heat transport mechanism of gyrotactic microorganisms in Carreau nanofluid flow over a linearly stretched surface, taking into account the influence of both opposing and assisting buoyancy forces. Their study found that the concentration distribution rises with a higher thermophoresis parameter and diminishes with elevated values of the Brownian motion parameter in both assisting and opposing flows. Mishra (2024) performed a comparative analysis of suspension of gyrotactic microorganism in a hybrid nanofluid flows over an exponentially stretching sheet using the Yamada-Ota and Xue models, revealing that both models predict a decrease in the density of motile microorganisms and concentration profiles with increase in key parameters.

Nabwey et al. (2022) presented the effects of swimming gyrotactic microorganisms in MHD Carreau nanofluid flow through an inclined cylinder with non-uniform thermal conductivity. Regarding the influence of bioconvection of microorganisms, thermal radiation, thermophoresis diffusion, and Brownian motion, Asjad et al. (2022) scrutinized the exponentially stretching surface flow of Williamson fluid. Recently, Gangadhar et al. (2024) investigated the effects of an elastic surface and magnetic field interactions on mixed convection flow of the Oldroyd-B fluid with gyrotactic microorganisms.

Unlike traditional bioconvection, thermo-bioconvection arises from two principal factors: the temperature gradient within the fluid and the upward swimming behavior of motile microorganisms (Abdelsalam and Bhatti (2020)). Studies on thermo-bioconvective flows that account for microorganisms' Brownian motion, reaction rates, and associated activation energy remains limited. Nevertheless, these factors are critical in the boundary layer heat and mass transfer analysis. For instance, Dhlamini et al. (2022) highlighted the significance of incorporating these effects in analyzing solute and microbial transport. Zhang et al. (2011) demonstrated that complex chemical reactions within or on microorganisms' surfaces could facilitate reliable and eco-friendly nanoparticle synthesis. Furthermore, Mandal et al. (2023) employed the spectral quasilinearization method to examine the activity of motile microorganisms in bioconvective nanofluid flows under the influence of heat generation and Arrhenius activation energy. Their findings reported a 95.99% decrease in the Nusselt number as the bioconvection Brownian motion parameter increased from 0.1 to 1.2. However, to the best of our knowledge, the combined effects of microorganisms' Brownian motion and reaction rates within non-Newtonian nanofluid regimes have yet to be thoroughly explored.

2.5 The Cattaneo–Christov Flux

The efficiency of manufacturing processes and the quality of finished products are critically dependent on the rates of heat and mass transfer. The ongoing exploration of the various applications of nanofluids mechanics necessitates viewing heat transfer as a wave phenomenon instead of the conventional Fourier's diffusion (Fourier (1888)). Cattaneo (1948) was the first to forward this insight by incorporating the thermal relaxation time into the classical Fourier's law of heat conduction. However, this model gives oscillatory heat convection when the Cattaneo number is sufficiently large. Subsequently, Christov (2009) advanced this theory by modifying Fourier's law of heat conduction to include a relaxation time term, employing the Oldroyd's upper convective derivative.

2.5.1 The CC flux over/between rotating disk(s)

Fluid flow over or between rotating disks is of significant interest due to its applications in energy production, aerodynamics, and rotating machinery industries. To enhance the efficiency of heat and mass transfer processes in such configurations, researchers have extensively employed advanced heat and mass flux models. In this context, Hafeez and Khan (2021) investigated the swirling flow of magnetized Oldroyd-B fluid induced by a rotating and stretching disk under the framework of the CC theory. Their study revealed that the thermal relaxation time and solutal relaxation time parameters attenuate the temperature and concentration profiles, respectively, highlighting the role of relaxation mechanisms in modulating transport phenomena in complex fluids. The heat transfer characteristics of $\mathrm{MoS_2} - \mathrm{SiO_2}$ /kerosene oil hybrid nanofluid and $\mathrm{MoS_2}$ /kerosene oil nanofluid flow with the CC heat flux between two parallel rotating disks was investigated by Yaseen et al. (2022). Their study revealed that an increase in the inertial coefficient from 3 to 7 resulted in a drag force increase of 31.77% and 30.79% for the lower plate in the hybrid nanofluid and nanofluid, respectively. Utilizing the CC heat flux model and magnetic induction, the authors in (Latha et al. (2023)) examined the elector-conductive stagnation point flow of ternary Williamson hybrid nanofluid. Sohail et al. (2022) developed a model to study the incorporation of trihybrid nanoparticles in the Prandtl fluid model, considering the effects of the non-Fourier heat flux approach. They observed that the non-Fourier model reduces thermal distribution and that the heat transfer rate decreases with higher values of the heat source number.

2.5.2 The CC flux over cylindrical surfaces

Makinde et al. (2017) have analyzed the Casson nanofluid flow over a stretching cylinder, incorporating the CC heat flux model. Their findings indicate that the thermal relaxation parameter significantly reduces the temperature field while enhancing the heat transfer rate per unit volume. Hussain et al. (2022) investigated the CC heat flux analysis for Jeffery fluid flow with double stratification over a stretching cylinder. The study reveals that increasing the Jeffery fluid relaxation time leads to a reduction in the magnitude of the drag coefficient. Conversely, an increase in the retardation time and the curvature parameter results in an opposite effect. The axisymmetric double diffusion flow of a viscous fluid over a cylinder has been investigated by Batool et al. (2021). They explored the effects of activation energy and entropy generation by employing the non-Fourier law of heat flux and the non-Fick's law of mass flux model, providing a comprehensive analysis of these phenomena under the specified conditions. Malik et al. (2022) conducted a comprehensive study on the heat transfer characteristics of Carreau fluid flow past a stretching cylinder, employing the non-Fourier's heat flux model and incorporating the effects of velocity slip and convective boundary conditions. Further investigations of the non- Fourier-Fick's heat and mass flux effects over cylindrical surfaces are presented in (Ibrahim and Hindebu (2019); Irfan et al. (2019a); Reddy et al. (2022)).

2.6 Convection with Variable Thermophysical Properties

When a significant temperature gradient exists within a boundary layer flow, the thermophysical properties of the fluid, particularly viscosity and thermal conductivity, are no longer constant. This variation arises because elevated temperatures enhance the molecular activity of the fluid, reducing its viscosity and altering its ability to conduct heat. Such problems have attracted considerable scientific interest as they offer a more realistic representation of fluid behavior under thermal gradients.

Convective transport with variable thermophysical properties find significant applications in diverse fields, including space heating, refrigeration, tribology, food processing, extraction of crude oil, and the design of viscometers. In (Qasim et al. (2019)), the boundary layer flow of a Jeffrey fluid with variable transport properties and nonlinear radiation over a radially stretching disk was analyzed. The study revealed an increase in temperature with higher values of the variable thermal conductivity parameter, the ratio of relaxation to retardation time, and the heating parameter. Additionally, Adegbie et al. (2016) investigated the impact of dynamic viscosity and thermal conductivity on the stagnation flow of micropolar fluids. Moreover, it has been observed that the specific diffusivity of nanofluids often depends linearly on nanoparticle concentration.

Although temperature-dependent viscosity, thermal conductivity, and concentration-dependent mass diffusivity are critical for accurately modeling transport phenomena in nanofluids, comprehensive investigations that simultaneously incorporate all three factors remain scarce. A few notable contributions exist in this context. For instance, Salahuddin et al. (2022) analyzed the effects of variable thermophysical properties on mixed convection flow of a non-Newtonian fluid past a continuously moving thin needle. In a related effort, Prasad et al. (2024) examined the behavior of tangent hyperbolic nanofluid flow over a coagulated stretching surface, integrating the influences of temperature-sensitive viscosity and thermal conductivity along with concentration-dependent solutal diffusivity. Their results indicated that increases in variable viscosity and thermal conductivity parameters led to elevated temperature distributions while suppressing fluid velocity.

In another study, Riasat et al. (2021) compared the Yamada–Ota and Xue hybrid nanofluid models in the context of flow between co-rotating disks, incorporating variable transport properties. The findings revealed that axial velocity diminishes with increasing values of the variable viscosity parameter for gaseous fluids, whereas an enhancement in velocity was observed for liquids when the parameter assumed negative values. Further insights into nanofluid flows accounting for variable thermophysical behavior can be found in works such as Hamid et al. (2018), Song et al. (2021), He et al. (2024), and Ramakrishna et al. (2024).

2.7 Chemical Reaction and Activation Energy

2.7.1 Chemical reaction

Understanding the dynamics of heat and mass transfer influenced by chemical reactions remains a significant area of research due to its broad industrial relevance, particularly in combustion processes, catalytic reactions, ceramic manufacturing, and biochemical systems. In many chemical engineering applications, chemical reactions occur between a solute species and the host fluid, encompassing both homogeneous (bulk) and heterogeneous (surface) reaction mechanisms. In this context, Merkin (1996) analyzed boundary-layer flow involving combined homogeneous and heterogeneous reactions, where the homogeneous reaction was modeled using cubic autocatalysis and the heterogeneous reaction followed a first-order process. Their study emphasized that near the leading edge of a flat surface exposed to a uniform free stream, surface reactions dominate the transport behavior.

Simultaneous heat and mass transfer, influenced by the combined buoyancy effects from thermal and solutal gradients, also plays a vital role in industrial processes. For example, Reddy (2014) examined unsteady magnetohydrodynamic flow of a reactive fluid past a vertical plate subject to sudden motion, incorporating the impact of thermal radiation. In another contribution, Khan et al. (2018) explored the influence of homogeneous and heterogeneous chemical reactions in the MHD flow of a Powell–Eyring fluid under Newtonian heating conditions. Their results demonstrated that the skin friction coefficient increases with stronger magnetic field and fluid material parameters, whereas the mass transfer rate is suppressed by larger values of the homogeneous reaction parameter.

The stagnation point flow towards radially stretching sheet of radiative and chemically reactive Carreau nanofluid was scrutinized by Jawwad et al. (2023). Alqahtani et al. (2024) investigated the chemically reactive Jeffery–Hamel-type flow of a non-Newtonian nanofluid over magnetized, contracting, and extending inclined surfaces. Their findings revealed that the mass fraction exhibited a decreasing trend with an increase in the first-order chemical reaction parameter. Further investigations on chemical reactions for various non-Newtonian fluids are found in (Shaw et al. (2013), Hayat et al. (2016b), Gireesha et al. (2017), Gholinia et al. (2019), Rao and Deka (2023)).

2.7.2 Microbial chemical reaction with activation energy

Analyzing thermo-bioconvective flow involves consideration of chemical reactions and the minimal energy required to initiate these reactions, known as activation energy. The activation energy is applicable in diverse areas such as emulsions containing different suspensions, the storage and drying of foodstuffs, drug delivery systems, the design of artificial organs, biofilters, and the development of efficient catalytic reactors and packed-bed reactors. A. Othman et al. (2023) investigated bio-convection flow of magneto-cross nanofluid with activation energy, thermal radiation, and binary chemical reactions. They obtained an increase in motile microorganism's density for an upsurge in bioconvection Lewis number and a reverse result for bioconvection Peclet number. The role of activation energy in bioconvection of third grade nanofluid flow towards a stretching surface was explored by Chu et al. (2020). Farooq et al. (2021) studied the radiative bioconvective flow of Carreau nanofluids incorporating CC heat flux and chemical reactions. In their study, the concentration profile rises with the mass concentration and concentration relaxation parameters, while the microorganism field diminishes with the Peclet number and bioconvection Lewis number.

2.8 Entropy Generation

Heat transfer processes are typically associated with energy losses. In this context, the thermodynamic properties of hybrid nanofluids offer critical insights into understanding the overall performance of systems in engineering and industrial processes through exergy analysis. This approach is based on the second law of thermodynamics and quantifies the system's deviation from ideal or reversible operation by calculating the destroyed exergy or entropy generation. Entropy generation optimization has gained increasing significance across various technological domains, such as heat converters, combustion, electronic cooling, refrigeration, solar energy, porous media, and gas turbines. In thermal systems, entropy generation often arises from convective heat and mass transport, thermal radiation, porous medium, viscous effects, and Ohmic heating. In 1979, Bejan (1979) provided the technique to minimize the associated irreversibility with convective heat transfer and viscous effects. Using differential transform method to execute numerical solution, Arikoglu et al. (2008) investigated the effect of velocity slip on entropy generation of MHD flow over a rotating disk.

Entropy generation functions as a practical tool for optimizing the flow of hybrid and ternary hybrid nanofluids. Entropy analysis of $\mathrm{SWCNT-MWCNT/water}$ hybrid nanofluid flow with temperature-dependent viscosity is considered in (Ahmad et al. (2020)), showing that entropy generation number increases with increase in the Brinkman number and decreases with increase in volume fraction of SWCNT and radiation parameter. The authors in (Hosseinzadeh et al. (2022)), scrutinized a comparative study on entropy generation characteristic of magneto radiative flow of $\mathrm{Fe_3O_4/water}$ and $\mathrm{Fe_3O_4}$/water−ethylene glycol nanofluid between two stretchable rotating disks. Khan et al. (2020b) presented the entropy generation of MHD flow in a water-based hybrid nanofluid consisting of Graphene oxide and Copper nanoparticles within a rotating system, where the fluid is confined between two parallel plates. Khan et al. (2022a) provided a detailed analysis of entropy generation on hydromagnetic radiative ternary nanofluid flow consisting of titanium dioxide, ferric oxide, and silicon dioxide in a mixture of water and ethylene glycol base liquid over an exponentially stretching surface. Recently, Ali et al. (2024) described the effect of porous medium, heat radiation, and heat source on entropy generation analysis of the flow of Carreau trihybrid nanofluid.

The literature review reveals several critical gaps in the study of heat and mass transfer in non-Newtonian nanofluid flows. The coupled effects of Lorentz and drag forces, nonlinear thermal radiation, Ohmic heating, and heat source/sink remain inadequately explored in the context of Carreau nanofluid flow through porous media. Another significant gap pertains to the interplay between Brownian motion and chemical reactions of both nanoparticles and microorganisms in thermo-bioconvective nanofluid flows within 3D rotating or 2D stretching disk/cylindrical configurations, particularly under the influence of Soret and Dufour diffusion, Hall currents, activation energy-driven chemical reactions, and non-Fourier-Fickian flux models. Moreover, while hybrid and trihybrid nanofluid studies predominantly focus on Newtonian base fluids, the complex thermophysical interactions in non-Newtonian host fluids, especially concerning entropy production trends, remain insufficiently addressed. Furthermore, investigations into unsteady boundary layer flows of non-Newtonian nanofluids over rotating cones, incorporating temperature-dependent viscosity, thermal conductivity, and solutal diffusivity, are notably scarce. Addressing these research gaps will provide deeper insights into non-Newtonian nanofluid dynamics and foster advancements in thermal management and industrial applications.

CHAPTER THREE

Research Methodology

The differential equations (PDEs/ODEs) that arise in applications can only rarely be solved in closed form. Even when they can be, the solutions are often impractical to work with and to visualize. Numerical methods, by contrast, offer robust tools for addressing virtually all well-posed DEs. Prominent numerical approaches include the finite element (FE) method, finite volume (FV) method, finite difference (FD) method, and, more recently, spectral methods. The choice of an appropriate technique is typically guided by the complexity of the problem domain and the desired level of solution accuracy.

3.1 Similarity Transformations in Boundary Layer Fluid Flow

Boundary layer fluid flow problems are of immense importance in fluid dynamics, as they describe the behavior of fluid layers close to solid surfaces. The mathematical models of these problems are typically governed by nonlinear partial differential equations (PDEs) that are challenging to solve.

A similarity solution in boundary layer fluid flow refers to the transformation that reduces the PDEs governing the flow into ODEs (Tsou et al. (1967)). This is achieved by combining the independent variables (e.g., spatial coordinates and time) into a single dimensionless variable, called the similarity variable. The similarity solution captures the self-similar nature of the boundary layer flow, where the flow profiles at different locations collapse onto a single curve when appropriately scaled.

Steps in similarity transformations

- Non-dimensionalization: Introduce dimensionless variables to normalize the governing equations.
- Introduction of Similarity Variables: Combine spatial and temporal variables into a single variable, say η.
- Stream Function: Define a stream function ψ to ensure the continuity equation is automatically satisfied.
- Reduction to ODEs: Substituting the similarity variables into the governing equations reduces the PDEs to ordinary differential equations (ODEs).

In the present dissertation, we have employed the similarity variables to transform the highly nonlinear PDEs into ODEs for applying numerical methods to the problems.

3.2 Numerical methods

Numerical methods for solving differential equations are broadly classified into two categories: local and global methods. Finite difference and finite element methods fall under the local category, relying on localized approximations to discretize the domain. Conversely, spectral methods are global in nature, utilizing global functions to discretize the entire domain. In practical applications, finite element methods are highly effective for handling problems involving complex geometries, while spectral methods offer higher accuracy but are generally limited in terms of geometric flexibility. Over the past two decades, spectral methods have seen significant advancements and have been successfully applied to numerical simulations across diverse fields, including heat conduction, fluid dynamics, and quantum mechanics.

This dissertation employs two numerical approaches to solve the governing differential equations of the studied problems. The first approach utilizes the built-in MATLAB solver $bvp4c$, integrated with a continuation technique. This method is based on finite difference principles and is well-suited for boundary value problems. The second approach involves spectral methods, which are combined with various linearization techniques to enhance their applicability and efficiency in addressing highly nonlinear problems.

3.2.1 The `bvp4c` Matlab Code

3.2.1.1 Collocation points

The *collocation method* is a numerical technique used to solve ODEs, PDEs, and integral equations, especially boundary value problems (BVPs). It involves approximating the solution by a smooth, piecewise-defined function and ensuring that the governing equation is satisfied at specific points called **collocation points**.

The idea behind the collocation method is:

1. **Approximation of the Solution:** The solution $v(x)$ is approximated using a trial function $v_{\text{aprx}}(x)$, typically expressed as a linear combination of basis functions:

$$v_{\text{aprx}}(x) = \sum_{i=1}^{n} c_i \phi_i(x), \tag{3.2.1}$$

   where $\phi_i(x)$ are the basis functions, and c_i are the unknown coefficients to be determined.

2. **Collocation Points:** A set of discrete points $\{x_1, x_2, \ldots, x_n\}$ within the domain is chosen as collocation points. The trial solution $v_{\text{aprx}}(x)$ is substituted into the governing

equation, and the residual $R(x)$ is computed:

$$R(x) = \mathcal{L}(v_{\text{aprx}}(x)) - f(x), \tag{3.2.2}$$

where $\mathcal{L}$ is the differential operator and $f(x)$ is the source term. The collocation method ensures that the residual $R(x)$ is zero at each collocation point:

$$R(x_i) = 0 \quad \text{for } i = 1, 2, \ldots, n.$$

The unique feature of collocation method is that the adaptive versions of the method improve efficiency by refining the collocation points and the solution is typically smooth, especially when using higher-order polynomials or splines. However, the method may become computationally expensive for large systems and requires a careful choice of collocation points and basis functions to ensure stability.

The `bvp4c` function in Matlab is a robust and widely used tool for solving boundary value problems (BVPs) for ordinary differential equations (ODEs). It implements a collocation method based on a finite difference approach, particularly a piecewise cubic Hermite polynomial to approximate the solution of BVPs. The key points of the numerical method to solve BVPs in `bvp4c` are:

- Discretizing the Problem: The solution domain is divided into subintervals, and the solution is approximated within each subinterval using piecewise cubic polynomials.

- Collocation Points: The collocation method enforces that the ODE is satisfied at specific points (collocation points) within each subinterval. These points are chosen to ensure accuracy and stability of the solution.

- Residual Minimization: The method adjusts the coefficients of the cubic polynomials such that the residuals of the ODE and boundary conditions are minimized.

The resulting solution is continuously differentiable across the intervals, ensuring smoothness. An adaptive mesh refinement technique is used to ensure that the solution meets a specified error tolerance. The method effectively accommodates various boundary conditions (Dirichlet, Neumann, Robin, or a mix).

Algorithmic Steps: The numerical algorithm in `bvp4c` involves the following key steps:

- Initialization: Define the ODEs as a system of first-order differential equations. Specify boundary conditions at the two ends of the domain.

- Mesh generation: An initial mesh is provided by the user or automatically generated by the solver.
- Collocation: Cubic polynomials are fitted to the solution over each subinterval of the mesh. The coefficients of these polynomials are determined such that the differential equations are satisfied at the collocation points.
- Nonlinear system solution: The collocation process leads to a system of nonlinear algebraic equations. These equations are solved iteratively using a Newton-Raphson method. The Jacobian matrix required for the Newton iteration is computed either analytically or numerically.
- Error estimation and mesh refinement: Estimate the error in the solution using the ODE residuals. If the error exceeds the user-defined tolerance, refine the mesh by adding more collocation points.
- Iterative convergence: Repeat the solution process until the residuals fall within the specified tolerance and the boundary conditions are satisfied.

`Bvp4c` employs a reliable error control mechanism to ensure the accuracy of the solution. It uses a relative tolerance (`RelTol`) and an absolute tolerance (`AbsTol`) to control the error. The solver adaptively refines the mesh to achieve these tolerances, placing more points in regions where the solution varies rapidly.

The standard approach in `bvp4c` typically requires an initial guess for the unknown boundary conditions. However, for certain boundary value problems that exhibit high sensitivity to initial or boundary estimates, this method may fail to converge. To address such challenges, the continuation technique proposed by Roberts and Shipman (1967) is employed. This method enables the resolution of boundary value problems that are not easily handled by traditional shooting techniques.

Initially, the system of higher-order differential equations is reformulated into a set of first-order equations. A dummy continuation parameter $\delta \in [0,1]$ is introduced to facilitate the numerical procedure. The steps followed in the `bvp4c` MATLAB implementation are outlined as follows:

1. Decompose the governing system into linear and nonlinear components, incorporating the dummy parameter δ to interpolate between them.
2. Begin by solving the linear portion of the system with $\delta = 0$, using standard boundary conditions and initial guesses.

3. Incrementally increase δ and, using the solution from the previous step as the new guess, solve the partially nonlinear system.

4. Continue this iterative process by gradually increasing δ until it reaches 1, yielding an approximate solution to the fully nonlinear system within a specified error tolerance.

3.2.2 The spectral method

Spectral methods are a subclass of weighted residual methods (WRMs), which serve as a foundational framework for various numerical approaches used to solve differential equations, including the boundary element, finite volume, spectral, and finite element methods.

3.2.2.1 Weighted Residual Methods

Let us consider a boundary value problem defined as:

$$\boldsymbol{L}u(x) = f(x), \quad x \in \Omega, \tag{3.2.3}$$

$$B_{x_0}[u(x_0)] = g_{x_0}, \quad B_{x_N}[u(x_N)] = g_{x_N}, \tag{3.2.4}$$

where $\boldsymbol{L}$ represents a linear differential operator, and B_{x_0} and B_{x_N} denote linear boundary operators that could correspond to Dirichlet, Neumann, or Robin-type conditions. The functions $f(x)$, g_{x_0}, and g_{x_N} are prescribed data ensuring the well-posedness of the problem. The domain Ω is a bounded subset of $\mathbb{R}^d$, with $d = 1, 2$, or 3.

The WRM seeks an approximate solution u in the form of a finite expansion:

$$u(x) \approx u_N(x) = \sum_{k=0}^{N} a_k \phi_k(x), \tag{3.2.5}$$

where $\{\phi_k(x)\}$ are known basis (trial) functions, and $\{a_k\}$ are the unknown coefficients to be determined. For time-dependent problems, the solution $u(x,t)$ is approximated as $u_N(x,t)$, where the coefficients $\{a_k(t)\}$ vary with time. This section, however, focuses solely on spatial discretization, assuming that temporal discretization is handled through a suitable time-stepping scheme.

Substituting the approximate solution $u_N(x)$ into Eq. (3.2.3) results in a residual:

$$\boldsymbol{R}_N(x) = \boldsymbol{L}u_N(x) - f(x) \neq 0, \quad x \in \Omega. \tag{3.2.6}$$

The essence of the WRM lies in minimizing this residual by enforcing its orthogonality to a set of test (or weight) functions $\{\psi_j(x)\}$ in a discrete weighted inner product sense:

$$(\boldsymbol{R}_N, \psi_j)_{N,\omega} := \sum_{k=0}^{N} \boldsymbol{R}_N(x_k)\psi_j(x_k)\omega_k = 0, \tag{3.2.7}$$

where $\{x_k\}_{k=0}^{N}$ are selected collocation (or quadrature) points, and $\{\omega_k\}_{k=0}^{N}$ are corresponding weights from a numerical integration scheme.

A distinguishing feature of spectral methods, compared to finite element or finite difference approaches, is the global nature of their basis and test functions. These functions are typically smooth across the entire domain, unlike the piecewise-defined functions used in other discretization techniques. Spectral methods often employ trigonometric functions for periodic domains or classical orthogonal polynomials (such as Chebyshev, Legendre, Laguerre, or Hermite polynomials) for non-periodic settings.

When choosing the basis and weight functions for spectral approximations, three essential criteria must be satisfied to ensure stability, accuracy, and computational efficiency.

- the approximations $\sum_{k=0}^{N} a_k\phi_k(x)$ of $u_N(x)$ must converge rapidly for reasonably smooth functions.
- given coefficients a_k, it should be easy to determine b_k such that,

$$\frac{d}{dx}\Big(\sum_{k=0}^{N} a_k\phi_k(x)\Big) = \sum_{k=0}^{N} b_k\phi_k(x).$$

- it should be fast to convert between coefficients $a_k,\ k = 0, \ldots, N$ and the values for the sum $u_N(x_i)$ at some set of nodes x_i, $i = 0, \ldots, N$.

3.2.2.2 Spectral collocation and collocation points

The spectral methods are generally categorized into the Galerkin, Petrov-Galerkin, and Collocation type based on the choice of the trial/test functions. In this study, we adopt the collocation spectral method in which the test functions $\{\psi_k\}$ are the Lagrange basis polynomials such that $\psi_k(x_j) = \delta_{jk}$, where δ_{jk} is the Kronecker Delta function and $\{x_k\}$ are preassigned collocation points.

The selection of collocation points plays a vital role in ensuring the stability and accuracy of the numerical scheme, as well as in simplifying the treatment of boundary conditions. These points are generally selected based on the nodes of Gauss-type quadrature rules, commonly corresponding to the roots of certain orthogonal polynomials. There are various collocation points in spectral methods, such as Gauss-lobatto points: $z_j = \cos\left(\dfrac{\pi j}{N}\right)$, Gauss-

Chebyshev points: $z_j = \cos\left(\frac{\pi(2j+1)}{2N+2}\right)$, and Gauss-Radau points: $z_j = \cos\left(\frac{2\pi j}{2N+1}\right)$, where $j = 0, 1, 2, \ldots, N$.

The core principle behind spectral methods is the representation of the solution using a global polynomial of degree N that interpolates the solution across all $N+1$ collocation points within the domain. Unlike finite difference methods, which typically use uniformly spaced nodes and are prone to significant interpolation errors at higher degrees, spectral methods employ Chebyshev-Gauss-Lobatto (CGL) nodes. These collocation points are chosen to minimize interpolation error across polynomial approximations, thereby making Chebyshev polynomials especially effective for achieving high accuracy and rapid convergence in the numerical solution of differential equations (Boyd (2001)).

The Chebyshev polynomials of the first kind $T_k(x)$ defined as (see Appendix):

$$T_k(x) = \cos(k \arccos(x)),\ |x| \leq 1. \tag{3.2.8}$$

and the CGL points:

$$x_j = \cos\left(\frac{\pi j}{N}\right),\ j = 0, 1, 2, \ldots, N, \tag{3.2.9}$$

where, $\{x_j\}$ are the extrema of the Chebyshev polynomials. The CGL points yield a set of clustered nodes on the standard interval [-1,1]. These points can be mapped into any other physical domain [a,b] by uing a linear transformation:

$$z_j = \frac{a+b}{2} + \frac{b-a}{2} x_j. \tag{3.2.10}$$

Figure 3.2.1 depicts the CGL points, which correspond to the extreme points of the Chebyshev polynomials. These points are distributed non-uniformly, with increased clustering near the interval boundaries. Geometrically, these points correspond to the projections of equally spaced points along the upper semicircle of the unit circle. This boundary clustering is particularly advantageous for resolving steep gradients in boundary layer flows, such as rapid changes in viscosity and temperature near walls. Using CGL points enhances the accuracy in capturing these critical boundary phenomena. This discretization strategy addresses key numerical challenges Shizgal (2015):

Gibbs Phenomenon: Spectral interpolation struggles with non-smooth functions, where artificial periodic extensions create boundary discontinuities, resulting in oscillations and reduced accuracy.

Runge Phenomenon: Interpolation with algebraic polynomials on non-uniform nodes clustered near boundaries improves accuracy, highlighting the importance of appropriately dis-

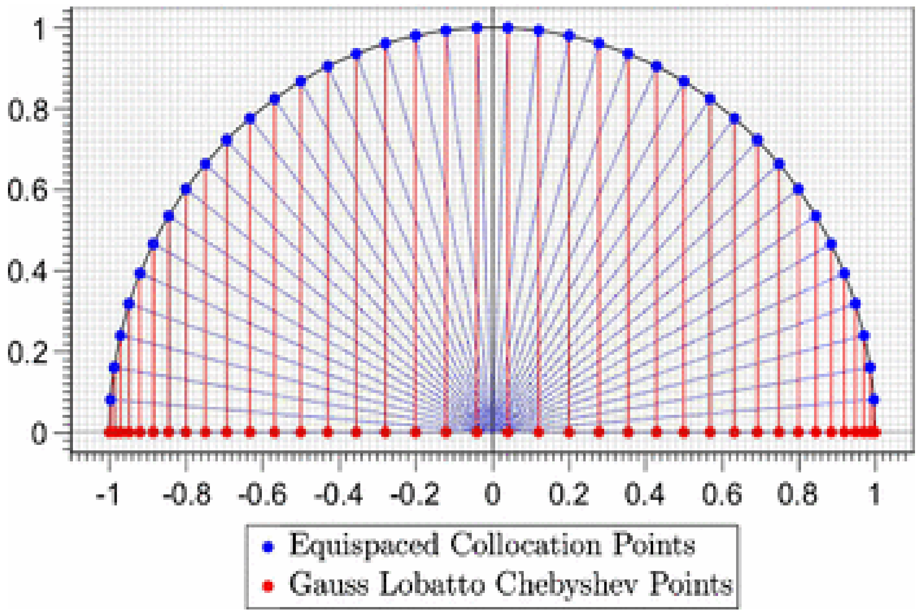

Figure 3.2.1: The CGL points (red points) are denser towards the edges of the interval compared to the equispaced points(blue points)
https://doi.org/10.1007/s11071-017-3654-3

tributed nodes like CGL points for spectral methods in boundary layer analyses.

3.2.2.3 The Chebyshev differentiation matrix

To determine the entries of the Chebyshev differentiation matrix to be used for problems on bounded interval with non-periodic data, we follow the following steps (Trefethen (2000)).

- discretize the interval [-1,1] using the CGL points, $\{x_j\}$ and sample the function y at those points to obtain the data vector $y = [y(x_0), y(x_1), \ldots, y(x_N)]^T$,
- find the Lagrange's polynomial, $L(x)$ of degree at most N that interpolate the data. That is, $L(x_i) = y_i, i = 0, 1, \ldots, N$,
- obtain the spectral derivative y' by differentiating $L(x)$ and evaluating at the grid points: $y'_i = L'(x_i)$,
- this procedure implicitly defines the differentiation matrix D_N that maps $y' = D_N y$. The entries of the differentiation matrix $D_N = [D_{ij}]$ are given by:

$$
\begin{aligned}
D_{00} &= \frac{2N^2+1}{6} = -D_{NN}, \text{ first and last elements on the diagonal} \\
D_{jj} &= \frac{-x_j}{2(2-x_j^2)}, \; j = 1, 2, \ldots, N-1, \text{ diagonal elements} \\
D_{ij} &= \frac{c_i(-1)^{i+j}}{c_j(x_i - x_j)}, \; i \neq j, \; i, j = 1, 2, \ldots, N-1, \text{ off diagonal elements} \qquad (3.2.11)
\end{aligned}
$$

where,

$$c_j = \begin{cases} 2, \; j = 0, N \\ 1, \; 1 \leq j \leq N-1 \end{cases}$$

3.2.2.4 The spectral quasilinearization method (SQLM)

The quasilinearization method was originally introduced by Bellman and Kalaba (1965). In using SQLM the nonlinear equations are linearized using a generalization of the Newton-Raphson quasilinearization method and integrated using the Chebyshev spectral collocation method.

Consider the non-linear differential equation:

$$F[x,\, y(x),\, y'(x),\, \cdots,\, y^n(x)] = 0, \tag{3.2.12}$$

with $x \in [a,b]$, subject to the boundary conditions

$$\begin{aligned} &H_{a,k}[y(a),\, y'(a),\, \cdots,\, y^n(a)] = 0, \quad k = 1,2,3,\cdots,m, \\ &H_{b,k}[y(b),\, y'(b),\, \cdots,\, y^n(b)] = 0, \quad k = m+1, m+2, \cdots, n, \end{aligned} \tag{3.2.13}$$

where, F and H are nonlinear operators, n is the order of derivative. We perform the quasilinearization method derived from Newton's method and Taylor series expansion. The method assumes that the difference between the approximate solution at the present iteration level and previous iteration level is very small. That is, $|y_{r+1} - y_r| \ll 1$. By using multi-variable Taylor series, we expand F as follows:

$$F[x,\, y(x),\, y'(x),\, \cdots,\, y^n(x)] + \sum_{p=0}^{n} \frac{\partial^{(p)} F}{\partial y_r^{(p)}} \left[x,\, y_r,\, y_r',\, \cdots,\, y_r^{(n)}\right] \times \left(y_{r+1}^{(p)} - y_r^{(p)}\right) = 0, \tag{3.2.14}$$

When $p = 0$, it coincides with $F[x, y(x)]$. Taking the $(r)^{th}$ iteration term to the right side, we get:

$$\sum_{p=0}^{n} \frac{\partial^{(p)} F}{\partial y_r^{(p)}} \left[y_{r+1}^{(p)}\right] = \sum_{p=0}^{n} \frac{\partial^{(p)} F}{\partial y_r^{(p)}} \left[y_r^{(p)}\right] - F[x,\, y_r,\, y_r',\, \cdots,\, y_r^n], \tag{3.2.15}$$

where, in Eq. (3.2.15) all terms on the right side of the equation and the coefficient $\dfrac{\partial^{(p)} F}{\partial y_r^{(p)}}$ are in the r^{th} iteration level, and hence known. Therefore, Eq. (3.2.15) is the linearized form of Eq. (3.2.12). We follow the same procedure to linearize the boundary condition Eq. (3.2.13).

3.2.2.5 The spectral local linearization method (SLLM)

The SLLM is a procedure of developing decoupled iterative scheme based on a smooth univariant linearization of nonlinear functions and using a spectral collocation discretization.

Consider a system of m nonlinear ODEs in m unknown functions, $\mathit{\Pi}_i(\zeta), i = 1, 2, \cdots, m$, where $\zeta \in [\zeta_l, \zeta_r]$ is independent variable. In SLLM, we express $\mathit{\Pi}_i(\zeta)$ as:

$$L_i\Big[\mathit{\Pi}_1, \mathit{\Pi}_2, \cdots, \mathit{\Pi}_m\Big] + N_i\Big[\mathit{\Pi}_1, \mathit{\Pi}_2, \cdots, \mathit{\Pi}_m\Big] = 0, \tag{3.2.16}$$

for each $i = 1, 2, \cdots, m$. Where L_i and N_i are the linear and nonlinear components of $\mathit{\Pi}_i$, respectively. To construct the iteration scheme, we employ local linearization of N_i about $\mathit{\Pi}_{i,r}$(the previous iteration) to the i^{th} nonlinear equation assuming that all the other $\mathit{\Pi}_{k,r}$ $(k < i)$ are known. Thus at the i^{th} equation, N_i is linearized as follows:

$$\begin{aligned} N_i\Big[\mathit{\Pi}_1, \mathit{\Pi}_2, \cdots, \mathit{\Pi}_m\Big] &= N_i\Big[\mathit{\Pi}_{1,r}, \mathit{\Pi}_{2,r}, \cdots, \mathit{\Pi}_{m,r}\Big] + \\ \frac{\partial N_i}{\partial Z_i}\Big[\mathit{\Pi}_{1,r}, \mathit{\Pi}_{2,r}, \cdots, \mathit{\Pi}_{m,r}\Big]\Big(\mathit{\Pi}_i - \mathit{\Pi}_{i,r}\Big). \end{aligned} \tag{3.2.17}$$

Thus, at the current iteration with $\mathit{\Pi}_i = \mathit{\Pi}_{i,r+1}$, for each $i = 1, 2, \ldots, m$, Eq. (3.2.16) becomes:

$$\begin{aligned} L_i\Big[\mathit{\Pi}_{1,r+1}, \cdots, \mathit{\Pi}_{m,r+1}\Big] + \frac{\partial N_i}{\partial \mathit{\Pi}_i}\Big[\cdots\Big]\mathit{\Pi}_{i,r+1} = \\ \frac{\partial N_i}{\partial \mathit{\Pi}_i}\Big[\cdots\Big]\mathit{\Pi}_{i,r} - N_i\Big[\mathit{\Pi}_{1,r}, \cdots, \mathit{\Pi}_{m,r}\Big], \end{aligned} \tag{3.2.18}$$

where $[\cdots]$ denotes $[\mathit{\Pi}_{1,r}, \mathit{\Pi}_{2,r}, \cdots, \mathit{\Pi}_{m,r}]$, $\mathit{\Pi}_{i,r+1}$ and $\mathit{\Pi}_{i,r}$ are the approximations of $\mathit{\Pi}_i$ at the current and previous iterations, respectively. To obtain a decoupled iteration scheme, we appeal to the Gauss-Seidel approach of decoupling linear algebraic systems in linear algebra applications.

3.2.2.6 The spectral relaxation method (SRM)

Consider a general system of m nonlinear ordinary differential equations in m unknown functions $z_i(\eta)$, where $i = 1, 2, ..., m$, and $\eta \in [a, b]$. Define the vector Z_i to represent the derivatives of the variable z_i with respect to η, that is,

$$Z_i(\eta) = [z_i^{(0)}, z_i^{(1)}, ..., z_i^{(n_i)}], \tag{3.2.19}$$

where $z_i^{(0)} = z_i$, $z_i^{(p)}$ is the p-th derivative of z_i with respect to η, and n_i $(i = 1, 2, ..., m)$ is the highest derivative order of the variable z_i appearing in the system of equations. Suppose that the system can be expressed in terms of Z_i as a sum of its linear (L_i) and nonlinear (N_i) components as follows:

$$L_i[Z_1, Z_2, ..., Z_m] + N_i[Z_1, Z_2, ..., Z_m] = H_i(\eta), \quad \text{for } i = 1, ..., m, \tag{3.2.20}$$

where $H(\eta)$ is a known function of η. If the nonlinear component in the above equation is a sum of nonlinear terms with at least one of them being a multiple of z_i, we can further split N_i into a sum of two nonlinear functions as:

$$N_i[z_1, z_2, ..., z_m] = z_i F_i[z_1, ..., \hat{z}_i, ..., z_m] + G_i[z_1, z_2, ..., z_m], \tag{3.2.21}$$

where $\hat{z}_i(\eta) = [z_i^{(1)}, ..., z_i^{(n_i)}]$, and F_i is a nonlinear function that includes z_i as a factor, while G_i is a nonlinear function of $z_1, z_2, ..., z_m$ in which either z_i is absent or appears as a nonlinear factor. To derive the iteration scheme, we adopt the concept of the Gauss-Seidel relaxation method. As discussed in Motsa (2014), it involves decoupling systems of linear algebraic equations and systematically using updated solutions during the process. Starting with an initial approximation $Z_{1,0}, Z_{2,0}, ..., Z_{m,0}$, the iterative technique is expressed as follows:

$$\begin{aligned}
&L_1[Z_{1,r+1}, Z_{2,r}, \ldots, Z_{m,r}] + Z_{1,r+1} F_1[\hat{Z}_{1,r}, Z_{2,r}, \ldots, Z_{m,r}] = H_1 - G_1[Z_{1,r}, Z_{2,r}, \ldots, Z_{m,r}],\\
&L_2[Z_{1,r+1}, Z_{2,r+1}, Z_{3,r}, \ldots, Z_{m,r}] + Z_{2,r+1} F_2[Z_{1,r+1}, \hat{Z}_{2,r}, Z_{3,r}, \ldots, Z_{m,r}] = H_2\\
&\qquad\qquad - G_2[Z_{1,r+1}, Z_{2,r}, \ldots, Z_{m,r}],\\
&\qquad\qquad \vdots,\\
&L_{m-1}[Z_{1,r+1}, \ldots, Z_{m-1,r+1}, Z_{m,r}] + Z_{m-1,r+1} F_{m-1}[Z_{1,r+1}, \ldots, Z_{m-2,r+1}, Z_{m-1,r}, Z_{m,r}]\\
&\qquad\qquad = H_{m-1} - G_{m-1}[Z_{1,r+1}, \ldots, Z_{m-1,r+1}, Z_{m-1,r}],\\
&L_m[Z_{1,r+1}, \ldots, Z_{m-1,r+1}, Z_{m,r+1}] + Z_{m-1,r+1} F_m[Z_{1,r+1}, \ldots, Z_{m-1,r+1}, \hat{Z}_{m,r}] = H_m -\\
&\qquad\qquad G_m[Z_{1,r+1}, \ldots, Z_{m-1,r+1}, Z_{m-1,r}],
\end{aligned} \tag{3.2.22}$$

where $Z_{i,r+1}$ and $Z_{i,r}$ represent the approximations of Z_i at the current and the previous iteration, respectively.

We note that Eq. (3.2.22) forms a system of m linear decoupled equations that can be solved iteratively for $r = 1, 2, \ldots$ starting from a given initial approximation $Z_{i,0}$. The iteration is repeated until convergence is achieved.

CHAPTER FOUR

Numerical Investigation of MHD Carreau Nanofluid Flow with Nonlinear Thermal Radiation and Joule Heating by Employing Darcy–Forchheimer Effect over a Stretching Porous Medium

A comprehensive review of the literature, including Aljuaydi et al. (2023), Jalili et al. (2023b), and Singh et al. (2024), underscores a notable gap in addressing the combined effects of key physical mechanisms on non-Newtonian nanofluid behavior. Specifically, no existing study has comparatively examined the heat and mass transfer characteristics of shear-thinning and shear-thickening regimes in MHD Carreau nanofluid flow while incorporating nonlinear thermal radiation, Ohmic heating, heat generation or absorption, and chemical reactions. Furthermore, the coupled effects of Brownian motion and thermophoresis in a Darcy–Forchheimer porous medium remain inadequately explored.

This chapter presents a numerical analysis of two-dimensional, incompressible MHD flow of Carreau nanofluids over a stretching sheet, accounting for the aforementioned phenomena. The findings of the study are expected to provide deeper insights into the heat and mass transfer mechanisms in non-Newtonian nanofluids, paving the way for optimizing their applications in industrial processes and engineering systems.

4.1 Mathematical Model and Formulation

The mathematical model of the present study is developed by considering the following assumptions.

1. A steady, two-dimensional, viscous, and incompressible flow of a nonlinear radiative magneto-Carreau nanofluid with dilute nanoparticle suspension ($\varphi < 1$) is considered over a stretching sheet embedded in a Darcy–Forchheimer porous medium.

2. The effects of Hall currents, ion slip, and viscous dissipation from the stress tensor are neglected.

3. Nanoparticles and base fluid are assumed to be in local thermal equilibrium, and nanoparticle chemical reactions are included.

4. The sheet stretches with a velocity $u_{\mathrm{w}} = ax$, where a is a positive stretching constant.

5. A uniform magnetic field B_0 is applied perpendicular to the sheet, with a low magnetic Reynolds number assumed to neglect the induced magnetic field.

6. The sheet is maintained at a constant temperature T_{w}, while the ambient fluid temperature is T_∞, with $T_{\mathrm{w}} > T_\infty$.

7. The x-axis is taken along the stretching direction of the sheet, and the y-axis is normal to it.

Furthermore, the physical sketch of the flow for the case where both mass and thermal diffusivities exceed momentum diffusivity, with mass diffusivity being dominant, is illustrated in Figure 4.1.1.

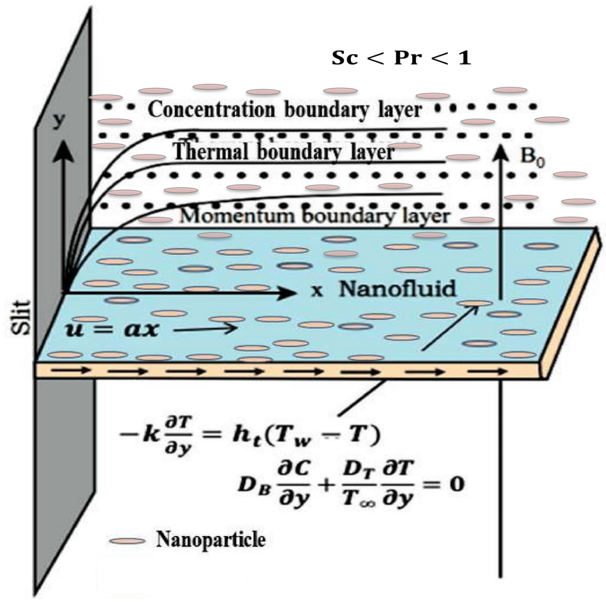

Figure 4.1.1: Geometry of the flow problem.

The fundamental balance equations for the flow of an incompressible Carreau nanofluid are the conservation of mass, linear momentum, and energy. The equations are derived as follows.

a. Conservation of Mass

The principle of conservation of mass states that, provided there are no sources or sinks within the control volume, the mass of fluid flowing from one region of the control volume to another remains the same. The principle is applied to fixed volumes, known as control volumes (or surfaces), as shown in Figure 4.1.2.

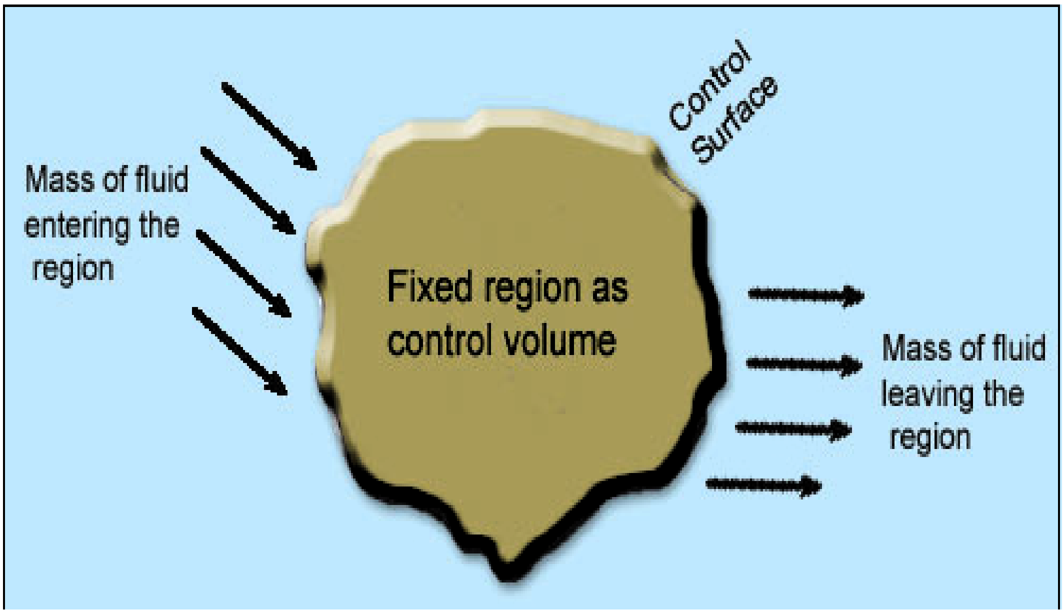

Figure 4.1.2: Control volume and control surface

Consider an arbitrary volume V having mass m. Then the average density is $\bar{\rho} = \frac{\Delta m}{\Delta V}$. For an arbitrary small volume,

$$\rho = \lim_{\Delta V \to 0} \frac{\Delta m}{\Delta V} = \frac{dm}{dV} \implies dm = \rho dV.$$

Integrating this equation results in

$$m = \int \rho dV. \tag{4.1.1}$$

Now by the principle of conservation of mass as stated above, m = constant. This implies that

$$\frac{dm}{dt} = \int_{CV} \frac{\partial \rho}{\partial t} dV + \int_S \rho \big(\boldsymbol{v}.\boldsymbol{n}\big) dS = 0 \qquad \text{(by RTT)},$$

$$\implies \int_{CV} \frac{\partial \rho}{\partial t} dV + \int_{CV} \nabla.\big(\rho \boldsymbol{v}\big) dV = \int_{CV} \left[\frac{\partial \rho}{\partial t} + \nabla.\big(\rho \boldsymbol{v}\big)\right] dV = 0 \qquad \text{(by DT)}.$$

As the volume is arbitrary,

$$\frac{\partial \rho}{\partial t} + \nabla.\big(\rho \boldsymbol{v}\big) = 0, \tag{4.1.2}$$

is the differential form of the continuity equation valid for both compressible and incompressible fluids. Eq. (4.1.2) is further expanded as:

$$\frac{\partial \rho}{\partial t} + \frac{\partial (\rho u)}{\partial x} + \frac{\partial (\rho v)}{\partial y} + \frac{\partial (\rho w)}{\partial z} = 0$$

$$\implies \frac{\partial\rho}{\partial t}+\rho\frac{\partial u}{\partial x}+\rho\frac{\partial v}{\partial y}+\rho\frac{\partial w}{\partial z}+u\frac{\partial\rho}{\partial x}+v\frac{\partial\rho}{\partial y}+w\frac{\partial\rho}{\partial z}=0,$$

$$\implies \frac{\partial\rho}{\partial t}+\rho(\nabla.\boldsymbol{v})+(\boldsymbol{v}.\boldsymbol{\nabla})\rho=\frac{D\rho}{Dt}+\rho(\nabla.\boldsymbol{v})=0 \quad \text{(by material derivative)}.$$

If the fluid is incompressible,

$$\nabla.\boldsymbol{v}=0. \tag{4.1.3}$$

Expanded in Cartesian coordinates, the 3D continuity equation becomes:

$$\frac{\partial u}{\partial x}+\frac{\partial v}{\partial y}+\frac{\partial w}{\partial z}=0. \tag{4.1.4}$$

b. Conservation of Momentum

The principle of conservation of linear momentum states that, for any material region or control volume, the time rate of change of momentum is equal to the sum of forces acting on the control volume. According to Newton's second law:

$$\mathbf{F}=m\frac{d\boldsymbol{v}}{dt}=\frac{d}{dt}(m\boldsymbol{v}) \quad\implies\quad \frac{\boldsymbol{F}}{V}=\frac{d}{dt}(\rho\boldsymbol{v}),$$

where division by the volume V yields the force per unit volume equal to the time rate of change of momentum per unit volume. Therefore, the time rate of change of momentum within a control volume is expressed as:

$$\frac{D}{Dt}\int_{CV}\rho\boldsymbol{v}\,dV.$$

Applying the Reynolds transport theorem gives:

$$\frac{D}{Dt}\int_{CV}\rho\boldsymbol{v}\,dV=\int_{CV}\frac{\partial(\rho\boldsymbol{v})}{\partial t}\,dV+\int_{S}\rho\boldsymbol{v}(\boldsymbol{v}\cdot\boldsymbol{n})\,dS, \tag{4.1.5}$$

where S denotes the surface bounding the control volume CV, and $\boldsymbol{n}$ is the outward unit normal vector.

There are two primary types of forces acting on the control volume:

- **Body forces**: Forces that act throughout the volume, given by

$$\boldsymbol{F}_b=\int_{CV}\rho\boldsymbol{f}_b\,dV,$$

where $\boldsymbol{f}_b$ is the body force per unit mass. Examples include gravitational, electromagnetic, and drag forces in porous media.

- **Surface forces**: Forces that act on the surface, represented as

$$\boldsymbol{F}_s = \int_S (\boldsymbol{n}\cdot\boldsymbol{\tau})\, dS,$$

where $\boldsymbol{\tau}$ is the stress tensor.

Thus, the conservation of linear momentum can be written as:

$$\int_{CV} \frac{\partial(\rho\boldsymbol{v})}{\partial t}\, dV + \int_S \rho\boldsymbol{v}(\boldsymbol{v}\cdot\boldsymbol{n})\, dS = \int_{CV} \rho\boldsymbol{f}_b\, dV + \int_S (\boldsymbol{n}\cdot\boldsymbol{\tau})\, dS. \tag{4.1.6}$$

Applying the DT to the surface integrals and combining terms, we obtain:

$$\int_{CV} \left[\frac{\partial(\rho\boldsymbol{v})}{\partial t} + \nabla\cdot(\rho\boldsymbol{v}\boldsymbol{v}) - \rho\boldsymbol{f}_b - \nabla\cdot\boldsymbol{\tau}\right] dV = 0. \tag{4.1.7}$$

Since the control volume CV is arbitrary, the integrand must vanish identically, leading to the differential form:

$$\frac{\partial(\rho\boldsymbol{v})}{\partial t} + \nabla\cdot(\rho\boldsymbol{v}\boldsymbol{v}) = \rho\boldsymbol{f}_b + \nabla\cdot\boldsymbol{\tau}. \tag{4.1.8}$$

Eq. (4.1.8) represents the general momentum balance and is applicable to all types of fluids–compressible and incompressible, Newtonian and non-Newtonian–across all flow regimes. It expresses the balance between inertial, body, and surface forces per unit volume at each point in the fluid.

In the above equation the dyadic product (also called tensor product) can be removed as follows.

$$\nabla\cdot(\rho\boldsymbol{v}\boldsymbol{v}) = \rho(\boldsymbol{v}\cdot\nabla)\boldsymbol{v} + \boldsymbol{v}(\boldsymbol{v}\cdot\nabla\rho + \rho\nabla\cdot\boldsymbol{v})$$

For incompressible flows the second term on the right vanishes leading to:

$$\nabla\cdot(\rho\boldsymbol{v}\boldsymbol{v}) = \rho\boldsymbol{v}\cdot\nabla\boldsymbol{v},$$

thus the substantial derivative form is:

$$\rho\frac{D\boldsymbol{v}}{Dt} = \rho\boldsymbol{f}_b + \nabla\cdot\boldsymbol{\tau}, \tag{4.1.9}$$

where $\dfrac{D}{Dt}$ denotes the material derivative.

The component forms of the momentum equation in rectangular coordinates are given below:

$$
\begin{aligned}
\rho\left(\frac{\partial u}{\partial t}+u\frac{\partial u}{\partial x}+v\frac{\partial u}{\partial y}+w\frac{\partial u}{\partial z}\right) &= -\frac{\partial p}{\partial x}+\frac{\partial \tau_{xx}}{\partial x}+\frac{\partial \tau_{yx}}{\partial y}+\frac{\partial \tau_{zx}}{\partial z}+\rho f_x,\\
\rho\left(\frac{\partial v}{\partial t}+u\frac{\partial v}{\partial x}+v\frac{\partial v}{\partial y}+w\frac{\partial v}{\partial z}\right) &= -\frac{\partial p}{\partial y}+\frac{\partial \tau_{xy}}{\partial x}+\frac{\partial \tau_{yy}}{\partial y}+\frac{\partial \tau_{zy}}{\partial z}+\rho f_y,\\
\rho\left(\frac{\partial w}{\partial t}+u\frac{\partial w}{\partial x}+v\frac{\partial w}{\partial y}+w\frac{\partial w}{\partial z}\right) &= -\frac{\partial p}{\partial z}+\frac{\partial \tau_{xz}}{\partial x}+\frac{\partial \tau_{yz}}{\partial y}+\frac{\partial \tau_{zz}}{\partial z}+\rho f_z.
\end{aligned}
\tag{4.1.10}
$$

Here, u, v, and w represent the velocity components in the x, y, and z directions for the rectangular coordinate system.

c. Conservation of Energy for Nanofluid Flow:

The principle of conservation of energy for a control volume is based on the first law of thermodynamics, which states that the overall change of energy for a volume of fluid is equal to the rate at which work is done on the fluid plus the rate at which heat is added to the fluid.

Mathematically, this is expressed as:

$$
\frac{D}{Dt}\int_{CV}\rho e_t\,dV=\frac{dQ}{dt}+\frac{dW}{dt}, \tag{4.1.11}
$$

where

- $e_{\mathrm{t}}=e+\frac{1}{2}|\boldsymbol{v}|^2+gz$ is the total energy per unit mass,
- $\frac{dQ}{dt}$ is the net rate of heat added to the control volume,
- $\frac{dW}{dt}$ is the net rate of work done by the control volume on its surroundings.

For most fluid flows, the potential energy gz is much smaller than the internal and kinetic energies and can be neglected. Thus, the total energy per unit mass simplifies to:

$$
e_{\mathrm{t}}=e+\frac{1}{2}|\boldsymbol{v}|^2.
$$

Applying Reynolds transport theorem to Eq. (4.1.11), we obtain:

$$
\int_{CV}\frac{\partial}{\partial t}(\rho e_{\mathrm{t}})\,dV+\int_S\rho e_{\mathrm{t}}(\boldsymbol{v}\cdot\boldsymbol{n})\,dS=\frac{dQ}{dt}+\frac{dW}{dt}, \tag{4.1.12}
$$

where $\boldsymbol{n}$ is the outward-pointing unit normal vector on the control surface S. Writing in differential form for a fixed control volume:

$$
\frac{\partial}{\partial t}(\rho e_{\mathrm{t}})+\nabla\cdot(\rho e_{\mathrm{t}}\boldsymbol{v})=\dot{Q}+\dot{W}, \tag{4.1.13}
$$

where $\dot{Q}$ and $\dot{W}$ are the volumetric rates of heat addition and work done. The total work rate $\dot{W}$ consists of:

$$\dot{W} = \nabla \cdot (\boldsymbol{\tau} \cdot \boldsymbol{v}) - \nabla \cdot (p\boldsymbol{v}), \tag{4.1.14}$$

where $\boldsymbol{\tau}$ is the viscous stress tensor and p is the pressure. The heat addition term for nanofluid flows is generalized as:

$$\dot{Q} = -\nabla \cdot \left(\boldsymbol{q} + \boldsymbol{q}_r\right) + h_p \nabla \cdot \boldsymbol{j}_p + q_s''', \tag{4.1.15}$$

Here,

$$\boldsymbol{j}_p = \boldsymbol{j}_{p,b} + \boldsymbol{j}_{p,t} = -\rho_p D_b \nabla C - \rho_p \frac{D_T}{T_\infty} \nabla T$$

is the diffusion mass flux for the nanoparticles, and $\boldsymbol{q} = -k\nabla T + h_p \boldsymbol{j}_p$ is the sum of the conduction heat flux and the heat flux due to nanoparticle diffusion, $\boldsymbol{q}_r$ is radiative heat transfer, q_s''' is the rate of heat supply per unit volume, k is the thermal conductivity, and $h_p = c_p T$ is the specific enthalpy of the nanoparticle. Substituting results of $\boldsymbol{j}_p$ and $\boldsymbol{q}$ into Eq. (4.1.15), we have:

$$\dot{Q} = \nabla\left(k\nabla T\right) + c_p \rho_p \left(D_b \nabla C + \frac{D_T}{T_\infty} \nabla T\right) \cdot \nabla T - \nabla \cdot \boldsymbol{q}_r + q_s'''. \tag{4.1.16}$$

Now, using Eqs. (4.1.14)-(4.1.16), Eq. (4.1.13) gives:

$$\begin{aligned} \frac{\partial}{\partial t}(\rho e_{\mathrm{t}}) + \nabla \cdot (\rho e_{\mathrm{t}} \boldsymbol{v}) &= \nabla\left(k\nabla T\right) + c_p \rho_p \left(D_b \nabla C \cdot \nabla T + \frac{D_T}{T_\infty} \nabla T \cdot \nabla T\right) - \nabla \cdot \boldsymbol{q}_r \\ &+ q_s''' + \nabla \cdot (\boldsymbol{\tau} \cdot \boldsymbol{v}) - \nabla \cdot (p\boldsymbol{v}). \end{aligned} \tag{4.1.17}$$

Now, expanding the left-hand side of Eq. (4.1.17), and since $e_{\mathrm{t}} = e + \frac{1}{2}|\boldsymbol{v}|^2$, we have:

$$\frac{\partial}{\partial t}(\rho e_{\mathrm{t}}) + \nabla \cdot (\rho e_{\mathrm{t}} \boldsymbol{v}) = \left[\frac{\partial}{\partial t}(\rho e) + \nabla \cdot (\rho e \boldsymbol{v})\right] + \left[\frac{\partial}{\partial t}\left(\frac{1}{2}\rho|\boldsymbol{v}|^2\right) + \nabla \cdot \left(\frac{1}{2}\rho|\boldsymbol{v}|^2 \boldsymbol{v}\right)\right]. \tag{4.1.18}$$

The kinetic energy terms can be expanded as $\frac{\partial}{\partial t}\left(\frac{1}{2}\rho v_i v_i\right) + \nabla \cdot \left(\frac{1}{2}\rho v_i v_i \boldsymbol{v}\right) = \rho v_i \frac{Dv_i}{Dt}$. Using the momentum conservation equation, $\rho \frac{Dv_i}{Dt} = \frac{\partial \tau_{ij}}{\partial x_j} - \frac{\partial p}{\partial x_i}$, thus

$$\rho v_i \frac{Dv_i}{Dt} = v_i \frac{\partial \tau_{ij}}{\partial x_j} - v_i \frac{\partial p}{\partial x_i}.$$

Applying the product rule:

$$v_i \frac{\partial \tau_{ij}}{\partial x_j} = \frac{\partial (v_i \tau_{ij})}{\partial x_j} - \tau_{ij} \frac{\partial v_i}{\partial x_j}, \quad v_i \frac{\partial p}{\partial x_i} = \frac{\partial (p v_i)}{\partial x_i} - p\nabla \cdot \boldsymbol{v}.$$

Thus:

$$\rho v_i \frac{Dv_i}{Dt} = \frac{\partial(v_i \tau_{ij})}{\partial x_j} - \tau_{ij}\frac{\partial v_i}{\partial x_j} - \frac{\partial(pv_i)}{\partial x_i} + p(\nabla\cdot\boldsymbol{v}).$$

In vectorial form:

$$\rho\boldsymbol{v}\cdot\frac{D\boldsymbol{v}}{Dt} = \nabla\cdot(\boldsymbol{\tau}\cdot\boldsymbol{v}) - \boldsymbol{\tau}:\nabla\boldsymbol{v} - \nabla\cdot(p\boldsymbol{v}) + p(\nabla\cdot\boldsymbol{v}). \tag{4.1.19}$$

If incompressiblity is assumed ($\nabla\cdot\boldsymbol{v} = 0$), this simplifies to:

$$\rho\boldsymbol{v}\cdot\frac{D\boldsymbol{v}}{Dt} = \nabla\cdot(\boldsymbol{\tau}\cdot\boldsymbol{v}) - \boldsymbol{\tau}:\nabla\boldsymbol{v} - \nabla\cdot(p\boldsymbol{v}). \tag{4.1.20}$$

Substituting Eq. (4.1.20) into Eq. (4.1.18), we obtain:

$$\frac{\partial}{\partial t}(\rho e_{\mathrm{t}}) + \nabla\cdot(\rho e_{\mathrm{t}}\boldsymbol{v}) = \left[\frac{\partial}{\partial t}(\rho e) + \nabla\cdot(\rho e\boldsymbol{v})\right] + \nabla\cdot(\boldsymbol{\tau}\cdot\boldsymbol{v}) - \boldsymbol{\tau}:\nabla\boldsymbol{v} - \nabla\cdot(p\boldsymbol{v}). \tag{4.1.21}$$

Using the thermodynamic relation $de = c_p dT$ for incompressible flows, the first term on the right side of Eq. (4.1.21), is expressed as:

$$\frac{\partial}{\partial t}(\rho e) + \nabla\cdot(\rho e\boldsymbol{v}) = \rho c_p\left[\frac{\partial T}{\partial t} + \boldsymbol{v}\cdot\nabla T\right] = \rho c_p\frac{DT}{Dt}. \tag{4.1.22}$$

Substituting Eqs. (4.1.21) and (4.1.22) back into the full energy Eq. (4.1.17) and simplifying, we finally obtain the nanofluid energy equation:

$$\begin{aligned}\rho c_p\frac{DT}{Dt} =& \nabla\cdot(k\nabla T) - \nabla\cdot\boldsymbol{q}_r + c_p\rho_p\left(D_b\nabla C\cdot\nabla T + \frac{D_T}{T_\infty}\nabla T\cdot\nabla T\right)\\ &+ q_s''' + \boldsymbol{\tau}:\nabla\boldsymbol{v}.\end{aligned} \tag{4.1.23}$$

d. Conservation of Mass for Nanoparticle:

The rate of increase of mass of A per unit volume equals to net rate of addition of mass of A per unit volume by convection and by diffusion plus rate of production of mass of A per unit volume by reaction, expressed mathematically as

$$\frac{d}{dt}\int_{CV}\rho C\,dV = -\int_S\left(\rho C\boldsymbol{v} + \boldsymbol{j}_p\right)\cdot\boldsymbol{n}\,dS + \int_V \rho R_a\,dV \tag{4.1.24}$$

where R_a is the rate of production of species per unit volume. Using divergence theorem:

$$\int_{CV}\left[\frac{\partial}{\partial t}\big(\rho C\big) + \nabla\cdot(\rho C\boldsymbol{v})\right]dV = -\int_{CV}\big(\nabla\cdot\boldsymbol{j}_p\big)dV + \int_V \rho R_a\,dV. \tag{4.1.25}$$

Since dV is arbitrary,

$$\frac{\partial}{\partial t}\Big(\rho C\Big) + \nabla\cdot(\rho C\boldsymbol{v}) = -\nabla\cdot\boldsymbol{j}_p + R_a. \tag{4.1.26}$$

Applying continuity equation and using $\boldsymbol{j}_p = -\rho_p D_b \nabla C - \rho_p \frac{D_T}{T_\infty}\nabla T$, Eq. (4.1.26) is simplified into:

$$\frac{\partial C}{\partial t} + \boldsymbol{v}\cdot\nabla C = D_b \nabla^2 C + \frac{D_T}{T_\infty}\nabla^2 T + R_a. \tag{4.1.27}$$

In the present study, the body force $\boldsymbol{f}_b$ in Eq. (4.1.9) is assumed to result from the combined effects of the Lorentz force due to the applied magnetic field and the Darcy–Forchheimer drag forces due to porous medium resistance, while buoyancy is neglected owing to its comparatively minor influence. Accordingly, the body force is modeled as

$$\boldsymbol{f}_b = \boldsymbol{f}_L + \boldsymbol{f}_P = -\Big[\sigma_0 B_0^2 \boldsymbol{v}\Big] - \left[\frac{\mu\xi}{k^\star}\boldsymbol{v} + \frac{c_F \rho\xi}{\sqrt{k^\star}}\boldsymbol{v}|\boldsymbol{v}|\right], \tag{4.1.28}$$

where the negative signs indicate that both forces oppose the fluid motion. The Lorentz term arises from the interaction of induced currents with the magnetic field, while the Darcy–Forchheimer terms account for linear and nonlinear drag within the porous medium.

The volumetric heat supply q_s''' originates from Joule heating and internal heat generation/absorption, modeled as a linear function of the temperature difference between the surface and the ambient fluid. Viscous dissipation is neglected due to moderate flow intensities. Thus,

$$q_s''' = q_j''' + q_g''' = \sigma_0 B_0^2 |\boldsymbol{v}|^2 + Q_a (T - T_\infty), \tag{4.1.29}$$

where Q_a represents the volumetric heat generation ($Q_a > 0$) or absorption ($Q_a < 0$) coefficient.

Similarly, the nanoparticle production rate R_a is assumed linearly proportional to the concentration difference between the surface and the ambient nanofluid:

$$R_a = -k_p^\star (C - C_\infty), \tag{4.1.30}$$

where $k_p^\star$ is the nanoparticle reaction rate constant, and the negative sign reflects a flux from higher to lower concentration.

The Cauchy stress tensor, $\boldsymbol{\tau}$ in Eq. (4.1.9) for Carreau model (Bird et al., 1987) is premeditated as follows,

$$\boldsymbol{\tau} = -p\mathbf{I} + \mu \mathbf{D}_1, \tag{4.1.31}$$

here p, $\mathbf{I}$, μ, and $\mathbf{D}_1$ are respectively the pressure, the identity tensor, viscosity, and the first

Rivlin-Erickson tensor. The constitutive equation of the Carreau rheological model is :

$$\frac{\mu-\mu_\infty}{\mu_0-\mu_\infty}=\left[1+\left(\Gamma\gamma'\right)^2\right]^{(n-1)/2}, \tag{4.1.32}$$

where Γ, n, μ_0, and μ_∞ denote the characteristic time, power law index, zero shear rate viscosity, and infinity shear rate viscosity, respectively. γ' is the shear rate given as:

$$\gamma'=\sqrt{\frac{1}{2}\sum_i\sum_j\gamma'_{ij}\gamma'_{ji}}=\sqrt{\frac{1}{2}\mathrm{tr}\left(\mathbf{D}_1^2\right)}, \tag{4.1.33}$$

where

$$\mathbf{D}_1=(\mathrm{grad}\mathbf{V})+(\mathrm{grad}\mathbf{V})^T=\begin{bmatrix}2\frac{\partial u}{\partial x} & \frac{\partial u}{\partial y}+\frac{\partial v}{\partial x}\\ \frac{\partial u}{\partial y}+\frac{\partial v}{\partial x} & 2\frac{\partial v}{\partial y}\end{bmatrix}. \tag{4.1.34}$$

In practical cases, μ_∞ vanishes. Hence, Eq. (4.1.31) takes the form:

$$\boldsymbol{\tau}=-p\mathbf{I}+\mu_0\left[1+\left(\Gamma\gamma'\right)^2\right]^{(n-1)/2}\mathbf{D}_1. \tag{4.1.35}$$

The Carreau model with fluid index in the range $0<n<1$ is commonly referred to as shear-thinning or pseudoplastic fluids, whereas Carreau fluids with a fluid index in the range $n>1$ are commonly referred to as shear-thickening or dilatant fluids.

In two-dimensional steady flow, the velocity, temperature, and concentration fields take the form:

$$\boldsymbol{v}=[u(x,y),v(x,y)],\, T=T(x,y),\, C=C(x,y), \tag{4.1.36}$$

where u and v represent the respective x- and y-direction velocities. Making use of Eq. (4.1.34) and (4.1.36),

$$\gamma'=\left[2\left[\left(\frac{\partial u}{\partial x}\right)^2+\left(\frac{\partial v}{\partial y}\right)^2\right]+\left(\frac{\partial u}{\partial y}+\frac{\partial v}{\partial x}\right)^2\right]^{1/2}. \tag{4.1.37}$$

Considering Eqs. (4.1.34), (4.1.35), and (4.1.37), and taking all the above assumptions a steady state 2D incompressible flow of Carreau nanofluid over a stretching sheet reduce Eqs. (4.1.4), (4.1.9), (4.1.23), and (4.1.27) into:

$$\frac{\partial u}{\partial x}+\frac{\partial v}{\partial y}=0, \tag{4.1.38}$$

$$\rho\left(u\frac{\partial u}{\partial x}+v\frac{\partial u}{\partial y}\right)=-\frac{\partial p}{\partial x}+\eta_0\left[2\frac{\partial^2 u}{\partial x^2}+\frac{\partial^2 u}{\partial y^2}+\frac{\partial^2 v}{\partial y\partial x}\right]\left[1+\Gamma^2\left(2\left(\frac{\partial u}{\partial x}\right)^2+2\left(\frac{\partial v}{\partial y}\right)^2\right.\right.$$
$$\left.\left.+\left(\frac{\partial u}{\partial y}+\frac{\partial v}{\partial x}\right)^2\right)\right]^{\frac{n-1}{2}}+2\eta_0\frac{\partial u}{\partial x}\frac{\partial}{\partial x}\left(\left[1+\Gamma^2\left(2\left(\frac{\partial u}{\partial x}\right)^2+2\left(\frac{\partial v}{\partial y}\right)^2\right.\right.\right.$$
$$\left.\left.\left.+\left(\frac{\partial u}{\partial y}+\frac{\partial v}{\partial x}\right)^2\right)\right]^{\frac{n-1}{2}}\right)+\eta_0\left(\frac{\partial u}{\partial y}+\frac{\partial v}{\partial x}\right)\frac{\partial}{\partial y}\left(\left[1+\Gamma^2\left(2\left(\frac{\partial u}{\partial x}\right)^2+2\left(\frac{\partial v}{\partial y}\right)^2\right.\right.\right.$$
$$\left.\left.\left.+\left(\frac{\partial u}{\partial y}+\frac{\partial v}{\partial x}\right)^2\right)\right]^{\frac{n-1}{2}}\right)-\sigma_0 B_0^2 u-\frac{\mu\xi}{k^\star}u-\frac{c_F\rho\xi}{\sqrt{k^\star}}u^2, \tag{4.1.39}$$

$$\rho\left(u\frac{\partial v}{\partial x}+v\frac{\partial v}{\partial y}\right)=-\frac{\partial p}{\partial y}+\eta_0\left[2\frac{\partial^2 v}{\partial y^2}+\frac{\partial^2 u}{\partial x\partial y}+\frac{\partial^2 v}{\partial x^2}\right]\left[1+\Gamma^2\left(2\left(\frac{\partial u}{\partial x}\right)^2+\right.\right.$$
$$\left.\left.2\left(\frac{\partial v}{\partial y}+\right)^2+\left(\frac{\partial u}{\partial y}+\frac{\partial v}{\partial x}\right)^2\right)\right]^{\frac{n-1}{2}}+\eta_0\left(\frac{\partial u}{\partial y}+\frac{\partial v}{\partial x}\right)\frac{\partial}{\partial x}\left(\left[1+\Gamma^2\left(2\left(\frac{\partial u}{\partial x}\right)^2+2\left(\frac{\partial v}{\partial y}\right)^2\right.\right.\right.$$
$$\left.\left.\left.+\left(\frac{\partial u}{\partial y}+\frac{\partial v}{\partial x}\right)^2\right)\right]^{\frac{n-1}{2}}\right)+2\eta_0\frac{\partial v}{\partial y}\frac{\partial}{\partial y}\left(\left[1+\Gamma^2\left(2\left(\frac{\partial u}{\partial x}\right)^2+2\left(\frac{\partial v}{\partial y}\right)^2\right.\right.\right.$$
$$\left.\left.\left.+\left(\frac{\partial u}{\partial y}+\frac{\partial v}{\partial x}\right)^2\right)\right]^{\frac{n-1}{2}}\right)-\sigma_0 B_0^2 v-\frac{\mu\xi}{k^\star}v-\frac{c_F\rho\xi}{\sqrt{k^\star}}v^2, \tag{4.1.40}$$

$$u\frac{\partial T}{\partial x}+v\frac{\partial T}{\partial y}=\frac{k}{\rho c_p}\left[\frac{\partial^2 T}{\partial x^2}+\frac{\partial^2 T}{\partial y^2}\right]+\tau\left[D_b\frac{\partial C}{\partial x}\frac{\partial T}{\partial x}+\frac{\partial C}{\partial y}\frac{\partial T}{\partial y}+\frac{D_T}{T_\infty}\left(\left(\frac{\partial T}{\partial x}\right)^2+\left(\frac{\partial T}{\partial y}\right)^2\right)\right]$$
$$-\frac{1}{\rho c_p}\left[\frac{\partial q_r}{\partial x}+\frac{\partial q_r}{\partial y}\right]+\frac{\sigma_0 B_0}{\rho c_p}u^2+\frac{1}{\rho c_p}Q_0(T-T_\infty), \tag{4.1.41}$$
$$u\frac{\partial C}{\partial x}+v\frac{\partial C}{\partial y}=D_b\left[\frac{\partial^2 C}{\partial x^2}+\frac{\partial^2 C}{\partial y^2}\right]+\frac{D_T}{T_\infty}\left[\frac{\partial^2 T}{\partial x^2}+\frac{\partial^2 T}{\partial y^2}\right]-k_p^*(C-C_\infty), \tag{4.1.42}$$

where $\tau(=(\rho c_p)_p/(\rho c_p)_f)$ denotes the effective heat capacity ratio of the nanoparticles to base fluid.

First, let's undergo the non-dimensional analysis of the continuity and the two momentum equations using the standard approach by taking L as characteristic length and U as stretching speed. The dimensionless variables are defined by:

$$\left(u^*,v^*\right)=\left(\frac{u}{U},\frac{v}{U}\right),\quad \left(x^*,y^*\right)=\left(\frac{x}{L},\frac{y}{L}\right),\text{ and } p^*=\frac{p}{\rho U^2}. \tag{4.1.43}$$

Using these non-dimensional variables, the governing equations become:

$$\frac{\partial u^*}{\partial x^*}+\frac{\partial v^*}{\partial y^*}=0, \tag{4.1.44}$$

$$\begin{aligned} u^*\frac{\partial u^*}{\partial x^*}+v^*\frac{\partial u^*}{\partial y^*} &= -\frac{1}{\rho}\frac{\partial p^*}{\partial x^*}+\epsilon_1\left[2\frac{\partial^2 u^*}{\partial x^{*2}}+\frac{\partial^2 u^*}{\partial y^{*2}}+\frac{\partial^2 v^*}{\partial y^*\partial x^*}\right]\left[1+\epsilon_2\left(2\left(\frac{\partial u^*}{\partial x^*}\right)^2+2\left(\frac{\partial v^*}{\partial y^*}\right)^2\right.\right.\\ &\left.\left.+\left(\frac{\partial u^*}{\partial y^*}+\frac{\partial v^*}{\partial x^*}\right)^2\right)\right]^{\frac{n-1}{2}}+2\epsilon_1\frac{\partial u^*}{\partial x^*}\frac{\partial}{\partial x^*}\left(\left[1+\epsilon_2\left(2\left(\frac{\partial u^*}{\partial x^*}\right)^2+2\left(\frac{\partial v^*}{\partial y^*}\right)^2\right.\right.\right.\\ &\left.\left.\left.+\left(\frac{\partial u^*}{\partial y^*}+\frac{\partial v^*}{\partial x^*}\right)^2\right)\right]^{\frac{n-1}{2}}\right)+\epsilon_1\left(\frac{\partial u^*}{\partial y^*}+\frac{\partial v^*}{\partial x^*}\right)\frac{\partial}{\partial y^*}\left(\left[1+\epsilon_2\left(2\left(\frac{\partial u^*}{\partial x^*}\right)^2+\right.\right.\right.\\ &\left.\left.\left.2\left(\frac{\partial v^*}{\partial y^*}\right)^2+\left(\frac{\partial u^*}{\partial y^*}+\frac{\partial v^*}{\partial x^*}\right)^2\right)\right]^{\frac{n-1}{2}}\right)-\frac{L}{\rho U}\sigma_0 B_0^2 u^*-\frac{L}{\rho U}\frac{\mu\xi}{k^\star}u^*-L\frac{c_F\xi}{\sqrt{k^\star}}u^{*2}, \end{aligned} \tag{4.1.45}$$

$$\begin{aligned} u^*\frac{\partial v^*}{\partial x^*}+v^*\frac{\partial v^*}{\partial y^*} &= -\frac{\partial p^*}{\partial y^*}+\epsilon_1\left[2\frac{\partial^2 v^*}{\partial y^{*2}}+\frac{\partial^2 u^*}{\partial x^*\partial y^*}+\frac{\partial^2 v^*}{\partial x^{*2}}\right]\left[1+\epsilon_2\left(2\left(\frac{\partial u^*}{\partial x^*}\right)^2+\right.\right.\\ &\left.\left.2\left(\frac{\partial v^*}{\partial y^*}\right)^2+\left(\frac{\partial u^*}{\partial y^*}+\frac{\partial v^*}{\partial x^*}\right)^2\right)\right]^{\frac{n-1}{2}}+\epsilon_1\left(\frac{\partial u^*}{\partial y^*}+\frac{\partial v^*}{\partial x^*}\right)\frac{\partial}{\partial x^*}\left(\left[1+\epsilon_2\left(2\left(\frac{\partial u^*}{\partial x^*}\right)^2+\right.\right.\right.\\ &\left.\left.\left.2\left(\frac{\partial v^*}{\partial y^*}\right)^2+\left(\frac{\partial u^*}{\partial y^*}+\frac{\partial v^*}{\partial x^*}\right)^2\right)\right]^{\frac{n-1}{2}}\right)+2\epsilon_1\frac{\partial v^*}{\partial y^*}\frac{\partial}{\partial y^*}\left(\left[1+\epsilon_2\left(2\left(\frac{\partial u^*}{\partial x^*}\right)^2+2\left(\frac{\partial v^*}{\partial y^*}\right)^2\right.\right.\right.\\ &\left.\left.\left.+\left(\frac{\partial u^*}{\partial y^*}+\frac{\partial v^*}{\partial x^*}\right)^2\right)\right]^{\frac{n-1}{2}}\right)-\frac{L}{\rho U}\sigma_0 B_0^2 v^*-\frac{L}{\rho U}\frac{\mu\xi}{k^\star}v^*-L\frac{c_F\xi}{\sqrt{k^\star}}v^{*2}, \end{aligned} \tag{4.1.46}$$

Here, the dimensionless parameters ϵ_1 and ϵ_2 are defined by,

$$\epsilon_1=\frac{\eta_0/\rho}{LU},\quad \epsilon_2=\frac{\Gamma^2}{\big(L/U\big)^2}. \tag{4.1.47}$$

Using the boundary layer approximations, the order of x and u is taken to be 1 while the order of v and y is δ, where δ is the boundary layer's vertical thickness, such that $\dfrac{\delta}{x}\ll 1$. Furthermore, the dimensionless parameter ϵ_1 and ϵ_2 have the order δ. Consequently, using the boundary layer analysis, the above equations in the dimensional form result in

$$\frac{\partial u}{\partial x}+\frac{\partial v}{\partial y}=0, \tag{4.1.48}$$

$$u\frac{\partial u}{\partial x}+v\frac{\partial u}{\partial y}=-\frac{1}{\rho}\frac{\partial p}{\partial x}+\nu\frac{\partial^2 u}{\partial y^2}\left[1+\Gamma^2\left(\frac{\partial u}{\partial y}\right)^2\right]^{\frac{n-1}{2}}+\nu\frac{\partial u}{\partial y}\times$$
$$\frac{\partial}{\partial y}\left[1+\Gamma^2\left(\frac{\partial u}{\partial y}\right)^2\right]^{\frac{n-1}{2}}-\sigma_0 B_0^2 u-\frac{\mu\xi}{k^\star}u-\frac{c_F\rho\xi}{\sqrt{k^\star}}u^2, \tag{4.1.49}$$

$$0=-\frac{1}{\rho}\frac{\partial p}{\partial y}, \tag{4.1.50}$$

where, $\nu=\dfrac{\eta_0}{\rho}$ is the kinematic viscosity.

Eq. (4.1.50) indicates that pressure in the boundary layer is independent of transverse direction. Therefore, $p=p(x)$ only. The governing equation Eq. (4.1.49) can further be written in the form:

$$u\frac{\partial u}{\partial x}+v\frac{\partial u}{\partial y}=-\frac{1}{\rho}\frac{\partial p}{\partial x}+\nu\frac{\partial^2 u}{\partial y^2}\left[1+\Gamma^2\left(\frac{\partial u}{\partial y}\right)^2\right]^{\frac{n-1}{2}}+\nu(n-1)\Gamma^2\frac{\partial^2 u}{\partial y^2}\left(\frac{\partial u}{\partial y}\right)^2\times$$
$$\left[1+\Gamma^2\left(\frac{\partial u}{\partial y}\right)^2\right]^{\frac{n-3}{2}}-\sigma_0 B_0^2 u-\frac{\mu\xi}{k^\star}u-\frac{c_F\rho\xi}{\sqrt{k^\star}}u^2. \tag{4.1.51}$$

Assuming $\dfrac{\partial T}{\partial x}\ll\dfrac{\partial T}{\partial y},\dfrac{\partial C}{\partial x}\ll\dfrac{\partial C}{\partial y}$ and taking similar procedure of the order of magnitude as done above the energy and nanoparticle concentration equations are further reduced.

Therefore, the set of equations governing the conservation of continuity, momentum, energy, and nanoparticle concentration in boundary layer are expressed respectively as follows:

$$\frac{\partial u}{\partial x}+\frac{\partial v}{\partial y}=0, \tag{4.1.52}$$

$$\begin{aligned}u\frac{\partial u}{\partial x}+v\frac{\partial u}{\partial y}=&\nu\frac{\partial^2 u}{\partial y^2}\left[1+\Gamma^2\left(\frac{\partial u}{\partial y}\right)^2\right]^{\frac{n-1}{2}}+\nu(n-1)\Gamma^2\frac{\partial^2 u}{\partial y^2}\left(\frac{\partial u}{\partial y}\right)^2\left[1+\Gamma^2\left(\frac{\partial u}{\partial y}\right)^2\right]^{\frac{n-3}{2}}\\&-\frac{\sigma_0 B_0^2}{\rho}u-\frac{\mu\xi}{\rho k^\star}u-\frac{c_F\xi}{\sqrt{k^\star}}u^2,\end{aligned} \tag{4.1.53}$$

$$u\frac{\partial T}{\partial x}+v\frac{\partial T}{\partial y}=\frac{k}{\rho c_p}\frac{\partial^2 T}{\partial y^2}+\frac{\sigma B_0^2}{\rho c_p}u^2+\tau D_b\left(\frac{\partial T}{\partial y}\frac{\partial C}{\partial y}\right)+\frac{\tau D_T}{T_\infty}\left(\frac{\partial T}{\partial y}\right)^2-\frac{1}{\rho c_p}\frac{\partial q_r}{\partial y}+$$
$$\frac{Q_a}{\rho c_p}(T-T_\infty), \tag{4.1.54}$$

$$u\frac{\partial C}{\partial x}+v\frac{\partial C}{\partial y}=D_b\frac{\partial^2 C}{\partial y^2}+\frac{D_T}{T_\infty}\left(\frac{\partial^2 T}{\partial y^2}\right)-k_p^\star(C-C_\infty). \tag{4.1.55}$$

All the notations are indicated in the acronyms and abbreviations section. As referenced in Ghani and Siri (2018), the boundary conditions suit for the current problem are:

$$\begin{aligned}&u=u_w=ax,\ v=v_w,\ -k\frac{\partial T}{\partial y}=h_t(T_w-T),\ D_b\frac{\partial C}{\partial y}+\frac{D_T}{T_\infty}\frac{\partial T}{\partial y}=0 \text{ at } y=0,\\&u\to 0,\ v\to 0,\ T\to T_\infty,\ C\to C_\infty,\ \text{as } y\to\infty,\end{aligned} \tag{4.1.56}$$

where v_w, h_t, T_w are mass transfer velocity, heat transfer coefficient, and wall temperature of the fluid respectively.

For optically thick medium the Rosseland approximation for the radiative heat flux provides,

$$q_r=\frac{-4\sigma^\star}{3k_e}\frac{\partial T^4}{\partial y}, \tag{4.1.57}$$

where k_e is the coefficient of mean absorption, $\sigma^\star$ is the Stefan-Boltzmann constant. For nonlinear radiation, $q_r=\frac{-16\sigma^\star}{3k_e}T^3\frac{\partial T}{\partial y}$. Hence,

$$\frac{\partial q_r}{\partial y}=\frac{-16\sigma^\star}{3k_e}\left[3T^2\left(\frac{\partial T}{\partial y}\right)^2+T^3\frac{\partial^2 T}{\partial y^2}\right]. \tag{4.1.58}$$

To transform the above system of nonlinear partial differential equations (PDEs) into a set of nonlinear ordinary differential equations (ODEs), the following similarity transformations are introduced:

$$\eta=y\sqrt{\frac{u_w}{\nu x}},\ \ \psi=\sqrt{\nu u_w x}\,f(\eta),\ \ \theta(\eta)=\frac{T-T_\infty}{T_w-T_\infty},\ \ \phi(\eta)=\frac{C-C_\infty}{C_w-C_\infty},\ \ \theta_w=\frac{T_w}{T_\infty}, \tag{4.1.59}$$

where η is the similarity variable and $\psi(x,y)$ denotes the stream function that satisfies the continuity equation through the definitions $u=\frac{\partial\psi}{\partial y}$ and $v=-\frac{\partial\psi}{\partial x}$.

The non-dimensional velocity components u and v can be expressed in terms of the stream function ψ as follows:

$$u=\frac{\partial\psi}{\partial y}=\frac{\partial}{\partial y}\left(x\sqrt{a\nu}\,f(\eta)\right)=x\sqrt{a\nu}f'(\eta)\cdot\sqrt{\frac{a}{\nu}}=xaf'(\eta), \tag{4.1.60}$$

$$v=-\frac{\partial\psi}{\partial x}=-\frac{\partial}{\partial x}\left(x\sqrt{a\nu}f(\eta)\right)=-\sqrt{a\nu}f(\eta). \tag{4.1.61}$$

Substituting Eqs. (4.1.60) and (4.1.61) into the continuity equation gives:

$$\frac{\partial u}{\partial x}+\frac{\partial v}{\partial y}=\frac{\partial}{\partial x}(xa_0 f'(\eta))+\frac{\partial}{\partial y}(-\sqrt{a\nu}f(\eta))$$
$$=af'(\eta)-\sqrt{a\nu}f'(\eta)\cdot\sqrt{\frac{a}{\nu}}=af'(\eta)-af'(\eta)=0. \tag{4.1.62}$$

This confirms that the stream function ψ automatically satisfies the continuity equation.

We now proceed to transform the momentum equation. The second derivative of u with respect to y is:

$$\frac{\partial^2 u}{\partial y^2}=\frac{\partial}{\partial y}\left(\frac{\partial u}{\partial y}\right)=\frac{\partial}{\partial y}\left(xa\sqrt{\frac{a}{\nu}}f''(\eta)\right)=xaf'''(\eta)\left(\frac{a}{\nu}\right)=\frac{xa^2}{\nu}f'''(\eta). \tag{4.1.63}$$

The square of the second derivative is given by:

$$\left(\frac{\partial^2 u}{\partial y^2}\right)^2=\left(\frac{\partial}{\partial y}(xaf'(\eta))\right)^2=\frac{a^3x^2}{\nu}(f'')^2. \tag{4.1.64}$$

The local Weissenberg number is defined as:

$$w_e^2=\frac{a^3\Gamma^2x^2}{\nu}.$$

Substituting Eqs. (4.1.60)–(4.1.64) into the original momentum equation yields:

$$\begin{aligned}xa_0f'(af')-\sqrt{a\nu}f\left(xaf''\sqrt{\frac{a}{\nu}}\right)&=\nu\left(\frac{xa^2}{\nu}f'''\right)\left[1+\frac{w_e^2\nu}{a^3x^2}\cdot\frac{a^3x^2}{\nu}(f'')^2\right]^{\frac{n-1}{2}}\\&+\nu(n-1)\left(\frac{w_e^2\nu}{a^3x^2}\right)\left(\frac{a^2x}{\nu}f'''\right)\left(\frac{a^3x^2}{\nu}(f'')^2\right)\left[1+\frac{w_e^2\nu}{a^3x^2}\cdot\frac{a^3x^2}{\nu}(f'')^2\right]^{\frac{n-3}{2}}\\&-\frac{\sigma B_0^2(xaf')}{\rho}-\frac{\mu\xi}{\rho k^\star}(xaf')-\frac{c_f}{\sqrt{k^\star}}\xi(xaf')^2.\end{aligned} \tag{4.1.65}$$

Simplifying Eq. (4.1.65), dividing through by xa^2, and introducing the following dimensionless parameters: magnetic parameter $\left(M^2=\frac{\sigma B_0^2}{\rho a}\right)$, Porosity parameter $\left(\lambda=\frac{\mu\xi}{\rho a k^\star}\right)$, and Forchheimer parameter $\left(\alpha=\frac{c_f\xi x}{\sqrt{k^\star}}\right)$, we obtain the non-dimensional momentum equation:

$$\left[1+nw_e^2(f'')^2\right]\left[1+w_e^2(f'')^2\right]^{\frac{n-3}{2}}f'''+ff''-(f')^2-M^2f'-\lambda f'-\alpha(f')^2=0. \tag{4.1.66}$$

Now, let us perform a similarity transformation on Eq. (4.1.54). First, the temperature gradients are:

$$\frac{\partial T}{\partial y}=\frac{\partial}{\partial y}(T_\infty+(T_w-T_\infty)\theta(\eta))=(T_w-T_\infty)\sqrt{\frac{a}{\nu}}\theta',$$
$$\frac{\partial T}{\partial x}=\frac{\partial}{\partial x}(T_\infty+(T_w-T_\infty)\theta(\eta))=0.$$

Substituting these expressions into the left-hand side of Eq. (4.1.54), we obtain:

$$u\frac{\partial T}{\partial x}+v\frac{\partial T}{\partial y}=axf'(\eta)\cdot 0-\sqrt{a\nu}f(\eta)(T_w-T_\infty)\sqrt{\frac{a}{\nu}}\theta'=-af(\eta)(T_w-T_\infty)\theta'. \quad (4.1.67)$$

Next, the first, second, fourth, and fifth terms on the right-hand side of Eq. (4.1.54) can be transformed as:

$$\begin{aligned}&\frac{k}{\rho c_p}\left(\frac{\partial^2 T}{\partial y^2}+\frac{1}{k}\frac{\partial}{\partial y}\left(\frac{16\sigma^\star T^3}{3k_e}\frac{\partial T}{\partial y}\right)\right)+\frac{Q_a}{\rho c_p}(T-T_\infty)+\frac{\sigma B_0^2}{\rho c_p}u^2\\ &=\frac{k}{\rho c_p}\frac{\partial}{\partial y}\left[\left(1+\frac{16\sigma^\star T^3}{3kk_e}\right)\frac{\partial T}{\partial y}\right]+\frac{Q_a}{\rho c_p}(T_w-T_\infty)\theta+\frac{\sigma B_0^2}{\rho c_p}(ax)^2(f')^2.\end{aligned}$$

Further substituting the similarity variables and defining the dimensionless thermal radiation parameter $R_d=\frac{16\sigma^\star T_\infty^3}{kk_e}$, we obtain:

$$\begin{aligned}&=\frac{k}{\rho c_p}\frac{a}{\nu}(T_w-T_\infty)\left[\left(1+R_d\left[1+(\theta_w-1)\theta\right]^3\right)\theta'\right]'\\ &+\frac{Q_a}{\rho c_p}(T_w-T_\infty)\theta+\frac{\sigma B_0^2}{\rho c_p}u_w^2(f')^2,\end{aligned}$$

where $u_w=ax$ implies $u_w^2=(ax)^2$.

The third term on the RHS of Eq. (4.1.54) transforms to:

$$\frac{a}{\nu}(T_w-T_\infty)\left[\tau D_b(C_w-C_\infty)\theta'\phi'+\frac{\tau D_T}{T_\infty}(T_w-T_\infty)(\theta')^2\right].$$

Equating and simplifying the transformed LHS and RHS of Eq. (4.1.54), we arrive at the dimensionless energy equation:

$$\begin{aligned}&\left[\left(1+R_d\left[1+(\theta_w-1)\theta\right]^3\right)\theta'\right]'+\frac{\nu\rho c_p}{k}f\theta'+\frac{\nu\rho c_p\sigma B_0^2u_w^2}{akc_p(T_w-T_\infty)}(f')^2\\ &+\frac{Q_a}{a\rho c_p}\cdot\frac{\nu\rho c_p}{k}\theta+\frac{\nu\rho c_p}{k}\cdot\frac{\tau D_b}{\nu}(C_w-C_\infty)\theta'\phi'+\frac{\nu\rho c_p}{k}\cdot\frac{\tau D_T}{\nu T_\infty}(T_w-T_\infty)(\theta')^2=0.\end{aligned}$$

Introducing the following non-dimensional parameters: Prandtl number $\left(Pr=\frac{\nu\rho c_p}{k}\right)$, Eckert number) $\left(Ec=\frac{u_w^2}{c_p(T_w-T_\infty)}\right)$, Magnetic parameter $\left(M^2=\frac{\sigma B_0^2}{\rho a}\right)$, Brownian motion parameter $\left(N_b=\frac{\tau D_b}{\nu}(C_w-C_\infty)\right)$, thermophoresis parameter $\left(N_t=\frac{\tau D_T}{\nu T_\infty}(T_w-T_\infty)\right)$, heat source/sink parameter $\left(Q_0=\frac{Q_a}{a\rho c_p}\right)$, the final dimensionless form of the energy equation becomes:

$$\begin{aligned}&\left[\left(1+R_d\left[1+(\theta_w-1)\theta\right]^3\right)\theta'\right]'+Prf\theta'+PrN_b\theta'\phi'+PrEcM^2(f')^2+PrQ_0\theta\\ &+PrN_t(\theta')^2=0. \quad (4.1.68)\end{aligned}$$

At last, let us transform Eq. (4.1.55). Here, D_b is the Brownian diffusion coefficient, D_T is the thermophoretic diffusion coefficient, $k_p^\star$ is the chemical reaction rate constant, C is the concentration of the nanofluid, and C_∞ is the ambient concentration.

Using the similarity transformation introduced in Eq. (4.1.59), the concentration can be expressed as:

$$C = C_\infty + (C_w - C_\infty)\phi(\eta).$$

The derivatives of C and T with respect to y are given by:

$$\frac{\partial C}{\partial y} = (C_w - C_\infty)\frac{d\phi}{d\eta}\cdot\frac{d\eta}{dy} = \sqrt{\frac{a}{\nu}}(C_w - C_\infty)\phi',$$

$$\frac{\partial^2 C}{\partial y^2} = (C_w - C_\infty)\frac{a}{\nu}\phi'', \quad \frac{\partial^2 T}{\partial y^2} = (T_w - T_\infty)\frac{a}{\nu}\theta''.$$

The partial derivative of C with respect to x becomes:

$$\frac{\partial C}{\partial x} = \frac{\partial}{\partial x}\left[C_\infty + (C_w - C_\infty)\phi(\eta)\right] = (C_w - C_\infty)\phi'\cdot\frac{\partial \eta}{\partial x} = 0,$$

since $\eta = \sqrt{\frac{a}{\nu}}y$ does not depend on x.

Substituting these expressions into Eq. (4.1.55) and simplifying, we obtain:

$$-af(\eta)(C_w - C_\infty)\phi' = D_b\frac{a}{\nu}(C_w - C_\infty)\phi'' + \frac{aD_T}{\nu T_\infty}(T_w - T_\infty)\theta'' - k_p^\star(C_w - C_\infty)\phi.$$

Dividing through by $(C_w - C_\infty)\frac{a}{\nu}$ and introducing the following non-dimensional parameters: Schmidt number $\left(Sc_p = \frac{\nu}{D_b}\right)$, ratio of thermophoresis to Brownian motion $\left(\frac{N_t}{N_b} = \frac{D_T}{D_b T_\infty}\cdot\frac{T_w - T_\infty}{C_w - C_\infty}\right)$, dimensionless chemical reaction parameter $\left(\gamma_c = \frac{k_p^\star}{a}\right)$, we obtain the dimensionless concentration equation:

$$\phi'' + Sc_p f\phi' + \frac{N_t}{N_b}\theta'' - Sc_p\gamma_c\phi = 0. \tag{4.1.69}$$

The boundary conditions are similarly reduced to:

$$\begin{aligned} &f(\eta) = \beta_w, f'(\eta) = 1, \theta'(\eta) = -\beta_{i1}(1-\theta(\eta)),\ N_b\phi'(\eta) + N_t\theta'(\eta) = 0,\ \text{at}\ \eta = 0,\\ &f' \to 0,\ \theta \to 0,\ \phi \to 0 \quad \text{as}\ \eta \to \infty, \end{aligned} \tag{4.1.70}$$

where, $\beta_{i1} = -\frac{h_t}{k}\sqrt{\frac{\nu}{a}}$ is the Biot number, and $\beta_w = -\frac{v_w}{\sqrt{a\nu}}$ is suction/injection parameter.

Quantities of engineering interest:

The surface skin friction, heat transfer rate, and nanoparticles mass transfer rate are delineated as follows.

$$C_{fx}=\frac{2\tau_w}{\rho u_w^2},\ \tau_w=\mu\frac{\partial u}{\partial y}\left[1+\Gamma^2\left(\frac{\partial u}{\partial y}\right)^2\right]^{\frac{n-1}{2}}\Bigg|_{y=0}, \tag{4.1.71}$$

$$Nu_x=\frac{xq_w}{k(T_w-T_\infty)},\ q_w=-k\frac{\partial T}{\partial y}\Big|_{y=0}+(q_r)_w, \tag{4.1.72}$$

$$Sh_x=\frac{xm_w}{D_b(Cw-C_\infty)},\ m_w=-D_b\frac{\partial C}{\partial y}\Big|_{y=0}. \tag{4.1.73}$$

In dimensionless form the local Reynolds number is $Re=\dfrac{u_w x}{\nu}$; and the local skin friction, Nusselt, and Sherwood number respectively take the form:

$$Re^{1/2}C_{fx}=-2f''(0)\left[1+W_e^2f''(0)^2\right]^{\frac{n-1}{2}},\ Re^{-1/2}Nu_x=-\left(1+R_d{\theta_w}^3\right)\theta'(0),$$
$$Re^{-1/2}Sh_x=-\phi'(0). \tag{4.1.74}$$

4.2 Numerical approaches

Bvp4c is a residual error-based, mesh-adaptive finite difference solver that implements the three-stage Lobatto IIIa formula. While the conventional approach in bvp4c estimates missing initial conditions, our problem exhibits high sensitivity to initial conditions and boundary values. To address this, we employed a continuation technique for improved solution stability.

Introducing variable χ_i for $i=1,2,\ldots 7$, we reduce the order of Eqs. (4.1.66), (4.1.68), and (4.1.69) into a system of 7 ODEs.

$$\begin{cases} f=\chi_1,\ f'=\chi_2,\ f''=\chi_3,\ f'''=\chi_3',\ \theta=\chi_4,\\ \theta'=\chi_5,\ \theta''=\chi_5',\ \phi=\chi_6,\ \phi'=\chi_7,\ \phi''=\chi_7'. \end{cases} \tag{4.2.1}$$

To implement continuation method, we follow the steps as discussed in subsection 3.2.1.1 and rewrite the system as follows.

$$\begin{pmatrix}\chi_1'\\ \chi_2'\\ \chi_3'\\ \chi_4'\\ \chi_5'\\ \chi_6'\\ \chi_7'\end{pmatrix}=\begin{pmatrix}\chi_2\\ \chi_3\\ 0\\ \chi_5\\ 0\\ \chi_7\\ Sc_p\gamma_c\chi_6\end{pmatrix}+\delta\times$$

$$\begin{pmatrix} 0 \\ 0 \\ \dfrac{(1+\alpha)\chi_2^2+(M^2+\lambda)\chi_2-\chi_1\chi_3}{(1+nW_e^2\chi_3^2)(1+W_e^2\chi_3^2)^{\frac{n-3}{2}}} \\ 0 \\ \dfrac{-3R_d\vartheta(1+\vartheta\chi_4)^2\chi_5^2-P_r(EcM^2\chi_2^2+\chi_1\chi_5+N_b\chi_5\chi_7+Q_0\chi_4+N_t\chi_5^2)}{\left(1+R_d(1+\vartheta\chi_4)^3\right)} \\ 0 \\ \dfrac{N_t}{N_b}\left(\dfrac{3R_d\vartheta(1+\vartheta\chi_4)^2\chi_5^2+P_r(EcM^2\chi_2^2+\chi_1\chi_5+N_b\chi_5\chi_7+Q_0\chi_4+N_t\chi_5^2)}{\left(1+R_d(1+\vartheta\chi_4)^3\right)}\right)-Sc_p\chi_1\chi_7 \end{pmatrix} \tag{4.2.2}$$

$$\begin{cases} \chi_1(0)=\beta_w,\ \chi_2(0)=1,\ \chi_5(0)=-\beta_{i1}(1-\chi_4(0)),\ N_b\chi_7(0)+N_t\chi_5(0)=0\ at\,\eta=0, \\ \chi_2(\eta)\longrightarrow 0,\ \chi_4(\eta)\longrightarrow 0,\ \chi_6(\eta)\longrightarrow 0\ as\,\eta\longrightarrow\infty. \end{cases} \tag{4.2.3}$$

where, $\vartheta=\theta_w-1$. For numerical computation, we have used the tolerance error, $RelTol=1e-8$.

4.3 Results and Discussion

The transformed first-order ODE, Eq. (4.2.2), along with the boundary conditions, Eq. (4.2.3), is numerically solved using a continuation technique implemented via MATLAB's `bvp4c` solver. The influence of key physical parameters on the dimensionless velocity, temperature, and nanoparticle concentration is investigated for both dilatant and pseudoplastic fluids, with results illustrated through graphs and tables. To ensure the accuracy and reliability of the method, a comparison of the local shear stress is performed with published results in (Siddiq et al. (2021)) under specific limiting cases. The parameter ranges employed in this study are: $0\le M\le 1.5$, $0.5\le We\le 8$, $0\le Ec\le 1.5$, $0.5\le\alpha\le 10$, $1.5\le Pr\le 3$, $0.1\le Rd\le 0.8$, $0.5\le\lambda\le 6$, $0.1\le Nb,Nt\le 0.4$, $0.5\le\theta_w\le 1.7$, $0\le\gamma_c\le 1$, $0.1\le\beta_{i1}\le 0.7$, $-0.1\le Q_0\le 0.2$, $0.5\le Sc_p\le 2$, $0.5\le n\le 2.5$, and β_w is fixed at 0.5.

Figures 4.3.1-4.3.2a highlight the role of the magnetic field through the Lorentz force on the flow field. An increase in M leads to a reduction in velocity for both fluid types, with pseudoplastic fluids showing a more pronounced decrease, as observed in Figure 4.3.1a. Moreover, higher values of M result in elevated temperature profiles and an increase in nanoparticle concentration near the boundary edge, while causing a reduction in concentration near the surface (Figures 4.3.1b-4.3.2a). These observations are consistent with the physical expectation that a stronger magnetic field enhances the Lorentz force, which contributes to temperature and nanoparticle volume fraction enhancement. Figures 4.3.2b-4.3.3 depict the influence of We, representing fluid relaxation time. As We increases, the disparity between shear-thinning and shear-thickening behaviors becomes more prominent in the fields. Specifically, higher We values enhance the velocity in shear-thickening fluids while reducing it in shear-thinning cases. Conversely, temperature and nanoparticle concentration exhibit opposite trends: they decrease in shear-thickening fluids and increase in shear-thinning ones.

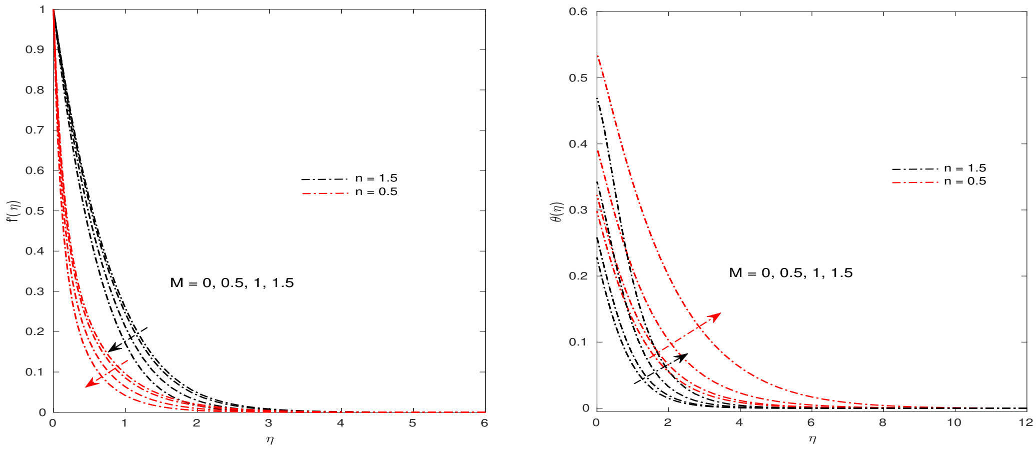

(a) (b)

Figure 4.3.1: Effect of M on (a): velocity profile, (b): temperature profile

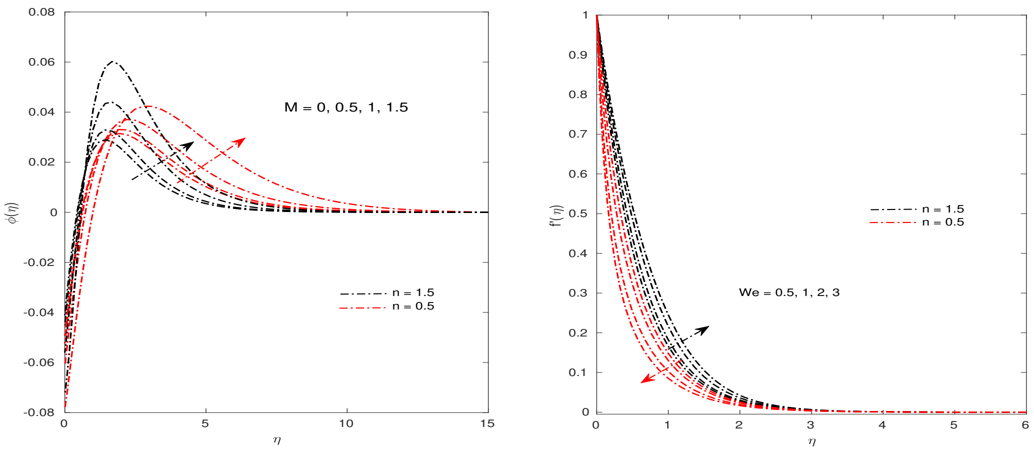

(a) (b)

Figure 4.3.2: Effect of (a): M on concentration profile, (b): We on velocity profile

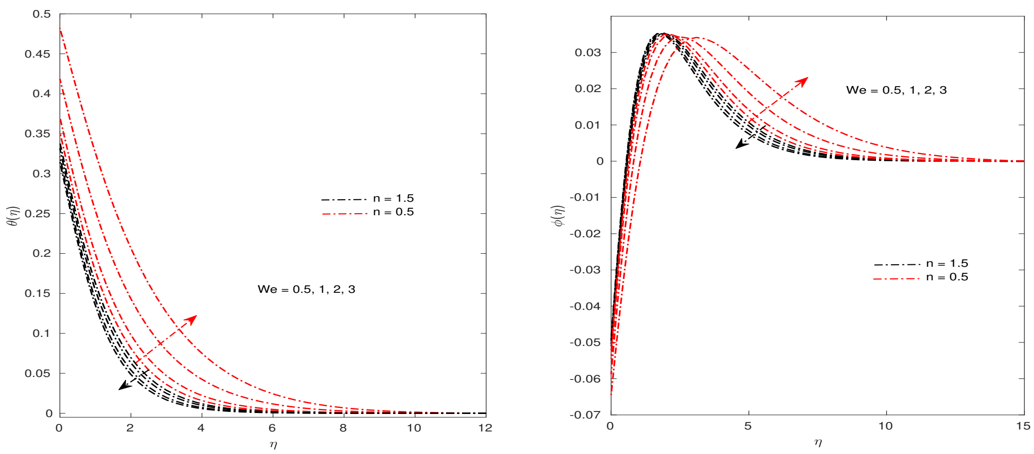

(a) (b)

Figure 4.3.3: Effect of We on (a): temperature profile, (b): concentration profile

The effects of the local inertia coefficient and porosity parameter on the velocity boundary layer are illustrated in Figure 4.3.4. For both shear-thickening and shear-thinning regimes, increasing these parameters suppresses the velocity profile and reduces the corresponding momentum boundary layer thickness due to enhanced resistance to fluid motion.

Figures 4.3.5-4.3.6a illustrate how porosity, thermophoresis parameter (Nt), and the temperature ratio parameter (θ_w) affect the temperature field. An increase in any of these parameters intensifies the temperature profile and broadens the thermal boundary layer. Specifically, Figure 4.3.5b confirms that an increase in Nt leads to enhanced thermophoretic transport of nanoparticles away from the heated surface, thereby increasing temperature field. In Figure 4.3.6a, a higher θ_w promotes thermal conductivity within the fluid, resulting in elevated temperature values. Notably, these parameters have a more pronounced impact on shear-thinning fluids compared to shear-thickening ones. Figure 4.3.6b presents the effect of the Eckert number (Ec) on the temperature distribution. As Ec increases, viscous dissipation becomes significant, converting kinetic energy into internal energy and thereby raising the temperature within the boundary layer.

Figures 4.3.7-4.3.8 highlight the influence of additional parameters on the thermal boundary layer. In Figure 4.3.7a, it is observed that increasing the Prandtl number (Pr) reduces the temperature profile in both fluid regimes due to reduced thermal diffusivity. Meanwhile, Figure 4.3.7b reveals that even a modest increase in the Biot number (β_{i1}) significantly enhances surface heat transfer, resulting in a notable rise in fluid temperature.

The influence of thermal radiation on the temperature field is depicted in Figure 4.3.8a. An increase in the radiation parameter (Rd) leads to a noticeable rise in temperature and an expansion of the thermal boundary layer. This occurs because higher radiation enhances energy transfer to the fluid, which in turn increases the thermal energy content and boundary layer thickness. It is also observed that the thermal boundary layer is more pronounced for shear-thinning fluids compared to shear-thickening ones. Figure 4.3.8b presents the effect of the heat source/sink parameter (Q_0) on the temperature field. As Q_0 increases, the temperature distribution intensifies, indicating the direct contribution of internal heat generation to temperature field enhancement within the boundary layer.

Figures 4.3.9-4.3.10a illustrate the combined effects of the Nt, Nb, and Schmidt number (Sc_p) on nanoparticle concentration. The variations in these parameters exhibit opposite behaviors near the wall and toward the outer edge of the boundary layer. As shown in Figure 4.3.9a, increasing Nt promotes the movement of nanoparticles from warmer regions toward cooler zones, thereby increasing concentration in the outer region. Conversely, Figure 4.3.9b indicates that a higher Nb enhances particle diffusion, resulting in a decrease in nanoparticle concentration near the wall. In Figure 4.3.10a, it is observed that increasing Sc_p-which signifies lower mass diffusivity-diminishes the concentration field and reduces the solutal boundary layer thickness. Finally, Figure 4.3.10b demonstrates that an increase in the chemical reaction parameter (γ_c) further decreases the nanoparticle concentration due to enhanced reactive depletion effects within the boundary layer.

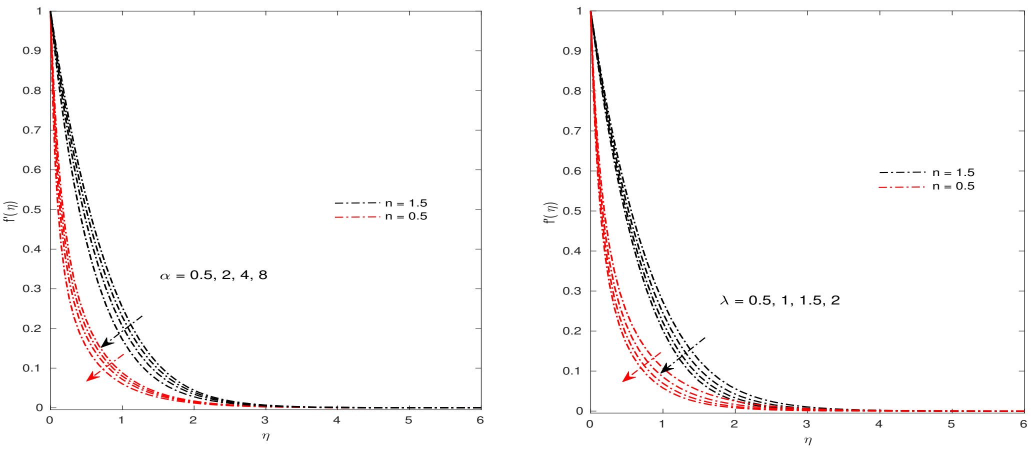

(a) (b)

Figure 4.3.4: Effect of (a): α, (b): λ on velocity profile

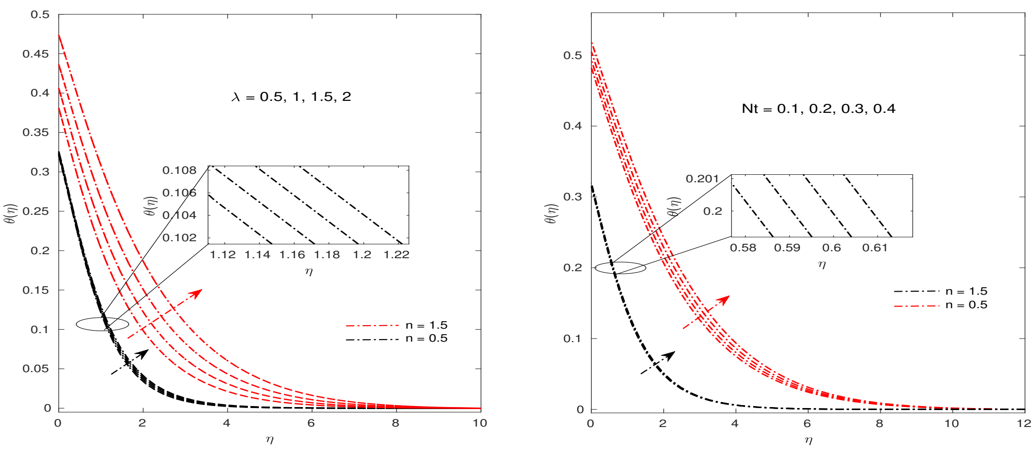

(a) (b)

Figure 4.3.5: Effect of (a): λ, (b): Nt on temperature profile

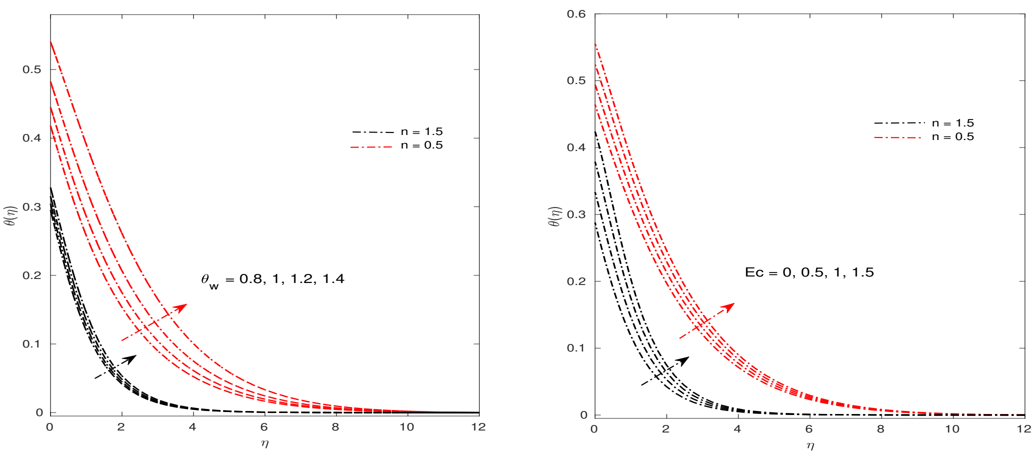

(a)

Figure 4.3.6: Effect of (a): θ_{w}, (b): Ec on temperature profile

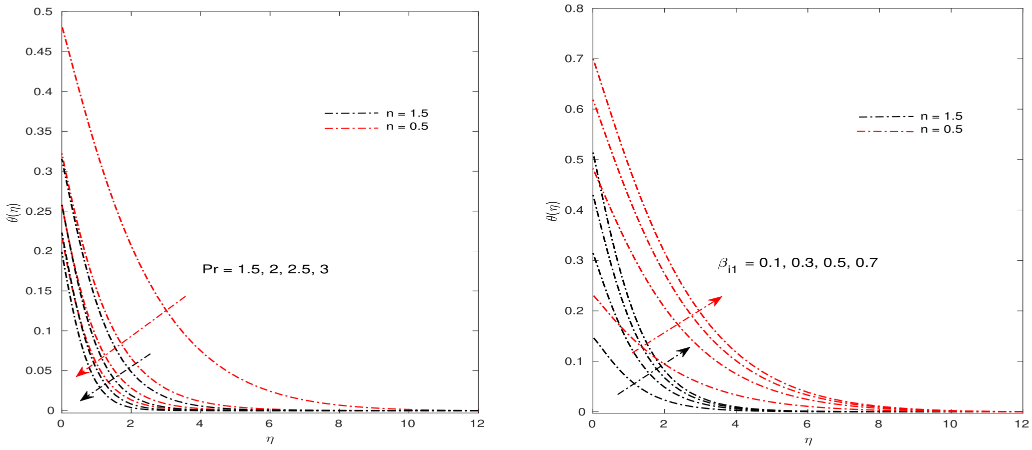

(a) (b)

Figure 4.3.7: Effect of (a): pr, (b): β_{i1} on temperature profile

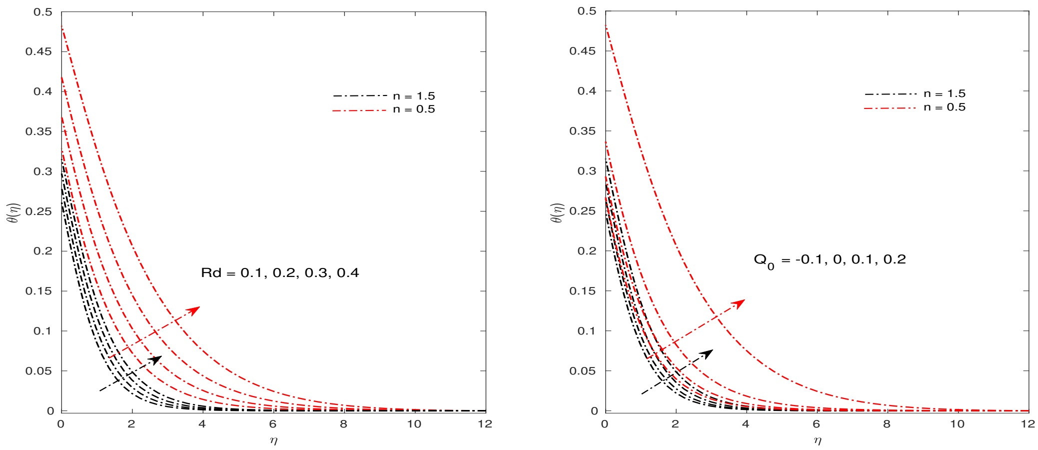

(a) (b)

Figure 4.3.8: Effect of (a): Rd, (b): Q_0 on temperature profile

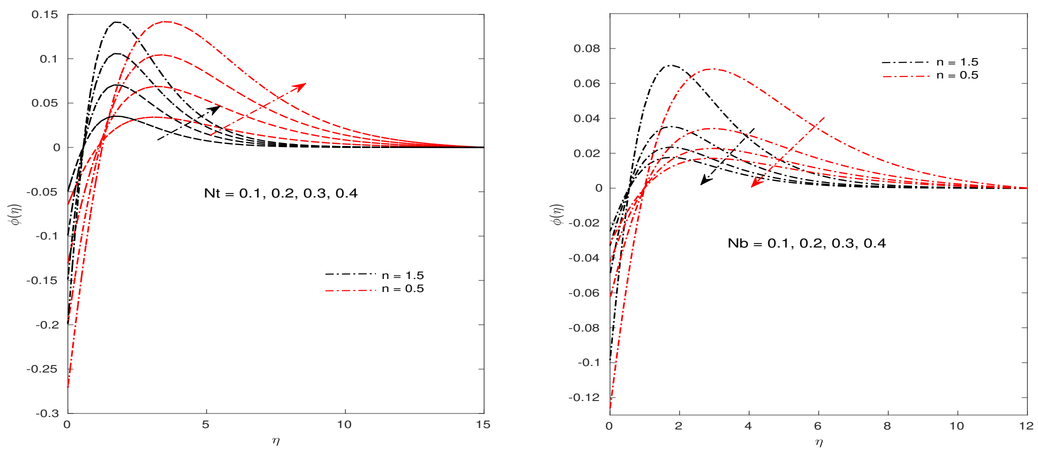

(a) (b)

Figure 4.3.9: Effect of (a): Nt, (b): Nb on concentration profile

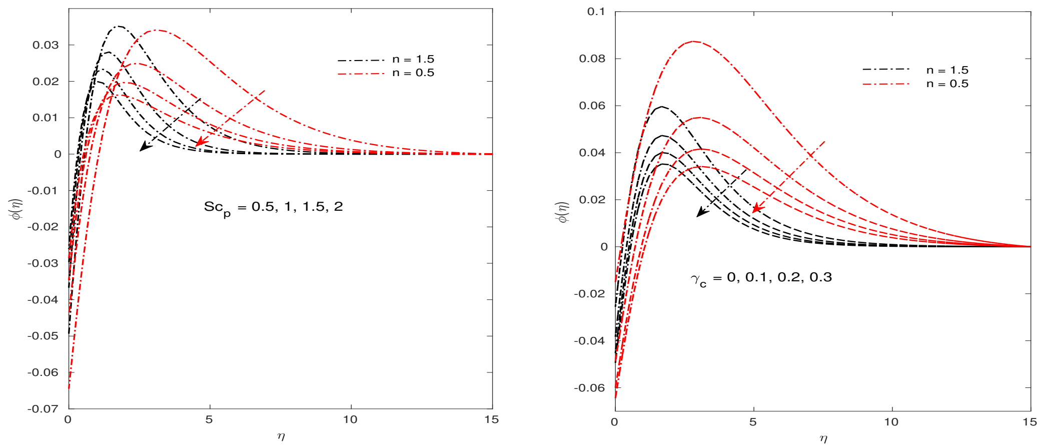

(a) (b)

Figure 4.3.10: Effect of (a): $\mathrm{Sc_p}$, (b): γ_c on concentration profile

Table 4.3.1 presents a comparison of the wall shear stress obtained from the current study with the results reported by Siddiq et al. (2021) under specific limiting conditions. The comparison reveals a high level of consistency between the two, indicating the validity of the present numerical method. The data in the table show that an increase in the M, λ, and α leads to a rise in wall shear stress. In contrast, increasing the n and We results in a decrease in shear stress at the wall.

Table 4.3.1: Comparison of $-f''(0)$ with related literature (Siddiq et al. (2021)), for various parameters when $\theta_w = 1$, $Nb = Nt = 0.1$

Parameters					$-f''(0)$	
M	λ	α	n	We	**Siddiq**	**Present**
0	1	1	1.5	3	1.214344	1.214344
0.7					1.288215	1.288216
1.5					1.508864	1.508864
0.5	1				1.252943	1.252945
	2				1.390551	1.390552
	4				1.613836	1.613836
	1	2			1.343451	1.343452
		5			1.570936	1.570939
		8			1.756682	1.756685
		1	0.5		5.340793	5.340800
			1		1.963674	1.963678
			1.5		1.252943	1.252945
			1.5	0.5	1.763376	1.763372
				2	1.366178	1.366179
				4	1.177725	1.177725

Table 4.3.2: Variations of $Re^{-1/2}Nu_x$ for various values of Pr, Rd, Ec, θ_w, and β_{i1} at $n = 0.5$ and $n = 1.5$

Parameters					$Re^{-1/2}Nu_x$	
Pr	R_d	Ec	θ_w	β_{i1}	$n = 0.5$	$n = 1.5$
0.5	0.4	0.3	1.2	0.3	0.102894	0.189184
1					0.168418	0.292977
1.5					0.284903	0.347547
2					0.344818	0.376245
1.5	0.2				0.257973	0.290954
	0.6				0.291301	0.396726
	0.8				0.279894	0.438540
	0.4	0.2			0.287578	0.352154
		0.4			0.282224	0.342942
		0.8			0.271514	0.324540
		0.3	0.8		0.219971	0.254794
			1		0.246961	0.292226
			1.4		0.331077	0.423023
			1.2	0.2	0.223443	0.257210
				0.4	0.328880	0.420800
				0.6	0.386372	0.531350

Table 4.3.3: Variations of $Re^{-1/2}Sh_x$ for various values of Nb, Nt, γ_c, Sc_p and pr at $n = 0.5$, and $n = 1.5$

Parameters					$Re^{-1/2}Sh_x$	
Nb	Nt	γ_c	Sc_p	Pr	$n = 0.5$	$n = 1.5$
0.1	0.1	0.3	0.5	1.5	0.168461	0.205503
0.2					0.084231	0.102752
0.3					0.056153	0.068501
0.2	0.2				0.166745	0.205073
	0.3				0.247369	0.306952
	0.4				0.325899	0.403757
	0.1	0.5			0.084212	0.102746
		0.8			0.084176	0.102735
		1			0.084153	0.102727
		0.3	0.8		0.084080	0.102689
			1		0.084014	0.102658
			1.2		0.083962	0.102633
			0.5	0.5	0.030420	0.055932
				1	0.049792	0.086618
				2	0.101942	0.111276
				3	0.117134	0.121000

Table 4.3.2 illustrates the variation in local heat transfer rate with respect to changes in several physical parameters. It is observed that the heat transfer rate improves with increasing values of the $Pr)$ R_d,

θ_w, and β_{i1} for both shear-thinning and shear-thickening fluids. However, an opposite trend is noted with the Ec, where higher values lead to a reduction in the rate of heat transfer due to enhanced viscous dissipation.

It is evident that the rate of heat transfer is more pronounced in the shear-thickening regime compared to the shear-thinning regime. Table 4.3.3 presents the behavior of the mass transfer rate in response to changes in key parameters, including Nb, Nt, γ_c, Sc_p, and Pr. The table indicates that increasing Nt and Pr enhances the rate of mass transfer for both types of fluid behavior. On the contrary, increasing Nb, γ_c, and Sc_p leads to a reduction in the mass transfer rate.

4.4 Summary

This chapter has presented a numerical study of boundary layer flow for an incompressible MHD Carreau nanofluid over a stretching surface. The model incorporates effects of nonlinear thermal radiation, Joule heating, internal heat generation or absorption, chemical reactions, and flow through a porous medium governed by the Darcy–Forchheimer model. Additionally, nanoparticle transport due to Brownian motion and thermophoresis is included, allowing the analysis to capture both shear-thinning and shear-thickening behaviors. The resulting boundary value problem is solved using the continuation technique implemented via MATLAB's `bvp4c` solver. The key findings are summarized as follows:

1. Increasing M suppresses the velocity field while enhancing both thermal and concentration boundary layers.
2. The We positively influences the velocity field in shear-thickening fluids and enhances temperature and concentration profiles in shear-thinning fluids. In contrast, it reduces velocity in shear-thinning fluids and lowers temperature and concentration in shear-thickening fluids.
3. Higher values of the porosity parameter and local inertia coefficient decrease the velocity profile due to increased resistance in the porous medium.
4. Raising the R_d from 0.1 to 0.4 increases the wall temperature by approximately 20.62% for $n = 1.5$ and by 46.76% for $n = 0.5$.
5. The temperature field rises with increasing values of λ, θ_w, β_{i1}, and Q_0, while it decreases with increasing Pr.
6. Nanoparticle concentration diminishes with an increase in Nb, Sc_p, and γ_c, but it increases with higher Nt parameter.
7. Wall shear stress increases with rising values of M, λ, and α, while it decreases with higher values of the n and We.

CHAPTER FIVE

MHD Thermo-bioconvective Flow of 3D Rotating Williamson Nanofluid with Arrhenius Activation Energy in a Darcy–Forchheimer Medium over an Exponentially Stretching Surface

A thorough review of the existing literature highlights the absence of comprehensive models addressing the combined effects of microorganismic Brownian motion and activation energy-based chemical reactions on the thermobioconvective flow of MHD Williamson nanofluids within a 3D rotating system. This study advances the field by incorporating Soret and Dufour diffusion, Hall and ion-slip currents, nonlinear thermal radiation, internal heat generation/absorption, and Arrhenius-type chemical reactions in the flow over an exponentially stretching vertical sheet.

Consequently, the novelty of this research is underscored as follows:

(i) Extending the 2D Newtonian nanofluid models of Dhlamini et al. (2022) and Mandal et al. (2023), which considered Brownian motion and chemical reactions, to a 3D non-Newtonian flow over an exponentially stretching surface.

(ii) Exploring the combined effects of Soret and Dufour diffusion and nanoparticle diffusion within the context of bioconvective flows.

(iii) Analyzing the impacts of nonlinear radiation, Hall current, and ion-slip effects on thermo-bioconvective flows.

(iv) Achieving exponentially convergent solutions for large systems of highly nonlinear differential equations using the spectral local linearization method.

5.1 Mathematical Model and Formulation

5.1.1 Flow geometry and assumptions

This study considers a steady, incompressible, and viscous 3D MHD flow of a Williamson nanofluid containing motile microorganisms. The flow is analyzed in a rotating reference frame with a uniform angular velocity $\bar{\Omega}$ about the z-axis, past a vertical surface in a porous medium. The sheet, located at $z = 0$, stretches in the x-direction with an exponential velocity profile $U_{\mathrm{w}} = U_0 e^{x/L}$, while the fluid domain occupies the half-space $z > 0$. A Cartesian coordinate system is employed such that the x- and y-axes lie along the surface and the z-axis is normal to it. A constant transverse magnetic field of strength B_0 is applied, influencing the fluid motion. The suspended gyrotactic microorganisms contribute to nanoparticle stabilization and mixing. The nanoparticle suspension is assumed dilute enough to neglect microbial interactions and prevent bioconvective instability. Thermobioconvective boundary conditions are imposed, with surface temperature T_{w}, nanoparticle concentration C_{w}, and microorganism density N_{w}. The corresponding ambient values are T_{∞}, C_{∞}, and N_{∞}, satisfying $T_{\infty} < T_{\mathrm{w}}$, $C_{\infty} < C_{\mathrm{w}}$, and $N_{\infty} < N_{\mathrm{w}}$. The schematic in Figure 5.1.1 depicts the configuration for the case where microbial diffusivity exceeds that of nanoparticles, heat, and momentum.

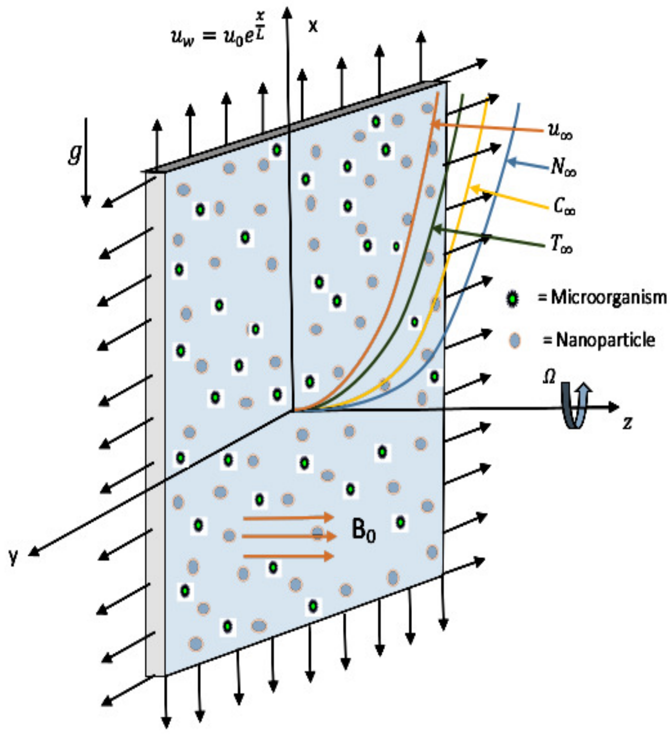

Figure 5.1.1: Geometry of the flow problem.

5.1.2 Model description

The Cauchy stress tensor, $\boldsymbol{\tau}$ for Williamson model rheology and its associated shear rate γ' are deliberated as follow (Shawky et al. (2019)).

$$\boldsymbol{\tau} = -p\mathbf{I} + \mu_1, \tag{5.1.1}$$

$$\mu_1 = \left(\mu_\infty + \frac{\mu_0 - \mu_\infty}{1 - \Gamma\dot{\gamma}}\right)\mathbf{D}_1, \tag{5.1.2}$$

$$\gamma' = \sqrt{\frac{1}{2}\sum_i\sum_j \gamma'_{ij}\gamma'_{ji}} = \sqrt{\frac{1}{2}tr(\mathbf{D}_1^2)}, \tag{5.1.3}$$

in which p, $\mathbf{I}$, μ_0, μ_∞, $\Gamma > 0$, and $\mathbf{D}_1 = (\mathrm{grad}\boldsymbol{V}) + (\mathrm{grad}\boldsymbol{V})^T$ denote pressure, identity tensor, zero-shear rate viscosity, infinite shear rate viscosity, the time material parameter, and the first Rivlin-Ericksen tensor, respectively. Considering the case $\mu_\infty = 0$, $\Gamma\dot{\gamma} < 1$, and using binomial expansion, Eq. (5.1.2) takes the form:

$$\mu_1 = \mu_0 \Big(1 + \Gamma \dot{\gamma} \Big) \mathbf{D}_1. \tag{5.1.4}$$

5.1.3 Governing equations

Based on the above assumptions and applying the boundary layer and Boussinesq approximations, the 3D governing equations for mass, momentum, energy, nanoparticle concentration, and motile microorganism density are given as:

$$\frac{\partial u}{\partial x} + \frac{\partial v}{\partial y} + \frac{\partial w}{\partial z} = 0, \tag{5.1.5}$$

$$u\frac{\partial u}{\partial x} + v\frac{\partial u}{\partial y} + w\frac{\partial u}{\partial z} - 2\bar{\Omega} v = \nu_f \left[1 + \sqrt{2}\Gamma \frac{\partial u}{\partial z} \right] \frac{\partial^2 u}{\partial z^2} - \frac{\sigma_0 B_0^2}{\rho_f \left[\beta_e^2 + (1+\beta_e\beta_i)^2 \right]} \Big[\beta_e v + (1+\beta_e\beta_i)\, u \Big] - \frac{\nu_f \xi}{k^\star} u - \frac{c_F \xi}{\sqrt{k^\star}} u^2 + \frac{g}{\rho_f} \Big[(1 - C_\infty)\rho_f \beta_T (T - T_\infty) - \beta_c(\rho_p - \rho_f)(C - C_\infty) - \beta_m(\rho_m - \rho_f)(N - N_\infty) \Big], \tag{5.1.6}$$

$$u\frac{\partial v}{\partial x} + v\frac{\partial v}{\partial y} + w\frac{\partial v}{\partial z} + 2\bar{\Omega} u = \nu_f \left[1 + \sqrt{2}\Gamma \frac{\partial v}{\partial z} \right] \frac{\partial^2 v}{\partial z^2} + \frac{\sigma_0 B_0^2}{\rho_f \left[\beta_e^2 + (1+\beta_e\beta_i)^2 \right]} \Big[\beta_e u - (1+\beta_e\beta_i)\, v \Big] - \frac{\nu_f \xi}{k^\star} v - \frac{c_F \xi}{\sqrt{k^\star}} v^2, \tag{5.1.7}$$

$$u\frac{\partial T}{\partial x} + v\frac{\partial T}{\partial y} + w\frac{\partial T}{\partial z} = \frac{k}{\rho c_p}\frac{\partial^2 T}{\partial z^2} + \frac{\sigma_0 B_0^2}{\rho_f c_p \left[\beta_e^2 + (1+\beta_e\beta_i)^2 \right]} \Big(u^2 + v^2 \Big) + \frac{D_M K_T}{c_s c_p}\frac{\partial^2 C}{\partial z^2} - \frac{1}{\rho_f c_p}\frac{\partial q_r}{\partial z} + \tau \left[D_b \frac{\partial T}{\partial z}\frac{\partial C}{\partial z} + D_m \frac{\partial T}{\partial z}\frac{\partial N}{\partial z} + \frac{D_T}{T_\infty}\left(\frac{\partial T}{\partial z} \right)^2 \right] + \frac{Q_a}{\rho_f c_p}(T - T_\infty), \tag{5.1.8}$$

$$u\frac{\partial C}{\partial x} + v\frac{\partial C}{\partial y} + w\frac{\partial C}{\partial z} = D_b \frac{\partial^2 C}{\partial z^2} + \frac{D_M K_T}{T_m}\frac{\partial^2 T}{\partial z^2} + \frac{D_T}{T_\infty}\frac{\partial^2 T}{\partial z^2} - k_p^\star (C - C_\infty) \times \left(\frac{T}{T_\infty} \right)^n exp(\frac{-E_a}{\kappa T}), \tag{5.1.9}$$

$$u\frac{\partial N}{\partial x} + v\frac{\partial N}{\partial y} + w\frac{\partial N}{\partial z} + \frac{b W_c}{(C_w - C_\infty)} \left[\frac{\partial}{\partial z}\left(N \frac{\partial C}{\partial z} \right) \right] = D_m \frac{\partial^2 N}{\partial z^2} + \frac{D_T}{T_\infty}\frac{\partial^2 T}{\partial z^2} - k_b^\star (N - N_\infty)\left(\frac{T}{T_\infty} \right)^n exp(\frac{-E_a}{\kappa T}). \tag{5.1.10}$$

The boundary conditions to which the equations are subjected to are:

$$u = U_0 e^{x/L},\ v = w = 0,\ -k\frac{\partial T}{\partial z} = h_t(T_w - T),\ D_b\frac{\partial C}{\partial z} + \frac{D_T}{T_\infty}\frac{\partial T}{\partial z} = 0, N = N_w,\ at\ z = 0,$$
$$u \longrightarrow 0,\ v \longrightarrow 0,\ T \longrightarrow T_\infty,\ C \longrightarrow C_\infty, N \longrightarrow N_\infty, \quad as \quad z \longrightarrow \infty, \tag{5.1.11}$$

in which (u,v,w) are velocity components, T is the fluid temperature, C denotes nanoparticles concentration, N is the density of motile microorganisms, U_0 is a constant having dimensions of velocity, L is the reference length, $\mathrm{T_m}$ is mean fluid temperature, K_T is thermal diffusion ratio, $\tau(=(\rho c_p)_p/(\rho c_p)_f)$ denotes ratio of effective heat capacity of nanoparticles to base fluid. The non-linear radiative heat flux, q_r is as described in Eq. (4.1.57)- (4.1.58). All the remaining notations are described in the acronyms and abbreviations section.

5.1.4 Nondimensionalization and reduction to ODEs

We introduce the following similarity variables (Javed et al. (2011)):

$$\eta = z\sqrt{\frac{U_0}{2\nu_f L}}e^{x/2L},\ u = U_0 e^{x/L} f'(\eta),\ v = U_0 e^{x/L} g(\eta), w = -\sqrt{\frac{\nu_f U_0}{2L}}e^{x/2L}\times$$
$$\Big(f(\eta) + \eta f'(\eta)\Big), \theta = \frac{T - T_\infty}{T_w - T_\infty}, \phi = \frac{C - C_\infty}{C_w - C_\infty},\ \chi = \frac{N - N_\infty}{N_w - N_\infty}, \tag{5.1.12}$$

where, η is the similarity variable. Invoking Eqs. (4.1.58), (5.1.4)), and (5.1.12) into Eqs. (5.1.5)-(5.1.11), the governing equations and their corresponding boundary conditions are reduced to the following non-dimensional forms.

$$f''' + W_e f'' f''' - \frac{M}{\beta_e^2 + \Big(1+\beta_e\beta_i\Big)^2}\Big[\beta_e g + \Big(1+\beta_e\beta_i\Big)f'\Big] - \lambda f' + f f'' - \alpha f'^2 - 2f'^2$$
$$+4\Omega g + \lambda_m\Big(\theta - N_r\phi - R_b\chi\Big) = 0, \tag{5.1.13}$$
$$g'' + W_e g' g'' + \frac{M}{\beta_e^2 + \Big(1+\beta_e\beta_i\Big)^2}\Big[\beta_e f' - \Big(1+\beta_e\beta_i\Big)g\Big] - \lambda g + f g' - \alpha g^2$$
$$-2f'g - 4\Omega f' = 0, \tag{5.1.14}$$

$$\theta'' + R_d[1 + (\theta_w - 1)\theta]^3\theta'' + 3R_d(\theta_w - 1)\Big[1 + (\theta_w - 1)\theta\Big]^2\theta'^2 + \frac{\mathrm{PrMEc}}{\beta_e^2 + \Big(1+\beta_e\beta_i\Big)^2}f'^2$$
$$+\mathrm{PrDu}\phi'' + \frac{\mathrm{PrMEc}}{\beta_e^2 + \Big(1+\beta_e\beta_i\Big)^2}g^2 + \mathrm{PrN_b}\theta'\phi' + \mathrm{PrN_m}\theta'\chi' + \mathrm{PrN_t}\theta'^2 +$$
$$Pr f\theta' + \mathrm{Pr}Q_0\theta = 0, \tag{5.1.15}$$

$$\phi'' + \frac{\mathrm{N_t}}{\mathrm{N_b}}\theta'' + \mathrm{SrLe_1}\theta'' + \mathrm{PrLe_1} f\phi' - \gamma_{\mathrm{c}}\mathrm{PrLe_1}\phi\Big[1+\big(\theta_w-1\big)\theta\Big]^n \times$$
$$\exp\left(\frac{-E}{1+\big(\theta_w-1\big)\theta}\right) = 0, \tag{5.1.16}$$
$$\chi'' + \mathrm{PrLe_2} f\chi' - P_b\chi'\phi' - \frac{P_b}{\big(\chi_w-1\big)}\phi'' - P_b\chi\phi'' - \mathrm{PrLe_2}\gamma_{\mathrm{b}}\Big[1+\big(\theta_w-1\big)\theta\Big]^n \times$$
$$\exp\left(\frac{-E}{1+\big(\theta_w-1\big)\theta}\right)\chi + \frac{N_t}{N_m}\theta'' = 0, \tag{5.1.17}$$

having boundary conditions:

$$f(\eta) = g(\eta) = 0,\ f'(\eta) = 1,\ \theta'(\eta) = -\beta_{i1}(1-\theta(\eta)),\ N_b\phi'(\eta) + N_t\theta'(\eta) = 0,$$
$$\chi(\eta) = 1, \quad \text{at } \eta = 0,\ f'(\eta)\to 0,\ g(\eta)\to 0,\ \theta(\eta)\to 0,\ \phi(\eta)\to 0,$$
$$\chi(\eta)\to 0, \quad \text{as } \eta\to\infty, \tag{5.1.18}$$

The dimensionless parameters are defined as follows. The Weissenberg number is given by $\mathrm{W_e^2} = \dfrac{\Gamma^2(\mathrm{U_0 e^{x/L}})^3}{\nu_{\mathrm{f}}\mathrm{L}}$, while the magnetic field parameter takes the form $\mathrm{M} = \dfrac{2\mathrm{L}\sigma_0\mathrm{B_0^2}}{\rho_{\mathrm{f}}\mathrm{U_0 e^{x/L}}}$. The porosity parameter is expressed as $\lambda = \dfrac{2L\nu_f\xi}{k^\star U_0 e^{x/L}}$, and the mixed convection parameter is written as $\lambda_m = \dfrac{2L\beta_T g(1-C_\infty)(T_w-T_\infty)}{(U_0e^{x/L})^2}$.

The activation energy is defined by $E = \dfrac{E_a}{\kappa T_\infty}$, and the buoyancy ratio parameter becomes $N_r = \dfrac{\beta_c(\rho_p-\rho_f)(C_w-C_\infty)}{\beta_T\rho_f(1-C_\infty)(T_w-T_\infty)}$. The Dufour number is expressed as $Du = \dfrac{D_M K_T(C_w-C_\infty)}{c_s C_p \nu_f(T_w-T_\infty)}$, while the Soret number takes the form $S_r = \dfrac{D_M K_T(T_w-T_\infty)}{T_m\nu(C_w-C_\infty)}$. The bioconvective Rayleigh number is $R_b = \dfrac{\beta_m(\rho_m-\rho_f)(N_w-N_\infty)}{\beta_T\rho_f(1-C_\infty)(T_w-T_\infty)}$, and the local inertia coefficient is defined as $\alpha = 2L\dfrac{c_F\xi}{\sqrt{k^\star}}$. The Prandtl number is $\mathrm{Pr} = \dfrac{\nu_{\mathrm{f}}\rho\mathrm{c_p}}{\mathrm{k}}$, while the Lewis numbers for nanoparticles and motile microorganisms are given by $Le_1 = \dfrac{k}{\rho c_p D_b}$ and $Le_2 = \dfrac{k}{\rho c_p D_m}$, respectively.

The Peclet number for bioconvection is $P_b = \dfrac{bW_c}{D_m}$, and the temperature and microorganism density ratios are given by $\theta_w = \dfrac{T_w}{T_\infty}$ and $\chi_w = \dfrac{N_w}{N_\infty}$. The Brownian motion parameter for motile microorganisms is expressed as $N_m = \dfrac{\tau D_m(N_w-N_\infty)}{\nu_f}$, and the Eckert number is $E_c = \dfrac{(u_0e^{x/L})^2}{c_p(T_w-T_\infty)}$. The Biot number for convective heat transfer is written as $\beta_{i1} = -\dfrac{h_t}{k_t}\left(\dfrac{2\nu_f L}{u_0}\right)e^{-x/2L}$, and the radiation parameter is $R_d = \dfrac{16\sigma^\star T_\infty^3}{3kk_e}$. The Brownian motion and thermophoresis parameters for nanoparticles are defined as $N_b = \dfrac{\tau D_b(C_w - C_\infty)}{\nu_f}$ and $N_t = \dfrac{\tau D_T(T_w - T_\infty)}{\nu_f T_\infty}$, respectively.

The heat generation/absorption parameter is $Q_0 = \dfrac{2LQ_a}{\rho c_p u_0 e^{x/L}}$, while the non-dimensional rotation rate is $\Omega = \bar{\Omega}\dfrac{L}{u_0}e^{-x/L}$. Finally, the local chemical reaction rates for nanoparticles and microorganisms are given by $\gamma_c = -k_p^\star\left(\dfrac{2L}{u_0 e^{x/L}}\right)$ and $\gamma_b = -k_b^\star\left(\dfrac{2L}{u_0 e^{x/L}}\right)$, respectively.

5.1.5 Engineering significance

To examine the engineering implications of the present model, key transport quantities-namely, the local surface shear stresses, heat and mass transfer rates, and microbial density flux-are evaluated as follows:

$$
\begin{aligned}
&C_{fx} = \frac{\tau_{wx}}{\frac{1}{2}\rho u_w^2}, \quad \tau_{wx} = \mu\left(\frac{\partial u}{\partial z} + \frac{\Gamma}{\sqrt{2}}\left(\frac{\partial u}{\partial z}\right)^2\right)\Bigg|_{z=0},\\
&C_{fy} = \frac{\tau_{wy}}{\frac{1}{2}\rho v_w^2}, \quad \tau_{wy} = \mu\left(\frac{\partial v}{\partial z} + \frac{\Gamma}{\sqrt{2}}\left(\frac{\partial v}{\partial z}\right)^2\right)\Bigg|_{z=0},\\
&Nu_x = -\frac{x}{k(T_w - T_\infty)}\left(k + \frac{16\sigma^\star}{3k_e}T^3\right)\left(\frac{\partial T}{\partial z}\right)\Bigg|_{z=0},\\
&Sh_x = -\frac{x}{(C_w - C_\infty)}\left(\frac{\partial C}{\partial z}\right)\Bigg|_{z=0}, \quad Nn_x = -\frac{x}{(N_w - N_\infty)}\left(\frac{\partial N}{\partial z}\right)\Bigg|_{z=0}.
\end{aligned} \tag{5.1.19}
$$

Using the similarity transformations introduced in Eq. (5.1.12), the dimensionless expressions for the local skin friction coefficients in both x and y directions, the Nusselt number, Sherwood number, and motile microorganism density number are formulated as:

$$
\begin{aligned}
&Re^{1/2}C_{fx} = \sqrt{2}f''(0)\left(1 + \frac{W_e}{2}f''(0)\right), \quad Re^{1/2}C_{fy} = \sqrt{2}g'(0)\left(1 + \frac{W_e}{2}g'(0)\right),\\
&Re^{-1/2}Nu_x = -\left(1 + R_d\theta_w^3\right)\theta'(0), \quad Re^{-1/2}Sh_x = -\phi'(0), \quad Re^{-1/2}Nn_x = -\chi'(0).
\end{aligned} \tag{5.1.20}
$$

5.2 Numerical approaches

5.2.1 Mathematical description of the method

The SLLM is simple, very efficient, and convergent iterative algorithm. This method uses fewer grid points and is numerically stable with a fast convergence rate for nonlinear problems, as compared to finite difference and finite element methods. The local linearization method (LLM) involves formulating a decoupled iterative scheme by employing a smooth, univariate linearization of the nonlinear component of functions and their corresponding derivatives using the Taylor series approximation.

The SLLM employs spectral collocation discretization to obtain numerical solutions to the problem. Below, key advantages of spectral methods are outlined:

- **Exact computation of derivatives**: The method utilizes a differentiation matrix, D, which ensures exact derivative calculations.
- **Adaptable basis functions**: Spectral methods allow the selection of basis functions that are well-suited for the specific characteristics of practical problems.
- **High accuracy**: For the same degrees of freedom, spectral methods typically achieve higher accuracy compared to finite difference methods.
- **Global basis functions**: Unlike the finite element method, which relies on local basis functions, the pseudospectral method utilizes global basis functions, leading to faster convergence for smooth solutions.

However, spectral methods typically exhibit poor performance in non-smooth problems due to their dependence on global basis functions. For a detailed discussion on spectral methods and the local linearization technique, see (Motsa (2013); Shahid et al. (2021)).

5.2.2 Linearization and decoupling of ODEs

The system of coupled ODEs defined in Eq. (5.1.13)-(5.1.17) together with their boundary conditions, Eq. (5.1.18) are highly nonlinear and difficult to attempt analytically. To use the SLLM, the set of equations are arranged in a specific order then solved successively by operating the results from the one equation into the subsequent equation using spectral method. First, we require a reduction in the order of Eq. (5.1.13) by letting $f'(\eta) = h(\eta)$. Assuming that anonymous functions that f and h are known at a particular iteration level, the local linearization iteration scheme may be stepped as follows.

$$\Big(1+W_e g_r'\Big)g_{r+1}'' + \Big(W_e g_r'' + f_r\Big)g_{r+1}' - \Big(t_2 + 2h_r + 2\alpha g_r\Big)\times g_{r+1} = W_e g_r'' g_r' - \alpha g_r^2 - t_1 h_r, \tag{5.2.1}$$

$$\phi_{r+1}'' + t_{13} f_r \phi_{r+1}' - t_{14}\Big(1+t_4\theta_r\Big)^n exp\Big(\frac{-E}{1+t_4\theta_r}\Big)\phi_{r+1} = -t_{12}\theta_r'', \tag{5.2.2}$$

$$\chi_{r+1}'' + \Big(t_{15} f_r - P_b \phi_{r+1}'\Big)\chi_{r+1}' - \Big(P_b\phi_{r+1}'' + t_{17}\Big(1+t_4\theta_r\Big)^n exp\Big(\frac{-E}{1+t_4\theta_r}\Big)\Big)\chi_{r+1} = \frac{P_b}{t_{16}}\phi_{r+1}'' - t_{18}\theta_r'', \tag{5.2.3}$$

$$\left(1+W_e h_r'\right)h_{r+1}''+\left(W_e h_r''\right)h_{r+1}'-\left(t_2+2t_3h_r-f_r\right)h_{r+1}=W_e h_r' h_r''-t_3h_r^2$$
$$+t_1g_{r+1}-\lambda_m\theta_r+\lambda_m N_r\phi_{r+1}+\lambda_m R_b\chi_{r+1}, \tag{5.2.4}$$

$$f_{r+1}'=h_{r+1}, \tag{5.2.5}$$

$$\left(1+R_d\left(1+t_4\theta_r\right)^3\right)\theta_{r+1}''+\left(\left(2t_5\left(1+t_4\theta_r\right)^2+2t_{10}\right)\theta_r'+t_8\phi_{r+1}'+t_9\chi_{r+1}'+P_rf_{r+1}\right)\theta_{r+1}'$$
$$+\left(t_{11}+3R_dt_4\left(1+t_4\theta_r\right)^2\theta_r''+2t_5t_4\left(1+t_4\theta_r\right)\theta_r'^2\right)\theta_{r+1}=3R_dt_4\left(1+t_4\theta_r\right)^2\theta_r''\theta_r+$$
$$t_5\left(1+t_4\theta_r\right)\left(2t_4\theta_r+\left(1+t_4\theta_r\right)\right)\theta_r'^2+t_{10}\theta_r'^2-t_6h_{r+1}^2-t_6g_{r+1}^2-t_7\phi_{r+1}''. \tag{5.2.6}$$

The correlative boundary conditions take the form:

$$g_{r+1}(0)=0,\ g_{r+1}(\infty)=0,\ \phi_{r+1}(\infty)=0,\ \phi_{r+1}'(0)=-\frac{\mathrm{Nt}}{\mathrm{Nb}}\theta_r'(0),\ \chi_{r+1}(0)=1,$$
$$\chi_{r+1}(\infty)=0, h_{r+1}(0)=1,\quad h_{r+1}(\infty)=0,\ f_{r+1}(0)=0,\ \theta_{r+1}'(0)=-Bi_1(1-\theta_{r+1}(0)),$$
$$\theta_{r+1}(\infty)=0, \tag{5.2.7}$$

where, r and r +1 denote the previous and current iteration values, respectively. $t_1=\dfrac{M\beta_e}{\left(\beta_e^2+\left(1+\beta_e\beta_i\right)^2\right)}-4\bar{\Omega},\ t_2=\dfrac{M(1+\beta_e\beta_i)}{\left(\beta_e^2+\left(1+\beta_e\beta_i\right)^2\right)}+\lambda,\ t_3=2+\alpha,\ t_4=\theta_w-1,\ t_5=3R_d\left(\theta_w-1\right),\ t_6=\dfrac{PrMEc}{\left(\beta_e^2+\left(1+\beta_e\beta_i\right)^2\right)},\ t_7=PrDu,\ t_8=PrN_b,\ t_9=PrN_m,\ t_{10}=PrN_t,$ $t_{11}=PrQ_0,\ t_{12}=S_rLe_1+\frac{N_t}{N_b},\ t_{13}=PrLe_1,\ t_{14}=\gamma_cPrLe_1,\ t_{15}=PrLe_2,\ t_{16}=\chi_w-1,$ $t_{17}=PrLe_2\gamma_b,\ t_{18}=\frac{N_t}{N_m}.$

After the LL has been achieved as in Eqs. (5.2.1)-(5.2.7), we set our focus on Chebyshev pseudospectral method. The basic idea in spectral method is given a set of grid points x_j, $j=0,1,\cdots,N$, and corresponding function values $v(x_j)$, to use this data to approximate the derivatives of function $v(x)$. The approximate solution in the form of series solution is obtained using the Lagrange interpolating polynomials,

$$v(x)=\sum_{i=0}^{N_x}\bar{v}(x_i)L_i(x), \tag{5.2.8}$$

$$\text{where,}\quad L_i(x)=\prod_{i=0,i\neq k}^{N_x}\left(\frac{x-x_i}{x_k-x_i}\right), \tag{5.2.9}$$

is the Lagrange's polynomial. In pseudospectral method to interpolate $v(x)$, we shall make use of Chebyshev grid points,

$$x_i = cos\Big(\pi i/N\Big), \tag{5.2.10}$$

$x \in [-1,1],\ i = 0,1,2,\ldots N$, where N is number of collocation points.

We now have a linear decoupled differential system of equation with variable coefficients and can be solved by SLLM taking the following steps.

(i) We transform $\eta \in [0,\eta_\infty]$ from physical domain to computational domain, $[-1,1]$ using the relation $\eta = \dfrac{\Big(x+1\Big)}{2}\eta_\infty$, where $\eta_\infty \in \mathbb{Z}^+$.

(ii) Using Gauss-Lobatto collocation points, we approximate the unknown functions f_{r+1}, g_{r+1}, θ_{r+1}, ϕ_{r+1}, and χ_{r+1} by Chebyshev interpolating polynomials and the derivatives of the approximating functions.

(iii) The Chebyshev differentiation matrix D, as stated by Trefethen (2000) is applied to approximate the derivatives of the unknown functions at the collocation points as the matrix vector product.

$$\begin{cases} \frac{d^n f_{r+1}}{dx}|_{x=x_i} = \sum_{j=0}^{n} D_{ij}^{n} f_{r+1}(x_j) = \mathbf{D}^n \mathbf{F}_{r+1}, \\ \frac{d^n h_{r+1}}{dx}|_{x=x_i} = \sum_{j=0}^{n} D_{ij}^{n} h_{r+1}(x_j) = \mathbf{D}^n \mathbf{H}_{r+1}, \\ \frac{d^n g_{r+1}}{dx}|_{x=x_i} = \sum_{j=0}^{n} D_{ij}^{n} g_{r+1}(x_j) = \mathbf{D}^n \mathbf{G}_{r+1}, \\ \frac{d^n \theta_{r+1}}{dx}|_{x=x_i} = \sum_{j=0}^{n} D_{ij}^{n} \theta_{r+1}(x_j) = \mathbf{D}^n \Theta_{r+1}, \\ \frac{d^n \phi_{r+1}}{dx}|_{x=x_i} = \sum_{j=0}^{n} D_{ij}^{n} \phi_{r+1}(x_j) = \mathbf{D}^n \varPhi_{r+1}, \\ \frac{d^n \chi_{r+1}}{dx}|_{x=x_i} = \sum_{j=0}^{n} D_{ij}^{n} \chi_{r+1}(x_j) = \mathbf{D}^n \varXi_{r+1}, \end{cases} \tag{5.2.11}$$

where $\mathbf{D} = \dfrac{2D}{\eta_\infty}$, n is order of derivative.

(iv) Chose suitable initial guesses which satisfy the given boundary conditions.

Applying Eq. (5.2.11) to Eqs. (5.2.1)-(5.2.7), we obtain,

$$\begin{aligned} &M_1 G_{r+1} = B_1,\ G_{r+1}(x_0) = 0,\ G_{r+1}(x_N) = 0,\ M_2 \varPhi_{r+1} = B_2,\ \varPhi_{r+1}(x_0) = 0, \\ &\varPhi'_{r+1}(x_N) = -\frac{\mathrm{Nt}}{\mathrm{Nb}}\Theta'_r(x_N),\ M_3 \Xi_{r+1} = B_3,\ \Xi_{r+1}(x_0) = 0,\ \Xi_{r+1}(x_N) = 1, \\ &M_4 H_{r+1} = B_4,\ H_{r+1}(x_0) = 0,\ H_{r+1}(x_N) = 1,\ F'_{r+1} = H_{r+1},\ F_{r+1}(x_0) = 0, \\ &M_5 \Theta_{r+1} = B_5,\ \Theta_{r+1}(x_0) = 0,\ \Theta'_{r+1}(x_N) = -Bi_1\Big(1 - \Theta_{r+1}(x_N)\Big), \end{aligned} \tag{5.2.12}$$

where,

$$
\begin{aligned}
M_1 =& diag\Big(1+W_e g_r'\Big)\mathbf{D}^2 + diag\Big(W_e g_r'' + f_r\Big)\mathbf{D} - diag\Big(t_2 + 2h_r + 2\alpha g_r\Big)\mathbf{I},\\
&B_1 = W_e g_r'' g_r' - \alpha g_r^2 - t_1 h_r,\\
M_2 =& \mathbf{D}^2 + diag\Big(t_1 3 f_r\Big)\mathbf{D} - diag\Big(t_{14}\Big(1+t_4\theta_r\Big)^n \exp\Big(\frac{-E}{1+t_4\theta_r}\Big)\Big)\times\mathbf{I},\\
&B_2 = -t_{12}\theta_r'',
\end{aligned}
\tag{5.2.13}
$$

$$
\begin{aligned}
M_3 =& \mathbf{D}^2 + diag\Big(t_{15} f_r - P_b \phi_{r+1}'\Big)\mathbf{D} - diag\Big(P_b \phi_{r+1}'' + t_{17}\Big(1+t_4\theta_r\Big)^n \exp\Big(\frac{-E}{1+t_4\theta_r}\Big)\Big),\\
&B_3 = \frac{P_b}{t_{16}}\phi_{r+1}'' - t_{18}\theta_r'',\\
M_4 =& diag\Big(1+Weh_r'\Big)\mathbf{D}^2 + diag\Big(Weh_r''\Big)\mathbf{D} - diag\Big(t_2 + 2t_3 h_r - f_r\Big)\times\mathbf{I},\\
&B_4 = -\lambda_m\theta_r + \lambda_m N_r \phi_{r+1} + \lambda_m R_b \chi_{r+1} + Weh_r' h_r'' - t_3 h_r^2 + t_1 g_{r+1},\\
M_5 =& diag\Big(1+R_d\Big(1+t_6\theta_r\Big)^3\Big)\mathbf{D}^2 + diag\Big(\Big(2t_5\Big(1+t_4\theta_r\Big)^2 + 2t_{10}\Big)\theta_r' + t_8\phi_{r+1}' +\\
&t_9\chi_{r+1}' + Prf_{r+1}\Big)\mathbf{D} + dig\Big(t_{11} + 3R_d t_4\Big(1+t_6\theta_r\Big)^2\theta_r'' + 2t_5\Big(1+t_4\theta_r\Big)\theta_r^2\Big)\times\mathbf{I},\\
&B_5 = 3R_d t_4\Big(1+t_4\theta_r\Big)^2\theta\theta_r'' + t_5\Big(1+t_4\theta_r\Big)\Big(2t_4\theta_r + \Big(1+t_4\theta_r\Big)\Big)\theta_r'^2 + t_{10}\theta_r'^2\\
&-t_6 h_{r+1}^2 - t_6 g_{r+1}^2 - t_7\phi_{r+1}''.
\end{aligned}
\tag{5.2.14}
$$

In the above definition $diag\Big(\dots\Big)$ and $\mathbf{I}$ represent an $\mathrm{N}+1$ by $\mathrm{N}+1$ diagonal and identity matrices, respectively. It is sufficient to use the initial approximate solutions $f_0 = 1 - e^{-\eta}$, $g_0 = \eta e^{-\eta}$, $\theta_0 = \dfrac{\beta_{i1}}{1+\beta_{i1}} e^{-\eta}$, $\phi_0 = -\Big(\dfrac{N_t}{N_b}\Big)\dfrac{\beta_{i1}}{1+\beta_{i1}} e^{-\eta}$, $\chi_0 = e^{-\eta}$.

5.2.3 Convergence and Stability Analysis of the SLLM Approach

To evaluate the robustness and convergence behavior of the SLLM, we compute the error in terms of the maximum (infinity) norm as follows:

$$
\begin{aligned}
Er = \mathrm{Max}\Big(&\|f_{r+1} - f_r\|_\infty,\ \|g_{r+1} - g_r\|_\infty,\ \|\theta_{r+1} - \theta_r\|_\infty,\\
&\|\phi_{r+1} - \phi_r\|_\infty,\ \|\chi_{r+1} - \chi_r\|_\infty\Big).
\end{aligned}
\tag{5.2.15}
$$

A tolerance threshold of $\epsilon = 10^{-9}$ is prescribed for the iterative process. Iterations proceed until the solution residuals for all dependent variables drop below this specified limit. To enhance convergence speed, the Successive Over-Relaxation (SOR) technique is employed.

Numerical experiments reveal that the method converges rapidly under the default parameter settings, particularly when the over-relaxation factor is chosen as $\bar{\omega} = 0.96$. Without employing SOR, the method converges in approximately 22 iterations; however, incorporating SOR reduces the required iterations to about 14.

The logarithmic error plots for both cases-with and without the SOR technique-are illustrated in Figure 5.2.1a and Figure 5.2.1b, respectively. These plots clearly show a consistent decline in the logarithmic error for all dependent variables after the initial few iterations, confirming the stability and convergence of the SLLM for solving the coupled nonlinear system given in Eqs. (5.1.13-5.1.17) along with the boundary conditions in Eq. (5.1.18).

The physical parameters used for the numerical simulation are drawn from the literature Mandal et al. (2023). Unless otherwise specified, the default values adopted are: $M = 1, W_e = 0.3, Rd = 0.4, Rb = 0.5, Nr = 0.1, pr = 5, \Omega = 0.2, Nb = 0.2, Nt = 0.1, Nm = 0.2, \alpha = 1, \lambda = 0.3, Du = 0.1, Sr = 0.2, \lambda_m = 0.2, Ec = 0.3, E = 1, \gamma_c = 0.2, \gamma_b = 0.3, le_1 = 0.3, le_2 = 0.3, \theta_w = 1.2, \chi_w = 1.2, \beta_e = 0.4, \beta_i = 0.4, \beta_{i1} = 0.3, pb = 0.2, Q_0 = 0.2, n = 2$.

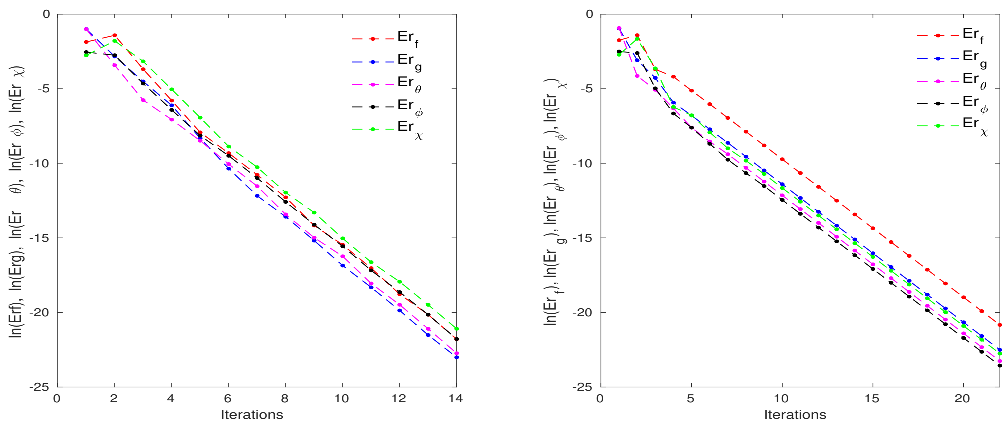

(a) (b)

Figure 5.2.1: Log-error profiles of Er versus iteration count for f, g, θ, ϕ, and χ: (a) utilizing SOR with relaxation factor $\bar{\omega} = 0.96$, (b) without employing the SOR technique.

Moreover, to validate our results, the outcomes of the present study are contrasted with Mandal et al. (2023) findings on the mass transfer rate of nanoparticles after reducing the problem to 2D and under certain restricted conditions. The comparison reveals very good agreement, as outlined in Table 5.3.1.

5.3 Results and Discussion

The transformed system of ODEs, Eqs. (5.1.13)-(5.1.17), along with the boundary conditions in Eq. (5.1.18), is numerically solved using the SLLM implemented in MATLAB. This section presents the influence of key dimensionless parameters on the velocity, temperature, nanoparticle concentration, and motile microorganism density profiles, providing physical insight into the observed trends.

Table 5.3.1: Comparison of $-\phi'(0)$ with the work in (Mandal et al. (2023)) for different values of M, Q_0, and Nm when $\Omega = \lambda = Sr = Du = \beta_i = \alpha = We = 0$

M	Q_0	Nm	Mandal $-\phi'(0)$	**Present value** $-\phi'(0)$
0.1	0.1	0.1	-0.05012968	-0.05012971
0.2			-0.04675591	-0.04675595
0.3			-0.04327275	-0.04327276
0.5			-0.03551047	-0.03551043
	0.15		-0.03863413	-0.03863418
	0.20		-0.03742939	-0.03742941
	0.25		-0.03587723	-0.03587729
		0.5	-0.04386713	-0.04386710
		0.9	-0.01994835	-0.01994829

5.3.1 Velocity Profile

Figures 5.3.1-5.3.3 examine how the parameters $\mathrm{W_e}$, M, α, λ, Ω, λ_m, β_e, and β_i affect the velocity field of the nanofluid. Figure 5.3.1a shows that both the Weissenberg number and magnetic parameter reduce the primary velocity. A higher $\mathrm{W_e}$ implies increased fluid elasticity, causing the nanofluid to resist deformation for a longer duration, thereby suppressing its inertial motion. Similarly, the Lorentz force induced by the magnetic field introduces resistive effects, lowering the velocity with increasing M. Figure 5.3.1b highlights the role of local inertia and porosity parameter, where their growth leads to enhanced resistance within the porous medium, further reducing fluid motion.

The combined influence of Ω and λ_m on the primary velocity is depicted in Figure 5.3.2a. Since both rotation and buoyancy-induced forces tend to oppose fluid motion, an increase in either parameter corresponds to a slower nanofluid flow. Moreover, Figure 5.3.2b reveals that the Hall and ion-slip effects contribute positively to the primary velocity, enhancing fluid transport in the tangential direction. The secondary velocity component g, as influenced by M and β_i, is shown in Figure 5.3.3. While M again demonstrates a decelerating effect, the ion-slip parameter β_i is observed to enhance the secondary velocity magnitude.

5.3.2 Temperature Profile

The influence of several dimensionless parameters-namely Nb, Nt, Ec, Rd, Q_0, Du, β_e, β_i, Pr, M, Rb, and Nm-on the temperature distribution is presented in Figures 5.3.4-5.3.6.

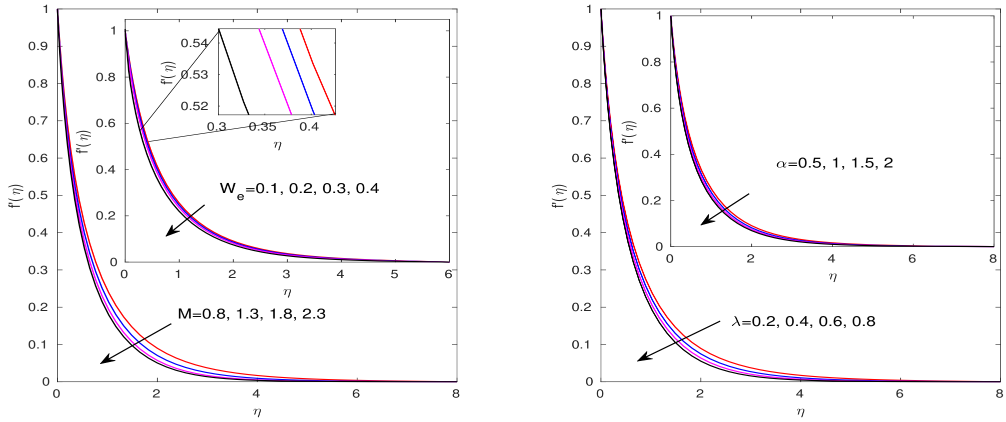

(a) (b)

Figure 5.3.1: Effect of (a): $\mathrm{W_e}$ and M, (b): α and λ on velocity profile

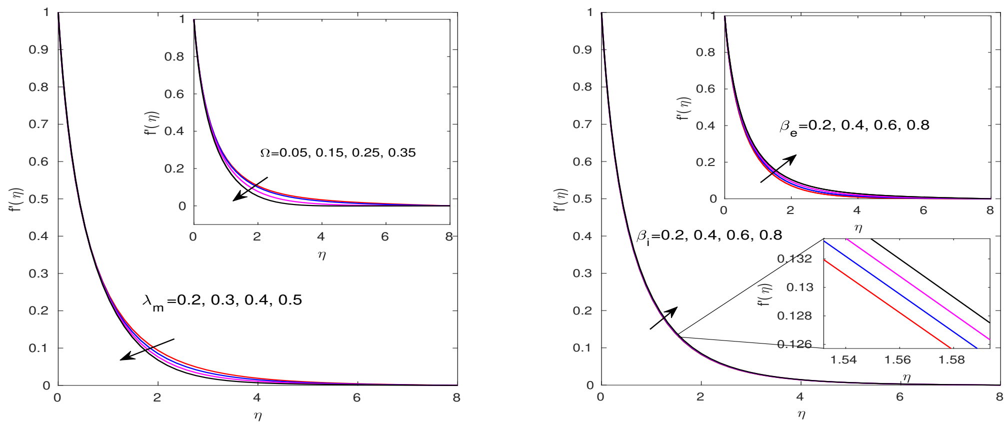

(a) (b)

Figure 5.3.2: Effect of (a): Ω and λ_m, (b): β_i and β_e on velocity profile

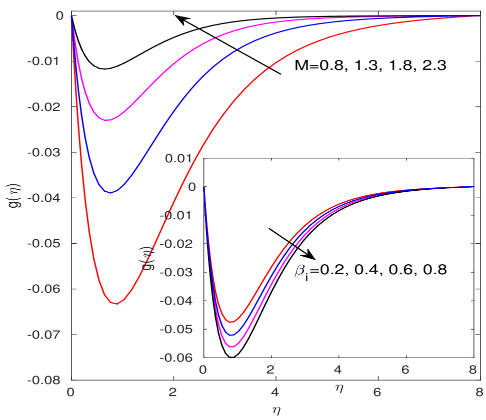

Figure 5.3.3: Effect of M and β_i on velocity g

Figure 5.3.4a reveals that an increase in Nb slightly enhances the temperature near the surface due to intensified nanoparticle random motion. The thermophoretic parameter, however, decreases temperature close to the wall while promoting heat transfer away from the surface. In Figure 5.3.4b, rising values of Ec, which represents viscous dissipation, significantly increase both the thermal boundary layer thickness and fluid temperature. Likewise, a higher Rd supplies additional radiative energy, resulting in a stronger temperature field. Quantitatively, increasing Ec from 0.1 to 0.7 and Rd from 0.2 to 0.8 raises the surface temperature by approximately 101.04% and 11.02%, respectively.

Figure 5.3.5a demonstrates that the heat generation parameter intensifies thermal energy within the boundary layer. Furthermore, Du, representing energy flux due to concentration gradients, suppresses the near-wall temperature while enhancing it toward the edge of the thermal boundary layer. The effects of Hall and ion-slip currents on the temperature field are illustrated in Figure 5.3.5b. These currents induce a transverse electromagnetic force, which introduces a secondary velocity gradient that enhances convective cooling. As a result, the temperature decreases with increasing β_e and β_i.

In Figure 5.3.6a, Pr and M exhibit opposing influences. A higher Pr reduces the thermal diffusivity, resulting in a thinner thermal layer and lower temperatures, while increasing M enhances thermal energy retention, raising the temperature profile. Figure 5.3.6b displays the impact of Rb and Nm. An elevated Rb suppresses fluid motion via buoyancy-induced resistance, which weakens convective heat transfer and thus raises the temperature. Conversely, increasing Nm also leads to a notable rise in temperature, likely due to intensified microbial activity near the thermal boundary, although the exact mechanism warrants further investigation.

5.3.3 Concentration Profile

Figures 5.3.7-5.3.9 depict the influence of key parameters on the distribution of nanoparticle concentration within the boundary layer. In Figure 5.3.7a, the contrasting effects of Nb and Nt are examined. An increase in Nt promotes particle migration from hotter to cooler regions, thereby enhancing nanoparticle concentration. In contrast, elevated Nb tends to reduce concentration near the surface due to enhanced random motion and dispersion.

Figure 5.3.7b highlights the impact of activation energy and the temperature ratio parameter. A higher E scales up the minimum energy required by reactants to commence the chemical reaction. That leads to the accumulation of nanoparticles, thus raises the nanoparticle concentration. Conversely, a larger temperature ratio initially reduces near-wall concentration due to steeper gradients, but it enhances species diffusion farther from the surface.

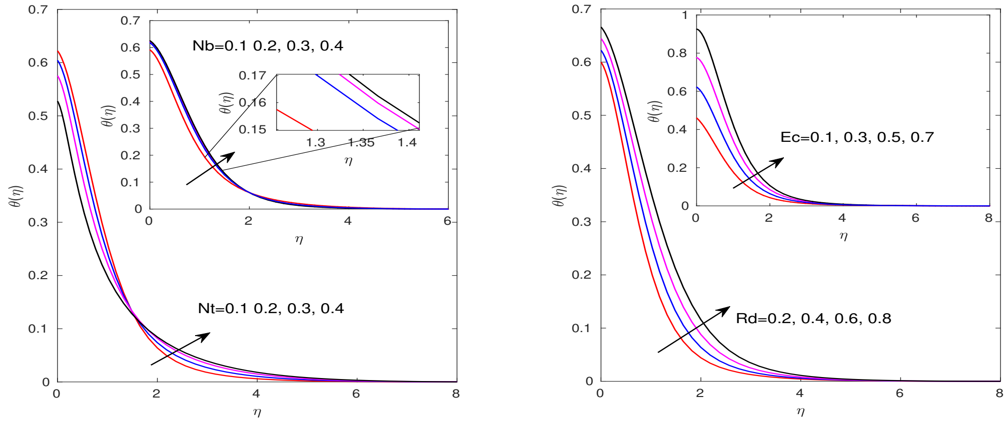

(a) (b)

Figure 5.3.4: Effect of (a): Nb and Nt, (b): Ec and Rd on temperature profile

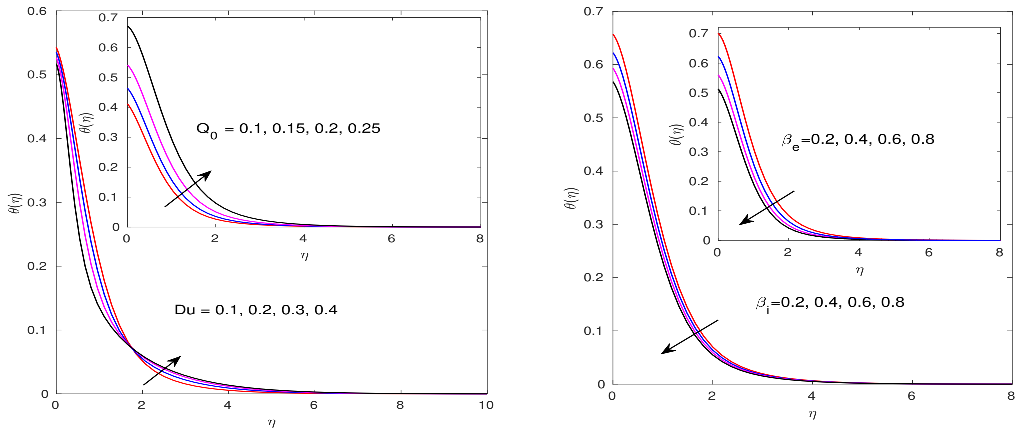

(a) (b)

Figure 5.3.5: Effect of (a): Q_0 and Du, (b): β_e and β_i on temperature profile

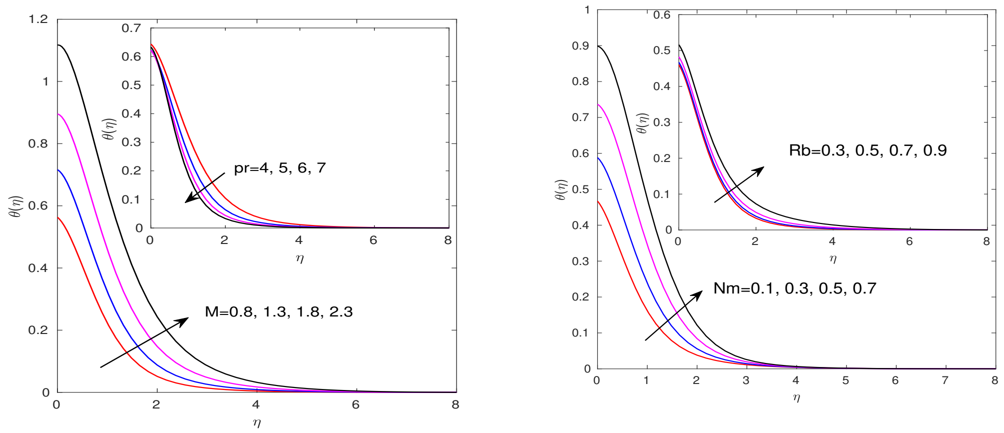

(a) (b)

Figure 5.3.6: Effect of (a): Pr and M, (b): Nm and Rb on temperature profile

Numerically, the peak concentration increases by approximately 19.35% as E varies from 0.5 to 2, and by 10.58% as θ_w rises from 1.1 to 2. The effects of M and W_e are demonstrated in Figure 5.3.8a. Both parameters contribute to an overall rise in nanoparticle concentration, with M exerting a more dominant influence over the selected range. Figure 5.3.8b shows how the concentration responds to variations in the Lewis number and Soret number. Since Le_1 is inversely proportional to mass diffusivity, increasing Le_1 reduces diffusion, thereby decreasing the nanoparticle concentration. On the other hand, the Soret effect, which captures thermodiffusion, becomes more pronounced with increasing Sr, promoting mass transfer from regions of high to low temperature. As Sr increases from 0.1 to 0.7, the peak concentration rises by approximately 38.12%.

Figure 5.3.9 examines the influence of Rb and Nm. A higher Rb suppresses fluid motion due to buoyancy-induced resistance, which in turn enhances nanoparticle accumulation, especially near the thermal boundary. Regarding Nm, its increase leads to an enhanced concentration further from the surface while reducing concentration near the wall, likely due to the reorientation of nanoparticle diffusion under intensified microbial agitation.

5.3.4 Microorganism Density Profile

Figures 5.3.10-5.3.12 illustrate the sensitivity of motile microorganism density to several controlling parameters, including γ_b, Nm, χ_w, E, pb, Rb, le_2, Pr, W_e, M, Ω, and Q_0.

Figure 5.3.10a examines the effects of Nm and γ_b. An increase in either parameter results in reduced microorganism density and a thinner microbial boundary layer. This trend is physically justified, as higher γ_b amplifies destructive microbial reactions that diminish motile density, while greater Nm enhances random microbial motion, disrupting their net directional movement. In Figure 5.3.10b, the impacts of the microorganism density ratio and activation energy are presented. Increasing χ_w reduces microbial density near the surface but enhances it in the outer boundary region. Conversely, a higher activation energy attenuates intracellular and extracellular destructive reactions, allowing more microorganisms to persist throughout the boundary layer.

Figure 5.3.11a investigates the roles of pb) and Rb. A higher pb, which characterizes the ratio of advective to diffusive transport, increases microorganism density near the wall but decreases it farther out. Increasing Rb signifies a stronger buoyancy force relative to viscous resistance, thereby slowing convection and promoting microbial accumulation near the boundary. The influence of the bioconvective Lewis number and Prandtl number is shown in Figure 5.3.11b. Both parameters are inversely related to bioconvective and thermal diffusivities, respectively. As they increase, diffusivity decreases, resulting in reduced microorganism concentration and a thinner microbial layer.

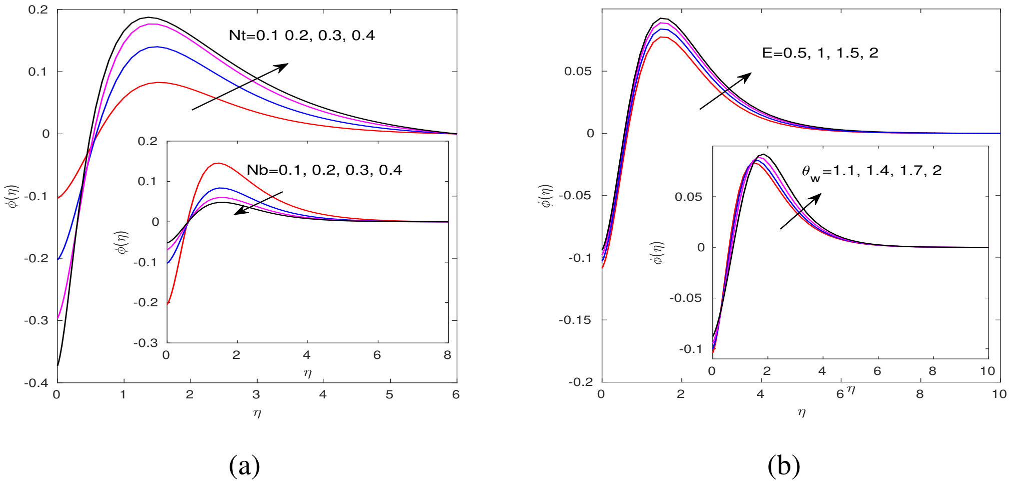

Figure 5.3.7: Effect of (a): Nb and Nt, (b): θ_{w} and E on concentration profile

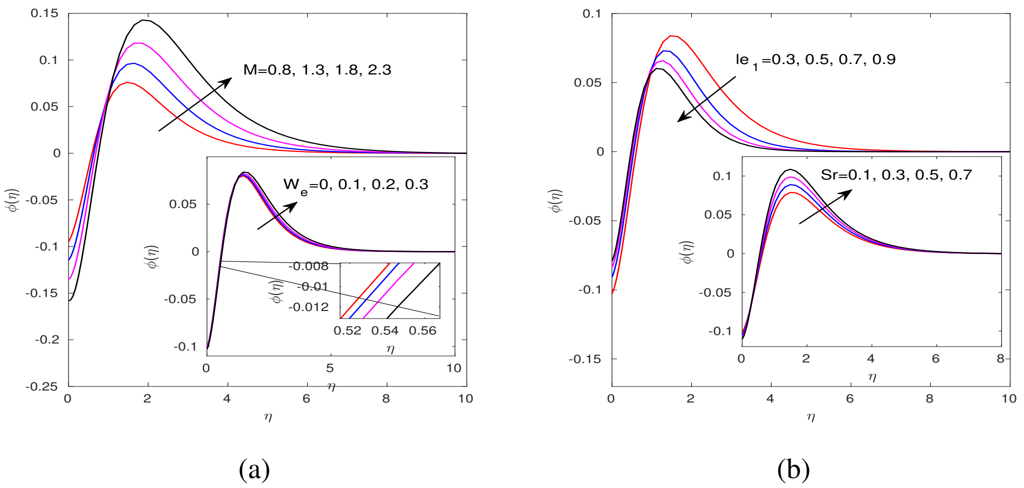

Figure 5.3.8: Effect of (a): $\mathrm{W_e}$ and M, (b): Sr and $\mathrm{le_1}$ on concentration profile

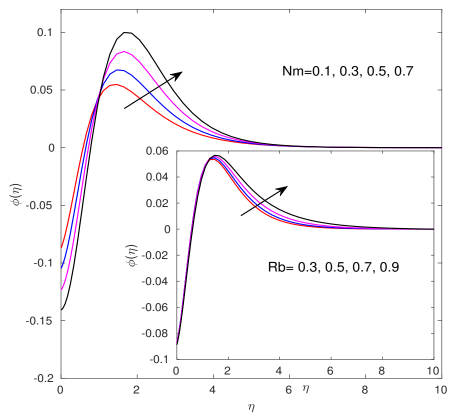

Figure 5.3.9: Effect of Nm and Rb on concentration profile

Figure 5.3.12a illustrates the effects of fluid rheology and magnetic field strength. Since Williamson fluid models shear-thinning behavior, a higher W_e reduces fluid resistance, facilitating bioconvective transport and enhancing microbial density. Additionally, a stronger magnetic field (through Lorentz force) suppresses fluid motion, further concentrating microorganisms near the surface.

Finally, Figure 5.3.12b presents the influence of rotational parameter and heat generation. Increased rotation slows the primary flow (see Figure 5.3.1a), allowing greater microbial accumulation in the boundary region. The heat source parameter enhances thermal energy, which stimulates microbial activity and elevates the motile microorganism concentration.

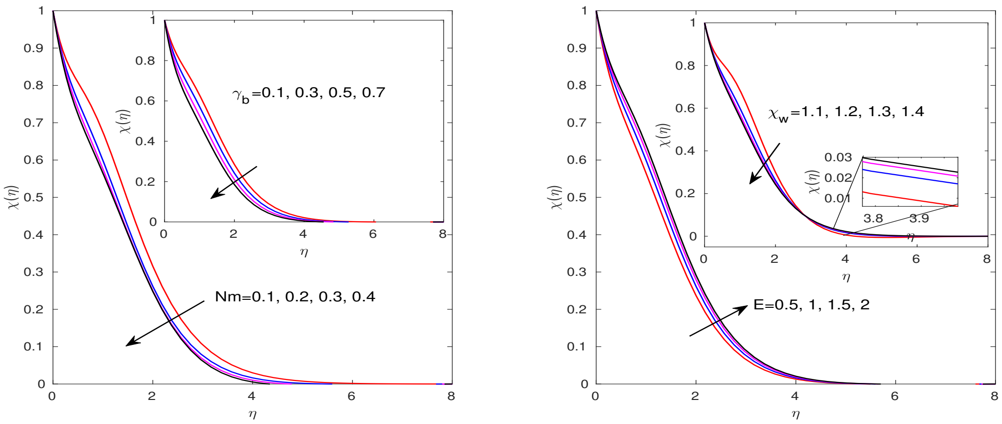

(a) (b)

Figure 5.3.10: Effect of (a): $\gamma_{\rm b}$ and Nm, (b): $\chi_{\rm w}$ and E on microbes density profile

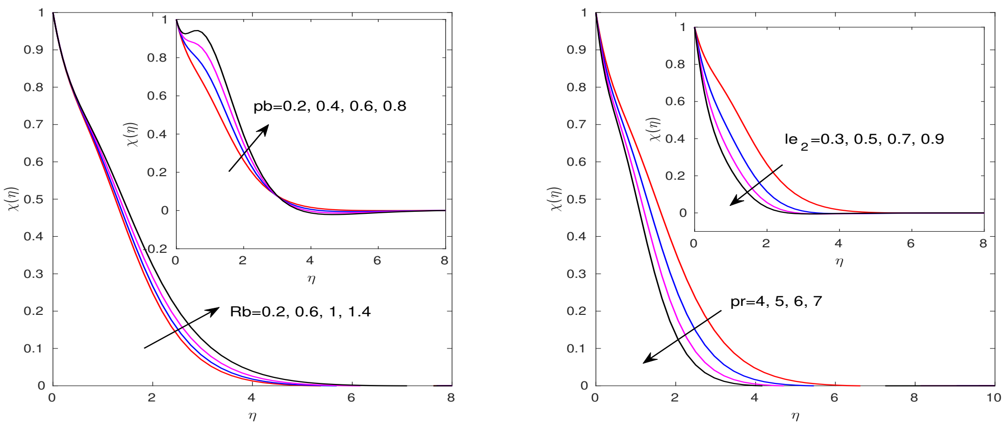

(a) (b)

Figure 5.3.11: Effect of (a): pb and Rb, (b): $\rm le_2$ and pr on microbes' density profile

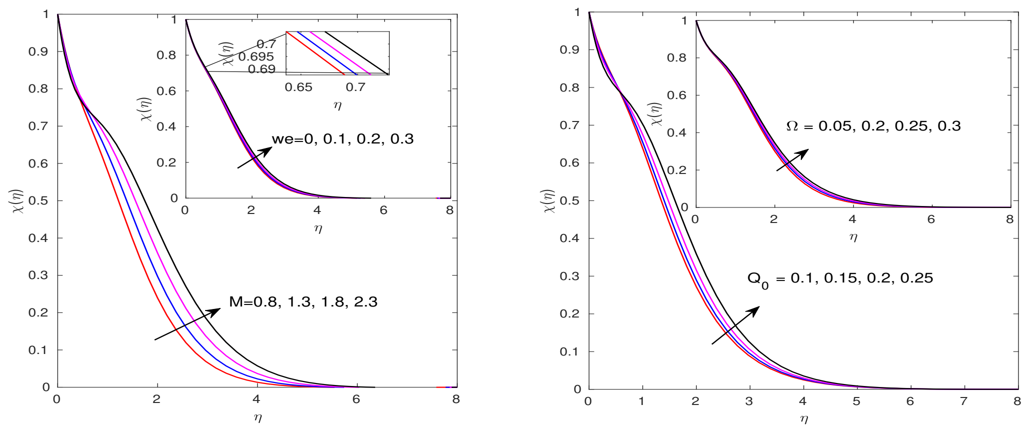

(a) (b)

Figure 5.3.12: Effect of (a): W_e and M , (b): Ω and Q_0 on microbes' density profile

5.3.5 Transfer Rate Analysis

Figures 5.3.13-5.3.14 illustrate the behavior of surface transfer rates for motile microorganisms, heat, and nanoparticle mass in response to variations in key governing parameters. In Figure 5.3.13a, the surface motile microorganism transfer rate is examined with respect to changes in the χ_w, E, and N_m. It is observed that for lower N_m values, an increase in χ_w enhances the microbial transfer rate. However, this trend reverses when N_m is relatively large. Additionally, increasing E results in a reduction in microbial transfer rate, while increasing N_m leads to its enhancement.

Figure 5.3.13b presents the surface heat transfer rate under the influence of Hall and ion-slip effects. Enhancing either parameter promotes greater heat transfer at the wall. Moreover, the thermophoretic parameter contributes positively to this effect-higher Nt values further amplify the heat transfer rate for each level of ion-slip considered. The nanoparticle mass transfer response is depicted in Figure 5.3.14, showing its dependence on E, le_1, and γ_c. The mass transfer rate diminishes with increasing le_1, due to reduced mass diffusivity. In contrast, greater E enhances the mass transfer rate. Furthermore, the role of γ_c is conditional: for $E \geq 1$, increasing γ_c boosts mass transfer, whereas for $E < 1$, it leads to a decline.

5.3.6 Tabular Interpretation of Surface Quantities

Tables 5.3.2-5.3.5 provide a quantitative overview of how selected physical parameters influence the surface characteristics-namely, the skin friction coefficients in both the x- and y-directions, as well as the heat, nanoparticle mass, and microorganism mass transfer rates. From Table 5.3.2, it is evident that increasing M, Ω, and α leads to a higher magnitude of the x-direction skin friction coefficient. In contrast, rising values of $\mathrm{W_e}$ and λ_m tend to suppress it.

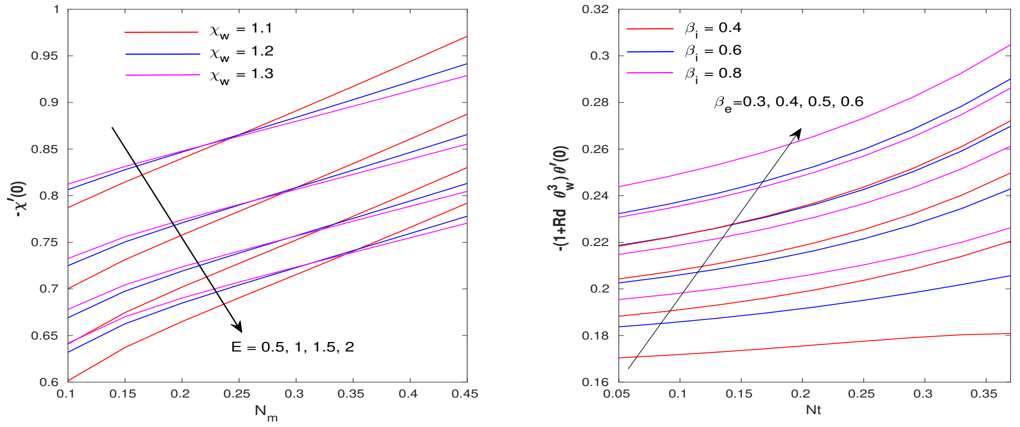

(a) (b)

Figure 5.3.13: Effect of (a):E, Nm, and χ_w on $-\chi'(0)$, (b): β_i, β_e and Nt on $-\left(1+R_d\theta_w^3\right)\theta'(0)$

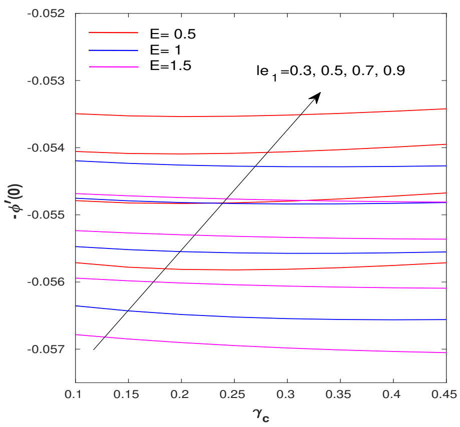

Figure 5.3.14: Effect of E, le_1 and γ_c on $-\phi'(0)$

For the y-direction friction coefficient, the results indicate a decreasing trend with respect to M, $\mathrm{W_e}$, α, and λ_m, whereas Ω contributes to its enhancement.

Table 5.3.3 presents the variation in the local Nusselt number as influenced by key thermal parameters. The Rd, Du, and θ_w are found to improve heat transfer. On the other hand, increasing the Ec, $\mathrm{W_e}$, and λ_m results in a reduction in the heat transfer rate.

As shown in Table 5.3.4, the Sherwood number is enhanced by increasing E, β_e, and β_i, indicating that these effects promote species transport at the surface. Conversely, a reduction in Sherwood number is observed with higher values of Ω, λ_m, and Nb, implying a weakening of mass diffusion in such cases.

Table 5.3.2: Variations of $Re^{1/2}Cf_x$ and $Re^{1/2}Cf_y$ for various values of M, Ω, $\mathrm{W_e}$, α, and λ_{m}

M	Ω	$\mathrm{W_e}$	α	λ_{m}	$Re^{1/2}Cf_x$	$Re^{1/2}Cf_y$
0.8	0.2	0.3	1	0.2	-2.097868	-0.298282
1.3					-2.195911	-0.207541
1.8					-2.279767	-0.134880
2.3					-2.342010	-0.073882
1	0.1				-2.131101	-0.065952
	0.16				-2.135762	-0.182559
	0.22				-2.144281	-0.295840
	0.28				-2.155776	-0.404531
	0.2	0			-2.395294	-0.277455
		0.1			-2.325351	-0272450
		0.2			-2.243453	-0.266626
		0.3			-2.138425	-0.259251
			0.5		-2.030687	-0.266076
			1		-2.138943	-0.259207
			1.5		-2.234626	-0.253126
			2		-2.315277	-0.247628
			1	0.5	-2.123431	-0.258326
				0.8	-2.107462	-0.257519
				1.1	-2.090320	-0.256908

Table 5.3.3: Variations of $Nu_x^{\star} = \mathrm{Re}^{-1/2}Nu_x$ for various values of $\mathrm{W_e}$, $\mathrm{R_d}$, Ec, Du, λ_m, and θ_w.

$\mathrm{W_e}$	$\mathrm{R_d}$	Ec	Du	λ_m	θ_w	$Nu_x^{\star}$
0.0	0.2	0.3	0.1	0.2	1.2	0.171542
0.1						0.169535
0.2						0.166540
0.3						0.161524
	0.4					0.191644
	0.6					0.217284
	0.8					0.238734
	0.4	0.1				0.273718
		0.3				0.191645
		0.5				0.113192
		0.3	0.2			0.191518
			0.3			0.191700
			0.4			0.192654
			0.1	0.3		0.190374
				0.4		0.189627
				0.5		0.188817
				0.2	1.1	0.175741
					1.3	0.228805
					1.4	0.251223

Table 5.3.4: Variations of $Re^{-1/2}Sh_x$ for various values of E, β_{e}, β_{i}, Ω, λ_{m}, and Nb

E	β_{e}	β_{i}	Ω	λ_{m}	Nb	$-\phi'(0)$
0.5	0.4	0.4	0.2	0.2	0.2	-0.058906
1						-0.060019
1.5						-0.060746
2						-0.061207
1	0.2					-0.048585
	0.4					-0.060019
	0.6					-0.069210
	0.4	0.2				-0.054692
		0.4				-0.060019
		0.6				-0.064541
		0.4	0.15			-0.061298
			0.25			-0.060019
			0.35			-0.056515
			0.2	0.6		-0.058228
				1		-0.055561
				1.3		-0.053396
				0.2	0.1	-0.129554
					0.3	-0.039370
					0.4	-0.029387

Table 5.3.5: Variations of $Re^{-1/2}Nn_x$ for various values of M, $\mathrm{W_e}$, pr, λ_{m}, γ_{b}, and Q_0

M	$\mathrm{W_e}$	pr	λ_{m}	γ_{b}	Q_0	$-\chi'(0)$
0.8	0.3	5	0.2	0.3	0.2	0.810487
1.3						0.874942
1.8						0.952120
1	0					0.850552
	0.1					0.845556
	0.2					0.840455
	0.3	3				0.610478
		4				0.720687
		5				0.835425
			0.4			0.834693
			0.6			0.834145
			0.8			0.833810
			0.2	0.3		0.835425
				0.5		0.953046
				0.7		1.057634
				0.3	0.1	0.741687
					0.15	0.779428
					0.2	0.835425
					0.25	0.926775

According to Table 5.3.5, the surface motile density transfer rate improves with rising values of M, Pr, γ_b, and Ω. However, this rate diminishes as W_e and λ_m increase, suggesting a suppression of microbial flux under strong non-Newtonian and buoyancy-induced flow influences.

5.4 Summary

This study explored the thermobioconvective transport characteristics of a 3D MHD Williamson nanofluid flow within a rotating frame, incorporating the effects of Hall and ion-slip currents, mixed convection, nonlinear thermal radiation, cross-diffusion, and chemical reactions in a porous medium. Additionally, thermophoretic and Brownian motion of nanoparticles and motile microorganisms were included. Key findings are summarized as follows:

1. The primary velocity of the nanofluid is suppressed by Ω, M , We, α, and λ_m. Notably, the Hall current exerts a more dominant influence on the velocity field than the ion-slip effect.

2. Temperature distribution and its boundary layer thickness are reduced by increasing β_e, β_i, and Pr, whereas enhancement Rd, Ec, M, and Nm elevate the temperature field. Furthermore, Nt and Du lower the temperature near the wall but increase it away from the surface.

3. The surface temperature increased by 11.02% due to a rise in Rd, and decreased by 26.88% and 13.54% when β_e and β_i were raised from 0.2 to 0.8, respectively.

4. Nanoparticle concentration peaks rose by 38.12%, 19.35%, and 10.58% with increases in Sr, E, and θ_w, respectively. Additionally, parameters such as Nt, Nm, Rb, M, and W_e enhanced concentration profiles in the far-field, while Nb and Le_1 reduced them.

5. Microbial density increased with higher values of E, Rb, Ω, M, W_e, and Q_0, whereas it decreased with greater values of γ_b, Nm, Le_2, and Pr.

6. Enhancing Rd, β_e, and β_i from 0.2 to 0.8 led to respective increases in the surface heat transfer rate by 47.80%, 63.00%, and 25.91%.

7. The surface nanoparticle mass transfer rate increased in magnitude with higher values of E, β_e, and β_i, while it decreased with increases in Ω, λ_m, and Nb.

CHAPTER SIX

Entropy Generation and Cattaneo–Christov Heat Flux Analysis of Binary and Ternary Hybrid Maxwell Nanofluid Flows with Slip and Convective Conditions

A substantial body of research on hybrid and trihybrid nanofluid flows has primarily focused on utilizing Newtonian base fluids, as can be noticed in the studies of Singh et al. (2023), Farooq et al. (2024), and Dey et al. (2024). Relatively few studies have incorporated non-Newtonian base fluid models. It is noteworthy that the heat transfer characteristics of binary and ternary hybrid nanofluids are significantly influenced by the thermophysical properties of the host fluid.

To address this gap, the present study investigates the flow and heat transfer characteristics of Maxwell binary and ternary hybrid nanofluids composed of copper oxide (CuO), ferric oxide ($\mathrm{Fe_3O_4}$), and molybdenum disulfide ($\mathrm{MoS_2}$) nanoparticles in a sodium alginate (SA) base fluid. These nanoparticles and the base fluid were chosen for their critical roles in various industrial and biomedical applications (Gu et al. (2013), Sulochana et al. (2020), Ramzan et al. (2023)).

This study examines the behavior of these hybrid nanofluids over a stretching rotating disk within a Darcy-Forchheimer porous medium. The flow considers multiple complex effects, including Cattaneo-Christov heat flux, nonlinear thermal radiation, velocity and thermal slip, heat source/sink, viscous dissipation, and Joule heating. Consequently, the novelty of this study is outlined as follows:

(i) The comparative study on ternary ($\mathrm{CuO + Fe_3O_4 + MoS_2/SA}$) and binary ($\mathrm{CuO + Fe_3O_4/SA}$) hybrid Maxwell nanofluids is presented.

(ii) The velocity and thermal slips, suction/injection, and convective boundary conditions in a Darcy-Forchheimer porous medium are investigated.

(iii) The effects of Cattaneo-Christov heat flux, nonlinear thermal radiation, heat source/sink, Joule heating, and viscous dissipation with entropy generation are studied.

(iv) The spectral quasilinearization method, known for its robustness and exponential convergence, is used for the numerical solutions.

6.1 Mathematical Model and Formulation

6.1.1 Flow Configuration and Assumptions

This study examines a steady, 3D, incompressible, viscous MHD flow of binary/ternary hybrid Maxwell nanofluids above a radially stretching and rotating disk embedded in a Darcy-Forchheimer porous medium. The trihybrid nanofluid consists of $\mathrm{CuO}+\mathrm{Fe_3O_4}+\mathrm{MoS_2/SA}$, while the bihybrid nanofluid includes $\mathrm{CuO}+\mathrm{Fe_3O_4/SA}$. Key effects considered include Cattaneo–Christov thermal relaxation, buoyancy-driven convection, nonlinear thermal radiation, Joule heating, viscous dissipation, and internal heat source or sink. A cylindrical coordinate system (r,ϕ,z) is employed, where the disk lies in the horizontal r–ϕ plane and rotates uniformly about the z-axis with angular velocity Ω. The fluid occupies the semi-infinite space $z \geq 0$. The flow is assumed to be axisymmetric following Kármán's classical formulation.

A constant transverse magnetic field of strength B_0 is applied to regulate the flow field. The model neglects chemical reactions and assumes local thermal equilibrium between nanoparticles and base fluid, with a well-stabilized nanofluid mixture. Both slip and convective boundary conditions are imposed. The disk surface is maintained at temperature T_w, while the ambient fluid temperature far from the surface is T_∞, with $T_w > T_\infty$. The physical model is illustrated in Figure 6.1.1.

6.1.2 Model description

The Cauchy stress tensor $\mathbf{T}$ and its associated constitutive equation for upper-convected Maxwell model as presented in (Kumari and Nath (2014), Bao et al. (2024)) is

$$\mathbf{T} = -p\mathbf{I}+\mathbf{S}, \tag{6.1.1}$$

$$\Big(1+\lambda_1^\star \frac{\delta}{\delta t}\Big)\mathbf{S} = 2\mu\mathbf{D}_1, \tag{6.1.2}$$

where p, $\mathbf{I}$, $\mathbf{S}$, $\lambda_1^\star$, μ, $\mathbf{D}_1 = \frac{1}{2}\Big((\mathrm{grad}\mathbf{V})+(\mathrm{grad}\mathbf{V})^T\Big)$ denote pressure, identity tensor, the extra stress tensor, the relaxation time, the zero-shear rate viscosity, the rate of deformation. The upper-convected derivative, $\frac{\delta}{\delta t}$ is given by:

$$\frac{\delta\mathbf{S}}{\delta t} = \frac{d\mathbf{S}}{dt} - \Big((grad\mathbf{V})\mathbf{S}+\mathbf{S}(grad\mathbf{V})^T\Big) \tag{6.1.3}$$

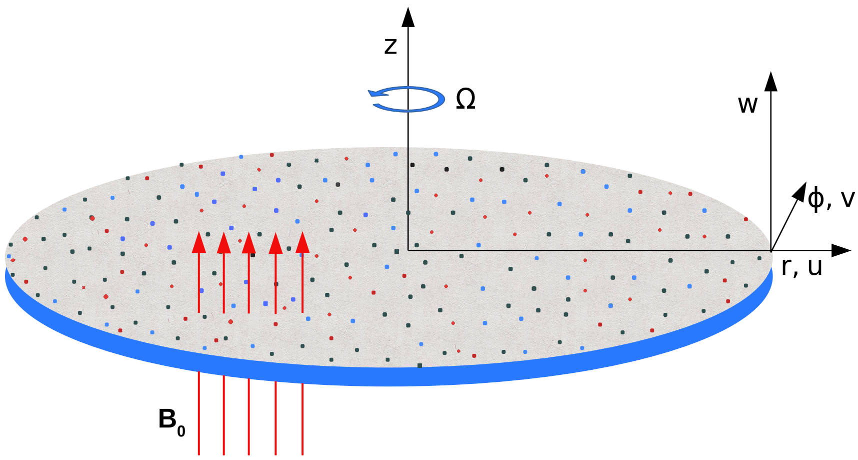

Figure 6.1.1: Geometry of the flow

The model's bihybrid and trihybrid nanofluid synthesis steps are shown in the schematic below.

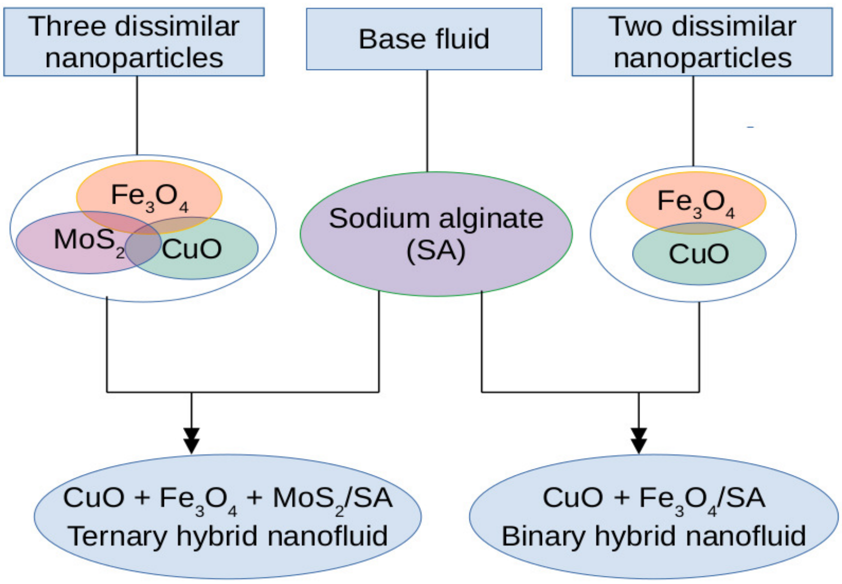

Figure 6.1.2: Steps in producing binary and ternary nanofluids

6.1.3 Governing equations

Based on the above assumptions and introducing the boundary layer approximations, the set of PDEs governing the conservation of mass, momentum, and energy are expressed in cylindrical coordinate as (Singh et al. (2023), Khan et al. (2021)):

$$\frac{\partial u}{\partial r} + \frac{u}{r} + \frac{\partial w}{\partial z} = 0, \tag{6.1.4}$$

$$\rho_{thnf}\left[u\frac{\partial u}{\partial r}-\frac{v^2}{r}+w\frac{\partial u}{\partial z}+\lambda_1^\star\Big(u^2\frac{\partial^2 u}{\partial r^2}+w^2\frac{\partial^2 u}{\partial z^2}+2uw\frac{\partial^2 u}{\partial r\partial z}-2\frac{uv}{r}\frac{\partial v}{\partial r}-2\frac{vw}{r}\frac{\partial v}{\partial z}+\right.$$

$$\left.\frac{uv^2}{r^2}+\frac{v^2}{r}\frac{\partial u}{\partial r}\Big)\right]=-pr+\mu_{thnf}\left[\frac{\partial^2 u}{\partial r^2}+\frac{1}{r}\frac{\partial u}{\partial r}-\frac{u}{r^2}+\frac{\partial^2 u}{\partial z^2}\right]-\sigma_{thnf}B_0^2\left[u+\lambda_1^\star w\frac{\partial u}{\partial z}\right]+$$

$$(\rho\beta_T^*)_{thnf}\,g\,(T-T_\infty)-\mu_{thnf}\frac{\xi}{k^\star}u-\rho_{thnf}\frac{c_F\xi}{\sqrt{k^\star}}u^2, \tag{6.1.5}$$

$$\rho_{thnf}\left[u\frac{\partial v}{\partial r}+\frac{uv}{r}+w\frac{\partial v}{\partial z}+\lambda_1^\star\Big(u^2\frac{\partial^2 v}{\partial r^2}+w^2\frac{\partial^2 v}{\partial z^2}+2uw\frac{\partial^2 v}{\partial r\partial z}+2\frac{uv}{r}\frac{\partial u}{\partial r}+2\frac{vw}{r}\frac{\partial u}{\partial z}-\right.$$

$$\left.2\frac{u^2v}{r^2}-\frac{v^3}{r^2}+\frac{v^2}{r}\frac{\partial v}{\partial r}\Big)\right]=\mu_{thnf}\left[\frac{\partial^2 v}{\partial r^2}+\frac{1}{r}\frac{\partial v}{\partial r}-\frac{v}{r^2}+\frac{\partial^2 v}{\partial z^2}\right]-\sigma_{thnf}B_0^2\left(v+\lambda_1^\star w\frac{\partial v}{\partial z}\right) \tag{6.1.6}$$

$$-\mu_{thnf}\frac{\xi}{k^\star}v-\rho_{thnf}\frac{c_F\xi}{\sqrt{k^\star}}v^2,$$

$$\begin{aligned}&\rho_{thnf}\left[u\frac{\partial w}{\partial r}+w\frac{\partial w}{\partial z}+\lambda_1^\star\left(u^2\frac{\partial^2 w}{\partial r^2}+w^2\frac{\partial^2 w}{\partial z^2}+2uw\frac{\partial^2 w}{\partial r\partial z}+\frac{v^2}{r}\frac{\partial w}{\partial r}\right)\right]=\\&-p_z+\mu_{thnf}\left(\frac{\partial^2 w}{\partial r^2}+\frac{1}{r}\frac{\partial w}{\partial r}+\frac{\partial^2 w}{\partial z^2}\right),\end{aligned} \tag{6.1.7}$$

$$(\rho c_p)_{thnf}\left[u\frac{\partial T}{\partial r}+w\frac{\partial T}{\partial z}+\lambda_2^\star\Bigg(\left(u\frac{\partial u}{\partial r}+w\frac{\partial u}{\partial z}\right)\frac{\partial T}{\partial r}+\left(u\frac{\partial w}{\partial r}+w\frac{\partial w}{\partial z}\right)\frac{\partial T}{\partial z}+u^2\frac{\partial^2 T}{\partial r^2}+\right.$$

$$\left.w^2\frac{\partial^2 T}{\partial z^2}+2uw\frac{\partial^2 T}{\partial r\partial z}\Bigg)\right]=k_{thnf}\left[\frac{\partial^2 T}{\partial r^2}+\frac{1}{r}\frac{\partial T}{\partial r}+\frac{\partial^2 T}{\partial z^2}\right]-\frac{\partial q_{rad}}{\partial z}+\sigma_{thnf}B_0^2\left(u^2+v^2\right)+ \tag{6.1.8}$$

$$\mu_{thnf}\left(\left(\frac{\partial u}{\partial z}\right)^2+\left(\frac{\partial v}{\partial z}\right)^2\right)+Q_a\,(T-T_\infty)\,.$$

The boundary conditions to which the equations are subjected to are:

$$\begin{aligned}&u=rC+L_1\frac{\partial u}{\partial z},\ v=r\Omega+L_1\frac{\partial v}{\partial z},\ w=w_0,\ -k_{thnf}\frac{\partial T}{\partial z}=h_t(T_w-T)+L_2\frac{\partial T}{\partial z},\ at\ z=0,\\&u\longrightarrow 0,\ v\longrightarrow 0,\ T\longrightarrow T_\infty,\ as\quad z\longrightarrow\infty,\end{aligned} \tag{6.1.9}$$

in which (u,v,w) are velocity components in the (r,ϕ,z) directions, Ω is a constant rotation of the disk, $\beta^\star=r\beta_T$, β_T is the fluid's thermal expansion coefficient, $\lambda_1^\star$ is the Maxwell relaxation factor, $\lambda_2^\star$ denotes the thermal relaxation coefficient, and $q_{rad}=-\frac{4\sigma^\star}{3k_e}T_z^4$ is nonlinear thermal radiation as described in Eq. (4.1.58). The remaining notations are described in the acronyms and abbreviation section.

6.1.4 Nondimensionalization and reduction to ODEs

The system of PDEs presented above can be nondimensionalized and transformed into ODEs by introducing the following similarity variables, as outlined by Acharya et al. (2020).

$$
\begin{aligned}
&\eta = z\sqrt{\frac{2\Omega}{\nu_f}},\ u = r\Omega f'(\eta),\ v = r\Omega g(\eta),\ w = -\sqrt{2\Omega\nu_f}\, f(\eta),\\
&T = T_\infty + \theta(\eta)\Big(T_w - T_\infty\Big),\ p = p_\infty + 2\Omega\mu_f p^\star(\eta),
\end{aligned}
\tag{6.1.10}
$$

where η is the similarity variable. Employing Eqs. (4.1.58), (6.1.2), and (6.1.10) into Eqs. (6.1.4)-(6.1.9), the governing equations and their corresponding boundary conditions are reduced to the following non-dimensional form.

$$
\begin{aligned}
2\zeta_2\lambda_1 f^2 f''' - 2\zeta_1 f''' - 2\zeta_2 f f'' - 2\zeta_2\lambda_1 f f' f'' - \zeta_3\lambda_1 M f f'' + \zeta_2 f'^2 + \zeta_3 M f' + \zeta_1\lambda f'&\\
+\zeta_2\alpha f'^2 + 2\zeta_2\lambda_1 g g' f - \zeta_2 g^2 - \zeta_4\lambda_m\theta = 0,&
\end{aligned}
\tag{6.1.11}
$$

$$
\begin{aligned}
-2\zeta_1 g'' + 2\zeta_2\lambda_1 f^2 g'' - 2\zeta_2 f g' - 2\zeta_2\lambda_1 f f' g' - \zeta_3 M\lambda_1 f g' + (\zeta_1\lambda + \zeta_3 M)g + \zeta_2\alpha g^2&\\
-2\zeta_2\lambda_1 f f'' g + 2\zeta_2 f' g = 0,&
\end{aligned}
\tag{6.1.12}
$$

$$
\zeta_1 f'' + \zeta_2 f f' - \zeta_2\lambda_1 f^2 f'' = 0,
\tag{6.1.13}
$$

$$
\begin{aligned}
&\zeta_6\theta'' + R_d\Big(1 + (\theta_w - 1)\theta\Big)^3\theta'' + 3R_d(\theta_w - 1)\Big(1 + (\theta_w - 1)\theta\Big)^2\theta'^2 + \zeta_5 Pr f\theta' +\\
&\frac{1}{2}\zeta_3 M Ec Pr\left(f'^2 + g^2\right) + \zeta_1 Ec Pr\left(f''^2 + g'^2\right) - \zeta_5\lambda_2 Pr\left(f f'\theta' + f^2\theta''\right) + Q_0 Pr\theta = 0.
\end{aligned}
\tag{6.1.14}
$$

The transformed boundary conditions are:

$$
\begin{aligned}
&f(\eta) = \beta_w,\ f'(\eta) = \beta_0 + \beta_2 f''(\eta),\ g(\eta) = 1 + \beta_2 g'(\eta),\ (\zeta_6 - \beta_3)\theta'(\eta) = -\beta_{i1}(1 - \theta(\eta)),\ \text{at } \eta = 0,\\
&f'(\eta) = 0,\ g(\eta) = 0,\ \theta(\eta) = 0,\ \text{as } \eta \longrightarrow \infty.
\end{aligned}
\tag{6.1.15}
$$

The dimensionless parameters utilized in this study are defined as follows: the magnetic parameter is given by $\mathrm{M} = \dfrac{\sigma_0 \mathrm{B}_0^2}{\Omega\rho_\mathrm{f}}$, while the porosity coefficient is expressed as $\lambda = \dfrac{\nu_f\xi}{\Omega k^\star}$. The local inertial parameter takes the form $\alpha = \dfrac{r c_F \xi}{\sqrt{k^\star}}$. The Grashof number, $Gr = \dfrac{\beta_T g(T_w - T_\infty)r^4}{\nu_f{}^2}$, represents the ratio of buoyancy to viscous forces, and the Reynolds number is $Re = \dfrac{Ur}{\nu_f}$. Their combination yields the mixed convection parameter, $\lambda_m = \dfrac{Gr}{Re^2}$.

The suction/injection effect is characterized by $\beta_w = -\dfrac{w_0}{\sqrt{2\Omega\nu_f}}$, while surface stretching is quantified by $\beta_0 = \dfrac{C}{\Omega}$. Velocity and thermal slip parameters are denoted by $\beta_2 = L_1\sqrt{\dfrac{2\Omega}{\nu_f}}$ and $\beta_3 = L_2\sqrt{\dfrac{2\Omega}{\nu_f}}$, respectively. The Biot number, which describes convective heat exchange at the surface, is defined as $\beta_{i1} = \dfrac{h_t}{k_f}\sqrt{\dfrac{\nu_f}{2\Omega}}$.

The thermal radiation parameter is expressed as $R_d = \dfrac{16\sigma^\star T_\infty^3}{3kk_e}$, and the Eckert number, indicating viscous dissipation, is $E_c = \dfrac{U_w^2}{c_p(T_w - T_\infty)}$. Heat generation or absorption is modeled using the parameter $Q_0 = \dfrac{Q_a}{2\Omega\rho c_p}$.

Thermal diffusivity is captured by the Prandtl number, $Pr = \dfrac{(\rho c_p)_f \nu_f}{k}$, while $\lambda_1 = 2\Omega\lambda_1{}^\star$ and $\lambda_2 = 2\Omega\lambda_2{}^\star$ denote the Deborah and thermal relaxation numbers, respectively. The temperature ratio is defined as $\theta_w = \dfrac{T_w}{T_\infty}$.

For trihybrid nanofluids, the following ratios are used:

$$\zeta_1 = \frac{\mu_{thnf}}{\mu_f}, \quad \zeta_2 = \frac{\rho_{thnf}}{\rho_f}, \quad \zeta_3 = \frac{\sigma_{thnf}}{\sigma_f}, \quad \zeta_4 = \frac{(\rho\beta)_{thnf}}{(\rho\beta)_f}, \quad \zeta_5 = \frac{(\rho c_p)_{thnf}}{(\rho c_p)_f}, \quad \zeta_6 = \frac{k_{thnf}}{k_f}.$$

For bihybrid and single nanoparticle nanofluids, the subscript '$thnf$' is substituted with '$bhnf$' and 'nf', respectively.

6.1.5 Entropy Generation Analysis

This section outlines the entropy production in the MHD flow of Maxwell's binary/ternary hybrid nanofluids within a porous medium, accounting for nonlinear thermal radiation, viscous dissipation, and Joule heating effects, following the methodology of Hosseinzadeh et al. (2022) and Khan (2021). The entropy generation per unit volume is given by:

$$\begin{aligned} S_G =& \frac{k_{thnf}}{T_\infty^2}\left[\left(\frac{\partial T}{\partial r}\right)^2 + \left(1 + \frac{16\sigma^\star T^3}{3k_{thnf}k_e}\right)\left(\frac{\partial T}{\partial z}\right)^2\right] + \frac{\mu_{thnf}}{T_\infty}\left[2\left(\left(\frac{\partial u}{\partial r}\right)^2 + \left(\frac{u}{r}\right)^2 + \left(\frac{\partial w}{\partial z}\right)^2\right) + \left(\frac{\partial v}{\partial r} - \frac{v}{r}\right)^2\right. \\ & \left. + \left(\frac{\partial u}{\partial z} + \frac{\partial w}{\partial r}\right)^2 + \left(\frac{\partial v}{\partial z}\right)^2\right] + \frac{\mu_{thnf}\xi}{T_\infty k^\star}\left(u^2 + v^2\right) + \frac{\rho_{thnf} c_F \xi}{T_\infty\sqrt{k^\star}}\left(u^3 + v^3\right) + \frac{\sigma_{thnf} B_0^2}{T_\infty}\left(u^2 + v^2\right), \end{aligned} \tag{6.1.16}$$

In the expression above: The first term represents thermal irreversibility due to conduction and radiation. The second term accounts for irreversibility from viscous friction. The third and fourth terms represent porous drag effects. The final term corresponds to electromagnetic dissipation via Joule heating.

By incorporating the similarity transformations from Eq. (6.1.10), the dimensionless entropy generation rate becomes:

$$\begin{aligned} N_G =& \zeta_6\bar{\alpha}\left[1 + \frac{R_d}{\zeta_6}(1 + (\theta_w - 1)\theta)^3\right]\theta'^2 + \zeta_1 Br\left[\frac{6}{Re}f'^2 + \bar{\gamma}^2(f'')^2 + \bar{\gamma}^2(g')^2\right] \\ & + \frac{1}{2}\zeta_1 Br\lambda\bar{\gamma}^2(f'^2 + g^2) + \frac{1}{2}\zeta_2\alpha Br\bar{\gamma}^3(f'^3 + g^3) + \frac{1}{2}\zeta_3 MBr\bar{\gamma}^2(f'^2 + g^2), \end{aligned} \tag{6.1.17}$$

where: $N_G = \dfrac{S_G}{\dfrac{2\Omega k_f \rho_f (T_w - T_\infty)}{\mu_f T_\infty}}$ is the dimensionless entropy generation rate. $\bar{\alpha} = \dfrac{T_w - T_\infty}{T_\infty}$ is the dimensionless temperature difference. $\bar{\gamma} = \dfrac{r}{R}$ is the normalized radial coordinate. $Br = \dfrac{\Omega^2 \mu_f R^2}{k_f(T_w - T_\infty)}$ is the rotational Brinkman number. $Re = \dfrac{R^2\Omega}{\nu_f}$ is the Reynolds number. To evaluate the dominance of thermal irreversibility relative to total entropy generation, the Bejan number is introduced as:

$$Be = \frac{\zeta_6 \bar{\alpha}\left[1 + \dfrac{R_d}{\zeta_6}\left(1+(\theta_w - 1)\theta\right)^3\right]\theta'^2}{N_G}. \tag{6.1.18}$$

6.1.6 Quantities of Engineering interest

To quantify engineering-relevant quantities, the shear stresses and heat transfer at the disk surface are determined as:

$$C_{fr} = \frac{\tau_{wr}}{\frac{1}{2}\rho_{thnf} u_w^2},\ \tau_{wr} = \mu_{thnf}\left(\frac{\partial u}{\partial z}\right)_{z=0},\ C_{f\phi} = \frac{\tau_{w\phi}}{\frac{1}{2}\rho_{thnf} v_w^2},\ \tau_{w\phi} = \mu_{thnf}\left(\frac{\partial v}{\partial z}\right)_{z=0},$$

$$Nu_w = \frac{-r}{(T_w - T_\infty)}\left(1 + \frac{16\sigma^\star}{3k_{thnf}k_e}T^3\right)\left(\frac{\partial T}{\partial z}\right)_{z=0}. \tag{6.1.19}$$

By employing similarity transformations, these quantities are expressed in nondimensional form as:

$$Re^{\frac{1}{2}} C_{fr} = 2\sqrt{2}\frac{\zeta_1}{\zeta_2} f''(0), \quad Re^{\frac{1}{2}} C_{f\phi} = 2\sqrt{2}\frac{\zeta_1}{\zeta_2} g'(0),$$

$$Re^{\frac{-1}{2}} Nu_w = -\sqrt{2}\left[\zeta_6 + R_d\left(1 + (\theta_w - 1)\theta(0)\right)^3\right]\theta'(0). \tag{6.1.20}$$

6.2 Numerical Approach

The system of coupled nonlinear ODEs given in Eqs. (6.1.11)-(6.1.14), subject to the boundary conditions in Eq. (6.1.15), is solved numerically using SQLM. This technique combines the high accuracy of spectral methods with the iterative linearization framework of the QLM, making it particularly effective for smooth boundary value problems due to its fast convergence and reduced computational cost compared to finite difference and finite element methods.

Initially introduced by Bellman and Kalaba (1965), QLM extends the Newton-Raphson method to nonlinear boundary value problems by iteratively approximating the nonlinear terms through multivariable Taylor expansions. At the r^{th} iteration, the approximate solutions for the unknowns are denoted as f_r, g_r, and θ_r, and at the $(r+1)^{\text{th}}$ level as f_{r+1}, g_{r+1}, and θ_{r+1}. Similar to the SLLM, SQLM assumes that the change in the solution between successive iterations is small. Applying QLM to Eqs. (6.1.11)-(6.1.14) results in a sequence of linearized equations.

$$a_{3,r} f'''_{r+1} + a_{2,r} f''_{r+1} + a_{1,r} f'_{r+1} + a_{0,r} f_{r+1} + b_{1,r} g'_{r+1} + b_{0,r} g_{r+1} + c_{0,r}\theta_{r+1} = R_{11}, \tag{6.2.1}$$

$$e_{2,r} f''_{r+1} + e_{1,r} f'_{r+1} + e_{0,r} f_{r+1} + h_{2,r} g''_{r+1} + h_{1,r} g'_{r+1} + h_{0,r} g_{r+1} = R_{21}, \tag{6.2.2}$$

$$l_{2,r}f''_{r+1}+l_{1,r}f'_{r+1}+l_{0,r}f_{r+1}+n_{1,r}g'_{r+1}+n_{0,r}g_{r+1}+m_{2,r}\theta''_{r+1}+m_{1,r}\theta'_{r+1}+m_{0,r}\theta_{r+1}=R_{31}, \tag{6.2.3}$$

where the variable coefficients and the right hand sides are known from the previous iteration and given respectively as follows.

$$\begin{aligned}
&a_{3,r}=2\lambda_1\zeta_2 f^2{}_r-2\zeta_1, \quad a_{2,r}=-2\zeta_2 f_r-2\lambda_1\zeta_2 f_r f'_r-\lambda_1\zeta_3 M f_r,\\
&a_{1,r}=-2\lambda_1\zeta_2 f_r f''_r+2\zeta_2 f'_r+\zeta_3 M+\zeta_1\lambda+2\zeta_2\alpha f'_r,\\
&a_{0,r}=4\lambda_1\zeta_2 f_r f''_r-2\zeta_2 f''_r-2\lambda_1\zeta_2 f'_r f''_r-\lambda_1\zeta_3 M f''_r+2\zeta_2\lambda_1 g_r g'_r,\\
&b_{1,r}=2\zeta_2\lambda_1 g_r f_r, \quad b_{0,r}=2\zeta_2\lambda_1 g'_r f_r-2\zeta_2 g_r, \quad c_{0,r}=-\zeta_4\lambda_m,\\
&l_{2,r}=2\zeta_1 EcPrf''_r, \quad l_{1,r}=-\zeta_5 Pr\lambda_2 f_r\theta'_r+\zeta_3 PrEcMf'_r,\\
&l_{0,r}=\zeta_5 Pr\theta'_r-2\zeta_5 Pr\lambda_2\theta''_r f_r-\zeta_5 Pr\lambda_2 f'_r\theta'_r, \quad n_{1,r}=2\zeta_1 EcPrg'_r,\\
&n_{0,r}=\zeta_3 PrEcMg_r, \quad m_{2,r}=\zeta_6+Rd(1+(\theta_w-1)\theta_r)^3-\zeta_5 Pr\lambda_2 f_r^2,\\
&m_{1,r}=6Rd(\theta_w-1)\Big(1+(\theta_w-1)\theta_r\Big)^2\theta'_r-\zeta_5 Pr\lambda_2 f_r f'_r+\zeta_5 Prf_r,\\
&m_{0,r}=3Rd(\theta_w-1)\Big(1+(\theta_w-1)\theta_r\Big)^2\theta''_r+6Rd(\theta_w-1)^2\Big(1+(\theta_w-1)\theta_r\Big)\theta'^2_r+PrQ_0.
\end{aligned} \tag{6.2.4}$$

$$\begin{aligned}
R_{11}=&-2\lambda_1\zeta_2 f_r f'_r f''_r+\zeta_2 f'^2_r+\zeta_2\alpha f'^2_r+4\lambda_1\zeta_2 f_r^2 f'''_r-2\zeta_2 f_r f''_r-2\lambda_1\zeta_2 f_r f'_r f''_r-\\
&\lambda_1\zeta_3 M f_r f''_r+4\zeta_2\lambda_1 g_r f_r g'_r-\zeta_2 g_r^2,\\
R_{21}=&-2\zeta_2\lambda_1 f_r f''_r g_r-2\lambda_1\zeta_2 f_r f'_r g'_r+2\zeta_2 g_r f'_r+4\lambda_1\zeta_2 g''_r f_r^2-2\zeta_2 g'_r f_r-2\lambda_1\zeta_2 f'_r f_r g'_r-\\
&\zeta_3 M\lambda_1 g'_r f_r-2\zeta_2\lambda_1 f_r f''_r g_r+\zeta_2\alpha g_r^2,\\
R_{31}=&\zeta_1 EcPrf''^2_r-\zeta_5 Pr\lambda_2 f_r f'_r\theta'_r+\frac{1}{2}\zeta_3 PrEcMf'^2_r-2\zeta_2 5\lambda_2 f_r{}^2\theta''_r-\zeta_5 Pr\lambda_2 f_r f'_r\theta'_r+\\
&\zeta_5 Prf_r\theta'_r+\zeta_1 EcPrg'^2_r+\frac{1}{2}\zeta_3 PrEcMg_r^2+3Rd(\theta_w-1)\Big(1+(\theta_w-1)\theta_r\Big)^2\theta'^2_r+\\
&3Rd(\theta_w-1)\Big(1+(\theta_w-1)\theta_r\Big)^2\theta_r\theta''_r+6Rd(\theta_w-1)^2\Big(1+(\theta_w-1)\theta_r\Big)\theta_r\theta'^2_r.
\end{aligned} \tag{6.2.5}$$

Similarly, the linearized boundary conditions take the form:

$$\begin{aligned}
&f'_{r+1}(0)=\beta_0+\beta_2 f''_{r+1},\ f_{r+1}(0)=\beta_w,\ g_{r+1}(0)=1+\beta_2 g'_{r+1},\\
&\Big(\zeta_6-\beta_3\Big)\theta'_{r+1}(0)=-\beta_{i1}\Big(1-\theta_{r+1}(0)\Big),\ f'_{r+1}(\eta_\infty)=0,\ g_{r+1}(\eta_\infty)=0,\ \theta_{r+1}(\eta_\infty)=0.
\end{aligned} \tag{6.2.6}$$

Now we employ the Chebyshev pseudospectral method (see Ref. Trefethen (2000)) to obtain the numerical solution to Eqs. (6.2.1)-(6.2.3) with the corresponding boundary conditions Eq.(6.2.6). First, we transform the physical domain $[0,\eta_\infty]$ into the computational domain $[-1,1]$ using the relation $\eta=\frac{1}{2}(x+1)\eta_\infty$, where $\eta\in[0,\eta_\infty]$, $x\in[-1,1]$, while η_∞ is large enough. Discretization of the solution domain is made at the Gauss-Lobatto collocation grid points, $x_i=cos(\frac{\pi i}{N})$, where $i=0,1,2,\dots,N$ and N is the number of grid points.

At the collocation points, the function f_{r+1}, g_{r+1}, and θ_{r+1} are approximated in the form of series solution.

$$f_{r+1}(\xi)=\sum_{k=0}^{N} f_{r+1}(\xi_k)L_k(\xi_j),\; g_{r+1}(\xi)=\sum_{k=0}^{N} g_{r+1}(\xi_k)L_k(\xi_j),\; \theta_{r+1}(\xi)=\sum_{k=0}^{N} \theta_{r+1}(\xi_k)L_k(\xi_j), \tag{6.2.7}$$

$$\text{where,}\quad L_k(x)=\prod_{k=0,k\neq i}^{N_x}\left(\frac{x-x_k}{x_i-x_k}\right), \tag{6.2.8}$$

is the Lagrange's polynomial and $j=0,1,2,\ldots,N$. The main ingredient of spectral method is the differentiation matrix D. This matrix maps a vector of function values,

$$Y=[y(x_0),y(x_1),\ldots,y(x_N)]^T$$

at the grid points to a vector of Y' of derivative values, i.e. $y'_j \longrightarrow Dy_j$. Since D is made for the domain $[-1,1]$, it needs to be calibrated for the physical domain $[0,\eta_\infty]$ by taking $\mathbf{D}=\dfrac{2D}{\eta_\infty}$. Thus we have,

$$\left(\frac{d^n f_{r+1}}{d\eta^n}\right)_{\eta=\eta_j}=\sum_{k=0}^{N} D^n_{jk} f_{r+1}(\eta_k)=\mathbf{D}^n\mathbf{F}_{r+1},\; \left(\frac{d^n g_{r+1}}{d\eta^n}\right)_{\eta=\eta_j}=\sum_{k=0}^{N} D^n_{jk} g_{r+1}(\eta_k)=\mathbf{D}^n_{r+1}\mathbf{G}_{r+1},$$
$$\left(\frac{d^n \theta}{d\eta^n}\right)_{\eta=\eta_j}=\sum_{k=0}^{N} D^n_{jk}\theta_{r+1}(\eta_k)=\mathbf{D}^n\Theta_{r+1}, \tag{6.2.9}$$

where $\mathbf{F}_{r+1}=\Big[f_{r+1}(\eta_0),f_{r+1}(\eta_1),\ldots,f_{r+1}(\eta_N)\Big]^T$, $\mathbf{G}_{r+1}=\Big[g_{r+1}(\eta_0),g_{r+1}(\eta_1),\ldots,g_{r+1}(\eta_N)\Big]^T$, $\Theta_{r+1}=\Big[\theta_{r+1}(\eta_0),\theta_{r+1}(\eta_1),\ldots,\theta_{r+1}(\eta_N)\Big]^T$, $j=0,1,\ldots,N$, and n is order of derivative.

Now, using Eq. (6.2.7) and (6.2.9) into Eqs. (6.2.1)-(6.2.3), we obtain the vector matrix equation,

$$\mathbf{A}_r\mathbf{X}_{r+1}=\mathbf{B}_r. \tag{6.2.10}$$

In Eq. (6.2.10), $\mathbf{A}_r$ is a $(3N+3)\times(3N+3)$ square matrix, $\mathbf{X}_{r+1}$ and $\mathbf{B}_r$ are $(3N+3)\times 1$ column vectors respectively, and are defined as,

$$\mathbf{A}_r=\begin{bmatrix} A_{11} & A_{12} & A_{13}\\ A_{21} & A_{22} & A_{23}\\ A_{31} & A_{32} & A_{33}\end{bmatrix},\; \mathbf{X}_{r+1}=\begin{bmatrix}\mathbf{F}_{r+1}\\ \mathbf{G}_{r+1}\\ \Theta_{r+1}\end{bmatrix},\; \mathbf{B}_r=\begin{bmatrix}\mathbf{R}_{11,r}\\ \mathbf{R}_{21,r}\\ \mathbf{R}_{31,r}\end{bmatrix}, \tag{6.2.11}$$

where

$$A_{11} = diag(a_{3,r})\mathbf{D}^3 + diag(a_{2,r})\mathbf{D}^2 + diag(a_{1,r})\mathbf{D} + diag(a_{0,r})\mathbf{I},$$
$$A_{12} = diag(b_{1.r})\mathbf{D} + diag(b_{0,r})\mathbf{I},\ A_{13} = diag(c_{0,r})\mathbf{I},$$
$$A_{21} = diag(e_{2,r})\mathbf{D}^2 + diag(e_{1,r})\mathbf{D} + diag(e_{0,r})\mathbf{I},\ A_{22} = diag(h_{2,r})\mathbf{D}^2 + diag(h_{1,r})\mathbf{D} + diag(h_{0,r})\mathbf{I},$$
$$A_{23} = \mathbf{0},\ A_{31} = diag(l_{2,r})\mathbf{D}^2 + diag(l_{1,r})\mathbf{D} + diag(l_{0,r})\mathbf{I},\ A_{32} = diag(n_{1,r})\mathbf{D} + diag(n_{0,r})\mathbf{I},$$
$$A_{33} = diag(m_{2,r})\mathbf{D}^2 + diag(m_{1,r})\mathbf{D} + diag(m_{0,r})\mathbf{I}, \tag{6.2.12}$$

here, $diag(\dots)$, $\mathbf{I}$, and $\mathbf{0}$ are $(N+1)\times(N+1)$ diagonal, identity, and zero matrices, respectively.

To commence the SQLM algorithm, it is essential to make an initial guess. This initial guess must adhere to the boundary conditions. The suggested guess below fulfills this requirement and serves the purpose adequately.

$$f_0(\eta) = \beta_w + 1 - e^{-\eta},\ g_0(\eta) = \frac{1}{1+\beta_2}e^{-\eta},\ \theta_0(\eta) = \frac{\beta_{i1}}{\zeta_6 - \beta_3 + \beta_{i1}}e^{-\eta}. \tag{6.2.13}$$

The thermophysical constants: density (ρ), thermal conductivity (k), electric conductivity (σ_0), specific heat capacity ($\mathrm{c_p}$), and thermal expansion (β) of the base fluid and nano additives adopted from (Ali et al. (2024), Alwawi et al. (2020)), are presented in table 6.2.1.

Table 6.2.1: Thermophysical constants of the base fluid and nanoparticles

Nanoparticles	$\rho\left(KgM^{-3}\right)$	$k\left(\mathrm{WM^{-1}K^{-1}}\right)$	$\sigma_0\left(\mathrm{SM^{-1}}\right)$	$\mathrm{c_p}\left(\mathrm{JKg^{-2}K^{-1}}\right)$	$\beta/10^{-5}\left(\mathrm{K^{-1}}\right)$
Sodium alginate	989	0.6376	2.6×10^{-4}	4175	99
Fe_3O_4	5180	9.7	2.5×10^{-4}	670	1.3
CuO	6320	76.5	6.9×10^{-2}	531.8	1.8
MOS_2	5060	34.5	2.09×10^{-5}	397.746	2.8424

Also, the mathematical formulae for the thermophysical characteristics of binary/ternary hybrid nanofluids (Singh et al. (2023)) are described in Table 6.3.1.

6.3 Convergence and Stability of SQLM

The stability and convergence behavior of the SQLM are assessed using the infinity norm, defined as:

$$Er = \max\left(\|f_{r+1} - f_r\|_\infty; \|g_{r+1} - g_r\|_\infty; \|\theta_{r+1} - \theta_r\|_\infty\right), \tag{6.3.1}$$

which quantifies the maximum residual between successive iterations. Figures 6.3.1a-6.3.1b display the convergence profiles of residual errors for heat sink ($Q=-0.2$) and heat source ($Q=0.1$) scenarios. A convergence tolerance of $\epsilon = 10^{-9}$ is employed with 80 spectral collocation points.

Table 6.3.1: Thermo-physical properties' relations for binary and ternary nanofluid

Physical properties	Mathematical equations
Dynamic viscosity	$\frac{\mu_{thnf}}{\mu_f}=\frac{1}{(1-\phi_1)^{2.5}(1-\phi_2)^{2.5}(1-\phi_3)^{2.5}}$
Density	$\frac{\rho_{thnf}}{\rho_f}=(1-\phi_1)\Big[(1-\phi_2)\Big((1-\phi_3)+\phi_3\frac{\rho_3}{\rho_f}\Big)+\phi_2\frac{\rho_2}{\rho_f}\Big]+\phi_1\frac{\rho_1}{\rho_f}$
Thermal conductivity	$\frac{k_{thnf}}{k_f}=\frac{k_1+2k_{hnf}-2\phi_1(k_{hnf}-k_1)}{k_1+2k_{hnf}+\phi_1(k_{hnf}-k_1)},\ \frac{k_{hnf}}{k_f}=\frac{k_2+2k_{nf}-2\phi_2(k_{nf}-k_2)}{k_2+2k_{nf}+\phi_2(k_{nf}-k_2)}$
	$\frac{k_{nf}}{k_f}=\frac{k_3+2k_f-2\phi_3(k_f-k_3)}{k_3+2k_f+\phi_3(k_f-k_3)}$
Electrical conductivity	$\frac{\sigma_{thnf}}{\sigma_{hnf}}=1+\frac{3\Big(\frac{\sigma_1}{\sigma_{hnf}}-1\Big)\phi_1}{\Big(\frac{\sigma_1}{\sigma_{hnf}}+2\Big)-\phi_1\Big(\frac{\sigma_1}{\sigma_{hnf}}-1\Big)}$
	$\frac{\sigma_{hnf}}{\sigma_{nf}}=1+\frac{3\Big(\frac{\sigma_2}{\sigma_{nf}}-1\Big)\phi_2}{\Big(\frac{\sigma_2}{\sigma_{nf}}+2\Big)-\phi_2\Big(\frac{\sigma_2}{\sigma_{nf}}-1\Big)}$
	$\frac{\sigma_{nf}}{\sigma_0}=1+\frac{3\Big(\frac{\sigma_3}{\sigma_f}-1\Big)\phi_3}{\Big(\frac{\sigma_3}{\sigma_f}+2\Big)-\phi_3\Big(\frac{\sigma_3}{\sigma_f}-1\Big)}$
Specific heat	$\frac{(\rho c_p)_{thnf}}{(\rho c_p)_f}=\phi_1\frac{(\rho c_p)_1}{(\rho c_p)_f}+(1-\phi_1)\Big[(1-\phi_2)\Big((1-\phi_3)+\phi_3\frac{(\rho c_p)_3}{(\rho c_p)_f}\Big)+\phi_1\frac{(\rho c_p)_2}{(\rho c_p)_f}\Big]$
Thermal expansion	$\frac{(\rho\beta)_{thnf}}{(\rho\beta)_f}=\phi_1\frac{(\rho\beta)_1}{(\rho\beta)_f}+(1-\phi_1)\Big[(1-\phi_2)\Big((1-\phi_3)+\phi_3\frac{(\rho\beta)_3}{(\rho\beta)_f}\Big)+\phi_1\frac{(\rho\beta)_2}{(\rho\beta)_f}\Big]$

The analysis reveals that, within nine iterations, residual norms for the ternary hybrid nanofluid fall below 10^{-9}, while those for the binary hybrid nanofluid reach below 10^{-10}. Moreover, the heat sink case consistently yields smaller errors compared to the heat source case. Once convergence is achieved, the error norms plateau, reflecting the limit of numerical accuracy for the selected discretization and confirming the robustness of the SQLM.

To further verify the accuracy of our results, a comparative analysis was performed against existing data from Singh et al. (2023) and Acharya et al. (2020), focusing on the wall shear parameter $f''(0)$ under varying suction/injection values within specific limiting cases. As shown in Table 6.3.2, the comparison confirms strong agreement, thereby validating the present model.

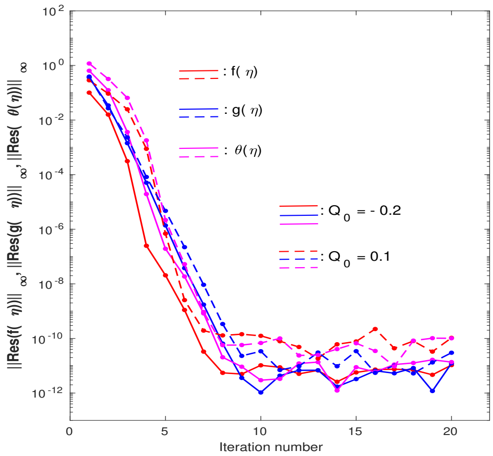

(a)

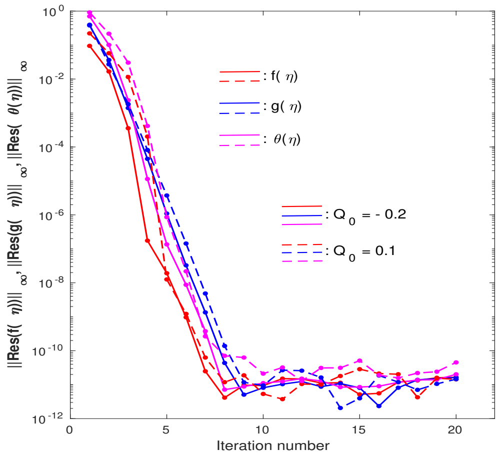

(b)

Figure 6.3.1: The residual error for $\mathrm{f}(\eta), \mathrm{g}(\eta)$ and $\theta(\eta)$ against iteration number in (a):Ternary nanofluid, (b): Binary nanofluid

Table 6.3.2: Comparison of $\mathrm{C_f^\star} = \mathrm{f}''(0)$ with the works in (Singh et al. (2023)) and ((Acharya et al., 2020)) for various values of β_w when $M = \lambda = \lambda_1 = \lambda_2 = \alpha = \beta_0 = \lambda_m = \beta_2 = \beta_3 = \phi_1 = \phi_2 = \phi_3 = 0$

	Acharya et al. (2020)	Singh et al. (2023)	Present value
β_w	$f''(0)$	$f''(0)$	$f''(0)$
-1	0.389642	0.3896432	0.3896434
1	0.489511	0.4895129	0.4895125
-2	0.242421	0.2424231	0.2424230
0	0.510205	0.5102108	0.5102104
2	0.398936	0.3989371	0.3989368

6.4 Results and Discussion

The nondimensionalized system of ODEs given by Eqs. (6.1.11)-(6.1.14), subject to boundary conditions in Eq. (6.1.15), is solved numerically using the SQLM implemented in `MATLAB`. Parametric influences on the nondimensional tangential and radial velocities, temperature distribution, skin friction, and heat transfer rate are explored through graphical and tabular illustrations. Entropy generation and Bejan number behavior are also investigated.

Unless otherwise specified, the following default parameter values are used: $M = 3$, $\lambda = 1.5$, $\lambda_1 = 1.2$, $\lambda_2 = 2$, $\alpha = 3.5$, $Rd = 4.5$, $\theta_w = 1.15$, $Pr = 8$, $Q_0 = 0.05$, $Ec = 0.3$, $\beta_0 = 0.15$, $\beta_w = 0.4$, $\lambda_m = 0.5$, $\beta_2 = 0.05$, $\beta_3 = 1.2$, $\beta_{i1} = 0.3$, and $\phi_1 = \phi_2 = \phi_3 = 0.03$. The variation ranges for each parameter are selected to ensure rapid convergence within minimal iterations.

6.4.1 Velocity variations

Figures 6.4.1-6.4.5 display the behavior of radial and tangential velocities under the influence of various physical parameters for both binary and ternary hybrid nanofluid configurations. As illustrated in Figure 6.4.1, the presence of a magnetic field introduces a Lorentz force that counteracts the momentum generated by rotation and stretching, thereby reducing both velocity components. The ternary hybrid nanofluid exhibits higher velocity magnitudes than its binary counterpart, attributed to its improved ability to overcome magnetic damping due to the inclusion of an additional nanoparticle species.

In Figure 6.4.2, increasing the permeability of the porous medium results in a decline in both radial and tangential velocities across both nanofluid types. Nonetheless, the ternary hybrid nanofluid maintains thicker momentum boundary layers, indicating enhanced resistance to the porous medium's damping effect.

Figure 6.4.3 investigates the impact of the Deborah number, which characterizes the fluid's elastic properties based on the relaxation time. An increase in this parameter suppresses both velocity components and reduces boundary layer thickness, reflecting stronger viscoelastic behavior. Specifically, as λ_1 rises, the dominance of elastic effects over viscous dissipation becomes more pronounced, further reducing flow velocities. Comparatively, the ternary hybrid nanofluid continues to sustain greater velocity magnitudes than the binary model.

The influence of velocity slip is presented in Figure 6.4.4, where an increasing slip parameter β_2 results in diminished velocity fields. This is due to partial fluid-surface interaction, where a higher slip coefficient reduces the effectiveness of momentum transfer between the rotating disk and fluid particles. Consequently, both velocity components decrease as β_2 increases.

Lastly, Figure 6.4.5 addresses the effects of suction/injection and mixed convection parameters. In subfigure (a), increasing the suction parameter ($\beta_w > 0$) draws fluid towards the wall, enhancing near-wall viscous resistance and reducing flow velocities. The ternary hybrid nanofluid again maintains a thicker velocity boundary layer compared to the binary fluid. Subfigure (b) illustrates that a higher mixed convection parameter intensifies buoyancy-driven acceleration within the boundary layer, thereby enhancing radial velocity. Once more, the ternary nanofluid configuration yields superior momentum transport compared to the binary formulation.

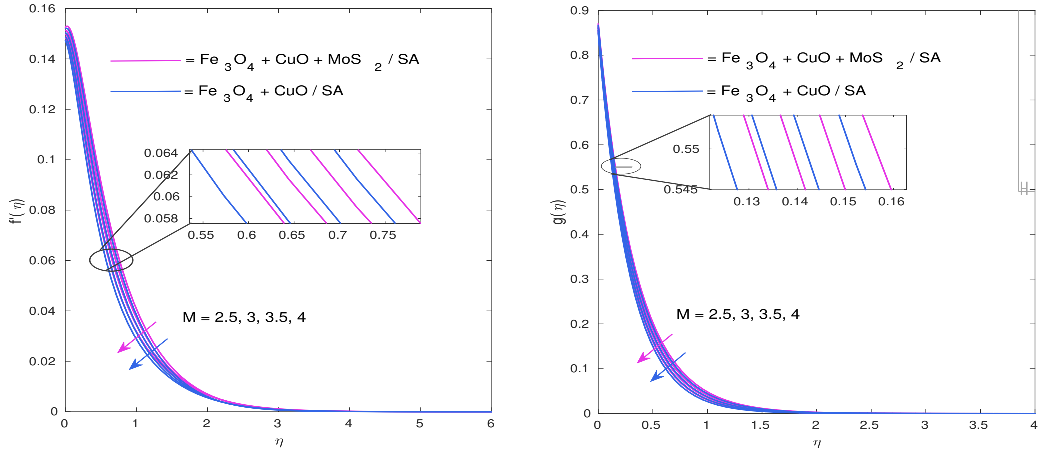

Figure 6.4.1: Effect of M on (a): radial velocity (b): tangential velocity profile

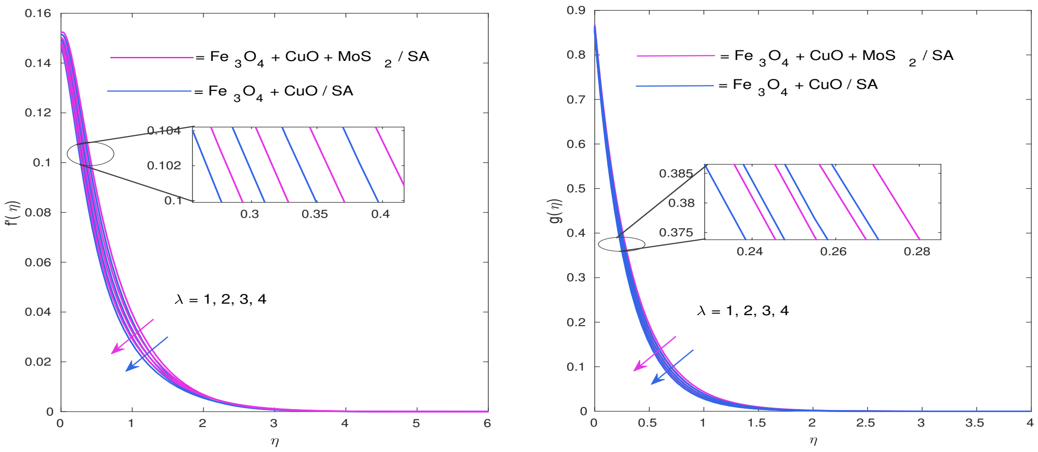

b

Figure 6.4.2: Effect of λ on (a): radial velocity (b): tangential velocity profile

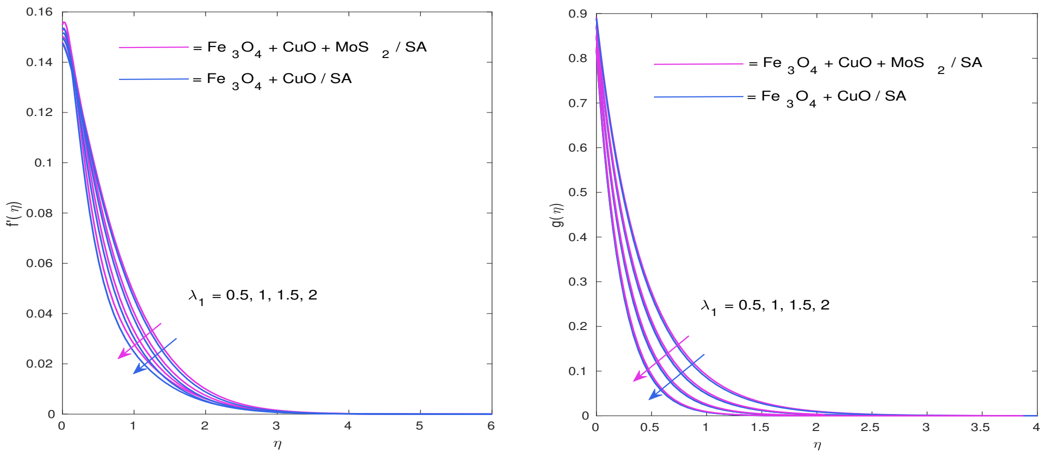

Figure 6.4.3: Effect of λ_1 on (a): radial velocity (b): tangential velocity profile

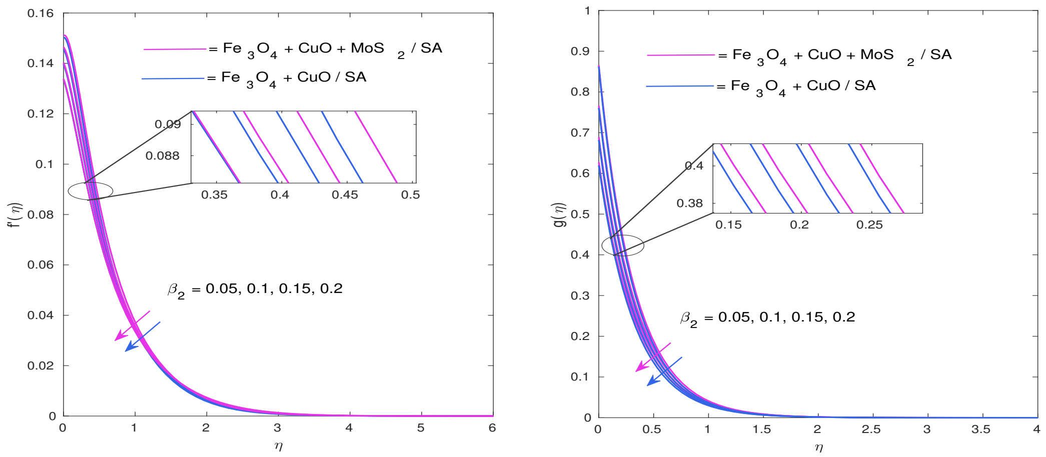

Figure 6.4.4: Effect of β_2 on (a): radial velocity (b): tangential velocity profile

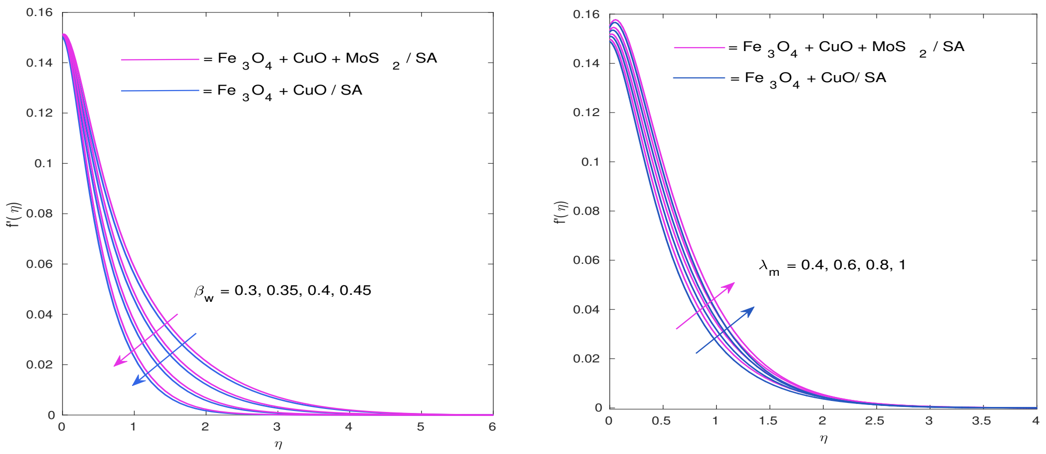

Figure 6.4.5: Effect of (a): β_{w} (b) λ_{m} on radial velocity profile

6.4.2 Temperature variations

Figures 6.4.6-6.4.11 illustrate how the temperature distribution within the thermal boundary layer responds to variations in key parameters for both binary and ternary hybrid nanofluid models. These parameters include M, λ, λ_2, β_w, λ_m,λ_1, β_3, R_d, Ec, θ_w, and Q_0.

Figure 6.4.6 shows that an increase in M and λ leads to elevated temperature profiles in the boundary layer. This occurs because the induced Lorentz and porous drag forces reduce the fluid velocity, converting mechanical energy into thermal energy. The effect is more pronounced in ternary hybrid nanofluids due to their superior thermal conductivity and nanoparticle synergy, resulting in higher temperature distributions than those observed in binary nanofluids.

In Figure 6.4.7, the temperature profile decreases with increasing values of λ_2 and β_w. Physically, λ_2 represents the thermal relaxation time based on the Cattaneo–Christov model, and higher values delay heat conduction, thereby reducing fluid temperature. When $\lambda_2 = 0$, infinite thermal propagation is assumed, yielding the maximum boundary layer temperature but implying minimal heat transfer to the fluid. Similarly, increased suction ($\beta_w > 0$) enhances the extraction of fluid and thermal energy from the boundary layer, reducing its temperature.

The influence of thermal slip and Deborah number is explored in Figure 6.4.8. In subfigure (a), the temperature and thermal boundary layer thickness decline with rising β_3, as slip reduces conductive heat transfer from the disk surface. In contrast, subfigure (b) reveals that increasing λ_1 enhances temperature levels due to strengthened elastic effects and energy storage capacity in the nanofluid, which collectively contribute to higher kinetic energy conversion into heat.

Figure 6.4.9 examines the effects of mixed convection and thermal radiation. An increase in the mixed convection parameter reduces temperature by enhancing buoyancy-induced convection, which promotes heat dissipation. Conversely, elevated thermal radiation augments the temperature distribution, particularly under high-temperature gradients, as relevant to applications such as space propulsion, solar energy systems, and high-temperature chemical reactors. Ternary nanofluids consistently show higher thermal responses due to their composite nanoparticle composition.

Figure 6.4.10 demonstrates that both the Ec and θ_w amplify temperature within the thermal boundary layer. Higher Ec values signify more viscous dissipation, producing additional thermal energy via internal friction. The effect is more pronounced near the disk surface. Likewise, increasing θ_w leads to elevated fluid temperatures, with ternary nanofluids exhibiting the most significant thermal rise due to enhanced heat absorption capacity.

Lastly, Figure 6.4.11 highlights the effects of Q_0 and nanoparticle volume fraction. An increase in Q_0 enhanced the temperature distribution in both nanofluid types. Additionally, the temperature enhancement scales with nanoparticle concentration, where the ternary nanofluid ($\mathrm{CuO} + \mathrm{Fe_3O_4} + \mathrm{MoS_2/SA}$) displays the highest temperature rise, followed by the binary blend ($\mathrm{CuO} + \mathrm{Fe_3O_4/SA}$) and the single-component nanofluid ($\mathrm{Fe_3O_4/SA}$).

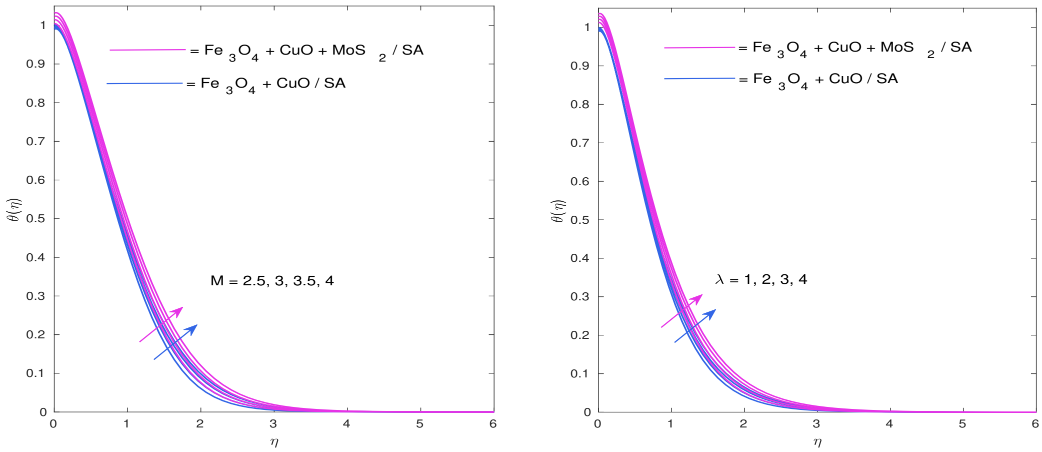

Figure 6.4.6: Effect of (a): M and (b): λ on temperature profile

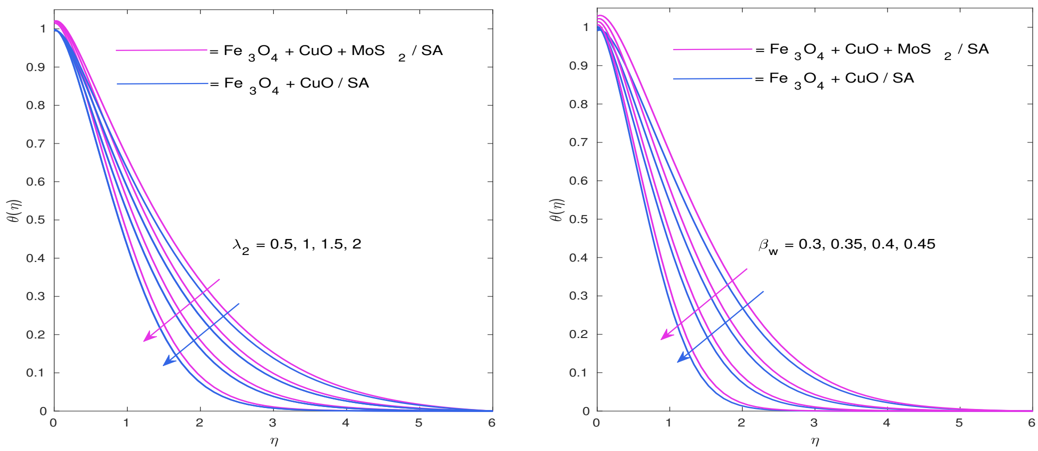

Figure 6.4.7: Effect of (a): λ_2 and (b): β_{w} on temperature profile

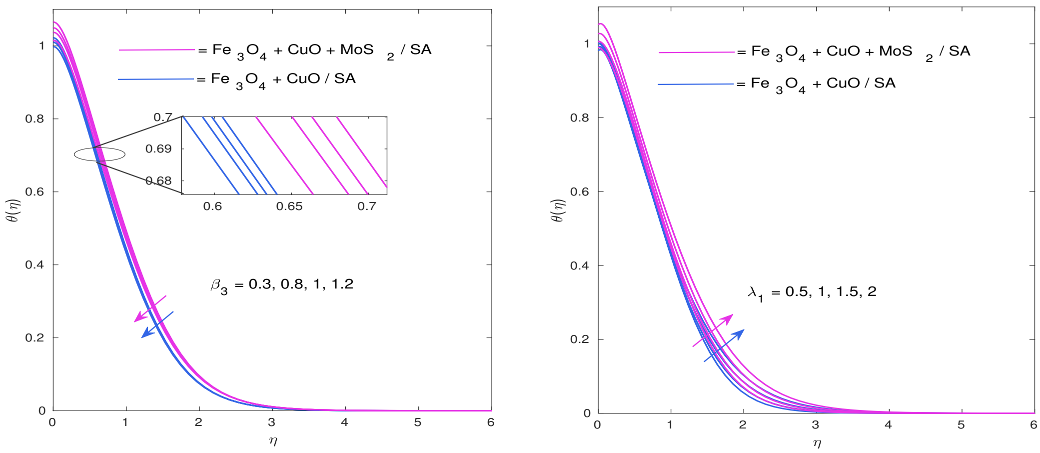

Figure 6.4.8: Effect of (a): β_3 and (b): λ_1 on temperature profile

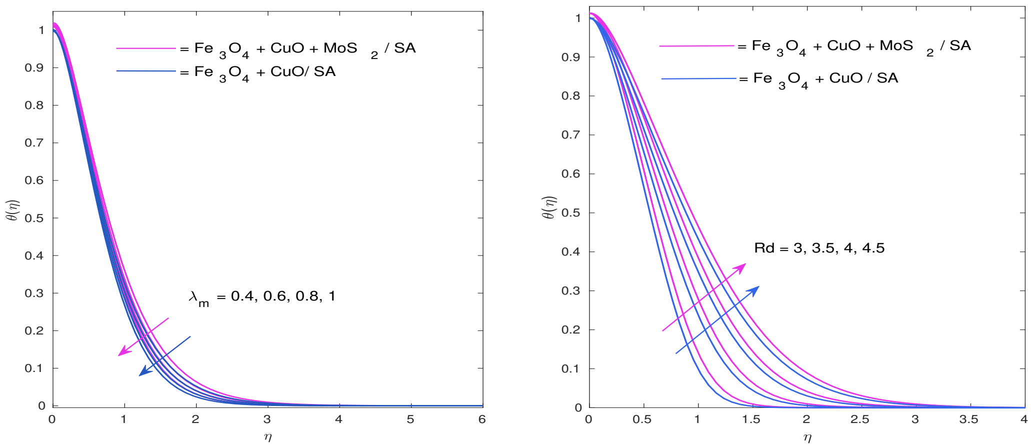

Figure 6.4.9: Effect of (a): λ_{m} and (b): Rd on temperature profile

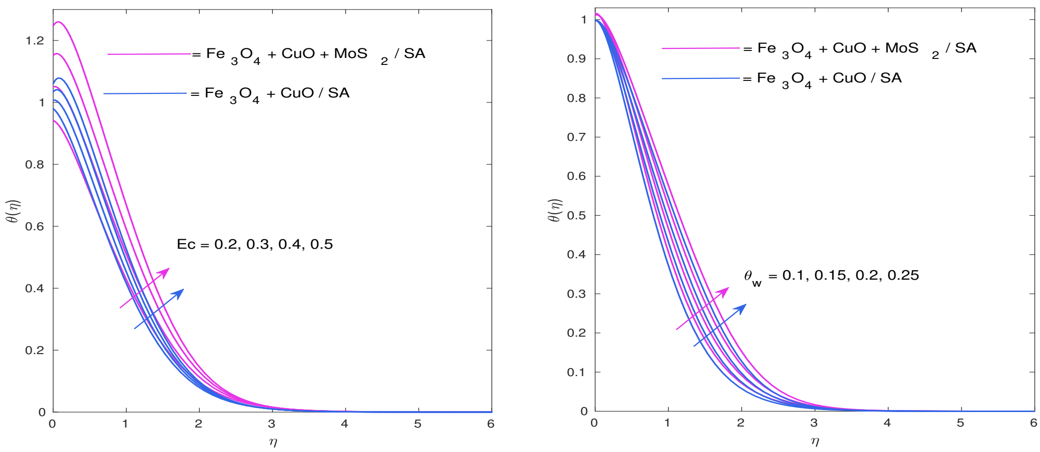

Figure 6.4.10: Effect of (a): Ec and (b): θ_{w} on temperature profile

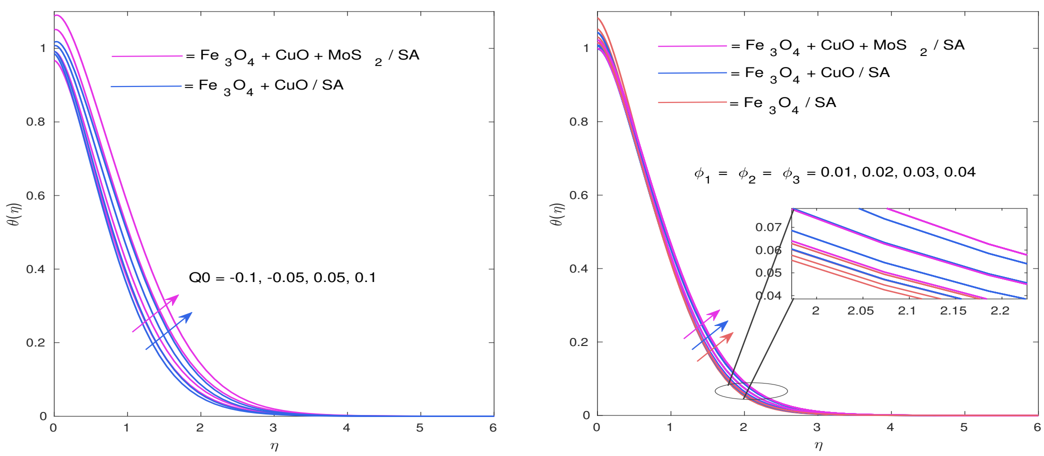

Figure 6.4.11: Effect of (a): Q_0 and (b): ϕ on temperature profile

6.4.3 Variations in Entropy Generation Rate and Bejan Number

Figures 6.4.12-6.4.17 present how the entropy generation rate and Bejan number respond to key thermophysical parameters in binary and ternary hybrid nanofluids.

Figure 6.4.12 shows that the entropy generation rate increases with the magnetic field parameter, particularly near the disk surface, and the increase is more substantial in ternary nanofluids. This is due to the enhanced Lorentz force acting as a resistive mechanism that disrupts fluid motion and increases thermodynamic irreversibility. Interestingly, although N_g is higher in ternary nanofluids, the Bejan number, which represents the ratio of heat transfer-related entropy to total entropy production, is higher for binary nanofluids. This suggests that thermal irreversibility plays a more dominant role in binary systems under increasing magnetic influence.

Figure 6.4.13 analyzes the effect of the Brinkman number on entropy generation and the Bejan number. An increase in Br elevates entropy production in both nanofluid types, especially near the disk surface. Since Br is inversely proportional to thermal conductivity, higher values indicate reduced conductivity, thereby increasing temperature gradients and entropy generation. As Br rises, entropy generation due to viscous effects overtakes that due to heat conduction, causing a decline in the Bejan number. Notably, at $Br = 0$, entropy production is purely from heat transfer, yielding $Be = 1$.

The impact of thermal radiation on entropy metrics is depicted in Figure 6.4.14. An increase in the radiation parameter initially reduces entropy production near the surface but enhances it further away from the disk. This trend results from the redistribution of thermal energy across the boundary layer. Concurrently, the Bejan number decreases with stronger radiation, indicating a shift toward increased irreversibility due to conduction and radiation interactions.

In Figure 6.4.15, variations in λ_2 are considered. As λ_2 increases, both entropy generation and Bejan number also rise in the binary and ternary nanofluids. This is attributed to a rise in the heat transfer rate under the Cattaneo–Christov thermal model, enhancing the irreversibility linked to conduction.

The effects of β_w on entropy and Bejan number are shown in Figure 6.4.16. Increasing suction ($\beta_w > 0$) leads to elevated entropy generation and Bejan number. Suction enhances the removal of thermal energy from the boundary layer, thus reducing the heat transfer rate and intensifying entropy production. Ternary nanofluids display a higher N_g under increased suction, while binary nanofluids register a greater Bejan number. Figure 6.4.17 explores the role of the porosity parameter. As porosity increases, resistance to fluid motion rises due to drag from the porous medium, thickening the thermal boundary layer and elevating entropy production. However, this resistance also amplifies fluid friction irreversibility, reducing the

Bejan number. The ternary nanofluid exhibits a sharper decline in Be compared to the binary model, highlighting its greater sensitivity to porous drag effects.

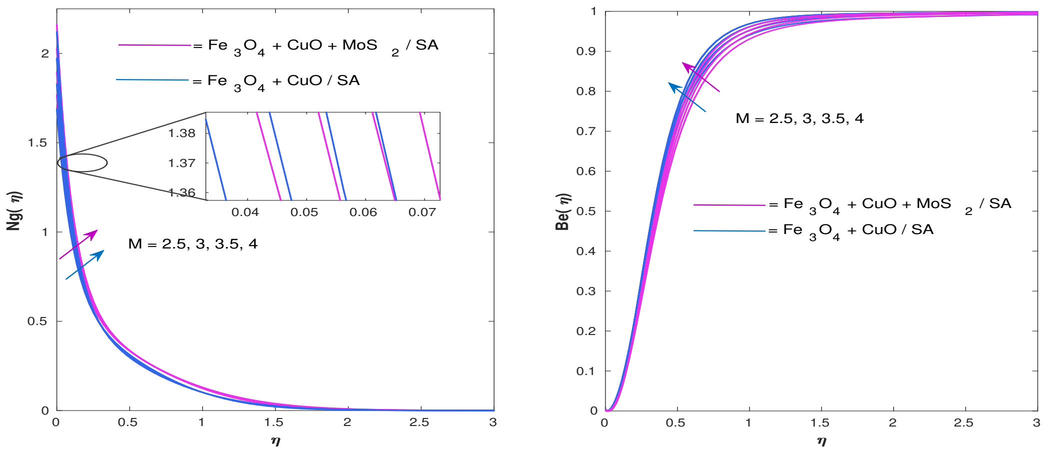

Figure 6.4.12: Effect of M on (a): Entropy generation (b): Bejan number

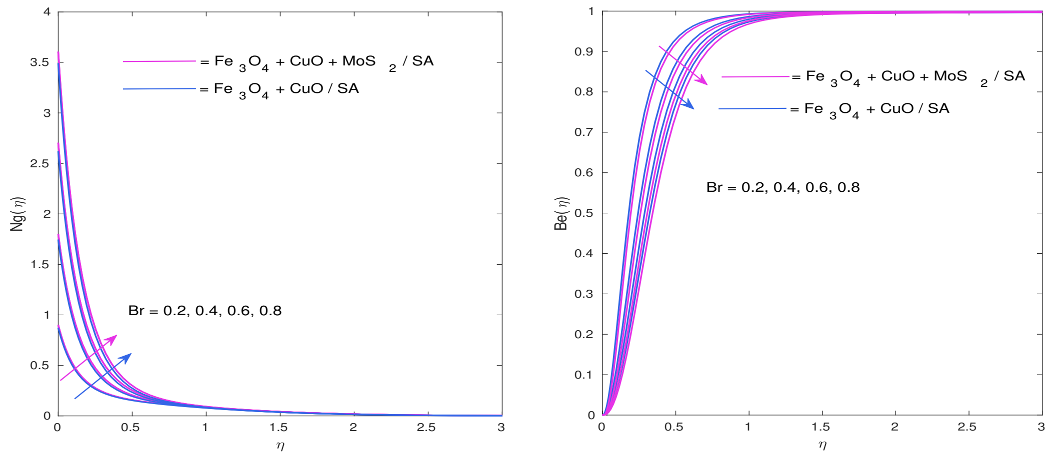

Figure 6.4.13: Effect of Br on (a): Entropy generation (b): Bejan number

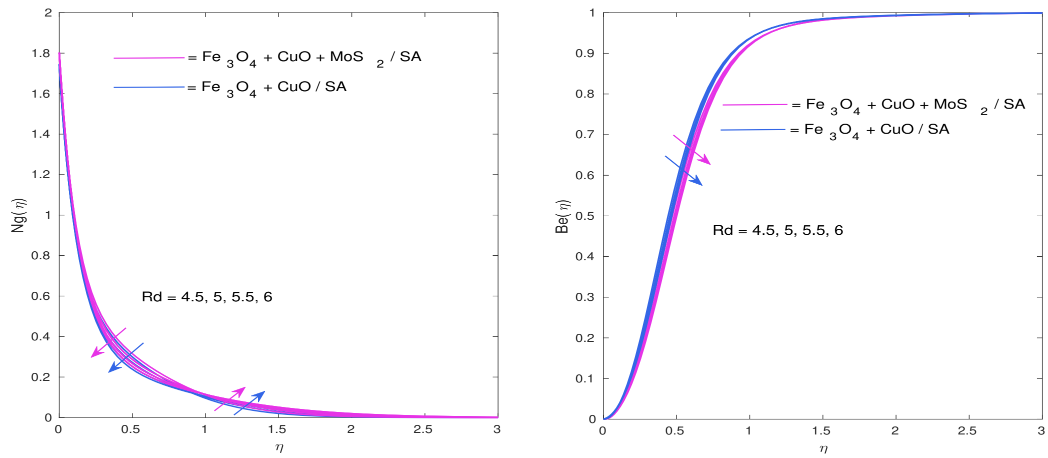

Figure 6.4.14: Effect of Rd on (a): Entropy generation (b): Bejan number

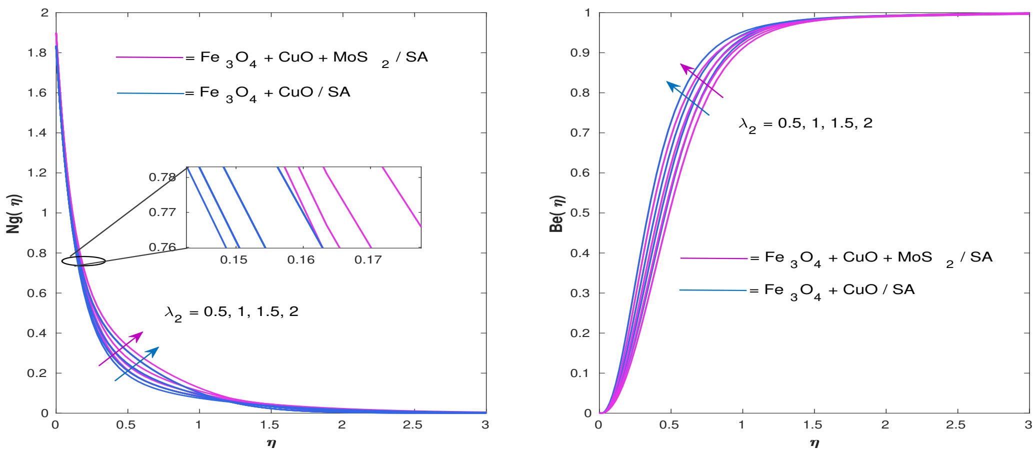

Figure 6.4.15: Effect of λ_2 on (a): Entropy generation (b): Bejan number

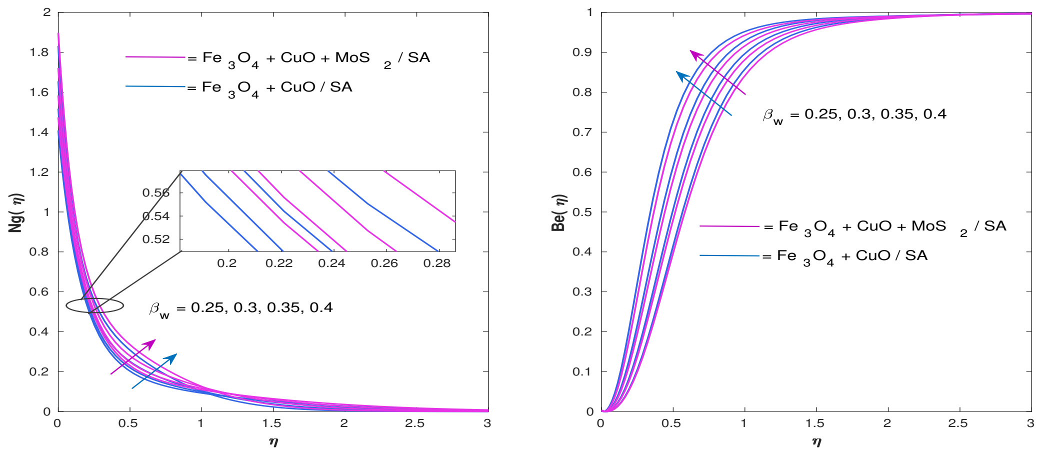

Figure 6.4.16: Effect of β_{w} on (a): Entropy generation (b): Bejan number

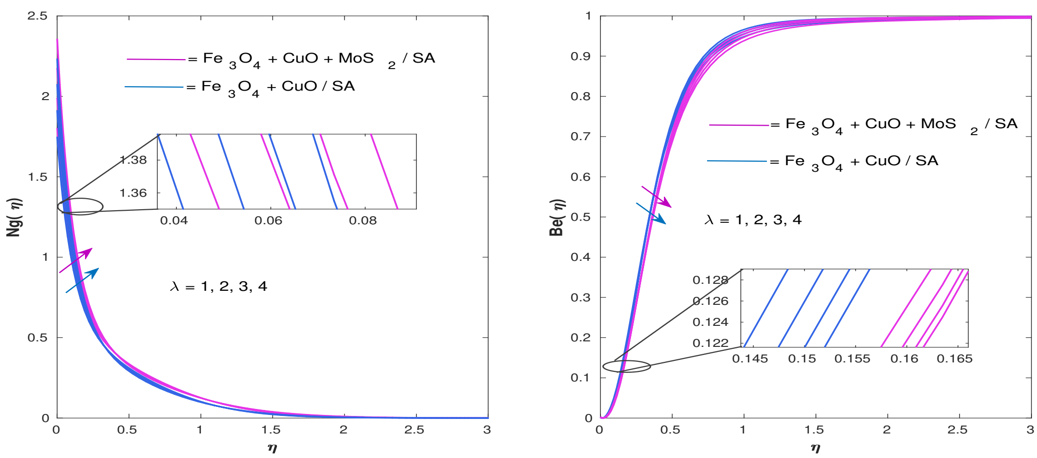

Figure 6.4.17: Effect of λ on (a): Entropy generation (b): Bejan number

6.4.4 Skin Friction Variations

Table 6.4.1 presents the influence of selected parameters on the tangential and radial skin friction coefficients for both binary and ternary hybrid nanofluid flows. An increase in M, λ, and β_w consistently leads to a reduction in both tangential and radial skin frictions in both nanofluid types. In contrast, an increase in the nanoparticle volume fraction enhances both skin friction components. The mixed convection parameter has opposing effects: it elevates radial skin friction while reducing tangential skin friction. Meanwhile, increasing the slip velocity parameter diminishes radial friction but raises tangential friction. Higher Deborah numbers amplify radial skin friction and simultaneously suppress tangential skin friction. Across all parametric conditions, the radial skin friction consistently exceeds the tangential component.

Table 6.4.1: Variations in $Re^{1/2}Cf_r$ and $Re^{1/2}Cf_\phi$ for various values of embedded parameters.

M	λ_1	λ	λ_m	β_2	β_w	ϕ	Trihybrid nanofluid		Bihybrid nanofluid	
							$Re^{1/2}Cf_r$	$Re^{1/2}Cf_\phi$	$Re^{1/2}Cf_r$	$Re^{1/2}Cf_\phi$
2	1.2	1.5	0.5	0.05	0.4	0.03	0.192196	-6.483921	0.175162	-6.654930
2.5							0.122040	-6.749914	0.093426	-6.952691
3							0.054651	-7.012029	0.015320	-7.245704
3	0.8						-0.042094	-6.171079	-0.066176	-6.361168
	1.2						0.054651	-7.012029	0.015320	-7.245704
	1.6						0.153702	-8.024857	0.093545	-8.304783
	1.2	1					0.102993	-6.896986	0.062810	-7.132761
		2					0.009039	-7.124508	-0.029598	-7.356188
		3					-0.075039	-7.342064	-0.112652	-7.570081
		1.5	0.4				0.002368	-6.991124	-0.040564	-7.224194
			0.6				0.105638	-7.032220	0.070025	-7.266558
			0.8				0.204258	-7.070761	0.176323	-7.306542
			0.5	0.1			-0.088967	-6.076680	-0.111724	-6.268970
				0.15			-0.164498	-5.367428	-0.176423	-5.530581
				0.2			-0.204774	-4.811616	-0.209424	-4.953004
				0.05	0.4		0.054651	-7.012029	0.015320	-7.245704
					0.45		0.038324	-7.606326	-0.007199	-7.861893
					0.5		0.004335	-8.333973	-0.050497	-8.613233
					0.4	0.02	0.038036	-7.199166	0.013952	-7.394404
						0.03	0.054651	-7.012029	0.015320	-7.245704
						0.04	0.072294	-6.8877952	0.020289	-7.129148

6.4.5 Heat Transfer Rate Variations

Table 6.4.2 summarizes how various dimensionless parameters affect the local heat transfer rate for binary and ternary hybrid nanofluids under both heat sink ($Q_0 = -0.2$) and heat source ($Q_0 = 0.1$) conditions. A rise in M and Ec leads to a reduction in surface heat transfer rate in both scenarios. In contrast, strengthening λ_2, β_w, and λ_m enhances the heat transfer rate in both nanofluid systems. Interestingly, the radiation and temperature ratio parameters suppress the heat transfer rate under heat source conditions, while promoting it under heat sink conditions. Increasing the Deborah number diminishes the heat transfer performance in both nanofluid models. Notably, under heat source conditions, ternary nanofluids exhibit superior heat transfer rates compared to binary ones, whereas the reverse trend is observed under heat sink conditions.

Table 6.4.2: Variations in $Re^{-1/2}Nu_w$ subject to various values of embedded parameters for $Q_0 = -0.2$ and $Q_0 = 0.1$

								$\mathrm{Re}^{-1/2}\mathrm{Nu_w}$			
								$Q = -0.2$		$Q = 0.1$	
M	Rd	λ_m	Ec	λ_2	λ_1	β_w	θ_w	Ternary	Binary	Ternary	Binary
2.5	4.5	0.5	0.3	2	1.2	0.4	1.15	2.546710	3.917469	-0.980020	-0.635299
3								2.200167	3.428951	-1.468531	-1.247930
3.5								1.876088	2.976043	-1.924275	-1.812127
3	4							1.995502	3.267706	–1.329890	-1.107258
	4.5							2.200167	3.428951	-1.468531	-1.247930
	5							2.398912	3.597880	-1.594182	-1.371205
	4.5	0.5						2.184700	3.397773	-1.607415	-1.407704
		1						2.214727	3.458559	-1.346938	-1.105325
		1.5						2.241328	3.513419	-1.142159	-0.859474
		2	0.2					4.335644	6.201888	0.973385	1.643273
			0.3					2.200167	3.348951	-1.468531	-1.247930
			0.4					0.073507	0.631664	-3.891236	-4.166084
			0.3	0.5				2.162576	3.095013	-1.982365	-1.854780
				1				2.171157	3.182467	-1.907154	-1.765231
				1.5				2.182469	3.289963	-1.726638	-1.556709
				2	0.8			2.776950	4.186648	-0.756959	-0.404313
					1.2			2.200167	3.428951	-1.468531	-1.247930
					1.6			1.498802	2.513808	-2.334973	-2.261905
					1.2	0.4		2.200167	3.428951	-1.468531	-1.247930
						0.45		2.281984	3.814435	-0.990314	-0.581347
						0.5		2.326867	4.311793	-0.505952	0.240035
						0.4	1.1	2.093701	3.438894	-1.407176	-1.209129
							1.15	2.200167	3.428951	-1.468531	-1.247930
							1.2	2.317650	3.462257	-1.530029	-1.290027

6.5 Summary

This work focused on analyzing the MHD flow and thermal behavior of Maxwell's binary and ternary hybrid nanofluids over a radially stretching, rotating disk embedded in a Darcy-

Forchheimer porous medium. The model incorporated several physical effects, including mixed convection, velocity and thermal slip, thermal radiation, heat source/sink, suction/injection, and convective boundary conditions. Heat transport was modeled using the Cattaneo-Christov framework. Comparative evaluations were performed for binary $(\mathrm{CuO}+\mathrm{Fe_3O_4}/\mathrm{SA})$ and ternary $(\mathrm{CuO}+\mathrm{Fe_3O_4}+\mathrm{MoS_2}/\mathrm{SA})$ nanofluids. Entropy generation and Bejan number analyses were also conducted under varying physical conditions.

Key findings from the study include:

1. The ternary nanofluid offered stronger resistance to magnetic and porous medium forces than its binary counterpart in both radial and tangential directions.

2. Elevating the Maxwell relaxation time, slip velocity, and suction intensity reduced flow velocities and momentum thickness, whereas enhanced mixed convection increased both.

3. Temperature profiles and thermal boundary layer thickness expanded with increases in M, Rd, Ec, λ, λ_1, θ_w, and Q_0, but contracted with rising values of β_{w}, β_3, λ_2, and λ_m.

4. The ternary hybrid nanofluid consistently exhibited higher thermal conductivity and temperature distribution than the binary formulation across all parametric variations.

5. N_g and Be were amplified with larger M, λ_2, and β_{w}, while Rd suppressed both. Higher Br andλ increased N_g but reduced Be.

6. Skin friction coefficients in both radial and tangential directions were greater for the ternary nanofluid across all tested conditions.

7. Under heat source conditions, the ternary hybrid nanofluid demonstrated superior heat transfer performance, whereas the binary nanofluid performed better under heat sink conditions.

8. Enhancing the thermal relaxation parameter promoted heat transfer in both nanofluids, while the Maxwell parameter exerted a diminishing effect.

Potential future research may explore mass transfer dynamics and bioconvection phenomena within more complex geometries, such as cylindrical and conical domains, utilizing two-phase nanofluid models.

CHAPTER SEVEN

Non-Fourier–Fick Effects in Bioconvective Nanofluid Flow Over a Stretching Cylinder with Suction/Injection and Convective Conditions

Bioconvective nanofluid flows over cylindrical geometries have been extensively explored due to their relevance in industrial and biomedical applications. However, limited studies (e.g., Dhlamini et al. (2022); Mkhatshwa (2023)) have addressed the combined influences of microbial Brownian motion and chemical reactions-especially under activation energy, non-Fourier heat conduction, and non-Fick mass diffusion–collectively referred to here as non-Fourier–Fick's flux. These factors significantly affect heat and mass transfer in the system. For instance, Mkhatshwa (2024) highlighted the crucial role of motile microorganisms and reactive dynamics in the context of radiative Williamson nanofluid flow past a cylindrical surface.

This chapter uniquely examines MHD, radiative, and convective Carreau nanofluid flow over an inclined, stretchable cylinder incorporating non-Fourier-Fick's flux, and convective boundary conditions. The study has practical relevance for applications such as polymer extrusion, thermal management systems, oil recovery processes, bioengineering devices, and the development of advanced filtration systems. By offering deeper insights into nonlinear transport phenomena in complex fluids, the investigation supports the advancement of energy-efficient technologies across chemical, biomedical, and environmental sectors.

The novel aspects of this work are outlined as follows:

(i) It integrates convective heat and mass transfer effects within a porous medium described by the Darcy–Forchheimer model.

(ii) The flow configuration involves non-Fourier–Fick diffusion of a Carreau nanofluid along an inclined cylindrical surface.

(iii) The model includes nonlinear thermal radiation, mixed convection, Joule heating, porous dissipation, and surface suction/injection.

(iv) Chemical reactions and Brownian motion effects are incorporated in both nanoparticle and microorganism conservation equations.

7.1 Mathematical Model and Formulation

7.1.1 Flow Configuration and Assumptions

This analysis considers steady, incompressible, viscous, and radiatively reactive bioconvective flow of a Carreau nanofluid in the presence of a transverse magnetic field over a stretching cylindrical surface. The cylinder is slender, implying that its radius is comparable to the boundary layer thickness, and the flow is therefore treated as axisymmetric. This geometry necessitates inclusion of curvature effects, which influence both velocity and thermosolutal distributions, as well as surface transport rates. The cylinder is oriented at an angle Ω to the horizontal axis, and the porous medium is uniformly saturated with gyrotactic microorganisms. Nanoparticles are dispersed at low volume fractions ($< 1\%$) to ensure stability and avoid agglomeration. A dilute nanofluid suspension is assumed such that nanoparticle presence does not impact microorganism motility.

The model incorporates the effects of non-Fourier heat flux, non-Fickian mass diffusion, buoyancy forces, nonlinear radiation, Joule heating, porous medium resistance, and internal heat sources or sinks. Cylindrical coordinates (r, x) are adopted, with corresponding velocity components (u, v). The flow domain is defined for $r \geq R$. A uniform magnetic field B_0 is applied radially to influence fluid momentum. The porous cylinder surface maintains prescribed values for velocity (u_w), temperature (T_w), nanoparticle concentration (C_w), and microorganism density (N_w), while the far-field conditions are given by u_∞, T_∞, C_∞, and N_∞, respectively. The analysis includes the slip velocities between both the nanoparticles and base fluid, and microorganisms and base fluid, in line with the approach of Buongiorno (2006). A schematic of the flow configuration is illustrated in Figure 7.1.1.

7.1.2 Governing equations

The governing system comprises the mass, momentum, energy, nanoparticle concentration, and microorganism density equations, modeled in vectorial form as referenced in (Akbar et al. (2017); Saleem and Hussain (2023)):

a. Continuity equation:

The conservation of mass is expressed as:

$$\nabla . \boldsymbol{V} = 0, \tag{7.1.1}$$

where, ∇ is differential operator, and $\boldsymbol{V}$ is the velocity field vector.

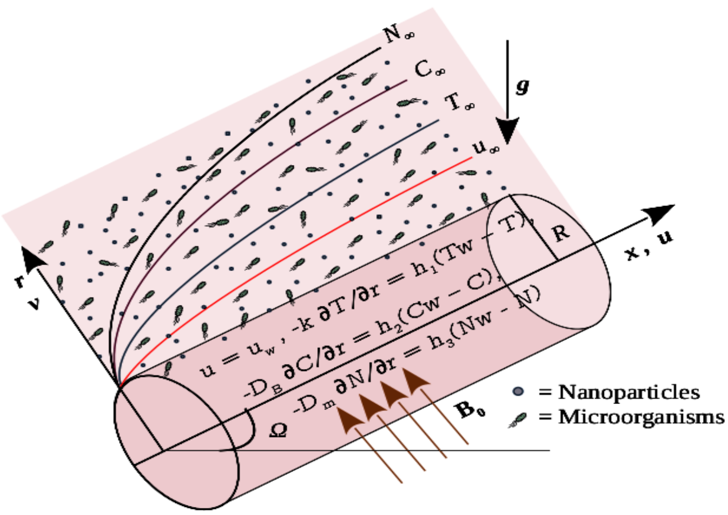

Figure 7.1.1: Schematic of the flow

b. Accounting for body forces, Lorentz force, and Darcy–Forchheimer porous resistance, the momentum balance is given by:

$$\rho_f\left[\frac{\partial \boldsymbol{V}}{\partial t}+\Big(\boldsymbol{V}.\nabla\Big)\boldsymbol{V}\right]=-\nabla P+\nabla.\boldsymbol{\tau}+\boldsymbol{J}_e\times\boldsymbol{B}-\left(\frac{\mu\xi}{k^\star}+\frac{c_F\rho_f\xi}{\sqrt{k^\star}}|\boldsymbol{V}|\right)\boldsymbol{V}-\rho_f\boldsymbol{f}_b, \tag{7.1.2}$$

where P denotes the pressure, $\boldsymbol{\tau}$ is the stress tensor, $\boldsymbol{J}_e=\sigma_0\Big(\boldsymbol{V}\times\boldsymbol{B}\Big)$ denotes the current density, and $\boldsymbol{f}_b$ is the buoyancy force.

c. Energy conservation equation:

Considering non-Fourier heat conduction via the Cattaneo–Christov model, Joule heating, thermophoresis, Brownian motion, and internal heat generation/absorption, the energy balance becomes:

$$(\rho c_p)_f\left[\frac{\partial T}{\partial t}+\Big(\boldsymbol{V}.\nabla\Big)T\right]=-\nabla.\boldsymbol{q}_h+(\rho c_p)_s\left[D_b\nabla C.\nabla T+\frac{D_T}{T_\infty}\nabla T.\nabla T\right]-\nabla.\boldsymbol{q}_r+\frac{\boldsymbol{J}_e^2}{\sigma_0}$$
$$+\Big(\frac{\mu\xi}{k^\star}+\frac{c_F\xi}{\sqrt{k^\star}}|\boldsymbol{V}|\Big)\boldsymbol{V}^2+Q_0^\star\Big(T-T_\infty\Big), \tag{7.1.3}$$

here, $\boldsymbol{q}_h$ is the heat flux satisfying,

$$\boldsymbol{q}_h+\lambda_2^\star\Big(\frac{\partial \boldsymbol{q}_h}{\partial t}+\boldsymbol{V}.\nabla\boldsymbol{q}_h-\boldsymbol{q}_h.\nabla\boldsymbol{V}+\Big(\nabla.\boldsymbol{V}\Big)\boldsymbol{q}_h\Big)=-k\nabla T, \tag{7.1.4}$$

$\boldsymbol{q}_r$ is radiation flux, $Q_0^\star$ is heat generation/absorption, k is thermal conductivity, D_b nanoparticles diffusion, and D_T is thermophoretic diffusion.

d. Nanoparticle conservation equation:

With non-Fickian diffusion and binary chemical reaction, the nanoparticle transport equation is formulated as:

$$\frac{\partial C}{\partial t}+\Big(\boldsymbol{V}.\nabla\Big)C=-\nabla.\boldsymbol{q}_c+\frac{D_T}{T_\infty}\nabla^2T+R_0^\star\Big(C-C_\infty\Big), \tag{7.1.5}$$

here, $\mathrm{R}_0^\star$ is the nanoparticles binary chemical reaction coefficient and $\boldsymbol{q}_c$ is the solute flux satisfying,

$$\boldsymbol{q}_c+\lambda_3^\star\Big(\frac{\partial \boldsymbol{q}_c}{\partial t}+\boldsymbol{V}.\nabla\boldsymbol{q}_c-\boldsymbol{q}_c.\nabla\boldsymbol{V}+\Big(\nabla.\boldsymbol{V}\Big)\boldsymbol{q}_c\Big)=-D_b\nabla C, \tag{7.1.6}$$

e. Microorganism concentration balance:

Considering microbial Brownian motion, swimming dynamics, and reaction effects, the conservation of microorganism concentration is modeled by: (Dhlamini et al. (2022)):

$$\frac{\partial N}{\partial t}=-\nabla.\boldsymbol{\Xi}_1, \tag{7.1.7}$$

where,

$$\boldsymbol{\Xi}_1=N\mathbf{V}+N\mathbf{W}_c\hat{\mathbf{p}}-D_m\nabla N+\frac{D_T}{T_\infty}\nabla^2T+R_1^\star\Big(N-N_\infty\Big), \tag{7.1.8}$$

is the total flux of microbes to fluid convection, self propelled swimming, and diffusion. N is the microorganism concentration, $\mathbf{W}_c\hat{\mathbf{p}}$ is the average relative swimming velocity, and $\mathrm{R}_1^\star$ is the microbes' binary chemical reaction coefficient.

7.1.3 Model description

The Cauchy stress tensor, $\boldsymbol{\tau}$ for Carreau model as presented in Eq. (4.1.35) is

$$\boldsymbol{\tau}=-p\mathbf{I}+\mu_0\left[1+\Big(\Gamma\gamma'\Big)^2\right]^{(n-1)/2}\mathbf{D}_1, \tag{7.1.9}$$

where, the shear rate $\gamma'=\sqrt{\frac{1}{2}\mathrm{tr}\Big(\mathbf{D}_1^2\Big)}$ and $\mathbf{D}_1=(\mathrm{grad}\mathbf{V})+(\mathrm{grad}\mathbf{V})^T$.

Taking into account the aforementioned assumptions and applying the boundary layer approximations to the governing equations (Eqs. (7.1.1) - (7.1.8)), the axisymmetric two dimensional steady and incompressible boundary layer equations are reformulated in cylindrical coordinates as follows (Nabwey et al. (2022), Farooq et al. (2021)):

$$\frac{\partial (ru)}{\partial x}+\frac{\partial (rv)}{\partial r}=0, \tag{7.1.10}$$

$$u\frac{\partial u}{\partial x}+v\frac{\partial u}{\partial r}=\nu\left[1+\Gamma^2\left(\frac{\partial u}{\partial r}\right)^2\right]^{\dfrac{n-1}{2}}\left(\frac{1}{r}\frac{\partial u}{\partial r}+\frac{\partial^2 u}{\partial r^2}\right)+\nu(n-1)\Gamma^2\frac{\partial^2 u}{\partial r^2}\left(\frac{\partial u}{\partial r}\right)^2$$
$$\left[1+\Gamma^2\left(\frac{\partial u}{\partial r}\right)^2\right]^{\dfrac{n-3}{2}}-\frac{\sigma_0 B_0^2}{\rho_f}u-\frac{\mu\xi}{\rho_f k^\star}u-\frac{c_F\xi}{\sqrt{k^\star}}u^2+\frac{g}{\rho_f}\Big[(1-C_\infty)\rho_f\beta_T(T-T_\infty)$$
$$-\beta_C(\rho_p-\rho_f)(C-C_\infty)-\beta_m(\rho_m-\rho_f)(N-N_\infty)\Big]\sin\Omega, \tag{7.1.11}$$
$$u\frac{\partial T}{\partial x}+v\frac{\partial T}{\partial r}+\lambda_2^\star\Bigg[u^2\frac{\partial^2 T}{\partial x^2}+v^2\frac{\partial^2 T}{\partial r^2}+2uv\frac{\partial^2 T}{\partial x\partial r}+u\frac{\partial u}{\partial x}\frac{\partial T}{\partial x}+u\frac{\partial v}{\partial x}\frac{\partial T}{\partial r}+v\frac{\partial u}{\partial r}\frac{\partial T}{\partial x}+$$
$$v\frac{\partial v}{\partial r}\frac{\partial T}{\partial r}\Bigg]=\frac{k}{\rho c_p}\left[\frac{1}{r}\frac{\partial T}{\partial r}+\frac{\partial^2 T}{\partial r^2}\right]-\frac{1}{\rho c_p}\frac{\partial q_r}{\partial r}+\frac{\sigma_0 B_0^2}{\rho c_p}u^2+\frac{\mu\xi}{\rho c_p k^\star}u^2+\frac{c_F\xi}{\rho c_p\sqrt{k^\star}}u^3+$$
$$\tau\left[D_b\frac{\partial C}{\partial r}\frac{\partial T}{\partial r}+D_m\frac{\partial N}{\partial r}\frac{\partial T}{\partial r}+\frac{D_T}{T_\infty}\left(\frac{\partial T}{\partial r}\right)^2\right]+\frac{Q_a}{\rho C_p}(T-T_\infty), \tag{7.1.12}$$

$$u\frac{\partial C}{\partial x}+v\frac{\partial C}{\partial r}+\lambda_3^\star\left[u^2\frac{\partial^2 C}{\partial x^2}+v^2\frac{\partial^2 C}{\partial r^2}+2uv\frac{\partial^2 C}{\partial x\partial r}+u\frac{\partial u}{\partial x}\frac{\partial C}{\partial x}+u\frac{\partial v}{\partial x}\frac{\partial C}{\partial r}+v\frac{\partial u}{\partial r}\frac{\partial C}{\partial x}+v\frac{\partial v}{\partial r}\frac{\partial C}{\partial r}\right]$$
$$=D_b\left[\frac{1}{r}\frac{\partial C}{\partial r}+\frac{\partial^2 C}{\partial r^2}\right]+\frac{D_T}{T_\infty}\left[\frac{1}{r}\frac{\partial T}{\partial r}+\frac{\partial^2 T}{\partial r^2}\right]-k_p^\star(C-C_\infty)\left(\frac{T}{T_\infty}\right)^{tt}e^{\left(\dfrac{-E_a}{\kappa T}\right)}, \tag{7.1.13}$$

$$u\frac{\partial N}{\partial x}+v\frac{\partial N}{\partial r}+\frac{bW_c}{(C_w-C_\infty)}\frac{1}{r}\frac{\partial}{\partial r}\left(rN\frac{\partial C}{\partial r}\right)=D_m\left[\frac{1}{r}\frac{\partial N}{\partial r}+\frac{\partial^2 N}{\partial r^2}\right]+\frac{D_T}{T_\infty}\Bigg[\frac{1}{r}\frac{\partial T}{\partial r}+$$
$$\frac{\partial^2 T}{\partial r^2}\Bigg]-k_b^\star(N-N_\infty)\left(\frac{T}{T_\infty}\right)^{tt}e^{\left(\dfrac{-E_a}{\kappa T}\right)}, \tag{7.1.14}$$

The system of equations is closed with the following boundary conditions:

$$\begin{aligned}
&u=U_w=u_0\frac{x}{l},\quad v=v_w,\quad -k_f\frac{\partial T}{\partial r}=h_t(T_w-T),\quad -D_b\frac{\partial C}{\partial r}=h_m(C_w-C),\\
&-D_m\frac{\partial N}{\partial r}=h_b(N_w-N)\quad \text{at}\quad r=R,\\
&u\to 0,\quad T\to T_\infty,\quad C\to C_\infty,\quad N\to N_\infty\quad \text{as}\quad r\to\infty,
\end{aligned} \tag{7.1.15}$$

where $\tau=\frac{(\rho c_p)_p}{(\rho c_p)_f}$ represents the ratio of the effective heat capacity of nanoparticles to that of the base fluid. Here, $\lambda_2^\star$ and $\lambda_3^\star$ denote the thermal and solutal relaxation times, respectively, while $k_p^\star$ and $k_b^\star$ are the chemical reaction rate constants for nanoparticles and microorganisms. All remaining symbols are defined in the list of acronyms and abbreviations.

In MHD thermal transport, radiation significantly influences energy transfer, particularly in high-temperature-gradient systems such as solar energy devices, nuclear reactors, biofuel generators, and space propulsion units Irfan et al. (2019b). Under such conditions, employing a linearized radiation model-typically derived from a Taylor series expansion-may lead to substantial inaccuracies. Consequently, for precise estimation and system reliability, the nonlinear formulation of radiative flux is preferred.

Assuming an optically thick medium, the Rosseland diffusion approximation for radiative heat flux Ali et al. (1984) is applied as:

$$q_r = -\frac{4\sigma^\star}{3k_e}\frac{\partial T^4}{\partial r}, \tag{7.1.16}$$

where $\sigma^\star$ is the Stefan-Boltzmann constant and k_e denotes the mean absorption coefficient. To reflect moderate temperature differences between the cylinder surface and ambient fluid, the nonlinear radiative heat flux is reformulated as:

$$q_r = -\frac{16\sigma^\star}{3k_e}T^3\frac{\partial T}{\partial r}. \tag{7.1.17}$$

7.1.4 Nondimensionalization and Similarity Transformation

To reduce the governing partial differential equations to a system of ODEs, we introduce the similarity variable η along with the stream function defined as $\psi = \sqrt{\frac{\nu U_0}{l}}\, xRf(\eta)$. This transformation inherently satisfies the continuity equation given in Eq. (7.1.10).

The momentum, energy, concentration, and microorganism transport equations-Eqs. (7.1.11)-(7.1.14)-together with the boundary conditions in Eq. (7.1.15), are rendered dimensionless using appropriate similarity variables. This approach transforms the coupled PDE system into a more tractable set of ODEs, following methodologies described in Farooq et al. (2021) and Hayat et al. (2016a).

$$\begin{aligned} &\eta = \frac{r^2 - R^2}{2R}\sqrt{\frac{\mathrm{U}_0}{l\nu}},\ u = \frac{1}{r}\frac{\partial\psi}{\partial r},\ v = -\frac{1}{r}\frac{\partial\psi}{\partial x},\ T - T_\infty = \theta(\eta)\Big(T_w - T_\infty\Big),\\ &C - C_\infty = \phi(\eta)\Big(C_w - C_\infty\Big),\ N - N_\infty = \chi(\eta)\Big(N_w - N_\infty\Big). \end{aligned} \tag{7.1.18}$$

In light of Eqs. (7.1.9), (7.1.17), and (7.1.18), the governing equations, Eqs. (7.1.11)-(7.1.14) and their corresponding boundary conditions, Eq. (7.1.15) are reduced to the following non-dimensional forms.

$$\Big(1+2\alpha_c\eta\Big)\Big[1+nWe^2f''^2\Big]\Big[1+We^2f''^2\Big]^{\dfrac{n-3}{2}}f'''+\Big[1+We^2f''^2\Big]^{\dfrac{n-3}{2}}\Big[2\alpha_c f''+(n+1)\times$$
$$We^2\alpha_c f''^3\Big]-f'^2+ff''-M^2f'-\lambda f'-\alpha f'^2+\lambda_m\Big(\theta-Nr\phi-Rb\chi\Big)\sin\Omega=0, \quad (7.1.19)$$

$$\Big(1+2\alpha_c\eta\Big)\Big[\theta''+\frac{4}{3}R_d\Big(\Big(1+(\theta_w-1)\theta\Big)^3\theta'\Big)'\Big]+\alpha_c\theta'+Prf\theta'-Pr\lambda_2\Big[f^2\theta''+ff'\theta'\Big]+$$
$$\frac{\alpha_c}{1+2\alpha_c\eta}Pr\lambda_2 f^2\theta'+Pr(1+2\alpha_c\eta)\Big[N_b\phi'\theta'+N_m\chi'\theta'+Nt\theta'^2\Big]+PrEc\Big[M^2f'^2+\lambda f'^2$$
$$+\alpha f'^3\Big]+PrQ_0\theta=0, \quad (7.1.20)$$

$$(1+2\alpha_c\eta)\phi''+\alpha_c\phi'+Sc_pf\phi'-\frac{Sc_p\lambda_3}{(1+2\alpha_c\eta)}\Big[(1+2\alpha_c\eta)f^2\phi''+(1+2\alpha_c\eta)ff'\phi'-\alpha_c f^2\phi'\Big]+$$
$$\frac{Nt}{Nb}\Big(\alpha_c\theta'+(1+2\alpha_c\eta)\theta''\Big)-Sc_p\gamma_{\mathrm{c}}\Big(1+(\theta_{\mathrm{w}}-1)\theta\Big)^{\mathrm{tt}}\mathrm{e}^{\Big(\dfrac{-\mathrm{E}}{1+(\theta_{\mathrm{w}}-1)\theta}\Big)}\phi=0, \quad (7.1.21)$$

$$(1+2\alpha_c\eta)\chi''+\alpha_c\chi'+Sc_bf\chi'-Pe\alpha_c(w+\chi)\phi'-Pe(1+2\alpha_c\eta)\chi'\phi'-Pe(1+2\alpha_c\eta)\times$$
$$(w+\chi)\phi''+\frac{Nt}{N_m}\Big(\alpha_c\theta'+(1+2\alpha_c\eta)\theta''\Big)-Sc_b\gamma_b\Big(1+(\theta_w-1)\theta\Big)^{tt}e^{\Big(\dfrac{-E}{1+(\theta_w-1)\theta}\Big)}\chi=0.$$
$$(7.1.22)$$

The corresponding boundary conditions are:

$$f(\eta)=f_w,\ f'(\eta)=1,\ \theta'(\eta)=-\gamma_1\Big(1-\theta(\eta)\Big),\ \phi'(\eta)=-\gamma_2\Big(1-\phi(\eta)\Big),\chi'(\eta)=-\gamma_3\Big(1-\chi(\eta)\Big),$$
$$\text{at } \eta=0,\ \mathrm{f}'(\eta)\longrightarrow 0,\ \theta\longrightarrow 0,\ \phi\longrightarrow 0,\ \chi\longrightarrow 0,\ \text{as},\ \eta\longrightarrow\infty, \quad (7.1.23)$$

The dimensionless quantities introduced in the model are defined as follows: the curvature number $\alpha_c=\frac{1}{R}\sqrt{\frac{\nu l}{U_0}}$, and the suction/injection parameter $f_w=-\frac{r}{R}\sqrt{\frac{l}{\nu U_0}}v_w$. The local porosity and inertia parameters are given by $\lambda=\frac{\nu\xi l}{k^\star U_0}$ and $\alpha=\frac{c_F\xi x}{\sqrt{k^\star}}$, respectively. The mixed convection parameter is $\lambda_m=\frac{g\beta_T(1-C_\infty)(T_w-T_\infty)x}{u_w^2}$.

The nanoparticle and microbial buoyancy effects are captured by the parameters $Nr=\frac{\beta_C(\rho_p-\rho_f)(C_w-C_\infty)}{\rho_f\beta_T(1-C_\infty)(T_w-T_\infty)}$ and $Rb=\frac{\beta_m(\rho_m-\rho_f)(N_w-N_\infty)}{\rho_f\beta_T(1-C_\infty)(T_w-T_\infty)}$, respectively. The temperature ratio is expressed as $\theta_w=\frac{T_w}{T_\infty}$, while the relaxation times for thermal and solutal diffusion are given by $\lambda_2=\lambda_2^\star\frac{U_0}{l}$ and $\lambda_3=\lambda_3^\star\frac{U_0}{l}$.

The heat source/sink parameter is denoted as $Q_0 = Q_a \frac{l}{U_0}$, and the Schmidt numbers for nanoparticles and microbes are $Sc_p = \frac{\nu}{D_b}$ and $Sc_b = \frac{\nu}{D_m}$. The nanoparticle and microbial reaction rates are $\gamma_c = k_p^\star \frac{l}{U_0}$ and $\gamma_b = k_b^\star \frac{l}{U_0}$, respectively. Additional dimensionless parameters include the microbe density difference $w = \frac{N_\infty}{N_m - N_\infty}$, the microbial Peclet number $p = \frac{bW_c}{D_m}$, and the Biot numbers for thermal, solutal, and microbial transfer:

$$\gamma_1 = \frac{Rh_t}{rk}\sqrt{\frac{\nu l}{U_0}}, \quad \gamma_2 = \frac{Rh_m}{rD_b}\sqrt{\frac{\nu l}{U_0}}, \quad \gamma_3 = \frac{Rh_b}{rD_m}\sqrt{\frac{\nu l}{U_0}}.$$

The magnetic field influence is characterized by $M = \sqrt{\frac{\sigma_0 B_0^2}{\rho_f}\frac{l}{U_0}}$, and the local Weissenberg number is defined as $We^2 = \Gamma^2 \frac{U_0^3 x^2}{l^3 \nu}\left(\frac{r}{R}\right)^2$. Other important dimensionless numbers include the radiation parameter $R_d = \frac{4\sigma_0 T_\infty^3}{kk_e}$, Brownian motion parameter $N_b = \frac{D_b(C_w - C_\infty)}{\nu}\tau$, thermophoretic parameter $N_t = \frac{D_T(T_w - T_\infty)}{T_\infty \nu}\tau$, and microbial motility parameter $N_m = \frac{D_m(N_w - N_\infty)}{\nu}\tau$. The viscous dissipation is quantified by the Eckert number $Ec = \frac{u_w^2}{C_p(T_w - T_\infty)}$, the Prandtl number is $Pr = \frac{\nu \rho_f C_p}{k}$, and the Arrhenius number is $E = \frac{E_a}{\kappa T_\infty}$.

7.1.5 Engineering Quantities of Interest

For engineering relevance, the following non–dimensional quantities are evaluated:

1. Local skin friction coefficient, indicating the shear stress on the surface.
2. Nusselt number, representing the relative strength of convective to conductive heat transfer.
3. Sherwood number, reflecting the convective versus diffusive transport of nanoparticles.
4. Microorganism mass transfer rate, signifying the balance of convective and diffusive transport of motile microbes.

$$C_f = \frac{\tau_{wr}}{\frac{1}{2}\rho_f u_w^2},\ \tau_{wr} = \mu_f \frac{\partial u}{\partial r}\left[1+\Gamma_1^2\left(\frac{\partial u}{\partial r}\right)^2\right]^{\frac{n-1}{2}},\ Sh_x = \frac{xq_c}{D_b(C_w - C_\infty)},\ q_c = -D_b \frac{\partial C}{\partial r}\bigg|_{r=R},$$
$$Nu_x = \frac{-x}{(T_w - T_\infty)}\left(1+\frac{16\sigma^*}{3kk_e}T^3\right)\left(\frac{\partial T}{\partial r}\right)_{r=R},\ Nm_x = \frac{xq_m}{D_m(N_w - N_\infty)},\ q_m = -D_m \frac{\partial N}{\partial r}\bigg|_{r=R}. \tag{7.1.24}$$

By applying the similarity transformations defined in Eqs. (7.1.18), the dimensionless forms of the surface shear stress ($C_f^\star$), local Sherwood number ($Sh_x^\star$), local Nusselt number ($Nu_x^\star$), and microorganism density transfer number ($Nm_x^\star$) are expressed as:

$$C_f^\star = -Re^{1/2}C_f = -2f''(0)\left(1+We^2 f''^2(0)\right)^{\frac{n-1}{2}}, \quad Sh_x^\star = Re^{-1/2}Sh_x = -\phi'(0),$$
$$Nu_x^\star = Re^{-1/2}Nu_x = -\left(1+4R_d\theta_w^3\right)\theta'(0), \quad Nm_x^\star = Re^{-1/2}Nm_x = -\chi'(0). \tag{7.1.25}$$

7.2 Numerical Methodology

The transformed set of highly nonlinear and coupled ODEs (Eqs. (7.1.19)-(7.1.22)) subject to boundary conditions (Eq. (7.1.23)) is analytically intractable. To resolve this, a robust and precise numerical technique known as SLLM is employed.

The implementation of SLLM begins by reordering the governing equations such that the equation with the lowest dependency on other variables appears first, followed by equations with increasing dependency. In each step, nonlinear terms and their derivatives are linearized by considering other functions and their derivatives as known from the preceding iteration. The solution process is iteratively executed using the Gauss-Seidel method until the solution converges within a prescribed tolerance.

To initiate this scheme, Eq. (7.1.19) is reduced in order by introducing the substitution $f'(\eta) = h(\eta)$. Assuming the difference between two successive approximations, $(r+1)$ and r, is sufficiently small, the iterative procedure is applied to derive the linearized and decoupled system of equations suitable for spectral solution.

$$\Big[s_1 - s_9\lambda_3 f_r^2\Big]\phi''_{r+1} + \Big[s_3 + s_9 fr - s_9\lambda_3 f_r h_r + \frac{s_9 s_3}{s_1}\lambda_3 f_r^2\Big]\phi'_{r+1} - \Bigg[s_9 s_{10}\Big(1 + x_w\theta_r\Big)^n \times$$

$$exp\Big(\frac{-E}{1 + x_w\theta_r}\Big)\Bigg]\phi_{r+1} = -\frac{Nt}{Nb}\Big(s_3\theta'_r + s_1\theta''_r\Big), \qquad (7.2.1)$$

$$\Bigg[s_1\Big(1 + s_8\Big(1 + x_w\theta_r\Big)^3\Big) - Pr\lambda_2 f_r^2\Bigg]\theta''_{r+1} + \Bigg[s_3 + 6s_1 s_8 x_w\Big(1 + x_w\theta_r\Big)^2\theta'_r + Prf_r -$$

$$Pr\lambda_2 f_r h_r + \frac{s_3}{s_1}Pr\lambda_2 f_r^2 + s_1 PrNb\phi'_{r+1} + s_1 PrNm\chi'_r + 2s_1 PrNt\theta'_r\Bigg]\theta'_{r+1} + \Bigg[PrQ_0 +$$

$$3s_1 s_8 x_w\Big(1 + x_w\theta_r\Big)^2\theta''_r 6s_1 s_8 x_w^2\Big(1 + x_w\theta_r\Big){\theta'}_r^2\Bigg]\theta_{r+1} = 3s_1 s_8 x_w\Big(1 + x_w\theta_r\Big)^2\theta_r\theta''_r +$$

$$6s_1 s_8 x_w^2\Big(1 + x_w\theta_r\Big){\theta'_r}^2\theta_r + 3s_1 s_8 x_w\Big(1 + x_w\theta_r\Big)^2{\theta'}_r^2 + s_1 PrNt{\theta'}_r^2 -$$

$$PrEc\Big(\Big(s_4 + s_5\Big)h_r^2 + s_6 h_r^3\Big), \qquad (7.2.2)$$

$$[s_1]\chi''_{r+1} + \Big[s_3 - Pes_1\phi'_{r+1} + s_{11}f_r\Big]\chi'_{r+1} - \Bigg[Pes_3\phi'_{r+1} - Pes_1\phi''_{r+1} - s_{11}t_{12}\Big(1 + x_w\theta_{r+1}\Big)^t$$

$$exp\Big(\frac{-E}{1 + x_w\theta_{r+1}}\Big)\Bigg]\chi_{r+1} = Pes_3 w\phi'_{r+1} + Pews_1\phi''_{r+1} - \frac{Nt}{Nm}\Big(s_3\theta'_{r+1} + s_1\theta''_{r+1}\Big), \quad (7.2.3)$$

$$\Bigg[s_1\Big(1 + ns_2{h'}_r^2\Big)\Big(1 + s_2{h'_r}^2\Big)^{\frac{n-3}{2}}\Bigg]h''_{r+1} + \Bigg[s_1 s_2(n-3)\Big(1 + s_2{h'_r}^2\Big)^{\frac{n-5}{2}}h'_r h''_r + 2ns_1 \times$$

$$s_2 h'_r h''_r\Big(1 + s_2{h'}_r^2\Big)^{\frac{n-3}{2}} + ns_1 s_2^2(n-3){h'}_r^3 h''_r\Big(1 + s_2{h'}_r^2\Big)^{\frac{n-5}{2}} + s_2(n-3)h'_r \times$$

$$\Big(1 + s_2{h'}_r^2\Big)^{\frac{n-5}{2}}\Big(2s_3 h'_r + (n+1)s_2 s_3{h'}_r^3\Big) + \Big(2s_3 + 3(n+1)s_2 s_3{h'}_2^2\Big)\Big(1 + s_2{h'}_2^2\Big)^{\frac{n-3}{2}}$$

$$+ f_r\Bigg]h'_{r+1} - \Big[s_4 + s_5 + 2h_r + 2s_6 h_r\Big]h_{r+1} = s_1 s_2(n-3)\Big(1 + s_2{h'}_r^2\Big)^{\frac{n-5}{2}}{h'}_r^2 h''_r +$$

$$2ns_1 s_2{h'}_r^2 h''_r\Big(1 + s_2{h'}_r^2\Big)^{\frac{n-5}{2}} + s_2{h'}_r^2(n-3)\Big(1 + s_2{h'}_r^2\Big)^{\frac{n-5}{2}}\Big(2s_3 h'_r + (n+1)s_2 s_3{h'}_r^3\Big)$$

$$+ 2(n+1)s_2 s_3{h'}_r^3\Big(1 + s_2{h'}_r^2\Big)^{\frac{n-3}{2}} - h_r^2 - s_6 h_r^2 - s_7\lambda_m\Big(\theta_{r+1} - Nr\phi_{r+1} - Rb\chi_{r+1}\Big),$$

$$(7.2.4)$$

$$f'_{r+1} = h_{r+1}. \qquad (7.2.5)$$

Correspondingly linearized boundary conditions are:

$$\phi'_{r+1}(\eta) = -\gamma_2\Big(1-\phi_{r+1}(\eta)\Big),\ \theta'_{r+1}(\eta) = -\gamma_1\Big(1-\theta_{r+1}(\eta)\Big),\ \chi'_{r+1}(\eta) = -\gamma_3\Big(1-\chi_{r+1}(\eta)\Big),$$
$$h_{r+1}(\eta) = 1,\ f_{r+1}(\eta) = f_w,\ \text{ at } \eta = 0,$$
$$\phi_{r+1}(\eta) \longrightarrow 0,\ \theta_{r+1}(\eta) \longrightarrow 0,\ \chi_{r+1}(\eta) \longrightarrow 0,\ h_{r+1} \longrightarrow 0,\ \text{as } \eta \longrightarrow 0, \tag{7.2.6}$$

here, $s_1 = 1+2\alpha_c\eta$, $s_2 = we^2$, $s_3 = \alpha_c$, $s_4 = M^2$, $s_5 = \lambda$, $s_6 = \alpha$, $s_7 = sin\Omega$, $s_8 = \frac{4}{3}Rd$, $s_9 = Sc_p$, $s_{10} = \gamma_c$, $s_{11} = Sc_b$, $s_{12} = \gamma_b$.

The linearized system of equations (Eqs. (7.2.1)-(7.2.5)) along with the associated boundary conditions (Eq. (7.2.6)) is numerically solved using the Chebyshev pseudo-spectral technique, as outlined in Trefethen (2000). The computational domain is discretized using Gaussâ€“Lobatto collocation nodes defined by $x_i = \cos\left(\frac{\pi i}{N}\right)$ for $i = 1,2,\ldots,N$, where N denotes the number of collocation points.

To implement the spectral approach, the physical domain $[0,\eta_\infty]$ is mapped onto the standard interval $[-1,1]$ using the coordinate transformation:

$$\eta = \frac{1}{2}(x+1)\eta_\infty,$$

where η_∞ is chosen large enough to approximate the asymptotic boundary conditions accurately.

At the collocation points,

- the unknown functions, ϕ_{r+1}, θ_{r+1}, χ_{r+1}, h_{r+1}, and f_{r+1} at the $(r+1)^{th}$ iteration level are approximated in the form of series solution using,

$$\begin{cases} \phi_{r+1}(\eta) = \sum_{k=0}^{N} \phi_{r+1}(\eta_k)L_k(\eta_j), \\ \theta_{r+1}(\eta) = \sum_{k=0}^{N} \theta_{r+1}(\eta_k)L_k(\eta_j), \\ \chi_{r+1}(\eta) = \sum_{k=0}^{N} \chi_{r+1}(\eta_k)L_k(\eta_j), \\ h_{r+1}(\eta) = \sum_{k=0}^{N} h_{r+1}(\eta_k)L_k(\eta_j), \\ f_{r+1}(\eta) = \sum_{k=0}^{N} f_{r+1}(\eta_k)L_k(\eta_j). \end{cases} \tag{7.2.7}$$

- The n^{th} order derivatives of the unknown functions are estimated using the Chebyshev differentiation matrix D. To account for the scaling between the computational and physical domains, this matrix is adjusted as $\mathbf{D} = \dfrac{2D}{\eta_\infty}$.

$$\begin{cases} \dfrac{d^n\phi_{r+1}}{d\eta^n}|_{\eta=\eta_j} = \sum_{k=0}^{N} D_{jk}^n \phi_{r+1}(\eta_k) = \mathbf{D}^n \mathbf{\Phi}_{r+1}, \\ \dfrac{d^n\theta_{r+1}}{d\eta^n}|_{\eta=\eta_j} = \sum_{k=0}^{N} D_{jk}^n \theta_{r+1}(\eta_k) = \mathbf{D}^n \mathbf{\Theta}_{r+1}, \\ \dfrac{d^n\chi_{r+1}}{d\eta^n}|_{\eta=\eta_j} = \sum_{k=0}^{N} D_{jk}^n \chi_{r+1}(\eta_k) = \mathbf{D}^n \mathbf{X}_{r+1}, \\ \dfrac{d^n h_{r+1}}{d\eta^n}|_{\eta=\eta_j} = \sum_{k=0}^{N} D_{jk}^n h_{r+1}(\eta_k) = \mathbf{D}^n \mathbf{H}_{r+1}, \\ \dfrac{d^n f_{r+1}}{d\eta^n}|_{\eta=\eta_j} = \sum_{k=0}^{N} D_{jk}^n f_{r+1}(\eta_k) = \mathbf{D}^n \mathbf{F}_{r+1}, \end{cases} \tag{7.2.8}$$

where

$$L_k(x) = \prod_{k=0, k\neq i}^{N_x} \left(\frac{x - x_k}{x_i - x_k} \right), \tag{7.2.9}$$

is the Lagrange's polynomial, $j = 0, 1, 2, \ldots, N$, $\mathbf{\Phi}_{r+1} = \Big[\phi_{r+1}(\eta_0), \phi_{r+1}(\eta_1), \ldots, \phi_{r+1}(\eta_N)\Big]^T$, $\mathbf{\Theta}_{r+1} = \Big[\theta_{r+1}(\eta_0), \theta_{r+1}(\eta_1), \ldots, \theta_{r+1}(\eta_N)\Big]^T$, $\mathbf{X}_{r+1} = \Big[\chi_{r+1}(\eta_0), \chi_{r+1}(\eta_1), \ldots, \chi_{r+1}(\eta_N)\Big]^T$, $\mathbf{H}_{r+1} = \Big[h_{r+1}(\eta_0), h_{r+1}(\eta_1), \ldots, h_{r+1}(\eta_N)\Big]^T$, $\mathbf{F}_{r+1} = \Big[f_{r+1}(\eta_0), f_{r+1}(\eta_1), \ldots, f_{r+1}(\eta_N)\Big]^T$.

In view of Eqs. (7.2.7) and (7.2.8), Eqs. (7.2.1) - (7.2.5), together with the boundary condition Eq. (7.2.6), can be formulated into:

$$\begin{aligned} &\mathbf{A}_1\mathbf{\Phi}_{r+1} = \mathbf{B}_1, \quad \mathbf{\Phi}'_{r+1}(x_N) = -\gamma_2\Big(1 - \mathbf{\Phi}_{r+1}(x_N)\Big), \quad \mathbf{\Phi}_{r+1}(x_0) = 0, \\ &\mathbf{A}_2\mathbf{\Theta}_{r+1} = \mathbf{B}_2, \quad \mathbf{\Theta}'_{r+1}(x_N) = -\gamma_1\Big(1 - \mathbf{\Theta}_{r+1}(x_N)\Big), \quad \mathbf{\Theta}_{r+1}(x_0) = 0, \\ &\mathbf{A}_3\mathbf{X}_{r+1} = \mathbf{B}_3, \quad \mathbf{X}'_{r+1}(x_N) = -\gamma_3\Big(1 - \mathbf{X}_{r+1}(x_N)\Big), \quad \mathbf{X}_{r+1}(x_0) = 0, \\ &\mathbf{A}_4\mathbf{H}_{r+1} = \mathbf{B}_4, \quad \mathbf{H}_{r+1}(x_N) = 1, \quad \mathbf{H}_{r+1}(x_0) = 0, \\ &\mathbf{F}'_{r+1} = \mathbf{H}_{r+1}, \quad \mathbf{F}_{r+1}(x_0) = f_w, \end{aligned} \tag{7.2.10}$$

where,

$$\begin{aligned} \mathbf{A}_1 =& diag\Big(s_1 - s_9\lambda_3 f_r^2\Big)\mathbf{D}^2 + diag\Big(s_3 + s_9 fr - s_9\lambda_3 f_r h_r + \frac{s_9 s_3}{s_1}\lambda_3 f_r^2\Big)\mathbf{D} - diag\Big(s_9 \times \\ & s_{10}\Big(1 + x_w\theta_r\Big)^n exp\Big(\frac{-E}{1 + x_w\theta_r}\Big)\Big)\mathbf{I}, \ \mathbf{B}_1 = -\frac{Nt}{Nb}\Big(s_3\theta'_r + s_1\theta''_r\Big), \end{aligned}$$

$$\begin{aligned}
\mathbf{A}_2 =& diag\Bigg(s_1\Big(1+s_8\big(1+x_w\theta_r\big)^3\Big)-Pr\lambda_2 f_r^2\Bigg)\mathbf{D}^2+diag\Big(s_3+6s_1s_8x_w\Big(1+x_w\theta_r\Big)^2\theta_r'+\\
& Prf_r-Pr\lambda_2 f_r h_r+\frac{s_3}{s_1}Pr\lambda_2 f_r^2+s_1PrNb\phi_{r+1}'+s_1PrNm\chi_r'+2s_1PrNt\theta_r'\Big)\mathbf{D}+\\
& diag\Big(PrQ_0+3s_1s_8x_w\Big(1+x_w\theta_r\Big)^2\theta_r''6s_1s_8x_w^2\Big(1+x_w\theta_r\Big)\theta'^2_r\Big)\times\mathbf{I},\quad \mathbf{B}_2=3s_1s_8x_w\times\\
& \Big(1+x_w\theta_r\Big)^2\theta_r\theta_r''+6s_1s_8x_w^2\Big(1+x_w\theta_r\Big)\theta_r'^2\theta_r+3s_1s_8x_w\Big(1+x_w\theta_r\Big)^2\theta'^2_r+s_1PrNt\theta'^2_r\\
& -PrEc\Big(\Big(s_4+s_5\Big)h_r^2+s_6h_r^3\Big),\\
\mathbf{A}_3 =& diag(s_1)\mathbf{D}^2+diag\Big(s_3-Pes_1\phi_{r+1}'+s_{11}f_r\Big)\mathbf{D}-diag\Big(Pes_3\phi_{r+1}'-Pes_1\phi_{r+1}''-\\
& s_{11}t_{12}\Big(1+x_w\theta_{r+1}\Big)^t exp\Big(\frac{-E}{1+x_w\theta_{r+1}}\Big)\Big),\\
\mathbf{B}_3 =& Pes_3w\phi_{r+1}'+Pews_1\phi_{r+1}''-\frac{Nt}{Nm}\Big(s_3\theta_{r+1}'+s_1\theta_{r+1}''\Big),
\end{aligned}$$

$$\begin{aligned}
\mathbf{A}_4 =& diag\Big(s_1\Big(1+ns_2h'^2_r\Big)\Big(1+s_2h'^2_r\Big)^{\frac{n-3}{2}}\Big)\mathbf{D}^2+diag\Big(s_1s_2(n-3)\Big(1+s_2h'^2_r\Big)^{\frac{n-5}{2}}\times\\
& h_r'h_r''+2ns_1s_2h_r'h_r''\Big(1+s_2h'^2_r\Big)^{\frac{n-3}{2}}+ns_1s_2^2(n-3)h'^3_rh_r''\Big(1+s_2h'^2_r\Big)^{\frac{n-5}{2}}+s_2\times\\
& (n-3)h_r'\Big(1+s_2h'^2_r\Big)^{\frac{n-5}{2}}\Big(2s_3h_r'+(n+1)s_2s_3h'^3_r\Big)+\Big(2s_3+3(n+1)s_2s_3h'^2_2\Big)\times\\
& \Big(1+s_2h'^2_2\Big)^{\frac{n-3}{2}}+f_r\Big)\mathbf{D}-diag\Big(s_4+s_5+2h_r+2s_6h_r\Big)\times\mathbf{I},\\
\mathbf{B}_4 =& s_1s_2(n-3)\Big(1+s_2h'^2_r\Big)^{\frac{n-5}{2}}h'^2_rh_r''+2ns_1s_2h'^2_rh_r''\Big(1+s_2h'^2_r\Big)^{\frac{n-5}{2}}+s_2h'^2_r\times\\
& (n-3)\Big(1+s_2h'^2_r\Big)^{\frac{n-5}{2}}\Big(2s_3h_r'+(n+1)s_2s_3h'^3_r\Big)+2(n+1)s_2s_3h'^3_r\Big(1+s_2h'^2_r\Big)^{\frac{n-3}{2}}\\
& -h_r^2-s_6h_r^2-s_7\lambda_m\Big(\theta_{r+1}-Nr\phi_{r+1}-Rb\chi_{r+1}\Big),\\
\mathbf{A}_5 =& \mathbf{D},\ \mathbf{B}_5=h_{r+1}.
\end{aligned}\tag{7.2.11}$$

To initialize the SLLM algorithm for Eq. (7.2.10), an initial guess conforming to the boundary conditions is essential. The suggested guess below meets this requirement effectively.

$$f_0=f_0w+1-e^{-\eta},\ \theta_0=\frac{\gamma_1}{1+\gamma_1}e^{-\eta},\phi_0=\frac{\gamma_2}{1+\gamma_2}e^{-\eta},\chi_0=\frac{\gamma_3}{1+\gamma_3}e^{-\eta}.\tag{7.2.12}$$

7.2.1 Convergence and Stability Analysis of SLLM

To assess the convergence and stability of the SLLM, the infinity norm of the residual is defined as:

$$Er = \max\left(\|f_{r+1}-f_r\|_\infty,\ \|\theta_{r+1}-\theta_r\|_\infty,\ \|\phi_{r+1}-\phi_r\|_\infty,\ \|\chi_{r+1}-\chi_r\|_\infty\right), \qquad (7.2.13)$$

which tracks the maximum difference between successive iterations across all dependent variables.

Figure 7.2.1 illustrates the error norm versus iteration count for both injection ($f_w = -0.5$) and suction ($f_w = 0.5$) cases, using 80 collocation points and a convergence tolerance of $\epsilon = 10^{-9}$. A nearly linear decline in residuals is observed for all variables. The injection case achieves convergence within 14 iterations, while the suction case requires 17 iterations to meet the prescribed tolerance.

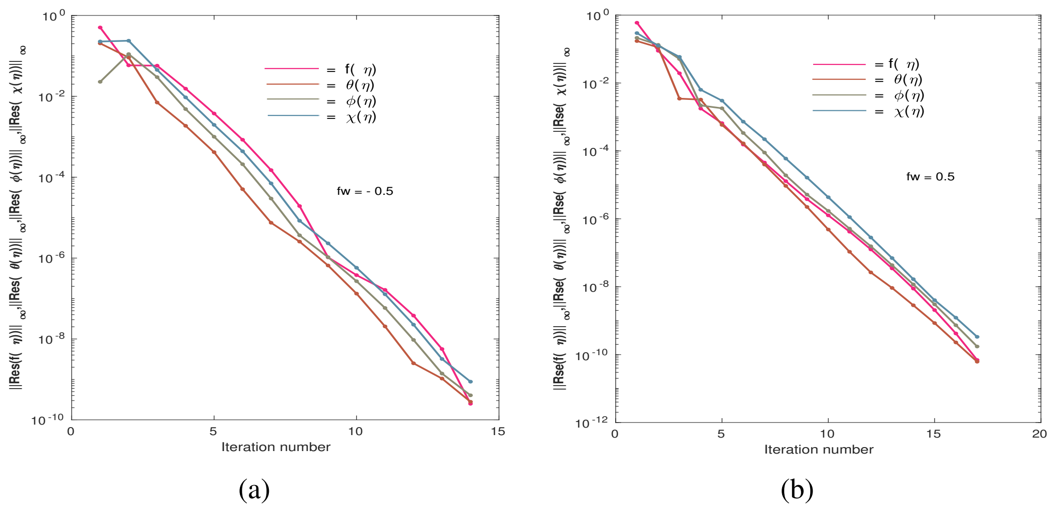

Figure 7.2.1: The residual error for $\mathrm{f}(\eta), \theta(\eta), \phi(\eta), \mathrm{and}\chi(\eta)$ against iteration number for (a): injection, (b): suction

7.2.2 Code Verification

To confirm the reliability of the numerical results:

a. The skin friction coefficient, $C_f^{\star} = -Re^{1/2}C_f$, was benchmarked against prior results from Hashim et al. (2017) and Nabwey et al. (2022) for various values of the curvature parameter α_c, under the limiting case $M = We = \lambda = \alpha = \lambda_m = f_w = 0$. Table 7.2.1 shows a strong agreement, validating the accuracy of the present computations.

Table 7.2.1: Comparison of $C_f^\star = -Re^{\frac{1}{2}}C_f$ with the results in (Hashim et al. (2017) and Nabwey et al. (2022)) for various values of α_c.

α_c	Hashim et al. (2017) $C_f^\star$	Nabwey et al. (2022) $C_f^\star$	**Present value** $C_f^\star$
0	1.000000	1.000000	1.000000
0.25	1.094373	1.094376	1.094378
0.50	1.188727	1.188728	1.188724
0.75	1.281819	1.281827	1.281827
1.0	1.453373	1.453361	1.453352

b. Additional validation was carried out by comparing skin friction outcomes for varying λ and α values in the range $[0.5,\ 2.5]$, using both the RKF45 and the SLLM, with $\Omega = 0$. The results, displayed in the contour plots of Figure 7.2.2 (a, b), follow the expression:

$$C_f^\star = -2f''(0)\left[1 + We^2 f''^2(0)\right]^{(n-1)/2}.$$

As summarized in Table 7.2.2, the skin friction coefficient increased by approximately 28.342548% for RKF45 and 28.342521% for SLLM over the examined range, confirming the consistency and high accuracy of the spectral method when compared with RKF45.

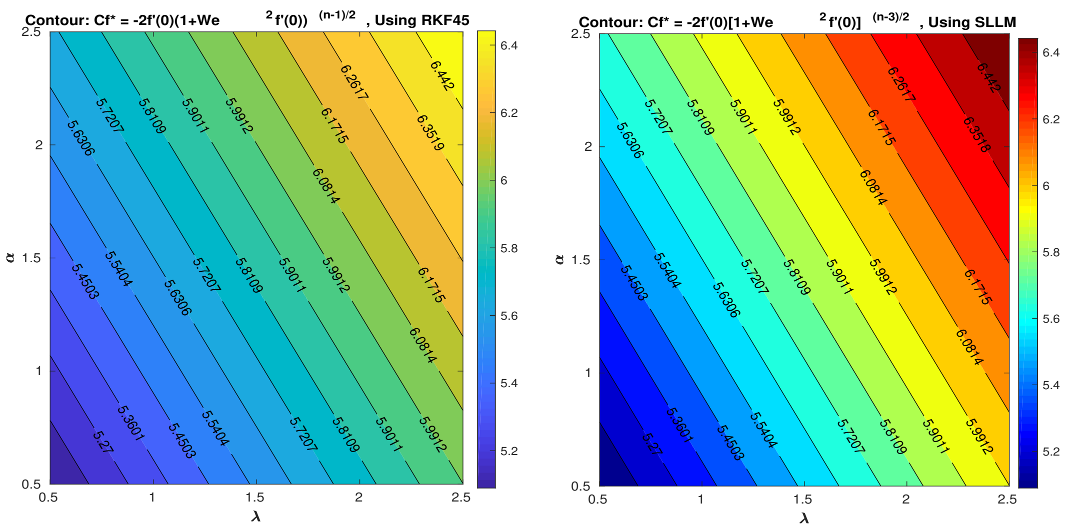

(a) (b)

Figure 7.2.2: Contour of $C_f^\star$ using (a): the RKF45 method (b) the SLLM for variations in λ and α

Table 7.2.2: Contrasting numerical results of $C_f^\star = -Re^{\frac{1}{2}} C_f$ computed using the RKF45 and SLLM.

λ, α	$C_f^\star$: RKF45	$Cf^\star$: SLLM
0.5	5.08963471	5.08963431
2.5	6.53216687	6.53216497

7.3 Results and Discussion

This section presents a detailed examination of the numerical solutions corresponding to the transformed system (Eqs. (7.1.19)-(7.1.22)) along with the boundary conditions specified in Eq. (7.1.23). The analysis is carried out using a variety of graphical tools such as curve plots, streamlines, isotherms, surface contours, and 3D visualizations to illustrate the effects of various dimensionless parameters on velocity, temperature, nanoparticle concentration, and microorganism density distributions. Furthermore, the behavior of critical engineering quantities–namely, the skin friction coefficient, Nusselt number, Sherwood number, and microbe transfer rate–is explored in response to changes in model parameters.

The parameter ranges considered in this study are selected to ensure numerical stability and convergence within a tolerance of 10^{-9}, achieved in no more than 14 iterations. These parameters include: $1.5 \le M \le 3$, $0.5 \le We \le 3.5$, $0.2 \le Ec \le 0.5$, $0.2 \le \alpha_c \le 3$, $1.2 \le Pr \le 5$, $1.5 \le Rd \le 5$, $2 \le \lambda \le 5$, $0.5 \le \alpha \le 12$, $0.5 \le Nr, \lambda_m, Rb \le 3.5$, $0 \le \Omega \le \pi/2$, $1 \le \theta_w \le 1.25$, $0.6 \le Nm, Nt \le 1.5$, $0.8 \le Nb \le 1.6$, $0.5 \le \lambda_2 \le 6$, $0.3 \le \lambda_3 \le 1.1$, $-5 \le Q_0 \le -0.5$, $0.5 \le sc_p, sc_b \le 3$, $0.4 \le \gamma_c, \gamma_b \le 2.2$, $1 \le E, p \le 2.5$, $0.4 \le w \le 1.2$, $1 \le n \le 2$, $-0.6 \le fw \le 0.5$, $0 < tt < 1$, and $0.2 \le \gamma_1, \gamma_2, \gamma_3 \le 0.6$. Variations beyond these thresholds, particularly in parameters such as M, Q_0, w, Pr, and Rd, tend to impair convergence and are therefore excluded from the study to maintain accuracy and consistency.

7.3.1 Velocity Variations

Figures 7.3.1-7.3.3a depict how changes in key parameters–such as M, We, Nr, λ_m, λ, α, f_w, w, Ω, and n–influence the velocity field.

In Figure 7.3.1a, an increase in M leads to a reduction in fluid velocity due to the Lorentz force, which acts in opposition to the flow. This retarding force is essential in applications like MHD pumps, flow control in metallurgical processes, and biomedical technologies such as targeted drug delivery and hyperthermia treatments. In contrast, a rise in We enhances the velocity profile by reducing the fluid's effective viscosity, thereby increasing momentum transfer.

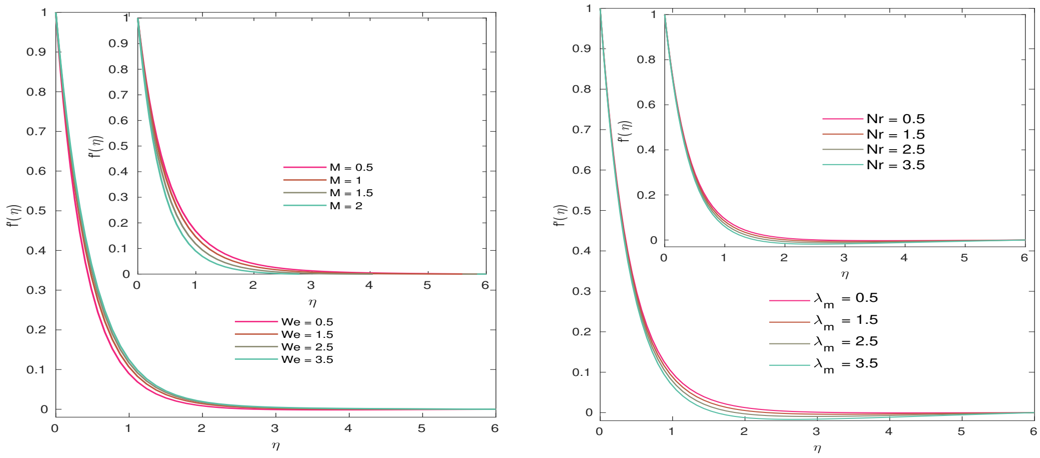

(a) (b)

Figure 7.3.1: Effect of (a): M and We, (b): Nr and λ_m on velocity profile

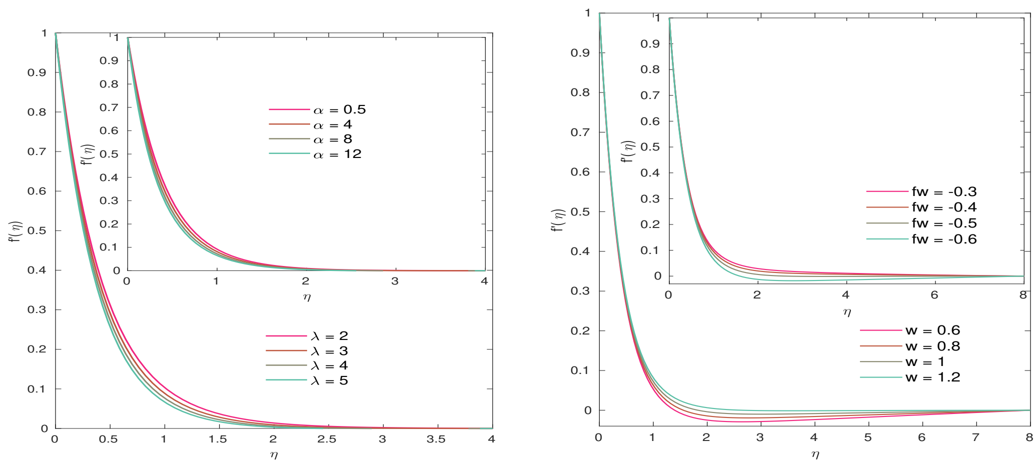

(a) (b)

Figure 7.3.2: Effect of (a): λ and α, (b): f_w and w on velocity profile

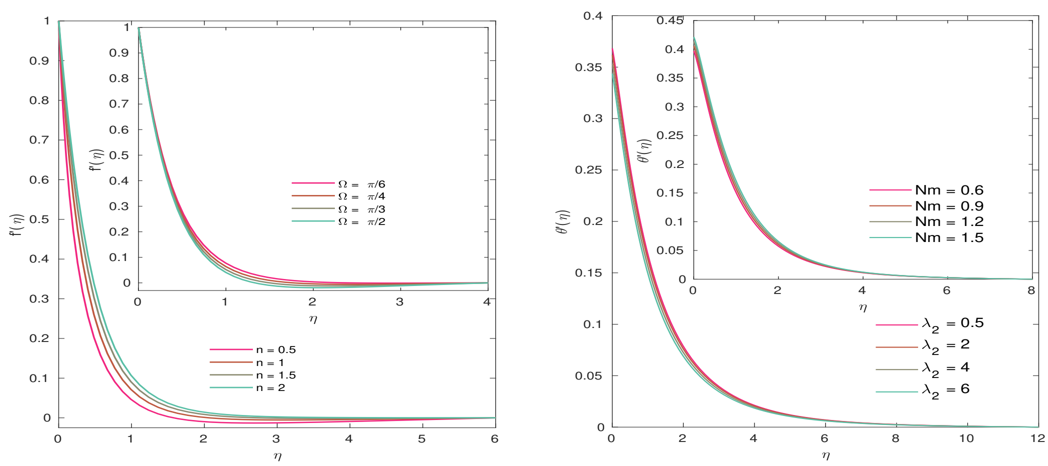

(a) (b)

Figure 7.3.3: Effect of (a): Ω and n on velocity profile, (b): Nm and λ_2 on temperature profile

Figure 7.3.1b illustrates the influence of the mixed convection parameter λ_m and the buoyancy ratio Nr. Both parameters increase the buoyant force, which, being transverse to the flow, suppresses the fluid velocity and momentum layer thickness. In Figure 7.3.2a, increasing the λ and α results in a decline in velocity. This is due to the increased drag and resistance encountered by the fluid as it flows through a more porous medium, which traps particles and reduces the flow's effective cross-sectional area. Figure 7.3.2b shows that higher values of the f_w (with negative f_w implying injection) tend to reduce the velocity field due to boundary layer thinning. Conversely, an increase in the microbial density difference parameter w leads to higher velocities, as enhanced microbial sedimentation induces instability and vertical mixing, counteracting the retarding buoyancy forces.

Lastly, Figure 7.3.3a examines the effect of the inclination angle Ω and the power-law index n of the Carreau fluid. A larger inclination angle introduces a gravitational component opposing the flow direction, thereby reducing velocity. However, increasing the power-law index n decreases fluid viscosity in regions of high shear, facilitating smoother and faster flow, which elevates the velocity profile and momentum thickness.

7.3.2 Temperature Variations

Figures 7.3.3b-7.3.5 illustrate how variations in key parameters–including Nm, λ_2, λ, α, f_w, γ_1, Q_0, and M–affect the temperature distribution within the thermal boundary layer.

Figure 7.3.3b examines the roles of the motile microorganisms parameter Nm and the thermal relaxation time parameter λ_2. As Nm increases, the temperature field also rises, which may be attributed to enhanced thermal agitation from intensified microbial activity near the boundary layer, despite the underlying mechanism remaining partly speculative. On the other hand, an increase in λ_2 reduces the temperature profile due to delayed thermal response introduced by the non-Fourier heat conduction model. This delay implies that thermal signals propagate at a finite speed, thereby causing delay in the temperature response, which in turn suppressing the temperature field. In Figure 7.3.4a, both λ and α are shown to enhance temperature distribution. A larger λ allows for greater fluid transport through the porous matrix, promoting convective heat transfer due to increased interfacial area. Similarly, an increase in α implies stronger flow resistance, which intensifies viscous dissipation. The associated conversion of mechanical energy to thermal energy elevates the fluid temperature.

Figure 7.3.4b shows the influence of wall mass flux (f_w) and the Biot number (γ_1). Injection ($f_w < 0$) introduces additional fluid into the domain, raising the energy content and thus increasing the temperature profile. As for γ_1, which quantifies the ratio of convective to conductive heat transfer, higher values signify more efficient heat exchange at the boundary.

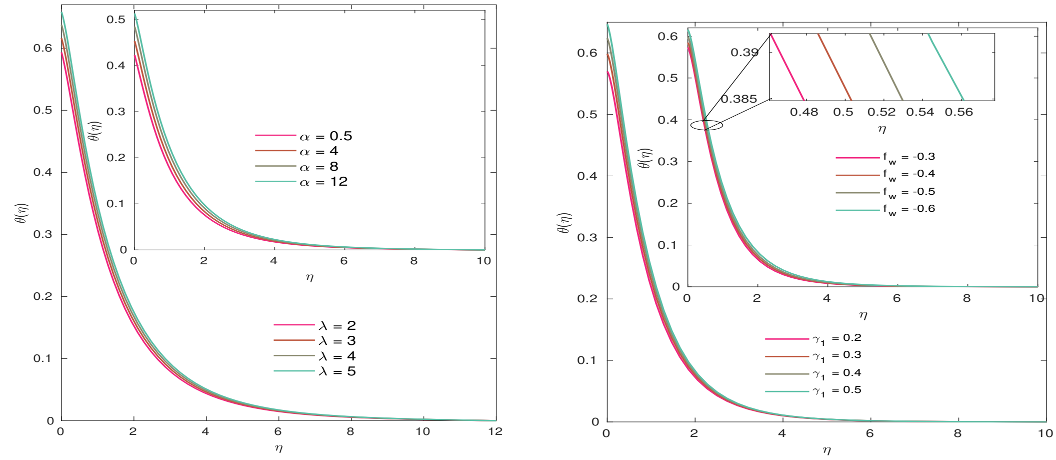

(a) (b)

Figure 7.3.4: Effect of (a): λ and α, (b): fw and γ_1 on temperature profile

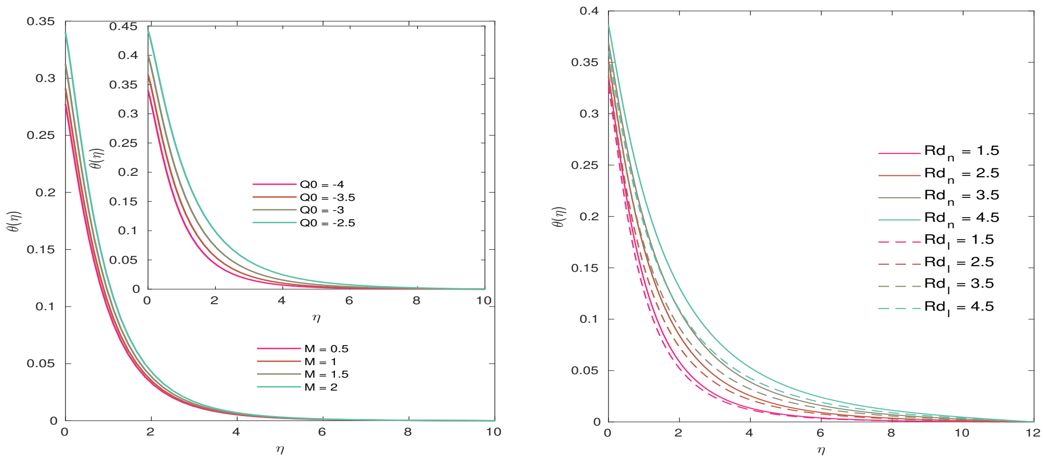

(a) (b)

Figure 7.3.5: Effect of (a): M and $\mathrm{Q_0}$, (b): linear ($\mathrm{Rd_l}$) and nonlinear ($\mathrm{Rd_n}$) radiation on temperature profile

This leads to greater thermal energy transfer into the fluid, thereby amplifying the non-dimensional temperature. In Figure 7.3.5a, the effects of Q_0 and M are analyzed. Increasing either parameter leads to a rise in the temperature distribution. The enhanced magnetic field strengthens the Lorentz force, which slows the flow and thickens the thermal boundary layer, allowing more time for heat diffusion near the wall. The presence of $Q_0 < 0$ further supplements internal energy, raising the overall temperature. These effects are significant in applications such as electronic cooling systems and MHD-based thermal management in nuclear reactors, where thermal regulation is critical.

Finally, Figure 7.3.5b contrasts the effects of linear and nonlinear thermal radiation (Rd_l and Rd_n). Linear radiation assumes small temperature gradients and approximates the Rosseland radiative term via Taylor expansion around the ambient temperature, simplifying

$\theta_w \approx 1$. Both radiation models elevate temperature, but nonlinear radiation exhibits a more pronounced effect due to stronger radiative energy transport in the presence of steeper temperature gradients.

7.3.3 Nanoparticle Concentration Variations

Figure 7.3.6a shows that the nanoparticle concentration profile decreases with increasing values of the curvature parameter α_c and the concentration relaxation time λ_3. A larger λ_3 implies a delayed diffusion response to concentration gradients, thereby reducing nanoparticle distribution. Additionally, an increase in α_c enlarges the effective surface area of the cylinder, promoting enhanced dispersion and contributing to the reduction in concentration. In contrast, Figure 7.3.6b reveals that higher values of λ_m and Nr enhance the nanoparticle concentration. This increase arises from the strengthening of buoyancy-driven convection, which promotes greater fluid mixing and upward transport of nanoparticles, thereby enriching the concentration field.

The effects of surface mass flux and mass Biot number are shown in Figure 7.3.7a. An increase in the injection parameter f_w leads to a higher nanoparticle concentration, as more particles are introduced into the flow domain. Similarly, an increase in γ_2 indicates more dominant convective mass transfer at the surface relative to molecular diffusion within the fluid. This enhanced surface transport fosters nanoparticle accumulation near the boundary, thereby elevating the overall concentration profile. Figure 7.3.7b explores the roles of the thermophoresis parameter Nt and the nanoparticle Schmidt number Sc_p. As these parameters increase, the nanoparticle concentration declines. A higher Nt induces stronger thermophoretic motion, which propels nanoparticles away from heated regions, reducing their accumulation near the surface. Moreover, an increased Sc_p–which corresponds to reduced mass diffusivity–limits the diffusion of nanoparticles through the fluid, leading to a thinner solutal boundary layer and a lower concentration distribution.

7.3.4 Microorganism Concentration Variations

Figure 7.3.8a presents the influence of λ_m and Rb on the microorganism concentration profile. An increase in both parameters enhances buoyancy-driven forces, thereby improving fluid mixing and promoting a higher microbial density distribution. In Figure 7.3.8b, the microorganism concentration is shown to increase with the Brownian motion parameter Nb, likely due to intensified interactions between nanoparticles and motile microorganisms, which enhance mixing and suppress local concentration gradients. In contrast, increasing Nm reduces the motile density distribution, as enhanced Brownian motion accelerates diffusion, leading to a more dispersed microbe distribution.

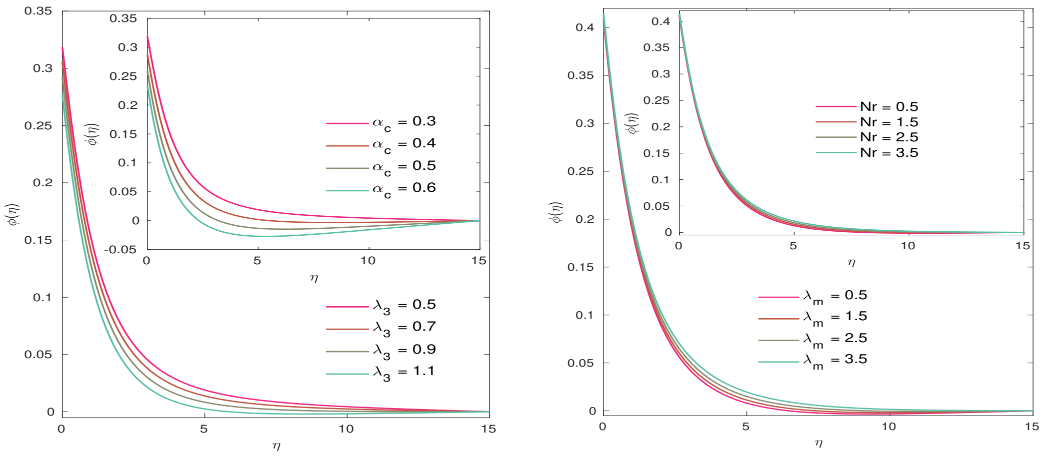

(a) (b)

Figure 7.3.6: Effect of (a): α_{c} and λ_3, (b): Nr and λ_{m} on nanoparticle concentration profile

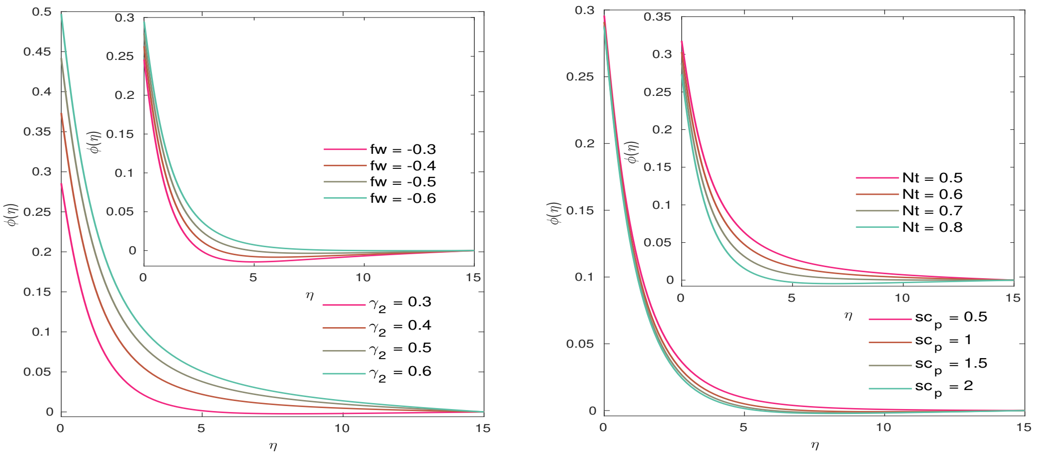

(a) (b)

Figure 7.3.7: Effect of (a): fw and γ_2, (b): Nt and $\mathrm{sc_p}$ on nanoparticle concentration profile

Figure 7.3.9a depicts the effects of microbe chemical reaction parameter γ_b and activation energy E on microbial concentration. A rise in γ_b corresponds to an increase in the rate of destructive reactions, thus reducing the microbial density. However, increasing E elevates the energy barrier required for chemical reactions, which lowers the reaction rate and leads to an increased concentration of microorganisms. Figure 7.3.9b illustrates the impact of f_w and the microorganism Biot number γ_3. Higher values of both parameters enhance the convective mass transfer at the boundary, resulting in a denser microorganism distribution within the boundary layer. Lastly, Figure 7.3.10 highlights the effects of the microbe Schmidt number Sc_b and Peclet number p. As Sc_b increases, reduced mass diffusivity coupled with higher momentum diffusivity leads to an elevated concentration of microorganisms. Conversely, a higher p signifies greater swimming velocity relative to diffusivity, which diminishes the microbial concentration profile.

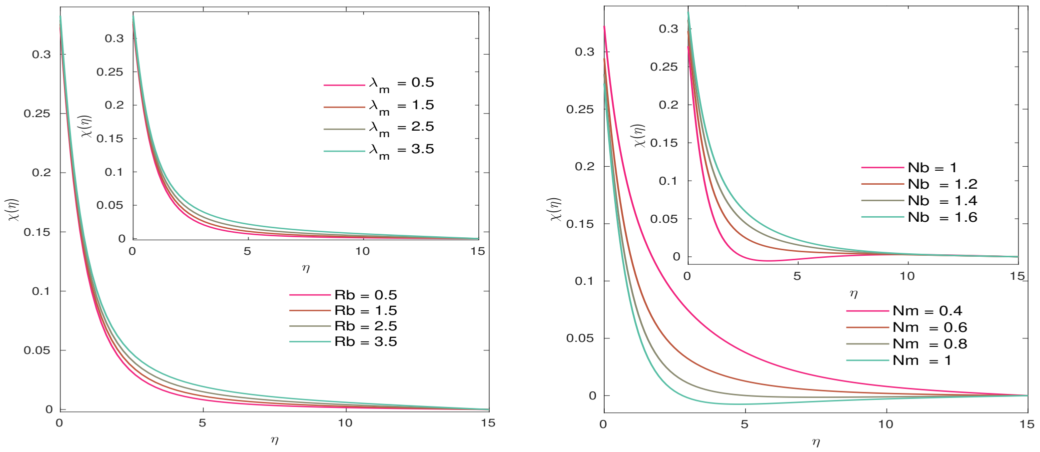

(a) (b)

Figure 7.3.8: Effect of (a): λ_{m} and Rb, (b): Nb and Nm on microbes concentration profiles

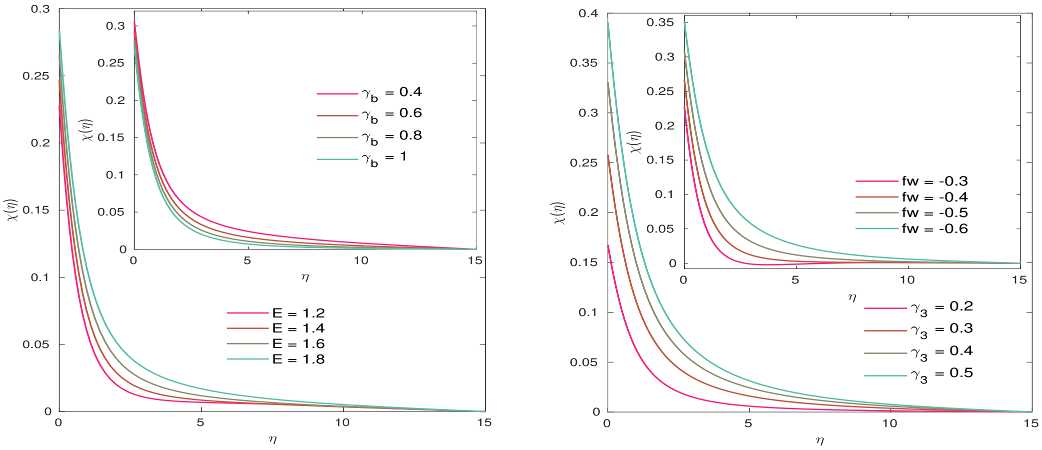

(a) (b)

Figure 7.3.9: Effect of (a): kb and E, (b): fw and γ_3 on microbes concentration profile

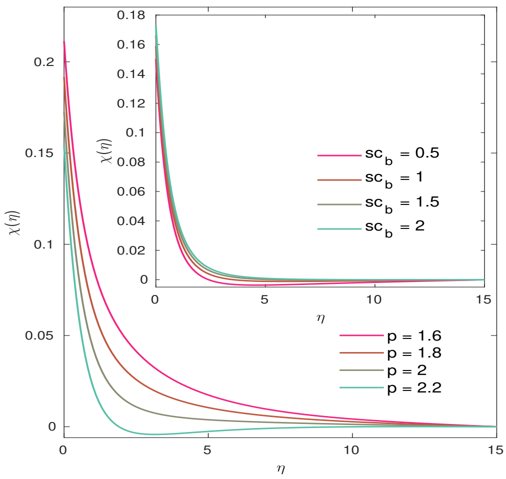

Figure 7.3.10: Effect of $\mathrm{Sc_b}$ and p on microbes concentration profile

7.3.5 Streamlines, Isotherms, and Contour Plots

Figures 7.3.11–7.3.12 present streamlines and isotherms that illustrate the hydromagnetic bioconvective flow over a stretching cylindrical surface, focusing on the influence of α_c. As seen in the streamlines of Figure 7.3.11, increasing α_c intensifies the streamline patterns. This is due to the enhanced curvature, which reduces the contact area among fluid particles and diminishes resistance, thereby accelerating fluid motion and shifting the velocity field outward toward the free stream. In Figure 7.3.12, the isotherm lines are observed to expand further into the free stream with increasing α_c, indicating an enhancement in temperature distribution within the boundary layer. The rise in curvature steepens the velocity gradients, which in turn amplifies viscous dissipation–the transformation of kinetic energy into thermal energy–resulting in higher fluid temperatures. Consequently, the thermal boundary layer becomes thicker, with more evenly distributed temperature profiles.

Figure 7.3.13 illustrates the contour plots of temperature distribution in response to variations in Ec and Rd. Initially, the temperature gradient is confined near the cylinder surface, but as Ec and Rd increase, the temperature field extends toward the free stream. Physically, higher Ec values signify more viscous dissipation due to greater fluid kinetic energy, which raises the internal temperature. Simultaneously, an increase in Rd indicates stronger thermal radiation effects, which further contribute to the rise in boundary layer temperature. Figure 7.3.14 depicts the effect of γ_c and E on concentration distribution. As γ_c increases, destructive chemical reactions become more prominent, reducing nanoparticle concentration, as indicated by the inward shift of contour lines toward the cylinder surface. In contrast, a higher E raises the energy threshold required for chemical reactions to occur, thereby reducing the rate of nanoparticle degradation. This leads to a greater accumulation of nanoparticles, reflected in the outward expansion of the concentration contours.

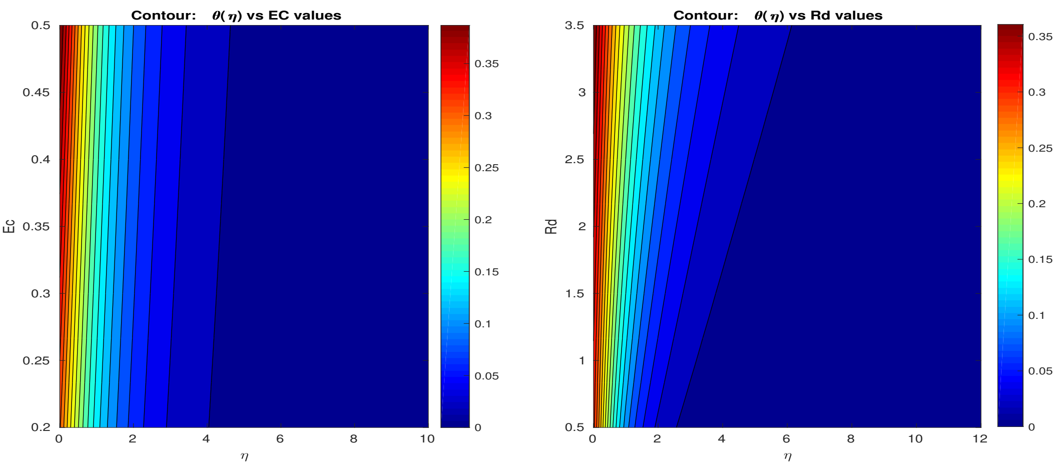

(a) (b)

Figure 7.3.13: Effect of (a): Ec, (b): Rd on temperature profile

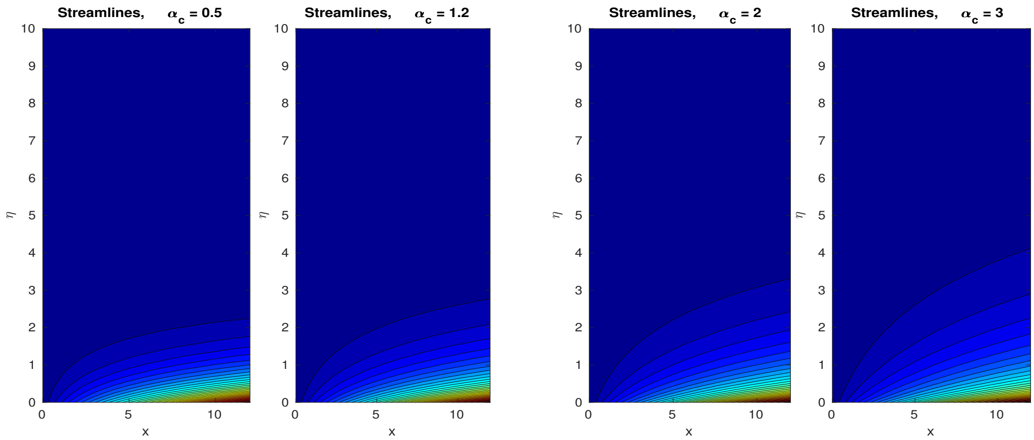

(a) (b)

Figure 7.3.11: Streamlines for (a): $\alpha_{\rm c} = 0.5, 1.2$, (b): $\alpha_{\rm c} = 2, 3$

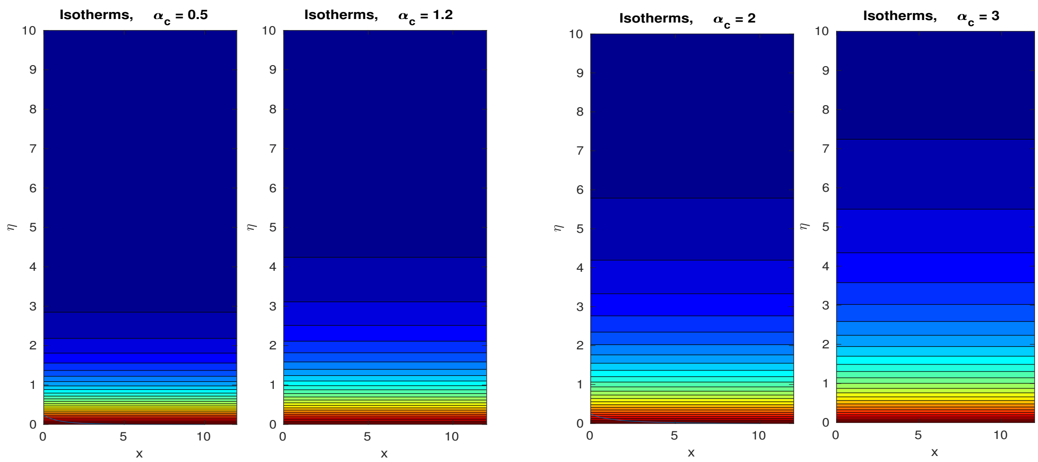

(a) (b)

Figure 7.3.12: Isotherms for (a): $\alpha_{\rm c} = 0.5, 1.2$, (b): $\alpha_{\rm c} = 2, 3$

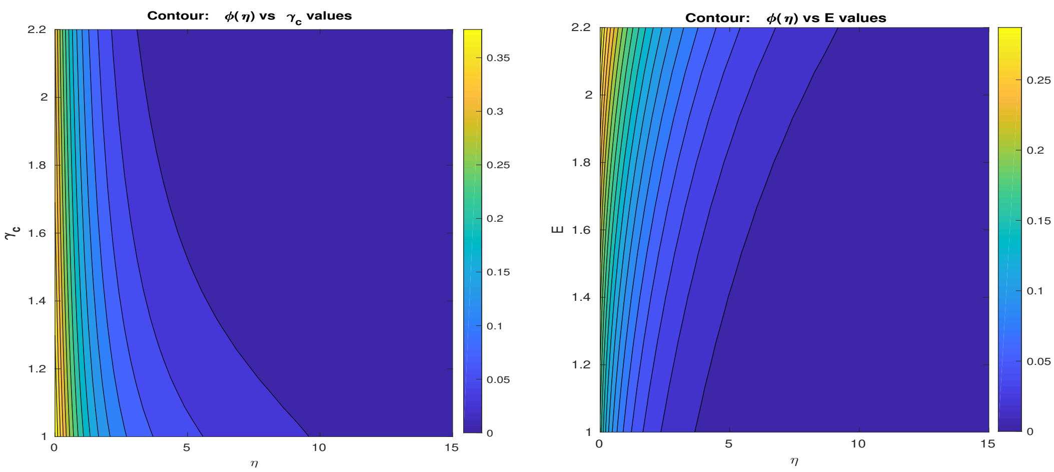

(a) (b)

Figure 7.3.14: Effect of (a): γ_c, (b): E on concentration profile

7.3.6 3D Visualization of Skin Friction, Heat, and Concentration Transfer Rates

Figure 7.3.15 illustrates the combined effects of λ_2 and λ_3 on the skin friction coefficient. The results show that increasing λ_2 enhances the skin friction, whereas a rise in λ_3 reduces it. This behavior suggests that the skin friction is more sensitive to solutal relaxation effects, highlighting the importance of non-Fickian diffusion mechanisms in modulating shear forces at the wall.

Figures 7.3.16a and 7.3.16b present a comparative study of the heat transfer rate under two scenarios: with and without the influence of nonlinear thermal radiation. The figures examine the roles of γ_1 and λ_2. The findings reveal that both parameters contribute to an increase in the Nusselt number, with γ_1 playing a more dominant role. Specifically, the heat transfer rate varies from 0.1500 to 0.3764 without radiation and from 2.1897 to 4.0690 in the presence of nonlinear thermal radiation, emphasizing the significant amplification of heat transfer when radiative effects are included.

Figures 7.3.17a and 7.3.17b depict the rates of nanoparticle and microorganism concentration transfer. In Figure 7.3.17a, the nanoparticle Sherwood number increases with both γ_2 and λ_3, with γ_2 exerting a more substantial influence. Figure 7.3.17b shows that the motile microorganism transfer rate improves as both γ_3 and γ_b increase. As these parameters are elevated, the corresponding transfer rate grows from 0.158026 to 0.387634, demonstrating their critical role in enhancing microbe-related mass transport processes.

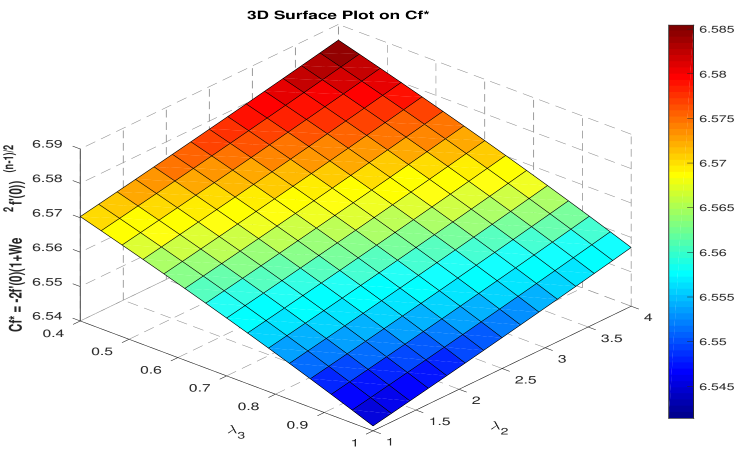

Figure 7.3.15: Effect of λ_2 and λ_3 on Cf*

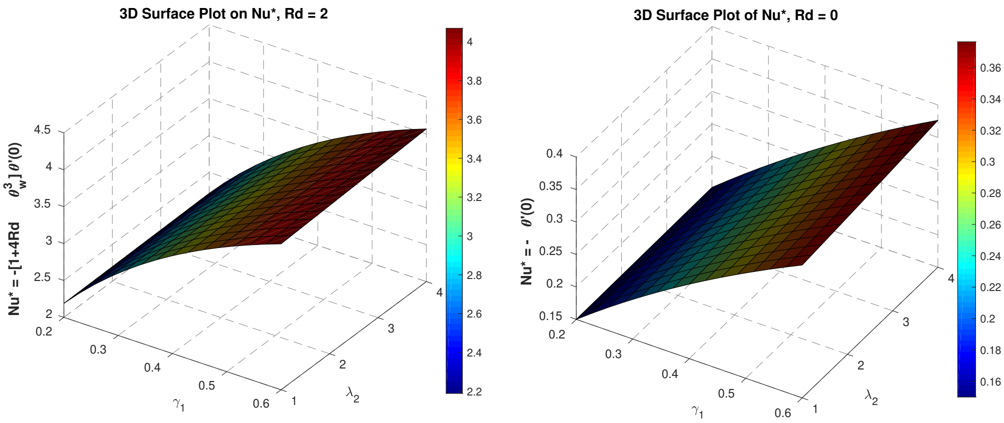

(a) (b)

Figure 7.3.16: Effect of γ_1 and λ_2 on $\mathrm{Nu}^{\star}$ (a): at $\mathrm{Rd} = 2$, (b): at $\mathrm{Rd} = 0$

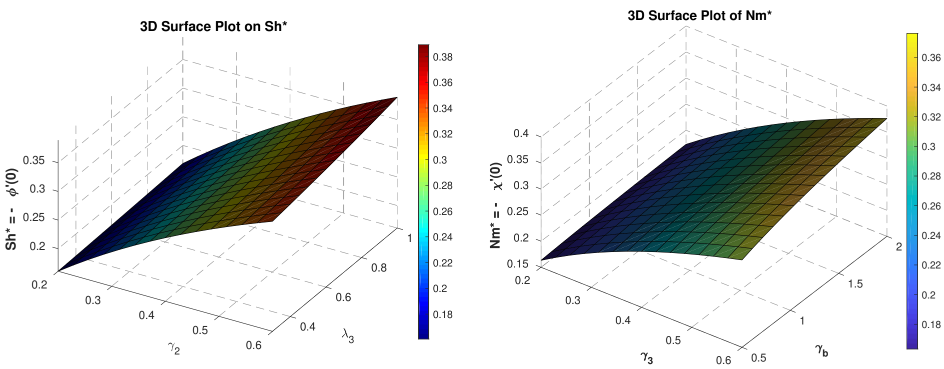

(a) (b)

Figure 7.3.17: Effect of (a): γ_2 and λ_3 on $Sh^{\star}$, (b): γ_3 and γ_b on $\mathrm{Nm}^{\star}$

7.3.7 Tabular Data: Skin Friction and Heat Transfer Rates

Table 7.3.1 presents the effects of various physical parameters on the skin friction coefficient at the surface of the cylinder. The results demonstrate that increasing the values of M, We, α_c, λ, α, λ_m, f_w, and Ω tends to elevate the skin friction. However, an increase in Nm leads to a decline in the wall shear stress. This indicates that enhanced Brownian motion of microbes helps reduce the surface drag, thereby influencing the momentum boundary layer behavior.

Table 7.3.2 details how key parameters affect the local heat transfer rate. It is observed that the Nusselt number increases with larger values of Rd, Nb, and λ_m. Conversely, increasing the values of Nm, Nt, α_c, λ, and Ec results in a reduction in heat transfer at the surface. These findings highlight the significance of incorporating both thermal radiation and buoyancy-driven convection effects in thermal system designs, as they play a crucial role in optimizing heat transfer performance.

Table 7.3.1: Skin friction coefficient, $Cf_r^{\star} = -Re^{1/2}Cf_r$ for various values of embedded parameters

M	We	Nm	α_c	λ	α	λ_m	fw	Ω	$Cf_r^{\star}$
2	0.5	0.6	0.4	3	1.5	1.5	-0.5	$\pi/6$	7.007016
2.5									7.934533
3									8.868022
2	1.5								7.651944
	2.5								8.016241
	3.5								8.277561
	0.5	0.9							6.951357
		1.2							6.924227
		1.5							6.908126
		0.6	0.4						7.007016
			0.5						7.129748
			0.6						7.275252
			0.4	3					7.007016
				4					7.430081
				5					7.835606
				3	0.5				6.722557
					4				7.684341
					8				8.687152
					1.5	1.5			7.007016
						2.5			7.160704
						3.5			7.329249
						1.5	-0.4		6.984814
							-0.5		7.007016
							-0.6		7.066934
							-0.5	$\pi/4$	7.100933
								$\pi/3$	7.176522
								$\pi/2$	7.242900

Table 7.3.2: Local heat transfer rate, $Nu_x^{\star} = Re^{-1/2} Nu_w$ for various values of embedded parameters

Rd	Nb	Nm	Nt	α_c	λ	λ_m	Ec	$Nu_x^{\star}$
3	1.4	0.6	0.8	0.4	3	1.5	0.3	4.838831
4								6.379198
5								7.876723
3	0.8							4.807274
	1							4.824437
	1.2							4.833995
	1.4	0.9						4.793367
		1.2						4.751820
		1.5						4.711762
		0.6	0.9					4.818538
			1					4.798451
			1.1					4.778561
			0.8	0.4				4.838831
				0.5				4.812788
				0.6				4.789040
				0.4	3			4.838831
					4			4.729069
					5			4.623205
					3	1.5		4.838831
						2.5		4.854921
						3.5		4.872432
						1.5	0.3	4.838831
							0.4	4.434192
							0.5	4.034808

7.4 Summary

This work presents a detailed numerical analysis of MHD bioconvective and radiative transport in a Carreau nanofluid flow over an axially stretching cylindrical surface. The model incorporates several intricate physical mechanisms, including non-Fourier and non-Fickian heat and mass transport, mixed convection, internal heat generation or absorption, viscous dissipation, Brownian and thermophoretic motion of nanoparticles and microorganisms, Arrhenius-type chemical reactions, and convective boundary conditions.

The velocity, temperature, concentration, and microorganism density profiles are systematically analyzed through graphical, contour, and three-dimensional visualizations, supported by tabular data. The major findings from this investigation are summarized as follows:

1. The velocity increases with rising values of We, w, α_c, and n, but decreases with M, Nr, λ_m, λ, α, f_w, and Ω.

2. The temperature field is enhanced by increasing values of Nm, λ, α, Ec, Q_0, M, α_c, and Rd.

3. Both temperature and concentration distributions are elevated by stronger suction/injection and their respective Biot numbers, but decline with increasing thermal and solutal relaxation times.

4. The nanoparticle concentration improves with increasing Nr, λ_m, and E, but is reduced for larger values of α_c, Nt, Sc_p, and γ_c.

5. Microorganism concentration rises with increasing λ_m, Rb, γ_3, Sc_b, f_w, Nb, and E, but decreases with higher γ_b, Nm, and p.

6. Skin friction increases with higher M, We, α_c, λ, α, λ_m, and f_w, but is notably reduced by non-Fickian diffusion and microorganism Brownian motion.

7. The surface heat transfer rate increases with greater Rd, Nb, λ_m, λ_2, and γ_1, while it diminishes with higher values of Nm, Nt, α_c, λ, and Ec.

Overall, this study offers significant insights into the role of various physical parameters on the flow and heat transfer behavior of Carreau nanofluids under bioconvective and MHD conditions, facilitating improved design and operation of advanced thermal and fluid systems in industrial and engineering contexts.

CHAPTER EIGHT

Unsteady Williamson Nanofluid Flow over a Rotating Cone: Influence of Variable Properties, Thermal Radiation, and Chemical Reactions

Convective heat and mass transfer in rotating systems holds considerable relevance across various industrial and engineering domains, such as nuclear cooling systems, rotating heat exchangers, rotor-stator assemblies, geothermal processes, and spin-stabilized aerospace structures (Shevchuk (2009), Nadeem and Saleem (2014), Harmand et al. (2013), Gaffar et al. (2017)). Although extensive studies exist for Newtonian fluids, investigations focusing on unsteady non-Newtonian nanofluid flows–particularly with variable thermophysical properties over rotating vertical cones–remain relatively scarce.

Introducing nanoparticles into non-Newtonian base fluids brings additional mechanisms like Brownian diffusion and thermophoresis, which enhance the thermal and solutal transport processes. Previous studies, such as Raju et al. (2016), analyzed these effects in Jeffrey, Maxwell, and Oldroyd-B nanofluids under magnetic fields with non-uniform heat sources. Similarly, Anilkumar and Roy (2004) showed that unsteady mixed convection over a rotating cone admits similarity solutions when the cone's angular velocity and that of the surrounding fluid are related inversely as a linear functions of time . More recently, Paul et al. (2023) explored the roles of suction and slip effects in Casson hybrid nanofluid flow over a rotating cone, reporting significant improvements in tangential and azimuthal skin friction.

Despite these efforts, comprehensive analysis of unsteady boundary layer flow of Williamson nanofluids over rotating cones–accounting for variable thermophysical properties, thermal radiation, chemical kinetics, and mixed convection in porous media–has yet to be fully addressed. This chapter aims to fill this research gap by investigating:

1. The effect of variable thermophysical properties on heat and mass transfer rates under specified wall temperature and concentration (SWTC) and thermosolutal flux (STSF) conditions.

2. The interplay of frictional and form drag within a Darcy–Forchheimer porous medium and their influence on momentum and thermal boundary layers.

3. Key parameters that affect skin friction, Nusselt, and Sherwood numbers.

4. The influence of linear and nonlinear thermal radiation on the temperature profile and flow development with variable thermophysical properties.

5. The role of binary chemical reactions governed by Arrhenius activation energy on mass diffusion and concentration gradients.

8.1 Mathematical Model and Formulation

8.1.1 Flow Geometry and Assumptions

This study considers the unsteady, incompressible, and laminar MHD flow of a Williamson nanofluid over a rotating, infinite cone embedded in a rotating ambient medium. The unsteadiness originates from time-dependent angular velocities of both the cone and the ambient nanofluid, denoted $\omega_1(t)$ and $\omega_2(t)$, respectively, resulting in an effective angular velocity $\omega = \omega_1 + \omega_2$ near the cone surface.

A curvilinear coordinate system (x, y, z) is adopted, where x is aligned with the cone's meridional direction, y is azimuthal, and z is normal to the surface. The corresponding velocity components are (u, v, w). The flow is assumed axisymmetric, and a constant magnetic field B_0 is applied perpendicular to the cone's surface, while the effect of magnetic Reynolds number is neglected.

The nanofluid comprises a base fluid with suspended nanoparticles at low volume fractions (below 1%) to ensure stability and suppress agglomeration. Thermal and solutal buoyancy forces, induced by gradients in temperature and nanoparticle concentration, significantly influence the flow. The cone may be subjected either to SWTC or to STSF, with ambient conditions denoted by T_∞ and C_∞. A schematic of the flow is depicted in Figure 8.1.1.

8.1.2 Governing Equations

Applying boundary layer approximations and the Boussinesq hypothesis, the two-dimensional, axisymmetric, unsteady flow equations describing mixed convection MHD flow of Williamson nanofluid over a rotating cone of half-angle α^*–including thermal radiation and Arrhenius–type chemical reactions–are formulated as follows (Chamkha (1999), Nadeem and Saleem (2013)):

8.1.3 Governing equations

Utilizing the boundary layer theory alongside the standard Boussinesq approximations, the axisymmetric, , unsteady, and incompressible boundary layer equations governing the mixed convective MHD flow of Williamson nanofluid over a vertically rotating cone of half apex angle, α^*, in the presence of thermal radiation and Arrhenius chemical reactions are formulated as follows (Chamkha (1999), Nadeem and Saleem (2013)):

$$\frac{\partial u}{\partial x} + \frac{\partial w}{\partial z} + \frac{u}{x} = 0, \tag{8.1.1}$$

$$\rho_f\left(u_t+uu_x+wu_z-\frac{v^2}{x}\right)=-\rho_f\frac{v_e^2}{x}+\frac{\partial}{\partial z}\left[\mu(T)u_z\right]+\frac{\Gamma}{\sqrt{2}}\frac{\partial}{\partial z}\left[\mu(T)\Big(\frac{\partial u}{\partial z}\Big)^2\right]+\rho_f g\times$$
$$\left[\beta_T\Big(T-T_\infty\Big)+\beta_C\Big(C-C_\infty\Big)\right]\cos\alpha^*-\sigma_0 B_0^2 u-\mu(T)\frac{\xi}{k^\star}u-c_F\frac{\rho_f\xi}{\sqrt{k^\star}}u^2, \tag{8.1.2}$$
$$\rho_f\left(v_t+uv_x+wv_z+\frac{uv}{x}\right)=\rho_f(v_e)_t+\frac{\partial}{\partial z}\left[\mu(T)v_z\right]+\frac{\Gamma}{\sqrt{2}}\frac{\partial}{\partial z}\left[\mu(T)\Big(\frac{\partial v}{\partial z}\Big)^2\right]-$$
$$\sigma_0 B_0^2(v-v_e)-\mu(T)\frac{\xi}{k^\star}(v-v_e)-c_F\frac{\rho_f\xi}{\sqrt{k^\star}}(v-v_e)^2, \tag{8.1.3}$$
$$(\rho c_p)_f\Big(T_t+uT_x+wT_z\Big)=\frac{\partial}{\partial z}\Big[k(T)T_z\Big]-\Big(q_r\Big)_z+(\rho c_p)_f\Big(\tau D_b(C)\Big)\Big(T_zC_z\Big)+$$
$$(\rho c_p)_f\frac{\tau D_T}{T_\infty}\Big(T_z\Big)^2, \tag{8.1.4}$$
$$C_t+uC_x+wC_z=\frac{\partial}{\partial z}\Big[D_b(C)C_z\Big]+\frac{D_T}{T_\infty}\Big(T_{zz}\Big)-k_r^2\Big(C-C_\infty\Big)\Big(\frac{T}{T_\infty}\Big)^{t_0}\times$$
$$exp\left(\frac{-E_a}{\kappa T}\right), \tag{8.1.5}$$

Initial conditions are

$$u(0,x,z)=u_0(x,z),\,v(0,x,z)=v_0(x,z),\,w(0,x,z)=w_0(x,z),$$
$$T(0,x,z)=T_0(x,z),\,C(0,x,z)=C_0(x,z), \tag{8.1.6}$$

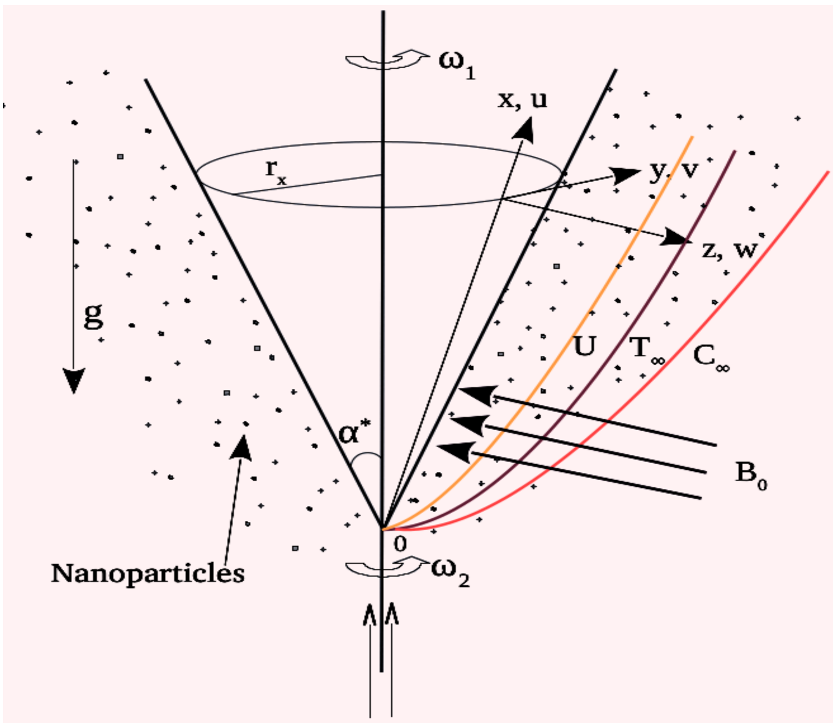

Figure 8.1.1: Schematic of the flow

The study considers the two surface conditions; the specified thermo-solutal flux (STSF) boundary conditions and the specified wall temperature and concentration (SWTC) boundary conditions, as given below.
The boundary conditions for the SWTC case are:

$$u(t,x,0)=0,\, v(t,x,0)=\omega_1 x\sin\alpha^*(1-s\bar{t})^{-1},\, w(t,x,0)=-w_0^\star,\, T=T_w,\; C=C_w,\; at\ z=0,$$
$$u(t,x,z)\longrightarrow 0,\; v(t,x,z)\longrightarrow v_e,\, T\longrightarrow T_\infty,\; C\longrightarrow C_\infty,\, as\ z\longrightarrow\infty, \tag{8.1.7}$$

The boundary conditions for the STSF case are:

$$u(t,x,0)=0,\, v(t,x,0)=\omega_1 x\sin\alpha^*(1-s\bar{t})^{-1},\, w(t,x,0)=-w_0^\star,\, -k(T)T_z=q_h,$$
$$-D_b(C)C_z=q_m,\; at\ z=0,$$
$$u(t,x,z)\longrightarrow 0,\; v(t,x,z)\longrightarrow v_e,\, T\longrightarrow T_\infty,\; C\longrightarrow C_\infty,\, as\ z\longrightarrow\infty, \tag{8.1.8}$$

where, $q_h=h_t(T_w-T)$, $q_m=h_m(C_w-C)$, and $\tau(=(\rho c_p)_p/(\rho c_p)_f)$ denotes ratio of effective heat capacity of nanoparticles to base fluid. All the remaining notations are mentioned in nomenclature.

In the optically thick radiation limit, the Rosseland approximation is employed to model the radiative heat flux, expressed as:

$$q_r=\frac{-4\sigma^\star}{3k_e}\frac{\partial T^4}{\partial z}. \tag{8.1.9}$$

To simplify the analysis, under the assumption of a small temperature gradient within the flow, the nanofluid temperature, T^4 can be expanded using Taylor series about the free stream temperature, T_∞ as:

$$T^4=T_\infty^4+4T_\infty^3(T-T_\infty)+6T_\infty^2(T-T_\infty)^2+\ldots, \tag{8.1.10}$$

and linearized to first-order term in $(T-T_\infty)$,

$$T^4\approx 4T_\infty^3T-3T_\infty^4. \tag{8.1.11}$$

Substituting this approximation into the Rosseland equation yields a linearized expression for the radiative heat flux gradient:

$$\frac{\partial q_r}{\partial z}=\frac{-16\sigma^\star T_\infty^3}{3k_e}\frac{\partial^2 T}{\partial z^2}. \tag{8.1.12}$$

This linearized form is valid when the temperature difference between the cone surface and the free stream is relatively small. However, in cases where there is a significant temperature variation, the nonlinear effects of thermal radiation become significant. In such scenarios, the nonlinear version, Eq. (4.1.37) of the radiative heat flux gradient is used. This formulation accounts for higher-order temperature variations and provides a more accurate representation of the thermal radiation effects in the presence of large temperature gradients.

8.1.4 Variable thermophysical properties

The fluid properties are considered variable, following the approach of Salahuddin et al. (2022),

Temperature-dependent viscosity:

The fluid viscosity is assumed to vary as an inverse linear function of temperature.

$$\frac{1}{\mu} = \frac{1}{\mu_\infty}\left(1+\zeta(T-T_\infty)\right), \tag{8.1.13}$$

where μ_∞ is the viscosity at the free stream temperature, T_∞, and ζ is a constant that characterizes the temperature dependence.
Introducing the substitutions $b = \dfrac{\zeta}{\mu_\infty}$, and $T_r = T_\infty - \dfrac{1}{\zeta}$, the viscosity can be reformulated as:

$$\mu(T) = \frac{1}{b(T-T_r)}. \tag{8.1.14}$$

Here, b and T_r are constants determined by the free stream conditions and the fluid's thermal properties. Notably, $b > 0$ for liquids, indicating an increase in viscosity with decreasing temperature, while $b < 0$ for gases, signifying an opposite trend.

Temperature-dependent thermal conductivity

The thermal conductivity of the fluid varies with temperature and is modeled as:

$$k = k_\infty\left(1+\epsilon_1\frac{T-T_\infty}{\Delta T}\right), \tag{8.1.15}$$

where, k_∞ is the thermal conductivity at the free stream temperature, ϵ_1 is a dimensionless coefficient that represents the sensitivity of k to temperature, and ΔT is a reference temperature difference.

Concentration-dependent solutal diffusivity

The solutal diffusivity, dependent on the concentration of solute, is given by:

$$D_b(C) = D_{b\infty}\left(1+\epsilon_2\frac{C-C_\infty}{\Delta C}\right), \tag{8.1.16}$$

where, $D_{b\infty}$ is the solutal diffusivity at the free stream concentration, C_∞, ϵ_2 is a dimensionless coefficient that represents the sensitivity of D_b to concentration, and ΔC is a reference concentration difference.

8.1.5 Nondimensionalization and reduction to ODEs

We introduce the following nondimensional variables and similarity solutions (Anilkumar and Roy (2004)). It was determined that the PDEs could be transformed into a system of ODEs by assuming the boundary layer edge velocity,v_e and the cone's angular velocity to vary inversely as linear functions of time.

$$\begin{aligned}
&\bar{t} = \omega t\sin\alpha^*,\ \eta = \left(\frac{\omega\sin\alpha^*}{\nu(1-s\bar{t})}\right)^{1/2} z,\ v_e = \frac{\omega_2 x\sin\alpha^*}{1-s\bar{t}},\ u = \frac{\omega x\sin\alpha^*}{1-s\bar{t}}f,\ v = \frac{\omega x\sin\alpha^*}{1-s\bar{t}}g,\\
&w = \left(\frac{\nu\omega\sin\alpha^*}{1-s\bar{t}}\right)^{1/2} h,\ T-T_\infty = \big(T_w-T_\infty\big)\theta,\ C-C_\infty = \big(C_w-C_\infty\big)\phi,\\
&T_w-T_\infty = \left(T_0-T_\infty\right)\frac{x}{L}\left(1-s\bar{t}\right)^{-2},\ C_w-C_\infty = \left(C_0-C_\infty\right)\frac{x}{L}\left(1-s\bar{t}\right)^{-2}.
\end{aligned} \tag{8.1.17}$$

By applying the aforementioned similarity variables and incorporating the variable transport properties, the system of PDEs (Eqs. (8.1.1)- (8.1.5)) along with the boundary conditions (Eqs. (8.1.7) and (8.1.8)) for the linearized thermal radiation case is transformed into the following form:

$$h' + 2f = 0, \tag{8.1.18}$$

$$\begin{aligned}
&\frac{\theta_0}{\theta_0-\theta}\left[\frac{\theta'}{\theta_0-\theta}f'+f''\right] + We^2\frac{\theta_0}{\theta_0-\theta}\left[\frac{\theta'}{\theta_0-\theta}f'^2+2f'f''\right] - s\left(f+\frac{\eta}{2}f'\right) - f^2 - hf' +\\
&\qquad g^2 + \lambda_m\big(\theta+N_r\phi\big) - Mf - \lambda\frac{\theta_0}{\theta_0-\theta}f - \alpha f^2 - (1-\alpha_1)^2 = 0,
\end{aligned} \tag{8.1.19}$$

$$\begin{aligned}
&\frac{\theta_0}{\theta_0-\theta}\left[\frac{\theta'}{\theta_0-\theta}g'+g''\right] + We^2\frac{\theta_0}{\theta_0-\theta}\left[\frac{\theta'}{\theta_0-\theta}g'^2+2g'g''\right] - s\left(g+\frac{\eta}{2}g'\right) - 2fg - hg' -\\
&\qquad M\big(g-(1-\alpha_1)\big) - \lambda\frac{\theta_0}{\theta_0-\theta}\big(g-(1-\alpha_1)\big) - \alpha\big(g-(1-\alpha_1)\big)^2 + s(1-\alpha_1) = 0,
\end{aligned} \tag{8.1.20}$$

$$\Big[(1+\epsilon_1\theta)+Rd\Big]\theta''+\epsilon_1\theta'^2-sPr\Big(2\theta+\frac{\eta}{2}\theta'\Big)+Pr\Big(Nt\theta'^2+Nb(1+\epsilon_2\phi)\theta'\phi'-f\theta-h\theta'\Big)=0, \tag{8.1.21}$$

$$\Big[1+\epsilon_2\phi\Big]\phi''+\epsilon_2\phi'^2+\frac{Nt}{Nb}\theta''-Sc\gamma_c\Big(1+\epsilon_3\theta\Big)^t exp\Big(\frac{-E}{1+\epsilon_3\theta}\Big)\phi-sSc\Big(2\phi+\frac{\eta}{2}\phi'\Big)$$
$$-Sc\Big(f\phi+h\phi'\Big)=0. \tag{8.1.22}$$

The transformed boundary conditions for the SWTC case are:

$$\text{at } \eta=0, f=0,\, g=\alpha_1,\, h=-w_0,\, \theta=1,\, \phi=1,$$
$$\text{as } \eta\longrightarrow\infty,\ f\longrightarrow 0,\, g\longrightarrow 1-\alpha_1,\ \theta\longrightarrow 0,\, \phi\longrightarrow 0. \tag{8.1.23}$$

The transformed boundary conditions for the STSF case are:

$$\text{at } \eta=0, f=0,\, g=\alpha_1,\, h=-w_0,\, (1+\epsilon_1\theta)\theta'=-\beta_{i1}(1-\theta),\, (1+\epsilon_2\phi)\phi'=-\beta_{i2}(1-\phi),$$
$$\text{as } \eta\longrightarrow\infty,\ f\longrightarrow 0,\, g\longrightarrow 1-\alpha_1,\ \theta\longrightarrow 0,\, \phi\longrightarrow 0, \tag{8.1.24}$$

where, β_{i1} and β_{i2} denote the thermal and solutal Biot numbers, respectively. For the nonlinear thermal radiation case the energy equation is replaced by:

$$\Big[(1+\epsilon_1\theta)+Rd\Big(1+\epsilon_3\theta\Big)^3\Big]\theta''+\Big[\epsilon_1+3Rd\epsilon_3\Big(1+\epsilon_3\theta\Big)^2\Big]\theta'^2-sPr\Big(2\theta+\frac{\eta}{2}\theta'\Big)+$$
$$Pr\Big(Nt\theta'^2+Nb(1+\epsilon_2\phi)\theta'\phi'-f\theta-h\theta'\Big)=0. \tag{8.1.25}$$

The nondimensional constants $M=\frac{\sigma_0 B_0^2}{\rho_f}\left(\frac{1-s\bar{t}}{\omega\sin\alpha^*}\right)$ denote magnetic, $We^2=\frac{\Gamma^2}{2\nu}x^2\left(\frac{\omega\sin\alpha^*}{1-s\bar{t}}\right)^3$ Weissenberg, $\theta_0=\frac{T_r-T_\infty}{T_w-T_\infty}$ variable viscosity, $\lambda=\frac{\nu\xi}{k^\star}\left(\frac{1-s\bar{t}}{\omega\sin\alpha^*}\right)$ porosity, $\alpha=\frac{c_F\xi}{\sqrt{k^\star}}$ inertia coefficient, $\lambda_m=\frac{g\beta_T\Big(T_0-T_\infty\Big)}{\Big(\omega\sin\alpha^*\Big)^2 L}\cos\alpha^*$ buoyancy force, $Nr=\frac{\beta_C\Big(C_0-C_\infty\Big)}{\beta_T\Big(T_0-T_\infty\Big)}$ buoyancy ratio, $Rd=\frac{16\sigma^\star T_\infty^3}{3k_e k_\infty}$ radiation, $Pr=\frac{\nu(\rho c)_f}{k_\infty}$ Prandtl number, $Nt=\frac{x}{\nu L}\frac{\tau D_T}{T_\infty}\frac{\Big(T_0-T_\infty\Big)}{\Big(1-s\bar{t}\Big)^2}$ thermophoresis, $Nb=\frac{x}{\nu L}\frac{\tau D_{b\infty}\Big(C_0-C_\infty\Big)}{\Big(1-s\bar{t}\Big)^2}$ Brownian motion, $\epsilon_3=\frac{x}{LT_\infty}\frac{(T_0-T_\infty)}{\Big(1-s\bar{t}\Big)^2}$ temperature difference, $E=\frac{E_a}{\kappa T_\infty}$ activation energy, $Sc=\frac{\nu}{D_{b\infty}}$ Schmidt number, $\gamma_c=\frac{k_r^2\Big(1-s\bar{t}\Big)}{\omega\sin\alpha^*}$

chemical reaction rate, and $\alpha_1 = \frac{\omega_1}{\omega}$ angular velocity ratio parameters.

8.1.6 Key engineering quantities

To evaluate the engineering aspects of the problem, the following parameters are considered:

1. The local skin friction coefficient: quantifies the surface shear stress.

2. The Nusselt number: represents the efficiency of convective heat transfer relative to conduction.

3. The Sherwood number: measures the effectiveness of convective mass transport compared to diffusion.

$$\begin{aligned}
&C_{f_x} = \frac{2\tau_{wx}}{\rho_f u_w^2},\ \tau_{wx} = \mu(T)\left[\frac{\partial u}{\partial z} + \frac{\Gamma}{\sqrt{2}}\left(\frac{\partial u}{\partial z}\right)^2\right],\ C_{g_y} = \frac{2\tau_{wy}}{\rho_f v_w^2},\ \tau_{wy} = \mu(T)\left[\frac{\partial v}{\partial z} + \frac{\Gamma}{\sqrt{2}}\left(\frac{\partial v}{\partial z}\right)^2\right],\\
&Nu_l = \frac{-x}{(T_w - T_\infty)}\left[1 + \frac{16\sigma^\star T_\infty^3}{3k(T)k_e}\right]\left(\frac{\partial T}{\partial z}\right)_{z=r_x},\ Nu_n = \frac{-x}{(T_w - T_\infty)}\left[1 + \frac{16\sigma^\star}{3k(T)k_e}T^3\right]\left(\frac{\partial T}{\partial z}\right)_{x=r_x},\\
&Sh = \frac{xq_m}{D_b(C_w - C_\infty)},\ q_m = -D_b\frac{\partial C}{\partial z}|_{z=r_x}.
\end{aligned} \tag{8.1.26}$$

By utilizing the above equations, the dimensionless forms of the x- and y-components of the local skin friction coefficients ($C_f^\star = Re^{\frac{1}{2}} C_{f_x}$, $C_g^\star = Re^{\frac{1}{2}} C_{g_y}$), the local Nusselt numbers ($Nu_l^\star = Re^{\frac{-1}{2}} Nu_l$ or $Nu_n^\star = Re^{\frac{-1}{2}} Nu_n$), and the local Sherwood number ($Sh^\star = Re^{\frac{-1}{2}} Sh$) are redefined as:

$$\begin{aligned}
&C_f^\star = \frac{2\theta_0}{\left[\theta_0 - \theta(0)\right]} f'(0)\left[1 + We^2 f'(0)\right],\ C_g^\star = \frac{-2\theta_0}{\left[\theta_0 - \theta(0)\right]} g'(0)\left[1 + We^2 g'(0)\right],\\
&Nu_l^\star = -\left[1 + \frac{Rd}{\left(1 + \epsilon_1\theta(0)\right)}\right]\theta'(0),\ Nu_n^\star = -\left[1 + \frac{Rd}{\left(1 + \epsilon_1\theta(0)\right)}(\epsilon_3 + 1)^3\right]\theta'(0),\\
&Sh^\star = -\phi'(0).
\end{aligned} \tag{8.1.27}$$

Here, $Nu_l^\star$ and $Nu_n^\star$ represent the Nusselt numbers in the cases of linear and nonlinear thermal radiation, respectively, $u_w = x\omega \sin\alpha^*(1 - s\bar{t})^{-1}$ is the reference velocity, $Re = \omega\nu^{-1}x^2\left[\sin\alpha^*(1 - s\bar{t})^{-1}\right]$ is the Reynolds's number.

8.2 Numerical approaches

This section details the numerical methodology utilized to solve the highly nonlinear system of ODEs (Eqs. (8.1.18)- (8.1.22)), along with their corresponding boundary conditions, Eq. (8.1.23) or (8.1.24). For cases involving nonlinear thermal radiation, Eq. (8.1.20) is replaced by Eq. (8.1.25) to incorporate the modified radiative heat transfer effects. The SRM is adopted to address this system of equations. It was originally developed to handle nonlinear differential equations in which the solution exhibits an exponentially decaying nature. It employs a Gauss-Seidel type relaxation strategy to decouple and linearize the governing system of differential equations. The method is simple and involves constructing an iterative scheme wherein the linear terms are evaluated at the current iteration level $(r+1)$ while the nonlinear terms are treated using the values from the previous iteration level (r). The following steps may be followed to decouple and linearize the system of equations.

a. The system of equations is organized such that the unknown function with the least dependence on other unknowns appears first, followed sequentially by those with increasing dependencies. In this study, the arrangement of the unknowns is chosen as h, ϕ, θ, g, and f.

b. An iteration scheme is developed for the first equation by assuming that only the linear terms in h and its higher derivatives are evaluated at the current iteration level $(r+1)$. All other terms, including linear and nonlinear terms in ϕ, θ, g, f, and their corresponding higher-order derivatives, as well as the nonlinear terms in h and its higher derivatives, are assumed to be known from the previous iteration level (r).

c. Similarly, the iteration scheme is developed for the next least dependent unknown, ϕ. As in step b, the scheme assumes that the linear terms in ϕ and its higher derivatives are evaluated at the current iteration level $(r+1)$. However, unlike step b, the already available current iteration values for h and its higher-order derivatives are incorporated directly.

d. This process is repeated for the remaining unknowns, θ, g, and f in sequence. At each step, the most recently available values of the functions and their corresponding higher-order derivatives, obtained from the earlier steps, are utilized to construct the iterative scheme.

For the linear thermal radiation and SWTC case, the above steps produce the following iteration scheme for Eqs. (8.1.18)-(8.1.22) and the corresponding boundary conditions, Eq. (8.1.23).

$$h'_{r+1} = -2f_r, \quad h_{r+1}(0) = -w_0, \tag{8.2.1}$$

$$\phi''_{r+1} + a_{1,r}\phi'_{r+1} + a_{2,r}\phi_{r+1} = R_{1,r}, \quad \phi_{r+1}(0) = 1,\ \phi_{r+1}(\infty) \to 0, \tag{8.2.2}$$

$$b_{1,r}\theta''_{r+1}+b_{2,r}\theta'_{r+1}+b_{3,r}\theta_{r+1}=R_{2,r}, \quad \theta_{r+1}(0)=1,\ \theta_{r+1}(\infty)\to 0, \tag{8.2.3}$$

$$c_{1,r}g''_{r+1}+c_{2,r}g'_{r+1}+c_{3,r}g_{r+1}=R_{3,r}, \quad g_{r+1}(0)=\alpha_1,\ g_{r+1}(\infty)\to 1-\alpha_1, \tag{8.2.4}$$

$$d_{1,r}h''_{r+1}+d_{2,r}f'_{r+1}+d_{3,r}f_{r+1}=R_{4,r}, \quad f_{r+1}(0)=0,\ f_{r+1}(\infty)\to 0, \tag{8.2.5}$$

where,

$$\begin{aligned}
a_{1,r}=&-Sc\frac{s\eta}{2}-Sch_{r+1},\ a_{2,r}=\epsilon_2\phi''_r-Sc\gamma_c\Big(1+\epsilon_3\theta_r\Big)^t\times exp\Bigg(\frac{-E}{1+\epsilon_3\theta_r}\Bigg)-2sSc-Scf_r,\\
R_{1,r}=&-\epsilon_2{\phi'}_r^2-\frac{Nt}{Nb}\theta''_r,\\
b_{1,r}=&1+Rd,\ b_{2,r}=-\frac{s\eta}{2}Pr+PrNb\Big(1+\epsilon_2\phi_{r+1}\Big)\phi'_{r+1}-h_{r+1},\ b_{3,r}=\epsilon_1\theta''_r-2sPr-f_r,\\
R_{2,r}=&-(\epsilon_1+PrNt){\theta'}_r^2,\\
c_{1,r}=&\frac{\theta_0}{\theta_0-\theta_{r+1}},\ c_{2,r}=\frac{\theta_0\theta'_{r+1}}{\Big(\theta_0-\theta_{r+1}\Big)^2}-\frac{s\eta}{2}-h_{r+1},\ c_{3.r}=-s-2f_r-M-\\
&\frac{\lambda\theta_0}{\theta_0-\theta_{r+1}}-2\alpha(1-\alpha_1)
\end{aligned}$$

$$\begin{aligned}
R_{3,r}=&-\frac{We^2\theta_0\theta'_{r+1}}{(\theta_0-\theta_{r+1})^2}{g'_r}^2-\frac{2We^2\theta_0}{(\theta_0-\theta_{r+1})}g'_rg''_r-M(1-\alpha_1)-\frac{\lambda\theta_0}{\theta_0-\theta_{r+1}}(1-\alpha_1)+\alpha g_r^2+\\
&\alpha(1-\alpha_1)^2-s(1-\alpha_1),\\
d_{1,r}=&\frac{\theta_0}{\theta_0-\theta_{r+1}},\ d_{2,r}=\frac{\theta_0\theta'_{r+1}}{\Big(\theta_0-\theta_{r+1}\Big)^2}-\frac{s\eta}{2}-h_{r+1},\ d_{3,r}=-s-M-\frac{\lambda\theta_0}{\theta_0-\theta_{r+1}},\\
R_{4,r}=&-\frac{We^2\theta_0\theta'_{r+1}}{(\theta_0-\theta_{r+1})^2}{f'_r}^2-\frac{2We^2\theta_0}{(\theta_0-\theta_{r+1})}f'_rf''_r+f_r^2-g_{r+1}^2-\lambda_m(\theta_{r+1}+Nr\phi_{r+1})\\
&+\alpha f_r^2+(1-\alpha_1)^2,
\end{aligned} \tag{8.2.6}$$

For the STSF case, the boundary equations in Eq. (8.1.24) is linearized as follows:

$$\begin{aligned}
&h_{r+1}(0)=-w_0,\ f_{r+1}(0)=0,\ g_{r+1}(0)=\alpha_1,\ \Big[1+\epsilon_1\theta_{r+1}(0)\Big]\theta'_{r+1}(0)=-\beta_{i1}\Big[1-\theta_{r+1}(0)\Big],\\
&\Big[1+\epsilon_2\phi_{r+1}(0)\Big]\phi'_{r+1}(0)=-\beta_{i2}\Big[1-\phi_{r+1}(0)\Big],\\
&f_{r+1}(\infty)\to 0,\ g_{r+1}(\infty)\to 1-\alpha_1,\theta_{r+1}(\infty)\to 0,\ \phi_{r+1}(\infty)\to 0.
\end{aligned} \tag{8.2.7}$$

In the case of nonlinear thermal radiation, instead of Eq. (8.2.3) the energy equation is linearized as follows:

$$\theta''_{r+1} + e_{1,r}\theta'_{r+1} + e_{2,r}\theta_{r+1} = R_{5,r}, \quad \theta_{r+1}(0) = 1,\ \theta_{r+1}(\infty) \to 0, \tag{8.2.8}$$

where

$$\begin{aligned} e_{1,r} &= -\frac{s\eta}{2}Pr + PrNb\Big(1+\epsilon_2\phi_{r+1}\Big)\phi'_{r+1} - h_{r+1},\ e_{2,r} = \epsilon_1\theta''_r - 2sPr - f_r,\\ R_{5,r} &= -Rd(1+\epsilon_3\theta_r)^3\theta''_r - (\epsilon_1 + PrNt + 3Rd\epsilon_3\Big(1+\epsilon_3\theta_r\Big)^2)\theta'^2_r. \end{aligned} \tag{8.2.9}$$

As the SLLM and SQLM, the SRM utilizes spectral collocation discretization and Gauss-Lobatto points to achieve numerical solutions for the problem (see sections 6.2 of chapter 6 and section 7.2 of chapter 7). At the collocation points,

- the unknown functions h_{r+1}, ϕ_{r+1}, θ_{r+1}, g_{r+1}, and f_{r+1}, at the $(r+1)^{th}$ iteration level are approximated in the form of series solution by:

$$\begin{cases} h_{r+1}(\eta) = \sum_{k=0}^{N} h_{r+1}(\eta_k)L_k(\eta_j),\\ \phi_{r+1}(\eta) = \sum_{k=0}^{N} \phi_{r+1}(\eta_k)L_k(\eta_j),\\ \theta_{r+1}(\eta) = \sum_{k=0}^{N} \theta_{r+1}(\eta_k)L_k(\eta_j),\\ g_{r+1}(\eta) = \sum_{k=0}^{N} g_{r+1}(\eta_k)L_k(\eta_j),\\ f_{r+1}(\eta) = \sum_{k=0}^{N} f_{r+1}(\eta_k)L_k(\eta_j). \end{cases} \tag{8.2.10}$$

- the corresponding n^{th} order derivatives are approximated using the Chebyshev differentiation matrix D. This matrix is subsequently transformed into $\mathbf{D} = \dfrac{2D}{\eta_\infty}$ to adjust for the domain of interest.

$$\begin{cases} \dfrac{d^n h_{r+1}}{d\eta^n}|_{\eta=\eta_j} = \sum_{k=0}^{N} D^n_{jk}h_{r+1}(\eta_k) = \mathbf{D}^n\boldsymbol{H}_{r+1},\\ \dfrac{d^n \phi_{r+1}}{d\eta^n}|_{\eta=\eta_j} = \sum_{k=0}^{N} D^n_{jk}\phi_{r+1}(\eta_k) = \mathbf{D}^n\boldsymbol{\Phi}_{r+1},\\ \dfrac{d^n \theta_{r+1}}{d\eta^n}|_{\eta=\eta_j} = \sum_{k=0}^{N} D^n_{jk}\theta_{r+1}(\eta_k) = \mathbf{D}^n\Theta_{r+1},\\ \dfrac{d^n g_{r+1}}{d\eta^n}|_{\eta=\eta_j} = \sum_{k=0}^{N} D^n_{jk}g_{r+1}(\eta_k) = \mathbf{D}^n\mathbf{G}_{r+1},\\ \dfrac{d^n f_{r+1}}{d\eta^n}|_{\eta=\eta_j} = \sum_{k=0}^{N} D^n_{jk}f_{r+1}(\eta_k) = \mathbf{D}^n\mathbf{F}_{r+1}, \end{cases} \tag{8.2.11}$$

$$\text{where, } L_k(x) = \prod_{k=0,k\neq j}^{N_x}\left(\frac{x-x_k}{x_j-x_k}\right), \tag{8.2.12}$$

is the Lagrange's polynomial. $j=0,1,2,\ldots,N$, $\boldsymbol{H}_{r+1}=\Big[h_{r+1}(\eta_0),h_{r+1}(\eta_1),\ldots,h_{r+1}(\eta_N)\Big]^T$, $\mathbf{\Phi}_{r+1}=\Big[\phi_{r+1}(\eta_0),\phi_{r+1}(\eta_1),\ldots,\phi_{r+1}(\eta_N)\Big]^T$, $\Theta_{r+1}=\Big[\theta_{r+1}(\eta_0),\theta_{r+1}(\eta_1),\ldots,\theta_{r+1}(\eta_N)\Big]^T$, $\mathbf{G}_{r+1}=\Big[g_{r+1}(\eta_0),g_{r+1}(\eta_1),\ldots,g_{r+1}(\eta_N)\Big]^T$, $\mathbf{F}_{r+1}=\Big[f_{r+1}(\eta_0),f_{r+1}(\eta_1),\ldots,f_{r+1}(\eta_N)\Big]^T$.

In view of Eqs. (8.2.10) and (8.2.11), for the SWTC boundary condition case Eqs. (8.2.1)-(8.2.5) can be formulated as:

$$
\begin{aligned}
&\mathbf{A}_1\mathbf{H}_{r+1}=\mathbf{B}_1,\ \mathbf{H}_{r+1}(x_N)=0,\\
&\mathbf{A}_2\mathbf{\Phi}_{r+1}=\mathbf{B}_2,\ \mathbf{\Phi}'_{r+1}(x_N)=1,\ \mathbf{\Phi}_{r+1}(x_0)=0,\\
&\mathbf{A}_3\mathbf{\Theta}_{r+1}=\mathbf{B}_3,\ \mathbf{\Theta}'_{r+1}(x_N)=1,\ \mathbf{\Theta}_{r+1}(x_0)=0,\\
&\mathbf{A}_4\mathbf{G}_{r+1}=\mathbf{B}_4,\ \mathbf{G}_{r+1}(x_N)=\alpha_1,\ \mathbf{G}_{r+1}(x_0)=1-\alpha_1,\\
&\mathbf{A}_5\mathbf{F}_{r+1}=\mathbf{B}_5,\ \mathbf{F}_{r+1}(x_N)=0,\ \mathbf{F}_{r+1}(x_0)=0,
\end{aligned}
\tag{8.2.13}
$$

where,

$$
\begin{aligned}
&\mathbf{A}_1=\mathbf{D},\ \mathbf{B}_1=-2f_r,\\
&\mathbf{A}_2=\mathbf{D}^2+diag\Big(a_{1,r}\Big)\mathbf{D}+diag\Big(a_{2,r}\Big)\mathbf{I},\ \mathbf{B}_2=R_{2,r},\\
&\mathbf{A}_3=diag(b_{1,r})\mathbf{D}^2+diag(b_{2,r})\mathbf{D}+diag(b_{3,r})\times\mathbf{I},\ \mathbf{B}_3=R_{2,r},\\
&\mathbf{A}_4=diag(c_{1,r})\mathbf{D}^2+diag(c_{2,r})\mathbf{D}+diag(c_{3,r})\times\mathbf{I},\ \mathbf{B}_4=R_{3,r},\\
&\mathbf{A}_5=diag(d_{1,r})\mathbf{D}^2+diag(d_{2,r})\mathbf{D}+diag(d_{3,r})\times\mathbf{I},\ \mathbf{B}_5=R_{4,r}.
\end{aligned}
\tag{8.2.14}
$$

For STSF case, the SWTC boundary conditions are replaced by:

$$
\begin{aligned}
&\Big[1+\epsilon_2\mathbf{\Phi}_{r+1}(x_N)\Big]\mathbf{\Phi}'_{r+1}(x_N)=-\beta_{i2}\Big(1-\mathbf{\Phi}_{r+1}(x_N)\Big),\\
&\Big[1+\epsilon_1\mathbf{\Theta}_{r+1}(x_N)\Big]\mathbf{\Theta}'_{r+1}(x_N)=-\beta_{i1}\Big(1-\mathbf{\Theta}_{r+1}(x_N)\Big).
\end{aligned}
\tag{8.2.15}
$$

In the case of nonlinear thermal radiation, the discretized energy equation is reformulated using the following matrix equation.

$$
\mathbf{A}_6\mathbf{\Theta}_{r+1}=\mathbf{B}_6,
\tag{8.2.16}
$$

where,

$$
\mathbf{A}_6=\mathbf{D}^2+diag(e_{1,r})\mathbf{D}+diag(e_{2,r})\times\mathbf{I},\ \mathbf{B}_6=R_{5,r}.
\tag{8.2.17}
$$

Initializing the SRM iteration requires an initial guess that satisfies the boundary conditions.

The suggested guess below meets this criterion.

$$f_0 = \eta e^{-\eta},\ g_0 = (1-\alpha_1) + (2\alpha_1 - 1)e^{-\eta},\ \theta_0 = e^{-\eta},\ \text{for SWTC},\ \theta_0 = \frac{1}{2}e^{-\vartheta_1\eta},\ \text{for STSF},$$
$$h_0 = -w_0 e^{-\eta},\ \phi_0 = e^{-\eta},\ \text{for SWTC},\ \phi_0 = \frac{1}{2}e^{-\vartheta_2\eta},\ \text{for STSF}, \tag{8.2.18}$$

where, $\vartheta_1 = \dfrac{\beta_{i1}}{1+0.5\epsilon_1}$, $\vartheta_2 = \dfrac{\beta_{i2}}{1+0.5\epsilon_2}$.

The decoupled system of matrices, as represented by Eq. (8.2.13), is numerically solved using the SRM, initialized with the conditions specified in Eq. (8.2.18). The iterative procedure is performed until convergence is achieved within a predefined tolerance level. To enhance the convergence rate, the Successive Over-Relaxation (SOR) technique is employed. For the present analysis, the optimal relaxation factor is selected as $\bar{\omega} = 0.96$.

8.2.1 Numerical convergence and stability of the SRM

The convergence and stability of the SRM scheme are assessed using the infinity norm to evaluate the residual error between successive iterations. The error is defined as:

$$Er = \max\Big(\|h_{r+1} - h_r\|_\infty, \|f_{r+1} - f_r\|_\infty, \|g_{r+1} - g_r\|_\infty, \|\theta_{r+1} - \theta_r\|_\infty, \|\phi_{r+1} - \phi_r\|_\infty\Big), \tag{8.2.19}$$

where h, f, g, θ, and ϕ are the dependent variables, and r denotes the iteration number. Figure 7.2.1 presents the SRM's norm of residual errors against the number of iterations for two boundary conditions: SWTC and STSF. For this analysis, the convergence tolerance error is set to $\epsilon = 10^{-9}$, with the number of collocation points fixed at 100. The error decreases almost linearly with iterations for all dependent functions. The SRM achieves rapid convergence, with the norm of residual errors for all variables falling below 10^{-9} after 20 iterations in the SWTC case and 10 iterations in the STSF case. These results highlight the robustness and efficiency of the SRM scheme for solving nonlinear boundary layer problems. The linear trend in error reduction indicates systematic convergence, while the faster convergence in the STSF case reflects the sensitivity to boundary conditions. The use of high tolerance and adequate collocation points ensures precise and reliable results.

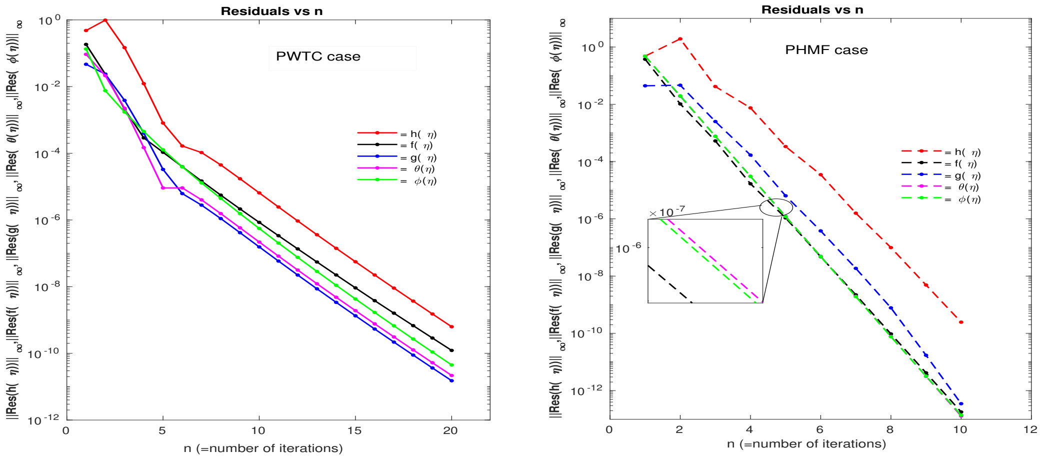

(a) (b)

Figure 8.2.1: Residuals against number of iteration for (a): SWTC, (b): STSF cases

8.2.2 Code validation

Additionally, the accuracy of the SRM has been validated by comparison with the SLLM and the built-in MATLAB solver `bvp4c`, as demonstrated in Table 8.2.1. The comparison focuses on the numerical values of surface shear stresses (both tangential and azimuthal components), as well as the heat and mass transfer rates for various values of the Prandtl number. The results demonstrate that the maximum variation between the SRM and SLLM solutions is $8.75 \times 10^{-7}\%$, while the maximum variation between the SRM and `bvp4c` solutions is $1.03 \times 10^{-6}\%$. These findings indicate that the SRM exhibits high accuracy and excellent agreement with both the SLLM and `bvp4c` methods, thereby confirming the reliability of the current numerical approach.

Table 8.2.1: Comparison of numerical results obtained using the SRM, SLLM, and MATLAB's `bvp4c` solver.

pr	Shear stresses and transfer rates	SRM	SLLM	`bvp4c`
0.5	$f'(0)$	1.0511638180	1.0511638088	1.0511638072
	$g'(0)$	-0.0446613088	-0.0446613088	-0.0446613085
	$\theta'(0)$	-0.5013161877	-0.5013161877	-0.5013161876
	$\phi'(0)$	-1.4471526403	-1.4471526406	-1.4471526401
1	$f'(0)$	1.0446418257	1.0446418173	1.0446418157
	$g'(0)$	-0.0441062237	-0.0441062237	-0.0441062234
	$\theta'(0)$	-0.6150455445	-0.6150455445	-0.6150455444
	$\phi'(0)$	-1.4391530463	-1.4391530463	-1.4391530458

Table 8.2.2 presents the grid independence test for shear stress and transfer rates across various grid resolutions. Convergence is achieved within 10 iterations for the tested grid points,

with no significant improvement observed beyond N = 50 within the prescribed tolerance. This confirms the reliability of the numerical method employed.

Table 8.2.2: Grid independence test for shear stress and transfer rates solutions

N	$f'(0)$	$g'(0)$	$\theta'(0)$	$\phi'(0)$
10	1.0772695113	-0.0612172990	-0.5527400676	-1.1372942347
20	1.0682499938	-0.0473997691	-0.5500495904	-1.1266242816
50	1.0682093225	-0.0473725483	-0.5500448194	-1.1265846995
75	1.0682093222	-0.0473725483	-0.5500448194	-1.1265846993
100	1.0682093222	-0.0473725483	-0.5500448194	-1.1265846993
120	1.0682093222	-0.0473725483	-0.5500448194	-1.1265846993

8.3 Results and Discussion

In this section, the numerical results of the transformed system of Eqs. (8.1.18)-(8.1.22) and (8.1.25), subject to the boundary conditions described by Eqs. (8.1.23) or (8.1.24), are presented and analyzed through contour and 3D plots and tables, illustrating the influence of various relevant parameters on dimensionless tangential, azimuthal, and radial velocities, temperature, and nanoparticle concentration. The investigation focuses on understanding the influence of variable transport properties on the thermally radiative and chemically reactive unsteady flow of rotating Williamson nanofluid over an axially rotating vertical cone. Since the impacts of various parameters on flow dynamics exhibit similar trends for the two boundary condition cases, we focus on the SWTC case for the primary analysis. However, it was observed that the variable thermal conductivity parameter (ϵ_1) and variable diffusivity parameter (ϵ_2) demonstrated contrasting effects for the two boundary conditions. Consequently, results for both boundary conditions are presented when examining the influence of these specific parameters. The numerical simulations were conducted using a range of parameters selected to ensure stable and rapidly convergent solutions. Additionally, the study investigates the responses of physical quantities such as the skin friction coefficient, the Nusselt and Sherwood numbers to variations in the prominent dimensionless parameters. These parameter ranges are defined as follows: $0.5 \leq Pr, M, Rd, Nr \leq 3.5$, $0.2 \leq We \leq 0.8$, $0.5 \leq \lambda, \alpha, \gamma_c \leq 3$, $0.05 \leq \epsilon_1, \epsilon_2 \leq 1.5$, $0.3 \leq \beta_{i1}, \beta_{i2} \leq 0.8$, $0.1 \leq \epsilon_3 \leq 0.35$, $0.5 \leq \lambda, Sc \leq 2.5$, $-1.5 \leq w0 \leq 1.5$, $-2 \leq \theta_0 \leq -0.5$, $0.3 \leq \alpha_1 \leq 0.7$, $0.5 \leq s \leq 2$, $0 \leq E \leq 2$, $0.2 \leq Nt \leq 1.2$, $0.2 \leq Nb \leq 1.6$, and $0 < t < 0.8$. The boundary layer edge, η_∞, was chosen to range from 6 to 15, depending on the minimum number of iterations required to achieve convergence within the specified tolerance for different parameter values.

8.3.1 Velocity variations

Figure 8.3.1-8.3.8 present the variations in tangential, circumferential, and radial velocities as influenced by changes in the parameters M, θ_0, λ_m, β_w, Nr, λ, and s. These parameters significantly impact the velocity distributions within the boundary layer of the rotating Williamson nanofluid over the axially rotating vertical cone. As depicted in Figure 8.3.1, an increase in M results in a decrease in the tangential velocity, while simultaneously enhancing the azimuthal velocity. This phenomenon occurs due to the opposing Lorentz force generated by the interaction between the magnetic field and the electrically conducting fluid. The Lorentz force inhibits the fluid's motion in the tangential direction and induces a rise in the azimuthal velocity, altering the flow structure within the boundary layer.

The effect of variable viscosity parameter (θ_0) on the velocity distributions is illustrated in Figure 8.3.2. Unlike the magnetic field, an increase in θ_0 leads to an increase in the tangential velocity while reducing the azimuthal velocity. This behavior can be explained by the reduction in fluid viscosity with increasing θ_0, which facilitates enhanced tangential motion. Additionally, the influence of θ_0 diminishes near the cone's surface and at the boundary layer edge for both velocity components. An increase in θ_0 from -2 to -0.5 results in a rise in the maximum primary velocity, which increases from approximately 0.3015 at $\eta = 0.696$ to 0.3489 at $\eta = 0.618$. Conversely, the minimum value of the secondary velocity (decreases from 0.4667 at $\eta = 1.146$ to 0.4568 at $\eta = 1.038$, demonstrating the localized effects of θ_0 on the flow structure.

Figure 8.3.3-8.3.4 illustrate the effects of λ_m and Nr on the tangential and azimuthal velocity profiles. In rotating systems, these parameters play a crucial role in shaping the flow dynamics by modulating the thermal and solutal buoyancy forces within the boundary layer. As shown in Figure 8.3.3 , an increase in λ_m leads to an enhancement in the tangential velocity profile, while the azimuthal velocity profile decreases. Physically, the buoyancy parameter quantifies the relative significance of buoyancy-driven forces compared to inertial forces in the flow.

A higher value of λ_m indicates stronger thermal buoyancy effects caused by the temperature gradient between the cone surface and the surrounding fluid. This enhanced thermal buoyancy force acts predominantly along the tangential direction, accelerating the fluid and thereby increasing the tangential velocity. Conversely, the redistribution of forces due to the increased thermal buoyancy reduces the energy available to sustain the azimuthal motion. Consequently, the azimuthal velocity diminishes as the flow becomes more aligned with the tangential direction. On the other hand, Nr quantifies the relative contribution of solutal buoyancy compared to thermal buoyancy.

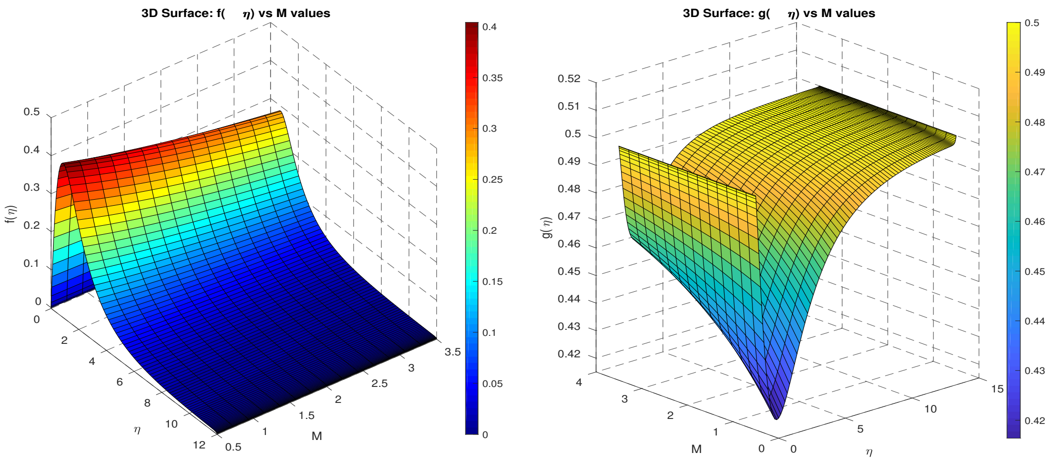

(a) (b)

Figure 8.3.1: Impact of M on (a): f, (b): g

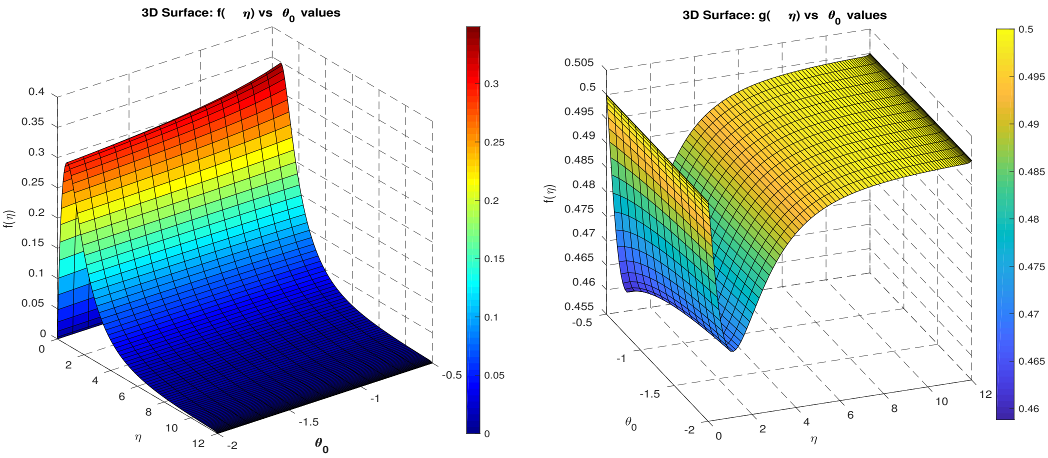

(a) (b)

Figure 8.3.2: Impact of θ_0 (a): f, (b): g

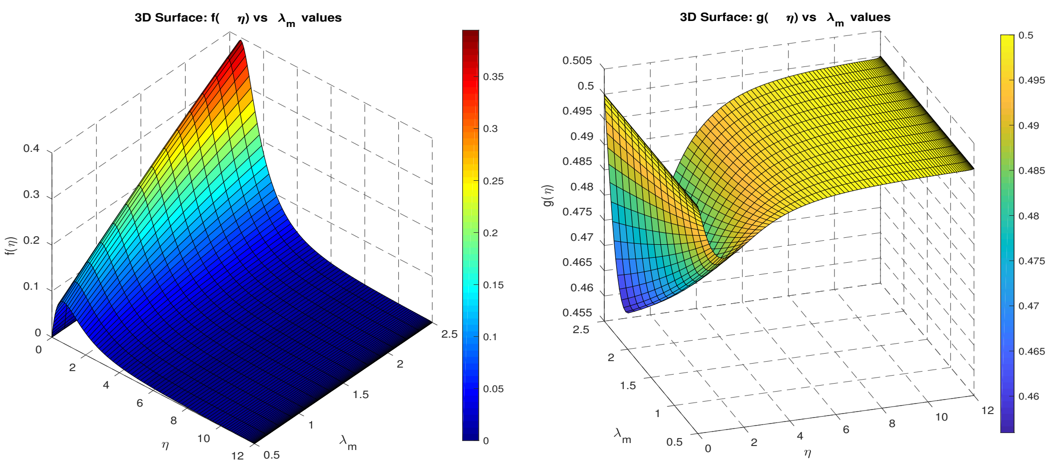

(a) (b)

Figure 8.3.3: Impact of λ_m on (a): f, (b): g

As Nr increases, the solutal buoyancy effects dominate, adding to the buoyancy forces that drive the fluid tangentially. This combined enhancement of thermal and solutal buoyancy forces leads to a further increase in the tangential velocity as depicted in Figure 8.3.4a. Similar to the effect of λ_m, the stronger solutal buoyancy forces associated with a higher Nr suppress the azimuthal velocity by diminishing the dominance of centrifugal effect. Consequently, as observed in Figure 8.3.4b, the azimuthal velocity decreases, and the flow becomes more aligned with the tangential direction.

The fluid velocity variation subject to the influence of the suction/injection (β_w) is demonstrated in Figure 8.3.5. As β_w increases, the tangential velocity decreases, while the azimuthal velocity increases. Specifically, as β_w scales from -1.5 to 1.5, the peak of f decreases by 29.5% , while the crest of g increases 2.4%. This behavior aligns with the physical significance of the suction/injection. When $\beta_w > 0$, fluid is drawn away from the boundary layer into the surface, reducing tangential momentum and causing a decline in tangential velocity. This energy redistribution enhances azimuthal velocity as the fluid aligns more with the rotational dynamics of the system. Conversely, for $\beta_w < 0$, fluid is introduced into the boundary layer, disrupting the tangential flow by adding low-momentum fluid, which further decreases tangential velocity. However, this added fluid contributes to rotational motion, resulting in a modest increase in azimuthal velocity. The quantitative trends demonstrate that suction primarily stabilizes the tangential flow by reducing boundary layer thickness, while injection redistributes energy, enhancing azimuthal motion.

Figure 8.3.6 illustrates the influence of λ on tangential and azimuthal velocity distribution. As λ increases, the tangential velocity contours (Figure 8.3.6a) demonstrate an expansion of regions with lower intensity, indicating a reduction in velocity magnitude. Conversely, the azimuthal velocity contours (Figure 8.3.6b) reveal a broader distribution of higher intensity regions, signifying an increase in velocity magnitude. This behavior highlights the opposing trends of tangential and azimuthal velocities in response to variations in the porosity parameter. λ characterizes the resistance induced by the porous medium on fluid flow. A higher λ signifies increased permeability of the medium, which exerts greater drag on the tangential motion of the fluid, thereby reducing its velocity. Simultaneously, the increased porosity facilitates enhanced radial flow interactions and swirl effects, leading to an amplification of azimuthal velocity.

This result may find applications in biomedical engineering, where porous rotating devices like artificial kidneys or blood filtration units rely on precise permeability to control fluid transport and separation of toxins, and in aerospace, where turbine blades often incorporate porous structures to improve cooling efficiency. Adjusting permeability allows tailored coolant flow rates under high rotational and thermal stresses.

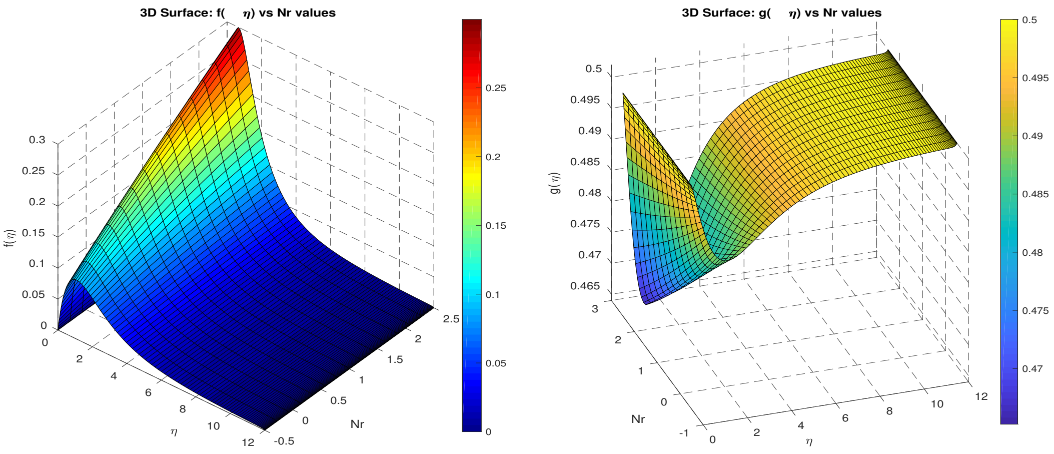

(a) (b)

Figure 8.3.4: Impact of Nr on (a): f, (b): g

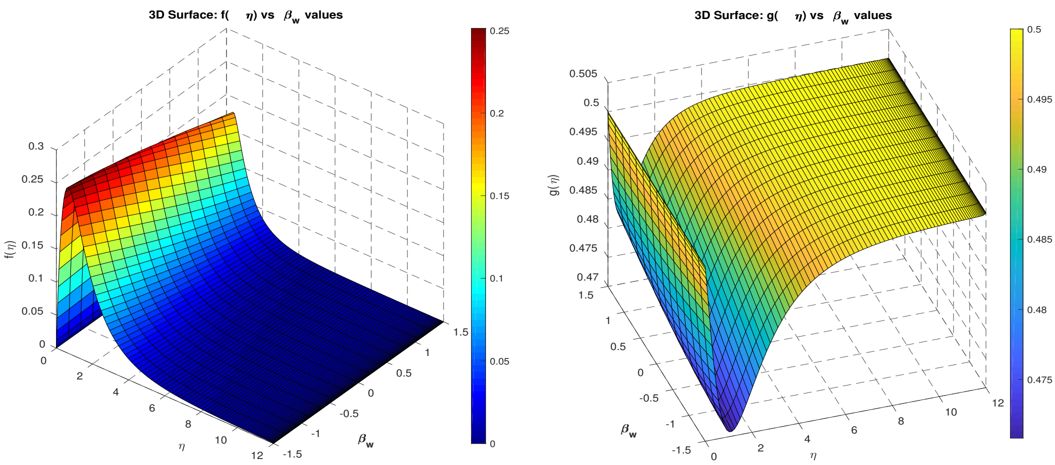

(a) (b)

Figure 8.3.5: Impact of β_{w} on (a): f, (b): g

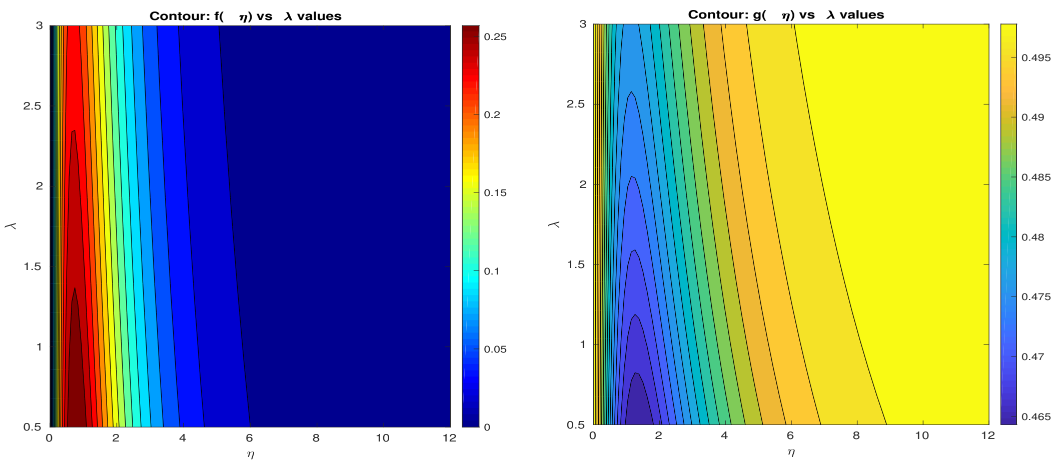

(a) (b)

Figure 8.3.6: Impact of λ (a): f, (b): g

Figure 8.3.7 depicts the variation of the normal velocity (h) component in response to changes in λ and s parameters. As the magnitudes of these parameters increase, the normal velocity exhibits a corresponding rise, evidenced by the expansion of regions with higher intensity colors in the figure. Physically, this behavior can be attributed to the combined effects of enhanced fluid permeability due to increased porosity, facilitating greater flow penetration, and the influence of unsteadiness, which induces temporal accelerations in the fluid, thereby augmenting the velocity magnitude. However, due to the influence of the free-stream velocity, v_e, the higher normal velocity values remain confined near the wall of the cone.

Figure 8.3.8 demonstrates the contrasting responses of f and g components to variations in s. Specifically, as s increases, the tangential velocity field diminishes, while the azimuthal velocity intensifies. Physically, this behavior can be explained by the interplay between the temporal acceleration induced by unsteadiness and the redistribution of momentum within the flow. Higher values of s amplify temporal effects, causing a deceleration in the tangential direction due to increased resistance from unsteady forces, while simultaneously enhancing rotational effects that strengthen the azimuthal velocity component.

8.3.2 Temperature variations

Figure 8.3.9- 8.3.12 present the temperature distribution within the boundary layer region as influenced by variations in key parameters, including Pr, β_w, ϵ_1, λ_m, s , and linear (Rd_l) and nonlinear (Rd_n) radiation parameters. In Fig. 8.3.9, both Pr and β_w exhibit a reducing effect on the temperature distribution. As these parameters increase, the thermal boundary layer becomes thinner, as evidenced by the expansion of lower-intensity contour colors. This behavior reflects enhanced thermal diffusivity associated with higher pr value and β_w values. Figure 8.3.10 presents a novel finding of this study. The increase in ϵ_1, produces a contrasting effect between the SWTC and the STSF cases. Specifically, for the SWTC case, an increase in ϵ_1 enhances the temperature field, whereas for the STSF case, it leads to a reduction in the temperature field. Physically, this behavior can be explained as follows: In the SWTC case, an increase in ϵ_1 leads to higher thermal diffusivity, which enhances the fluid's capacity to conduct thermal energy, thereby increasing its kinetic energy and resulting in an elevated temperature distribution. In contrast, in the STSF case, a higher ϵ_1 corresponds to an increase in the heat flux at the cone's surface. This enhanced heat flux reduces the temperature gradient within the fluid, leading to a decrease in the overall temperature field.

The influence of λ_m and s on the temperature profile is illustrated in Figure 8.3.11. As observed, an increase in λ_m leads to a reduction in the temperature field within the boundary layer.

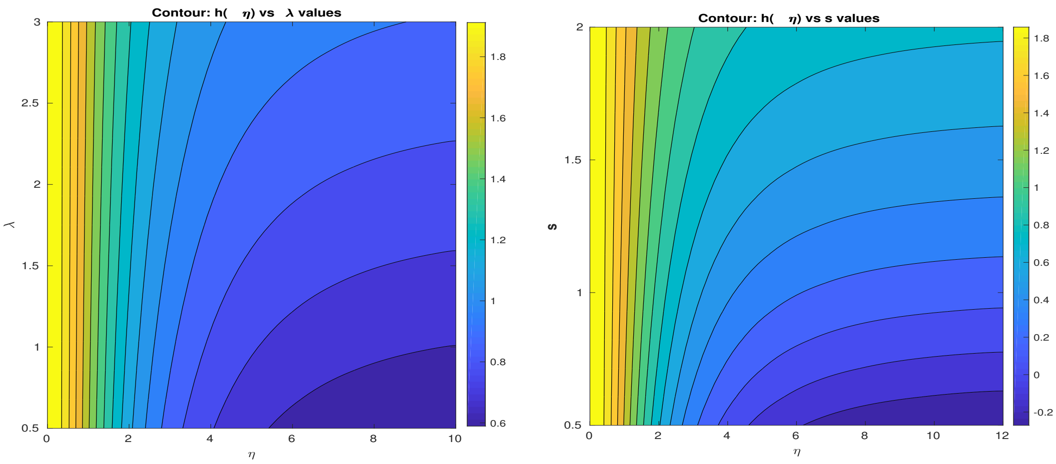

(a) (b)

Figure 8.3.7: Impact of (a): λ , (b): s on h

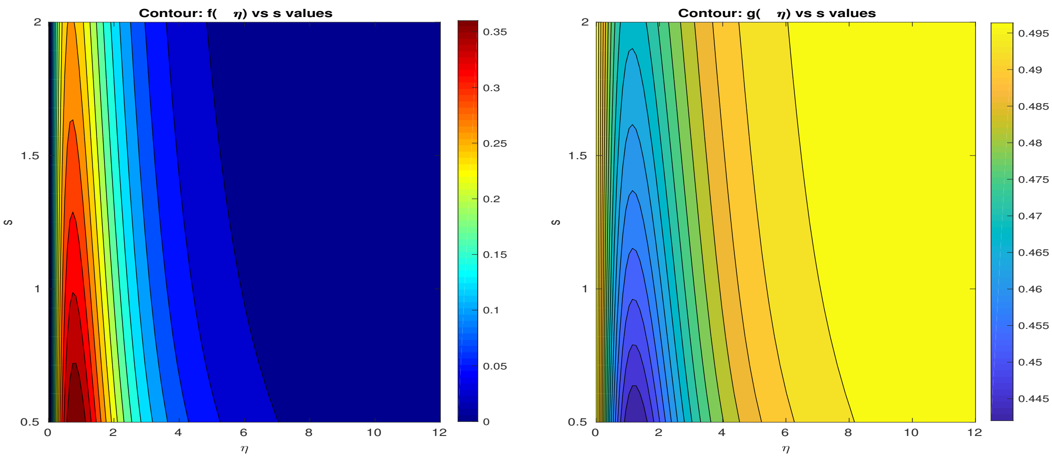

(a) (b)

Figure 8.3.8: Impact of s on (a): f, (b): g

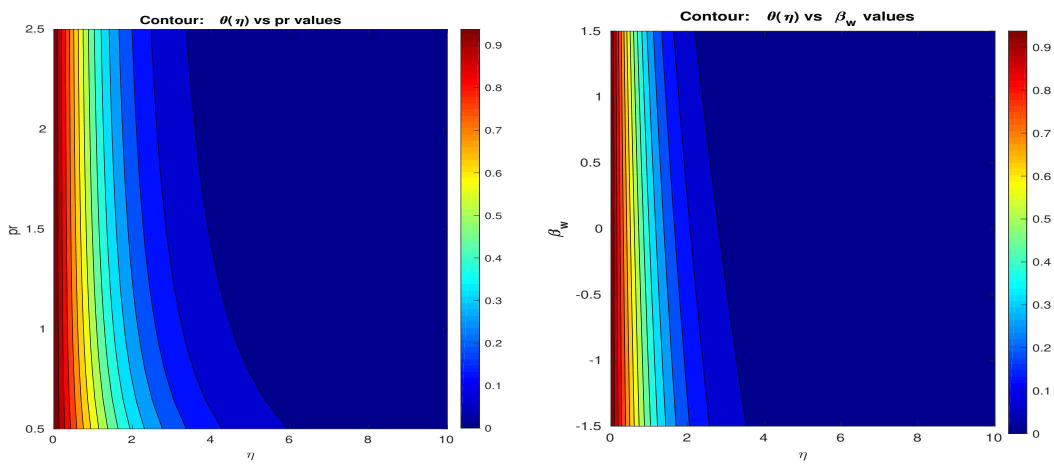

(a) (b)

Figure 8.3.9: Impact of (a): pr, (b): β_{w} on θ

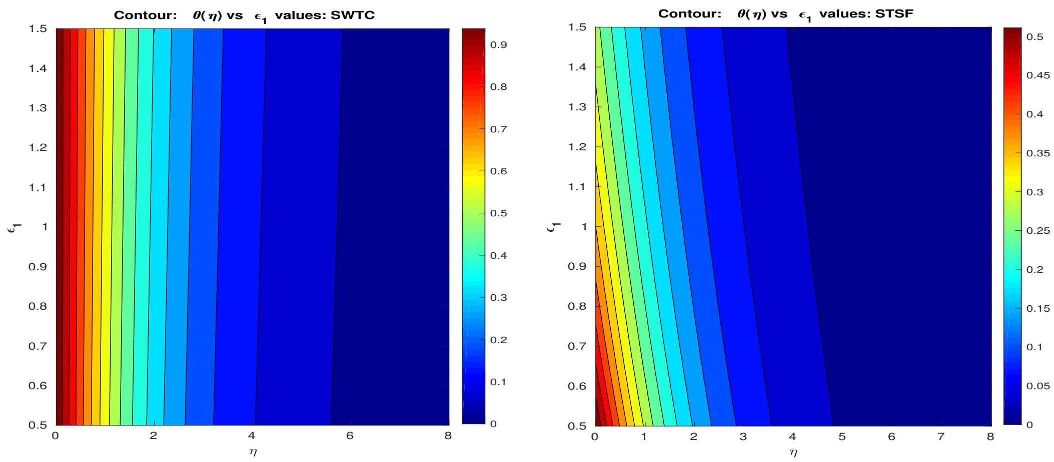

(a) (b)

Figure 8.3.10: Impact of ϵ_1 on θ for (a): SWTC case , (b): STSF case

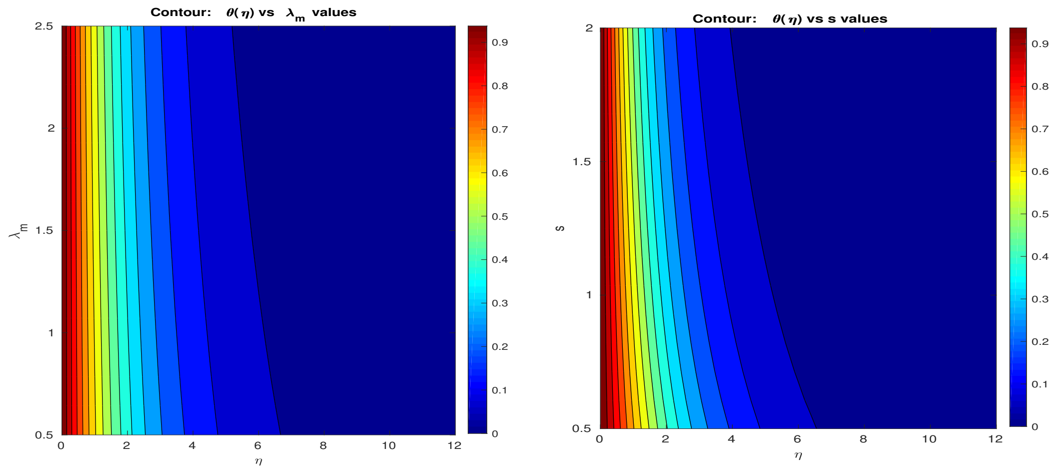

(a) (b)

Figure 8.3.11: Impact of (a): λ (b): s on θ

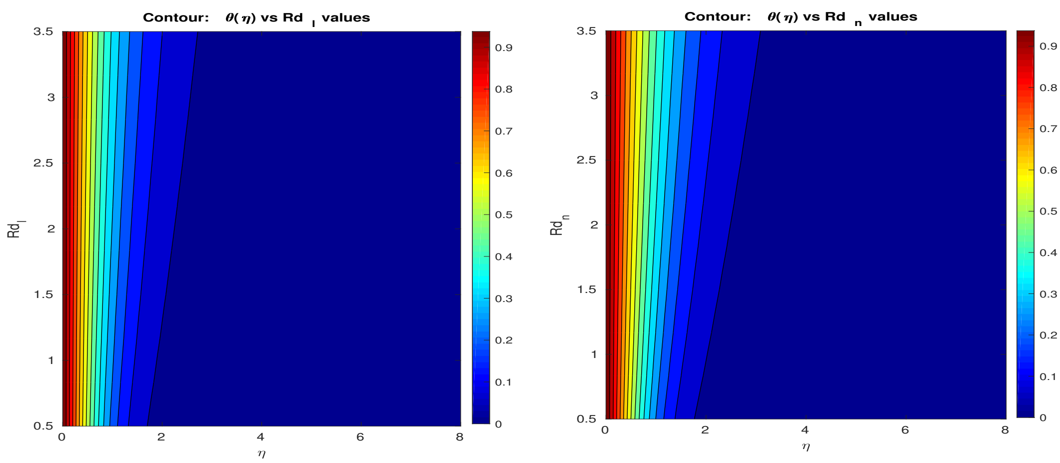

(a) (b)

Figure 8.3.12: Impact of (a): $\mathrm{Rd_l}$, (b): $\mathrm{Rd_n}$ on θ

Physically, this can be attributed to the buoyancy-induced convection, which enhances the fluid's upward motion, thereby thinning the thermal boundary layer and reducing the overall temperature in the region.

Similarly, an increase in s diminishes the temperature distribution. This behavior occurs because higher s implies stronger temporal variations in the flow field, which reduce the duration of thermal interaction between the fluid particles and the heated surface. Consequently, the fluid absorbs less heat, resulting in a reduced temperature profile. Figure 8.3.12 illustrates the effects of Rd_l and Rd_n on the thermal distribution. Both parameters enhance the thermal boundary layer thickness, indicating increased heat transfer. However, in the case of nonlinear radiation, the temperature contours (Figure 8.3.12b) exhibit higher intensity in contour coloration, signifying a more pronounced rise in the temperature field compared to the linear radiation case. This difference arises from the nonlinear dependency of radiative heat transfer on temperature, which amplifies thermal energy transfer in the boundary layer.

8.3.3 Nanoparticles concentration variations

Figure 8.3.13-8.3.16 depict the changes in nanoparticle concentration (ϕ) under the influence of various parameters, including ϵ_2, β_w, s, γ_c, E, Nr, and Sc parameters. Similar to the behavior observed in the thermal boundary layer, the nanoparticle concentration profile demonstrates contrasting trends between the SWTC and STSF scenarios for variations in ϵ_2. Specifically, an increase in ϵ_2 enhances the nanoparticle concentration in the SWTC scenario, whereas it reduces the concentration in the STSF scenario, as shown in Figure 8.3.13, respectively. This disparity highlights the differing mechanisms of diffusion and boundary conditions influencing the nanoparticle transport in each case. The nanoparticle concentration declines with increasing β_w and s, as depicted in Figure 8.3.14a and Figure 8.3.14b, respectively. This behavior arises from enhanced nanoparticle removal via suction or dilution due to injection for higher β_w, while increasing s induces temporal accelerations that destabilize the concentration boundary layer, attenuating nanoparticle accumulation. These phenomena underscore the pronounced sensitivity of nanoparticle transport to boundary dynamics and flow unsteadiness.

In Figure 8.3.15a, an increase in γ_c leads to a suppression of the nanoparticle concentration, whereas in Figure 8.3.15b, an increase in E enhances the concentration profile. For the rotating Williamson nanofluid over a vertical cone, the decline in concentration with higher γ_c can be attributed to intensified reactive consumption of nanoparticles, exacerbated by the centrifugal forces in the unsteady rotating flow, which enhance the interaction of nanoparticles with the reactive medium near the cone surface. Conversely, an increase in E raises the energy barrier for chemical reactions, thereby reducing reaction rates.

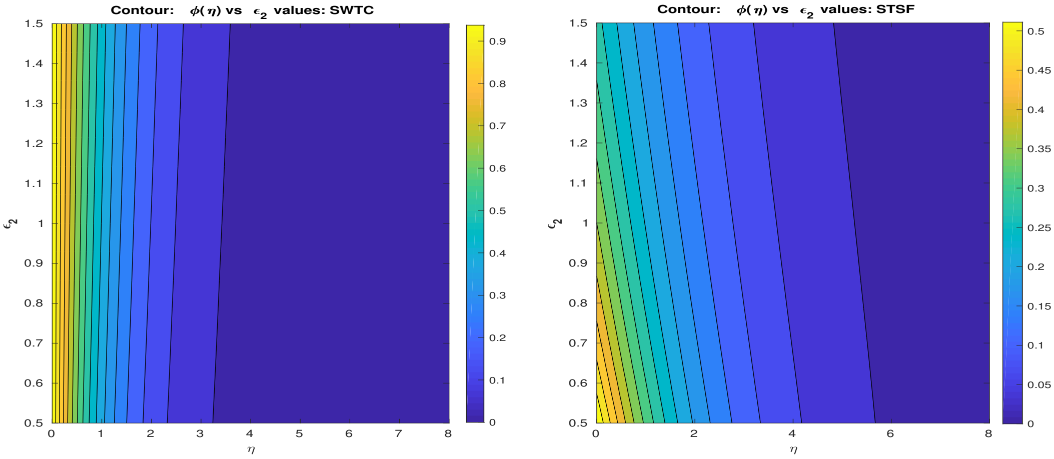

(a) (b)

Figure 8.3.13: Impact of ϵ_2 on ϕ for (a): SWTC case , (b): STSF case

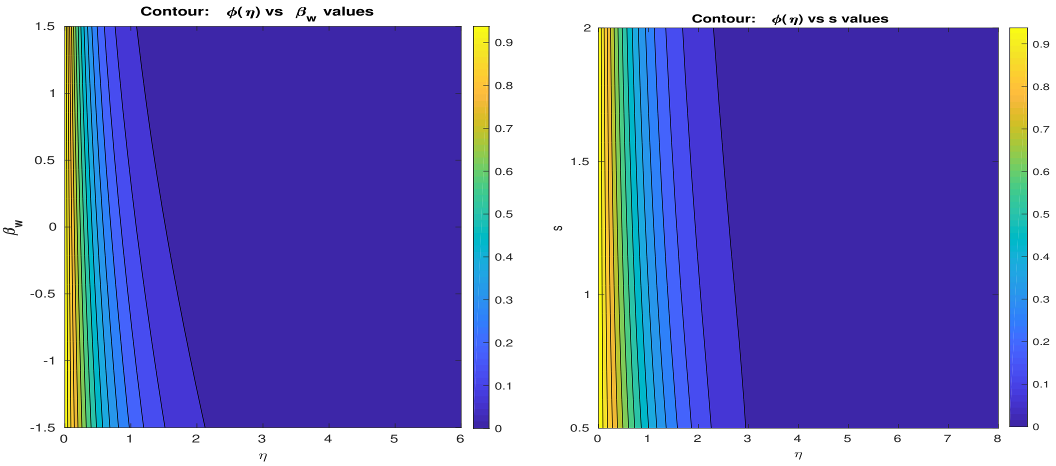

(a) (b)

Figure 8.3.14: Impact of (a): β_{w}, (b): s on ϕ

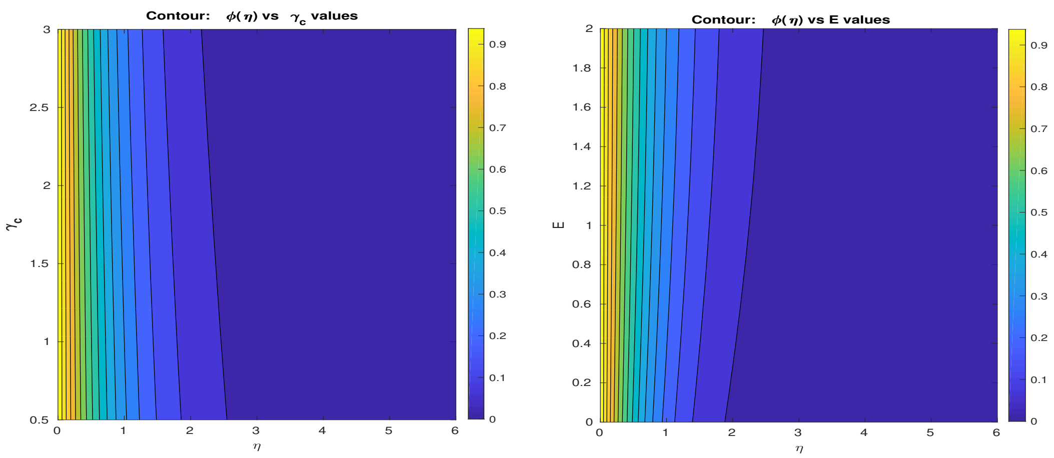

(a) (b)

Figure 8.3.15: Impact of (a): γ_{c}, (b): E on ϕ

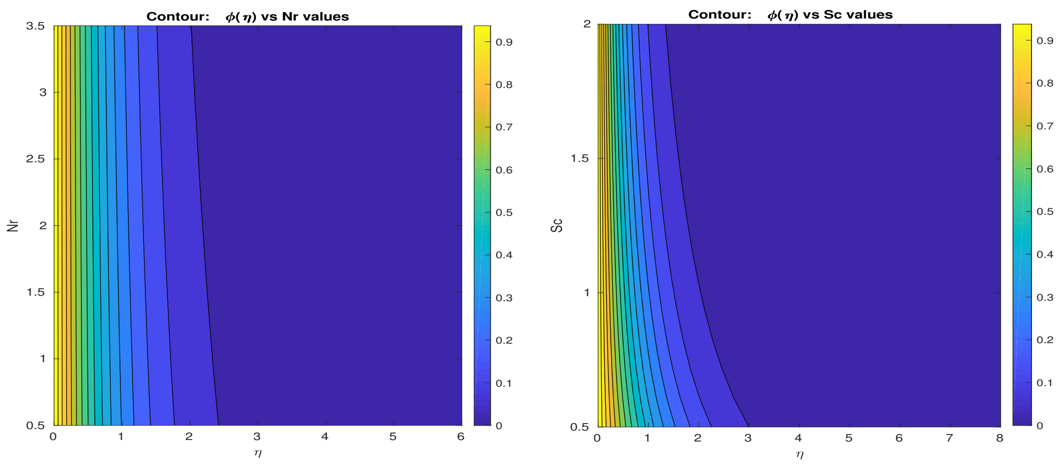

(a) (b)

Figure 8.3.16: Impact of (a): Nr, (b): Sc on ϕ

This preservation of nanoparticle integrity, coupled with the inherent shearing effects of the Williamson fluid in the rotating boundary layer, facilitates greater nanoparticle retention within the fluid domain, resulting in an enhanced concentration profile.

Figure 8.3.16a and 8.3.16b examine the influence of Nr and Sc on the concentration distribution. As evident from the figures, an increase in both parameters results in a decline in the concentration profile and a corresponding reduction in the solutal boundary layer thickness. Physically, a higher buoyancy ratio intensifies the competition between thermal and solutal buoyancy forces, enhancing the dominance of concentration-driven flow. As a result the concentration profile diminishes due to this enhanced solutal buoyancy force. Similarly, an increase in Sc, indicative of reduced mass diffusivity relative to momentum diffusivity, inhibits solute diffusion across the boundary layer, leading to a sharper concentration gradient and a thinner solutal boundary layer. This behavior underscores the intricate interplay between buoyancy effects and diffusive transport in the unsteady rotating flow of Williamson nanofluids.

8.3.4 Contour and 3D visualization of skin friction, heat, and mass transfer rates

This section analyzes the influence of key parameters on the tangential and azimuthal skin friction coefficients, as well as the heat and nanoparticle mass transfer rates. The contour plot in Figure 8.3.17a reveals that maintaining the suction/injection parameter at its lower value while increasing the variable viscosity parameter from -2 to -0.5 results in a 27.85% reduction in the tangential skin friction coefficient. Conversely, fixing the variable viscosity parameter at its lower value and increasing the suction/injection parameter from -1.5 to 1.5 leads to a 28.69% increase in the tangential skin friction coefficient. For the azimuthal skin friction coefficient, as shown in Figure 8.3.17b, the former case results in a 37.85% decrease. In the latter case, the azimuthal skin friction coefficient increases significantly by 106.14%. When both parameters are simultaneously increased within their respective ranges, the tangential skin friction coefficient experiences an overall rise of 20.32%, whereas the azimuthal skin friction coefficient exhibits an impressive 128.98% enhancement.

Figure 8.3.18a depicts the heat transfer rate as a function of temperature-dependent thermal conductivity and linear radiation, whereas Figure 8.3.18b illustrates the heat transfer rate variations with temperature-dependent thermal conductivity and nonlinear radiation. For both scenarios, an increase in the variable thermal conductivity parameter leads to a reduction in the heat transfer rate, while an increase in the linear or nonlinear radiation parameter enhances it. When both parameters are simultaneously increased within their respective ranges, the heat transfer rate rises by 58.34% in the linear radiation case and 81.10% in the nonlinear radiation case, demonstrating the pronounced impact of radiation mechanisms on thermal energy transfer.

Figure 8.3.19a examines the influence of surface and form drag forces on the tangential skin friction coefficient in the context of a Darcy-Forchheimer porous medium. Both λ and α are observed to decrease the tangential skin friction coefficient, suggesting that in systems involving rotating fluids within a rotating frame, incorporating a Darcy-Forchheimer medium effectively accounts for surface and form drag forces. This, in turn, implies that reducing energy losses due to surface drag forces necessitates careful consideration of these parameters within the porous medium framework. Figure 8.3.19b depicts the impact of the γ_c and ϵ_2 on the mass transfer rate.

An increase in γ_c enhances the mass transfer rate, whereas a rise in ϵ_2 suppresses it. Specifically, for the prescribed variation in γ_c with ϵ_2 fixed at 0.5, the mass transfer rate increases by 17.49%. Conversely, for the indicated variation in ϵ_2, the mass transfer rate decreases by 19.80%. When both parameters are simultaneously increased within the specified ranges, the competing effects result in an overall reduction of the mass transfer rate by 6.76%. This behavior underscores the intricate interplay between chemical reactivity and diffusivity in governing mass transport in the boundary layer.

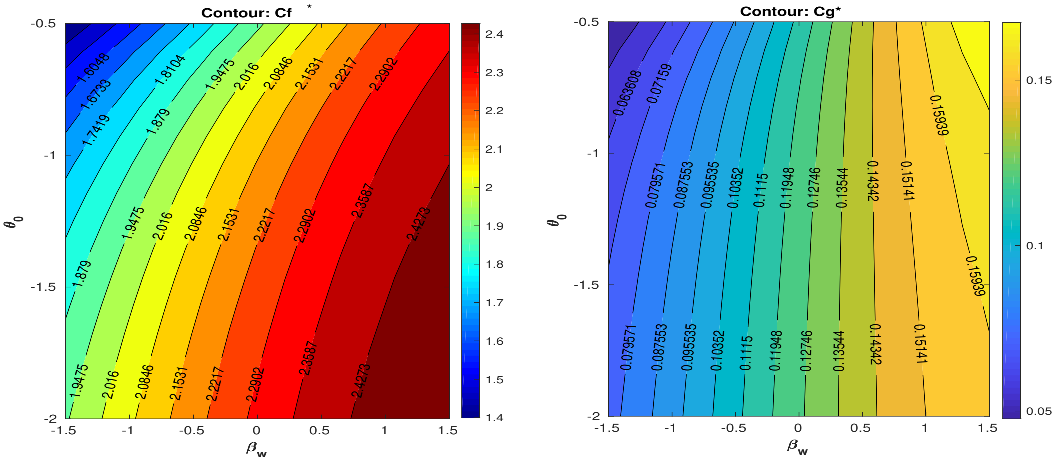

(a) (b)

Figure 8.3.17: Impact of θ_0 and $\beta_{\rm w}$ on (a): $\rm Cf^\star$, (b): $\rm Cg^\star$

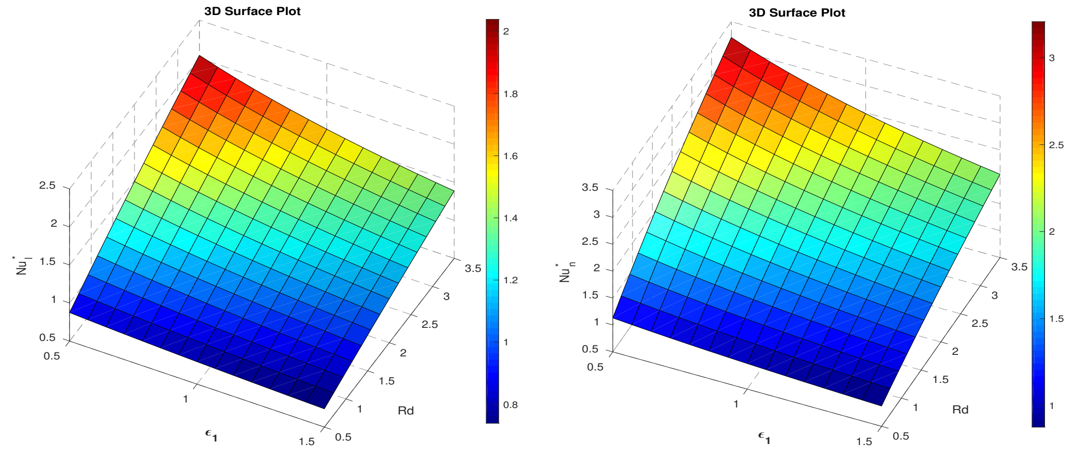

(a) (b)

Figure 8.3.18: Impact of ϵ_1 and $\rm Rd$ on (a): $\rm Nu_l^\star$, (b): $\rm Nu_n^\star$

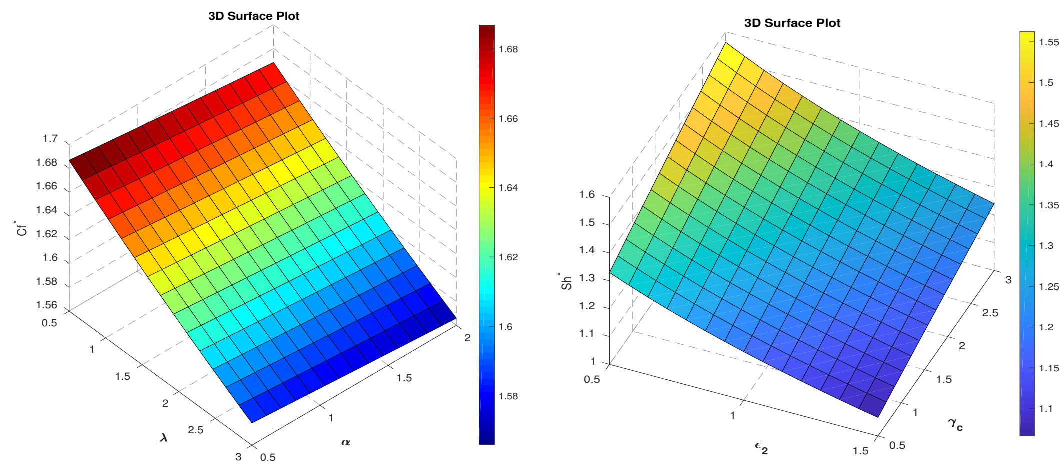

(a) (b)

Figure 8.3.19: Impact of (a): λ and α on $\rm Cf^\star$, (b): ϵ_2 and γ_c on $\rm Sh^\star$

8.3.5 Tabulated analysis of skin friction, heat and mass transfer variations

The tabulated results reveal the influence of various physical parameters on the skin friction coefficients (Cf^* and Cg^*), the surface heat (Nu^*) and mass (Sh^*) transfer rates. An increase in M, s, and pr reduces Cf^*, whereas higher values of θ_0 and Nt increase Cf^*. Conversely, these parameters exert an opposite effect on Cg^*. Additionally, We, and Nb are found to enhance both Cf^* and Cg^*. The buoyancy force plays a significant role, as increasing λ_m enhances Cf^*, Nu^*, and Sh^*, while simultaneously reducing Cg^*. Moreover, the Nusselt and Sherwood numbers exhibit pronounced sensitivity to variations in s.

Table 8.3.1: Variations in skin friction coefficient, heat and mass transfer rates

M	Pr	We	λ_m	α_1	s	θ_0	Nb	Nt	Cf^*	Cg^*	Nu^*	Sh^*
1	1.5	0.5	1.5	0.5	1	-2	1.4	0.8	2.556815	-0.166226	2.201653	1.401881
2									2.389273	-0.132850	2.178503	1.392921
3									2.250977	-0.109441	2.159686	1.385502
	0.5								2.286116	-0.113071	1.493701	1.394450
	1								2.264133	-0.110802	1.915674	1.388483
	1.5								2.250977	-0.109441	2.159686	1.385502
		0.3							2.140147	-0.115650	2.165544	1.389699
		0.6							2.314528	-0.105954	2.156417	1.383211
		0.8							2.448064	-0.098771	2.149746	1.378638
		0.5	0.5						0.733050	-0.042148	2.048070	1.332329
			1.5						2.250977	-0.109441	2.159686	1.385502
			2.5						3.803491	-0.162449	2.249002	1.428898
			1.5	0.2					1.958301	1.962598	2.143109	1.377004
				0.4					2.165378	0.543133	2.155302	1.383219
				0.6					2.323057	-0.705767	2.162950	1.387233
				0.5	0.5				2.441675	-0.130976	1.632112	1.148035
					1.5				2.099553	-0.093255	2.594696	1.597153
					2				1.975413	-0.080722	2.973509	1.789122
					1	-0.5			1.770657	-0.085745	2.199822	1.410056
						-1			2.047222	-0.100551	2.176377	1.395500
						-2			2.250977	-0.109441	2.159686	1.385503
							0.2		2.326993	-0.115928	2.582446	1.211401
							0.8		2.255446	-0.109861	2.352090	1.363891
							1.4		2.250977	-0.109441	2.159686	1.385502
								0.2	2.241343	-0.108500	2.225680	1.392192
								0.8	2.250977	-0.109441	2.159686	1.385502
								1.2	2.256720	-0.110008	2.118186	1.382076

8.4 Summary

This study examines the impact of variable thermophysical properties on the chemically reactive and thermally radiative unsteady rotating MHD Williamson nanofluid flow over a vertical rotating cone in a Darcy-Forchheimer porous medium. By modeling the angular velocities of the cone and ambient fluid as inverse linear functions of time, a self-similarity transformation was applied to reduce the governing nonlinear PDEs to a system of ODEs. The resulting equations were solved numerically using the SRM, with accuracy confirmed through comparison with the SLLM and MATLAB's `bvp4c`, demonstrating excellent consistency. Parametric analyses revealed significant insights into the flow dynamics, as well as heat and mass transfer characteristics, leading to the following key findings:

1. The tangential velocity increases with higher values of θ_0, λ_m, Nr, and λ, while it decreases with increases in M, β_w, and s. Conversely, the azimuthal velocity exhibits an inverse trend with respect to these parameters.

2. Variable thermal conductivity and solutal diffusivity enhance the respective temperature and concentration fields in the SWTC case, while these distributions are diminished in the STSF case.

3. Both linear and nonlinear radiation elevate the temperature distribution and heat transfer rates, with nonlinear radiation exerting a more pronounced effect.

4. Buoyancy force and buoyancy ratio parameters suppress thermal and concentration profiles, thereby enhancing surface heat and mass transfer rates.

5. The tangential skin friction coefficient is strongly influenced by surface and form drag forces.

6. Higher values of θ_0 increase Cf^* while reducing Cg^*, Nu^*, and Sh^*.

7. γ_c enhances the surface mass transfer rate by 17.49%, while ϵ_2 reduces it by 19.80% within their respective ranges.

8. Higher Nb values enhances Sh^* and Cg^* while reducing Cf^* and Nu^*. In contrast, higher Nt values increase Cf^* and moderately decrease Cg^*, Nu^*, and Sh^*.

Conclusion and Recommendations

Conclusion

This dissertation presents a comprehensive investigation into heat and mass transfer mechanisms in non-Newtonian nanofluid boundary layer flow, incorporating a range of complex physical phenomena, including MHD, bioconvection, thermal radiation, viscous dissipation, mixed convection, heat generation/absorption, and suction/injection over stretching and/or rotating surfaces. The study aimed to bridge the existing gaps in the literature by integrating multiple transport mechanisms and variable fluid properties into a unified numerical framework. A rigorous literature review was conducted to contextualize the study within the broader field of fluid dynamics. The existing research that primarily focused on non-Newtonian nanofluids flow dynamics sparsely investigated critical aspects such as nonlinear thermal radiation effects, the Brownian motion of microorganisms, and the impact of chemical reactions on microbial species. Furthermore, comparative analyses of binary and ternary nanofluid heat transfer mechanisms remained underexplored, particularly in the context of modified thermal and solutal convection and dynamic thermosolutal properties in radiative and chemically reactive rotating systems. These gaps in the literature necessitated the formulation of the problem statement, addressing the intricate interplay of variable transport properties, chemical reactions, and external forcing mechanisms. The research employed a robust methodological framework, utilizing spectral methods and continuation technique in finite difference-based collocation method to solve the governing equations. These numerical approaches ensured accuracy and computational efficiency in capturing the intricate dynamics of non-Newtonian nanofluids. Model validation against existing benchmark solutions and the convergence analysis using norm of the residual error confirmed the reliability of the developed numerical schemes. Key findings from individual chapters include:

1. Numerical simulations of MHD Carreau nanofluid flow over a stretching porous medium revealed that increasing the radiation parameter enhances heat transfer efficiency, with shear-thickening fluids exhibiting a 47.78% improvement in thermal transport. The Forchheimer drag term was found to significantly modulate velocity and temperature distributions, highlighting the importance of inertia effects in porous media.

2. The analysis of rotating Williamson nanofluids over exponentially stretching vertical surfaces demonstrated that activation energy enhances mass transfer rate, whereas mixed convection reduces it. The study further revealed the intricate interplay of double diffusion effects, Hall, and ion-slip currents, significantly modifying the velocity, thermal, and concentration boundary layers. Moreover, the impact of microorganisms' Brownian motion and their reaction kinetics in chemically reactive bioconvective

environments was highlighted, underscoring the importance of micro-scale transport phenomena in influencing overall system behavior.

3. Investigation of binary and ternary hybrid Maxwell nanofluids highlighted that ternary nanofluids offer superior thermal management and demonstrated greater resistance to the retarding Lorentz and porous medium forces. The impact of nanoparticle volume fraction on entropy generation was also explored, revealing optimal conditions for minimizing thermal losses. The comparative analysis of binary and ternary nanofluids demonstrated the efficiency of ternary systems in dissipating heat more effectively.

4. The study on non-Fourier–Fick's heat and mass flux in bioconvective nanofluid flow demonstrated that thermal Biot numbers and non-Fickian flux mechanisms significantly modulate heat and mass transfer rates. Results indicated that classical Fourier and Fick models may underestimate transport efficiency in biological and industrial applications, particularly when microorganisms' Brownian motion and chemical reactions are considered.

5. Unsteady Williamson nanofluid analysis over a rotating cone under variable transport properties showed a higher enhancement in the Nusselt number under nonlinear radiation effects compared to the linear radiation case. The study underscored the importance of thermophysical property variations in shaping temperature and concentration profiles under transient conditions. Additionally, the modified thermosolutal convection model was introduced, capturing the complex interactions of variable thermal and solutal diffusivity in rotating systems with radiative and chemically reactive effects.

Overall, this research significantly advances the understanding of convective heat and mass transport in engineering and environmental applications. The integration of multiple physical effects into a single computational model provides a robust framework for future explorations of non-Newtonian nanofluids under diverse boundary conditions. The findings have direct implications for industrial processes, energy systems, and biomedical applications, particularly in optimizing thermal management and enhancing the efficiency of heat exchangers.

Recommendations

Based on the findings of this study, the following recommendations are proposed for future research and practical applications:

1. Incorporate additional non-Newtonian rheological models, such as nonlinear viscoelastic fluids, to enhance predictive capabilities for real-world applications.

2. Investigate the impact of surface roughness and wall deformations on heat and mass transfer rates in technologically relevant microfluidic and biomedical systems.

3. Explore hybrid nanofluid compositions incorporating multiple metallic and carbon-based nanoparticles for optimized thermal management in electronic cooling and energy storage applications.

4. Extend the study to two-phase nanofluid systems to account for phase transition effects in condensation and evaporation processes.

5. Consider coupling artificial intelligence and machine learning techniques with numerical simulations (spectral, finite volume, and finite element) to improve predictive modeling and optimization of non-Newtonian nanofluid flow behavior.

6. Investigate bio-inspired nanofluid transport mechanisms for enhanced mass transfer efficiency, drawing insights from biological systems such as blood flow and microbial locomotion.

7. Further investigate radiation effects, microorganisms' Brownian motion, and chemical reaction mechanisms in thermosolutal convection, particularly within rotating and radiative systems with more complex geometries.

8. Extend the study to non-Newtonian nanofluid flow within confined geometries, such as a square cavity with obstacles, to assess the impact of geometric constraints on convective heat and mass transfer, providing valuable insights for industrial and environmental applications such as thermal regulation in confined spaces and biomedical fluid transport.

These recommendations provide a strong foundation for further advancements in the field of non-Newtonian nanofluid dynamics, with implications for engineering, biomedical, and energy-related applications. The integration of advanced numerical methods with experimental validations will be instrumental in shaping future research directions.

REFERENCES

A. Othman, H., Ali, B., et al. (2023). Numerical simulation of the nanofluid flow consists of gyrotactic microorganism and subject to activation energy across an inclined stretching cylinder. *Scientific Reports*, 13(1):7719.

Abdelmalek, Zahra, et al. (2021). A mathematical model for bioconvection flow of Williamson nanofluid over a stretching cylinder featuring variable thermal conductivity, activation energy and second-order slip. *Journal of Thermal Analysis and Calorimetry*, 144:205–217.

Abdelsalam, S. I. and Bhatti, M. (2020). Anomalous reactivity of thermo-bioconvective nanofluid towards oxytactic microorganisms. *Applied Mathematics and Mechanics*, 41:711–724.

Aboulhasanzadeh, B, et al. (2012). Multiscale computations of mass transfer from buoyant bubbles. *Chemical Engineering Science*, 75:456–467.

Acharya, Nilankush, et al. (2020). Framing the hydrothermal features of magnetized $\mathrm{TiO_2}$–$\mathrm{CoFe_2O_4}$ water-based steady hybrid nanofluid flow over a radiative revolving disk. *Multidiscipline Modeling in Materials and Structures*, 16(4):765–790.

Adegbie, Kolawole, S., et al. (2016). Melting heat transfer effects on stagnation point flow of micropolar fluid with variable dynamic viscosity and thermal conductivity at constant vortex viscosity. *Journal of the Nigerian Mathematical Society*, 35(1):34–47.

Ahmad, Shafiq, et al. (2020). Entropy generation and temperature-dependent viscosity in the study of SWCNT–MWCNT hybrid nanofluid. *Applied Nanoscience*, 10:5107–5119.

Akbar, Sher, N., et al. (2017). Cattaneo-Christov heat flux model study for water-based CNT suspended nanofluid past a stretching surface. *Nanofluid heat and mass transfer in engineering problems*.

Akram, Mohammad, et al. (2024). Exploring the dynamic behavior of the two-phase model in radiative non-Newtonian nanofluid flow with Hall current and ion slip effects. *Journal of Radiation Research and Applied Sciences*, 17(4):101112.

Al-Chlaihawi, Kadhim, et al. (2022). Newtonian and non-newtonian nanofluids with entropy generation in conjugate natural convection of hybrid nanofluid-porous enclosures: A review. *Heat Transfer*, 51(2):1725–1745.

Ali, Farhan, et al. (2024). Impact of thermal radiative Carreau ternary hybrid nanofluid dynamics in solar aircraft with entropy generation: significance of energy in solar aircraft. *Journal of Thermal Analysis and Calorimetry*, 149(4):1495–1513.

Ali, Kashif, et al. (2023). Thermal attributes of hybrid (MWCNT-$\mathrm{NiZnFe_2O_4}$) nanofluid flow having motile microbes and activation energy: A computational approach. *Case Studies in Thermal Engineering*, 47:103088.

Ali, M. M., Chen, T., and Armaly, B. F. (1984). Natural convection-radiation interaction in boundary-layer flow overhorizontal surfaces. *AIAA journal*, 22(12):1797–1803.

Aljuaydi, Fahad, et al. (2023). Numerical investigations of ion slip and Hall effects on Cattaneo-Christov heat and mass fluxes in Darcy-Forchheimer flow of Casson fluid within a porous medium, utilizing non-Fourier double diffusion theories through artificial neural networks ANNS. *International Journal of Thermofluids*, 20:100475.

Almanassra, W, I., et al. (2020). An experimental study on stability and thermal conductivity of water/CNTs nanofluids using different surfactants: A comparison study. *Journal of Molecular Liquids*, 304:111025.

Alqahtani, M, A., et al. (2024). Chemically reactive flow of non-Newtonian nano-liquid over different magnetized and slippery inclined surfaces. *ZAMM-Journal of Applied Mathematics and Mechanics/Zeitschrift für Angewandte Mathematik und Mechanik*, page e202300976.

Alqawasmi, Khaled, et al. (2023). Numerical approach toward ternary hybrid nanofluid flow with nonlinear heat source-sink and Fourier heat flux model passing through a disk. *International Journal of Thermofluids*, 18:100367.

Alwawi, F. A. et al. (2020). MHD natural convection of sodium alginate casson nanofluid over a solid sphere. *Results in physics*, 16:102818.

Alzahrani, Khamis, A., et al. (2021). Hybrid nanofluid flow in a Darcy-Forchheimer permeable medium over a flat plate due to solar radiation. *Case Studies in Thermal Engineering*, 26:100955.

Anilkumar, D. and Roy, S. (2004). Unsteady mixed convection flow on a rotating cone in a rotating fluid. *Applied Mathematics and computation*, 155(2):545–561.

Anwar, M. S. and Rasheed, A. (2017). A microscopic study of mhd fractional inertial flow through forchheimer medium. *Chinese journal of physics*, 55(4):1690–1703.

Arikoglu, Aytac, et al. (2008). Effect of slip on entropy generation in a single rotating disk in MHD flow. *Applied Energy*, 85(12):1225–1236.

Arshad, Mubashar, et al. (2023). Exploration of heat and mass transfer subjected to first order chemical reaction and thermal radiation: Comparative dynamics of nano, hybrid and tri-hybrid particles over dual stretching surface. *International Communications in Heat and Mass Transfer*, 146:106916.

Asjad, Imran, M., et al. (2022). Impact of activation energy and MHD on Williamson fluid flow in the presence of bioconvection. *Alexandria Engineering Journal*, 61(11):8715–8727.

Babu, Srinivasa, K., et al. (2021). Non-linear MHD convective flow of Carreau nanofluid over an exponentially stretching surface with activation energy and viscous dissipation. *SN Applied Sciences*, 3(3):382.

Bahloul, A, et al. (2005). Bioconvection of gravitactic microorganisms in a fluid layer. *International communications in heat and mass transfer*, 32(1-2):64–71.

Bao, C. et al. (2024). Analysis of the absorbing boundary condition for the Maxwell fluid flow over a semi-infinite plate with considering the magnetic field. *Computers & Mathematics with Applications*, 154:212–223.

Baron Fourier, J. B. J. et al. (2003). *The analytical theory of heat*. Courier Corporation.

Batchelor, G. K. (2000). *An introduction to fluid dynamics*. Cambridge university press.

Batool, Samina, et al. (2021). Double diffusion in stretched flow over a stretching cylinder with activation energy and entropy generation. *Case Studies in Thermal Engineering*, 26:101119.

Bejan, A. (1979). A study of entropy generation in fundamental convective heat transfer.

Bellman, R. E. and Kalaba, R. E. (1965). Quasilinearization and nonlinear boundary-value problems. *(No Title)*.

Bilal, S, et al. (2024). Heat transfer analysis of carreau nanofluid flow with gyrotactic microorganisms: A comparative study. *Case Studies in Thermal Engineering*, page 104617.

Bird, Byron, R., et al. (1987). *Dynamics of polymeric liquids, volume 2: Kinetic theory*. Wiley.

Blasius, H. (1908). The boundary layers in fluids. *Zeitschrift fixr Mathematik und Physik*, 56(1).

Borode, Adeola, et al. (2023). Stability and thermophysical properties of GNP-Fe_2O_3 hybrid nanofluid: effect of volume fraction and temperature. *Nanomaterials*, 13(7):1238.

Bouslimi, Jamel, et al. (2021). MHD mixed convection nanofluid flow over convectively heated nonlinear due to an extending surface with Soret effect. *Complexity*, 2021:1–20.

Boyd, J. P. (2001). *Chebyshev and Fourier spectral methods*. Courier Corporation.

Buongiorno, J. (2006). Convective transport in nanofluids.

Byron, Bird, et al. (2002). *Transport Phenomena*. John Wiley & Sons.

Cant, S. (2001). Sb pope, Turbulent Flows, Cambridge University press, CAmbridge, UK, 2000, 771 pp. *Combustion and Flame*, 125(4):1361–1362.

Capra, F. (2008). *The science of Leonardo: Inside the mind of the great genius of the Renaissance*. Anchor.

Carreau, P. J. (1972). Rheological equations from molecular network theories. *Transactions of the Society of Rheology*, 16(1):99–127.

Cattaneo, C. (1948). Sulla conduzione del calore. *Atti Sem. Mat. Fis. Univ. Modena*, 3:83–101.

Cengel, Y. A. and Ghajar, A. J. (2020). *(TEE-815): Heat and Mass Transfer: Fundamentals and Applications (Chap No. 15, 16 & 17 Includes)*. McGraw-Hill Education.

Chakraborty, S. and Panigrahi, P. K. (2020). Stability of nanofluid: A review. *Applied Thermal Engineering*, 174:115259.

Chalmers, A. F. and Chalmers, A. F. (2017). Pascal's equilibrium of liquids. *One Hundred Years of Pressure: Hydrostatics from Stevin to Newton*, pages 83–98.

Chamkha, A. J. (1999). Magnetohydrodynamic mixed convection from a rotating cone embedded in a porous medium with heat generation. *Journal of Porous Media*, 2(1).

Chandel, S. and Sood, S. (2022). Numerical analysis of Williamson-micropolar nanofluid flow through porous rotatory surface with slip boundary conditions. *International Journal of Applied and Computational Mathematics*, 8(3):134.

Choi, S. U. and Eastman, J. A. (1995). Enhancing thermal conductivity of fluids with nanoparticles. Technical report, Argonne National Lab.(ANL), Argonne, IL (United States).

Christov, C. (2009). On frame indifferent formulation of the Maxwell–Cattaneo model of finite-speed heat conduction. *Mechanics research communications*, 36(4):481–486.

Chu, Yu-Ming, et al. (2020). Significance of activation energy, bio-convection and magnetohydrodynamic in flow of third grade fluid (non-Newtonian) towards stretched surface: A Buongiorno model analysis. *International communications in heat and mass transfer*, 118:104893.

Crowther, Gerald, J., et al. (1948). William Thomson: 1824-1907. *(No Title)*.

Darcy, H. (1856). *Les fontaines publiques de la ville de Dijon: exposition et application des principes à suivre et des formules à employer dans les questions de distribution d'eau*, volume 1. Victor dalmont.

Darrigol, O. (2005). *Worlds of flow: A history of hydrodynamics from the Bernoullis to Prandtl*. Oxford University Press.

Dey, Subhalaxmi, et al. (2024). Convective heat transfer of tri-hybrid nanofluid through a curved expanding surface with the impact of velocity slip and exponential heat source. *Colloid and Polymer Science*, 302(10):1573–1590.

Dhlamini, Mlamuli, et al. (2022). A mathematical model for bioconvection flow with activation energy for chemical reaction and microbial activity. *Pramana*, 96(2):112.

Eastman, A, J., et al. (2001). Anomalously increased effective thermal conductivities of ethylene glycol-based nanofluids containing copper nanoparticles. *Applied physics letters*, 78(6):718–720.

Fagbenle, RO, et al. (2020). *Applications of heat, mass and fluid boundary layers*. Woodhead Publishing.

Farooq, Umar, et al. (2021). Thermally radioactive bioconvection flow of Carreau nanofluid with modified Cattaneo-Christov expressions and exponential space-based heat source. *Alexandria Engineering Journal*, 60(3):3073–3086.

Farooq, Umer, et al. (2024). Nonsimilar mixed convection analysis of ternary hybrid nanofluid flow near stagnation point over vertical Riga plate. *Multidiscipline Modeling in Materials and Structures*, 20(2):261–278.

Ferziger, J. H. and Perić, M. (2002). *Computational methods for fluid dynamics*. Springer.

Fourier, J. B. J. (1888). *Théorie analytique de la chaleur*, volume 1. Gauthier-Villars.

Gaffar, Abdul, S., et al. (2017). Magnetohydrodynamic free convection boundary layer flow of non-Newtonian tangent hyperbolic fluid from a vertical permeable cone with variable surface temperature. *Journal of the Brazilian Society of Mechanical Sciences and Engineering*, 39:101–116.

Gamachu, D. and Ibrahim, W. (2023). Entropy production on couple-stress hybrid nanofluid flow in a rocket engine nozzle with non-Fourier's and non-Fick's law. *Ain Shams Engineering Journal*, 14(1):101818.

Gangadhar, Kotha, et al. (2024). Bioconvection-enhanced oblique motion of chemically reactive Oldroyd-B liquid over a convectively heated elastic surface. *Indian Journal of Physics*, pages 1–11.

Ghani, N. A. C. and Siri, Z. (2018). MHD flow of Carreau nanofluid over a stretching surface with suction/injection and slip effects by using Haar wavelet quasilinearization method. In *Journal of Physics: Conference Series*, volume 1139, page 012073. IOP Publishing.

Ghara, Nirmal, et al. (2012). Effects of hall current and ion-slip on unsteady MHD couette flow. *open journal of fluid dynamics*, 2(01):1.

Gholinia, M, et al. (2019). Investigation of MHD Eyring–Powell fluid flow over a rotating disk under effect of homogeneous–heterogeneous reactions. *Case Studies in Thermal Engineering*, 13:100356.

Gireesha, BJ, et al. (2017). Nonlinear 3D flow of Casson-Carreau fluids with homogeneous–heterogeneous reactions: a comparative study. *Results in physics*, 7:2762–2770.

Gu, Shuying, et al. (2013). Solvent-free ionic molybdenum disulfide (MoS_2) nanofluids with self-healing lubricating behaviors. *Materials Letters*, 97:169–172.

Guedda, M. (2007). Similarity and pseudosimilarity solutions of degenerate boundary layer equations. In *Handbook of Differential Equations: Stationary Partial Differential Equations*, volume 4, pages 117–202. Elsevier.

Gupta, Sumit, et al. (2024). Investigation of radiative MHD Carreau nanofluid over an inclined stretching cylinder with activating energy, Wu's slip, and convective heating. *Numerical Heat Transfer, Part B: Fundamentals*, 85(1):1–19.

Habibishandiz, Mohammadreza, et al. (2023). Thermo-bioconvection performance of nanofluid containing oxytactic microorganisms inside a square porous cavity under constant and periodic temperature boundary conditions. *International Journal of Thermofluids*, 17:100269.

Haddad, Zoubida, et al. (2012). Natural convection in nanofluids: are the thermophoresis and Brownian motion effects significant in nanofluid heat transfer enhancement? *International Journal of Thermal Sciences*, 57:152–162.

Hafeez, A. and Khan, M. (2021). Flow of Oldroyd-B fluid caused by a rotating disk featuring the Cattaneo-Christov theory with heat generation/absorption. *International Communications in Heat and Mass Transfer*, 123:105179.

Haider, Abbas, J., et al. (2024a). Impact of heat transfer on peristaltic flow of nanofluid and its applications in real world problems. *Modern Physics Letters B*, 38(06):2350244.

Haider, Abbas, J., et al. (2024b). Results validation by using finite volume method for the blood flow with magnetohydrodynamics and hybrid nanofluids. *Modern Physics Letters B*, 38(24):2450208.

Hamid, Aamir, et al. (2021). Impact of Hall current and homogenous–heterogenous reactions on MHD flow of GO-$\mathrm{MoS_2}$/water ($\mathrm{H_2O}$)-ethylene glycol ($\mathrm{C_2H_6O_2}$) hybrid nanofluid past a vertical stretching surface. *Waves in Random and Complex Media*, pages 1–18.

Hamid, Muhammad, et al. (2018). Shape effects of $\mathrm{MoS_2}$ nanoparticles on rotating flow of nanofluid along a stretching surface with variable thermal conductivity: A galerkin approach. *International Journal of Heat and Mass Transfer*, 124:706–714.

Hamid, A., Khan, M., et al. (2019). Multiple solutions for MHD transient flow of Williamson nanofluids with convective heat transport. *Journal of the Taiwan Institute of Chemical Engineers*, 103:126–137.

Harmand, Souad, et al. (2013). Review of fluid flow and convective heat transfer within rotating disk cavities with impinging jet. *International Journal of Thermal Sciences*, 67:1–30.

Hashim, Khan, et al. (2017). Characteristics of melting heat transfer during flow of Carreau fluid induced by a stretching cylinder. *The European Physical Journal E*, 40:1–9.

Hayat, T, et al. (2011). Falkner–Skan wedge flow of a power-law fluid with mixed convection and porous medium. *Computers & Fluids*, 49(1):22–28.

Hayat, T, et al. (2016a). Convective heat and mass transfer in flow by an inclined stretching cylinder. *Journal of Molecular Liquids*, 220:573–580.

Hayat, T, et al. (2016b). On 2D stratified flow of an Oldroyd-B fluid with chemical reaction: an application of non-Fourier heat flux theory. *Journal of Molecular Liquids*, 223:566–571.

He, Ji-Huan, et al. (2024). A stretching cylindrical Carreau nanofluid border layer movement with motile microorganisms and variable thermal characteristics. *International Journal of Modern Physics B*, 38(17):2450223.

Heath, T. (2002). *The works of Archimedes*. Dover.

Hosseinzadeh, Kh, et al. (2022). Entropy generation analysis of mixture nanofluid ($H_2O/C_2H_6O_2$)–Fe_3O_4 flow between two stretching rotating disks under the effect of MHD and nonlinear thermal radiation. *International Journal of Ambient Energy*, 43(1):1045–1057.

Howell, R, J., et al. (2020). *Thermal radiation heat transfer*. CRC press.

Hsu, C.-T. and Cheng, P. (1990). Thermal dispersion in a porous medium. *International Journal of Heat and Mass Transfer*, 33(8):1587–1597.

Hussain, Zakir, et al. (2022). Analysis of Cattaneo–Christov heat flux in Jeffery fluid flow with heat source over a stretching cylinder. *Journal of Thermal Analysis and Calorimetry*, 147(4):3391–3402.

Ibrahim, W. and Anbessa, T. (2020). Hall and ion slip effects on mixed convection flow of Eyring-Powell nanofluid over a stretching surface. *Advances in Mathematical Physics*, 2020:1–16.

Ibrahim, W. and Anbessa, T. (2021). Hall and ion-slip effects on mixed convection flow of Williamson nanofluid over a nonlinear porous stretching sheet with variable thermal conductivity. *Heat Transfer*, 50(6):5627–5651.

Ibrahim, W. and Hindebu, B. (2019). Magnetohydrodynamic (MHD) boundary layer flow of Eyring-Powell nanofluid past stretching cylinder with Cattaneo-Christov heat flux model. *Nonlinear Engineering*, 8(1):303–317.

Idrees, Muhammad, et al. (2022). New insights into the heat transfer dynamics of a hybrid (SWCNT-MWCNT) nanofluid: A case of 3D rotational flow. *International Communications in Heat and Mass Transfer*, 138:106311.

Irfan, Muhammad, et al. (2022). Thermal phenomenon of joule heating in the radiative flow of Carreau nanofluid. *Pramana*, 96(2):90.

Irfan, M. (2021). Study of Brownian motion and thermophoretic diffusion on non-linear mixed convection flow of Carreau nanofluid subject to variable properties. *Surfaces and Interfaces*, 23:100926.

Irfan, M., Khan, M., and Khan, W. (2019a). Impact of homogeneous–heterogeneous reactions and non-Fourier heat flux theory in Oldroyd-B fluid with variable conductivity. *Journal of the Brazilian Society of Mechanical Sciences and Engineering*, 41(3):135.

Irfan, M., Khan, M., Khan, W., and Ahmad, L. (2019b). Influence of binary chemical reaction with Arrhenius activation energy in MHD nonlinear radiative flow of unsteady Carreau nanofluid: dual solutions. *Applied Physics A*, 125:1–11.

Ishak, A., Nazar, R., and Pop, I. (2008). Hydromagnetic flow and heat transfer adjacent to a stretching vertical sheet. *Heat and Mass Transfer*, 44(8):921–927.

Jalili, Bahram, et al. (2023a). Squeezing flow of Casson fluid between two circular plates under the impact of solar radiation. *ZAMM-Journal of Applied Mathematics and Mechanics/Zeitschrift für Angewandte Mathematik und Mechanik*, 103(9):e202200455.

Jalili, Payam, et al. (2022). Heat transfer analysis in cylindrical polar system with magnetic field: a novel hybrid analytical and numerical technique. *Case Studies in Thermal Engineering*, 40:102524.

Jalili, Payam, et al. (2023b). Analytical and numerical investigation of thermal distribution for hybrid nanofluid through an oblique artery with mild stenosis. *SN Applied Sciences*, 5(4):95.

Jalili, Payam, et al. (2023c). A novel analytical approach to micro-polar nanofluid thermal analysis in the presence of thermophoresis, Brownian motion and Hall currents. *Soft Computing*, 27(2):677–689.

Javed, T., Sajid, M., Abbas, Z., and Ali, N. (2011). Non-similar solution for rotating flow over an exponentially stretching surface. *International Journal of Numerical Methods for Heat & Fluid Flow*, 21(7):903–908.

Jawwad, Abdul, A. K., et al. (2023). Radiative transport of MHD stagnation point flow of chemically reacting Carreau nanofluid due to radially stretched sheet. *Alexandria Engineering Journal*, 69:699–714.

Jubair, Sidra, et al. (2025). Analyzing the impact of non-newtonian nanofluid flow on pollutant discharge concentration in wastewater management using an artificial computing approach. *Applied Water Science*, 15(1):1–13.

Khan, A, S., et al. (2022a). Thermal conductivity performance for ternary hybrid nanomaterial subject to entropy generation. *Energy Reports*, 8:9997–10005.

Khan, Ahmad, M. W., et al. (2020a). Numerical solution of MHD flow of power law fluid subject to convective boundary conditions and entropy generation. *Computer Methods and Programs in Biomedicine*, 188:105262.

Khan, Ijaz, M., et al. (2020b). Magneto rotating flow of hybrid nanofluid with entropy generation. *Computer methods and programs in biomedicine*, 183:105093.

Khan, Ijaz, M., et al. (2022b). Heat and mass transfer analysis for bioconvective flow of Eyring Powell nanofluid over a Riga surface with nonlinear thermal features. *Numerical Methods for Partial Differential Equations*, (4):777–793.

Khan, Imad, et al. (2018). Homogenous–heterogeneous reactions in MHD flow of Powell–Eyring fluid over a stretching sheet with Newtonian heating. *Neural Computing and Applications*, 30:3581–3588.

Khan, M, et al. (2017). Effects of melting and heat generation/absorption on unsteady Falkner-Skan flow of Carreau nanofluid over a wedge. *International Journal of Heat and Mass Transfer*, 110:437–446.

Khan, Masood, et al. (2021). Thermal analysis for radiative flow of magnetized Maxwell fluid over a vertically moving rotating disk. *Journal of Thermal Analysis and Calorimetry*, 143:4081–4094.

Khan, Sohail, et al. (2024). Heat and mass transfer enhancement in nonlinear mixed convective flow: Buongiorno model and melting heat phenomenon. *International Communications in Heat and Mass Transfer*, 153:107330.

Khan, M. I. (2021). Transportation of hybrid nanoparticles in forced convective Darcy-Forchheimer flow by a rotating disk. *International Communications in Heat and Mass Transfer*, 122:105177.

Khan, N. A. and Khan, H. (2014). A boundary layer flows of non-Newtonian Williamson fluid. *Nonlinear Engineering*, 3(2):107–115.

Krishnamurthy, MR, , et al. (2016). Effect of chemical reaction on MHD boundary layer flow and melting heat transfer of Williamson nanofluid in porous medium. *Engineering Science and Technology, an International Journal*, 19(1):53–61.

Kumar, Vinay, et al. (2023). Updated formulation of magnetic body force in ferrofluids. *International Journal of Engineering Science*, 192:103929.

Kumari, M. and Nath, G. (2014). Steady mixed convection flow of Maxwell fluid over an exponentially stretching vertical surface with magnetic field and viscous dissipation. *Meccanica*, 49:1263–1274.

Kuznetsov, A. (2005). The onset of bioconvection in a suspension of gyrotactic microorganisms in a fluid layer of finite depth heated from below. *International Communications in Heat and Mass Transfer*, 32(5):574–582.

Kuznetsov, A. V. (2010). The onset of nanofluid bioconvection in a suspension containing both nanoparticles and gyrotactic microorganisms. *International Communications in Heat and Mass Transfer*, 37(10):1421–1425.

Latha, Swetha, K. B., et al. (2023). Computation of stagnation coating flow of electro-conductive ternary williamson hybrid GO-AU-Co_3O_4/EO nanofluid with a Cattaneo–Christov heat flux model and magnetic induction. *Scientific Reports*, 13(1):10972.

Li, Shuguang, et al. (2024). Influence of variable fluid properties on mixed convective Darcy–Forchheimer flow relation over a surface with Soret and Dufour spectacle. *Open Physics*, 22(1):20240010.

Magagula, VM, et al. (2020). Applications of heat, mass and fluid boundary layers.

Mahdi, Abed, R., et al. (2015). Review of convection heat transfer and fluid flow in porous media with nanofluid. *Renewable and Sustainable Energy Reviews*, 41:715–734.

Mahmood, Zafar, et al. (2023). Numerical analysis of MHD tri-hybrid nanofluid over a nonlinear stretching/shrinking sheet with heat generation/absorption and slip conditions. *Alexandria Engineering Journal*, 76:799–819.

Majeed, Aaqib, et al. (2021). Significance of thermophoretic and Brownian motion on MHD nanofluids flow towards a circular cylinder under the inspiration of multiple slips: An industrial application. *Mathematical Problems in Engineering*, 2021(1):8634185.

Makinde, Daniel, O., et al. (2017). Effects of Cattaneo-Christov heat flux on Casson nanofluid flow past a stretching cylinder. In *Defect and Diffusion Forum*, volume 378, pages 28–38. Trans Tech Publ.

Malik, Rabia, et al. (2022). Cattaneo–Christov heat flux model impact for Carreau fluid flow past a stretched cylinder with velocity slip and convective boundary conditions. *Journal of Thermal Analysis and Calorimetry*, 147(24):14621–14630.

Mandal, Arpita, et al. (2023). Activity of motile microorganism in bioconvective nanofluid flow with Arrhenius activation energy. *Journal of Thermal Analysis and Calorimetry*, 148(17):9113–9130.

Masuda, Hidetoshi, et al. (1993). Alteration of thermal conductivity and viscosity of liquid by dispersing ultra-fine particles. Dispersion of $\mathrm{Al_2O_3}$, $\mathrm{SiO_2}$ and $\mathrm{TiO_2}$ ultra-fine particles.

Merkin, J. (1996). A model for isothermal homogeneous-heterogeneous reactions in boundary-layer flow. *Mathematical and Computer Modelling*, 24(8):125–136.

Mishra, A. (2024). Hydrothermal performance of hybrid nanofluid flow over an exponentially stretching sheet influenced by gyrotactic microorganisms: A comparative evaluation of Yamada-Ota and Xue models. *Numerical Heat Transfer, Part A: Applications*, pages 1–30.

Mkhatshwa, M. P. (2023). Bioconvective flow of fourth-grade nanofluid via a stretchable porous surface with microbial activity and activation energy. *Case Studies in Thermal Engineering*, 51:103526.

Mkhatshwa, M. P. (2024). Overlapping grid-based spectral collocation technique for bioconvective flow of MHD Williamson nanofluid over a radiative circular cylindrical body with activation energy. *Computation*, 12(4):75.

Motsa, S. (2014). A new spectral relaxation method for similarity variable nonlinear boundary layer flow systems. *Chemical Engineering Communications*, 201(2):241–256.

Motsa, S. S. (2013). A new spectral local linearization method for nonlinear boundary layer flow problems. *Journal of Applied Mathematics*, 2013(1):423628.

Muntazir, Akram, R., et al. (2021). A numerical study of MHD Carreau nanofluid flow with gyrotactic microorganisms over a plate, wedge, and stagnation point. *Mathematical Problems in Engineering*, 2021(1):5520780.

Mustafa, M, et al. (2017). Rotating flow of Maxwell fluid with variable thermal conductivity: an application to non-Fourier heat flux theory. *International Journal of Heat and Mass Transfer*, 106:142–148.

Nabwey, A, H., et al. (2022). Influence of bioconvection and chemical reaction on magnetoâ€”Carreau nanofluid flow through an inclined cylinder. *Mathematics*, 10(3):504.

Nadeem, S. and Saleem, S. (2013). Analytical treatment of unsteady mixed convection MHD flow on a rotating cone in a rotating frame. *Journal of the Taiwan Institute of Chemical Engineers*, 44(4):596–604.

Nadeem, S. and Saleem, S. (2014). Unsteady mixed convection flow of nanofluid on a rotating cone with magnetic field. *Applied Nanoscience*, 4:405–414.

Nazari, Saeed, et al. (2020). Numerical study on mixed convection of a non-Newtonian nanofluid with porous media in a two lid-driven square cavity. *Journal of Thermal Analysis and Calorimetry*, 140:1121–1145.

Needham, J. (1974). *Science and civilisation in China*, volume 5. Cambridge University Press.

Oppenheim, A. L. (2013). *Ancient Mesopotamia: Portrait of a dead civilization*. University of Chicago Press.

Paul, Ashish, et al. (2023). Mixed convection of shear-thinning hybrid nanofluid flow across a radiative unsteady cone with suction and slip effect. *Materials Today Communications*, 37:107522.

Pedley, T. and Kessler, J. O. (1992). Hydrodynamic phenomena in suspensions of swimming microorganisms. *Annual Review of Fluid Mechanics*, 24(1):313–358.

Pordanjani, Hajatzadeh, A., et al. (2021). Nanofluids: Physical phenomena, applications in thermal systems and the environment effects-a critical review. *Journal of Cleaner Production*, 320:128573.

Prandtl, L. (1905). Uber Flussigkeitsbewegung bei sehr kleiner Reibung. *Verhandl. 3rd Int. Math. Kongr. Heidelberg (1904), Leipzig*.

Prasad, KV, et al. (2024). Tangent hyperbolic MHD nanoliquids on non-isothermal stretched sheets: Analyzing the impact of transport parameters, variable fluid properties and convective boundary conditions. *Results in Physics*, 66:108008.

Qasim, M, et al. (2019). Influence of variable transport properties on nonlinear radioactive Jeffrey fluid flow over a disk: utilization of generalized differential quadrature method. *Arabian Journal for Science and Engineering*, 44(6):5987–5996.

Rafique, Khadija, et al. (2023). Investigation of thermal stratification with velocity slip and variable viscosity on MHD flow of Al_2O_3- Cu- TiO_2/H_2O nanofluid over disk. *Case Studies in Thermal Engineering*, 49:103292.

Ragupathi, P, et al. (2019). Non-uniform heat source/sink effects on the three-dimensional flow of Fe_3O_4/Al_2O_3 nanoparticles with different base fluids past a Riga plate. *Case Studies in Thermal Engineering*, 15:100521.

Raju, CSK, et al. (2016). Free convective heat and mass transfer of MHD non-Newtonian nanofluids over a cone in the presence of non-uniform heat source/sink. *Journal of Molecular Liquids*, 221:108–115.

Ramakrishna, Ogiboina, et al. (2024). Thermodynamics of variable thermophysical properties of non-Newtonian fluids with the exploration of antiviral and antibacterial mechanisms using silver nanoparticles. *International Journal of Thermofluids*, 22:100648.

Ramesh, GK, et al. (2012). MHD flow of a dusty fluid near the stagnation point over a permeable stretching sheet with non-uniform source/sink. *International Journal of Heat and Mass Transfer*, 55(17-18):4900–4907.

Ramzan, Muhammad, et al. (2020). Significance of Hall effect and ion slip in a three-dimensional bioconvective tangent hyperbolic nanofluid flow subject to Arrhenius activation energy. *Scientific Reports*, 10(1):18342.

Ramzan, Muhammad, et al. (2023). A theoretical analysis of the ternary hybrid nanofluid flows over a non-isothermal and non-isosolutal multiple geometries. *Heliyon*, 9(4).

Rao, S. and Deka, P. (2023). A numerical study on unsteady MHD Williamson nanofluid flow past a permeable moving cylinder in the presence of thermal radiation and chemical reaction. *Biointerface Research in Applied Chemistry*, 13(5):436.

Rashad, A. and Nabwey, H. A. (2019). Gyrotactic mixed bioconvection flow of a nanofluid past a circular cylinder with convective boundary condition. *Journal of the Taiwan Institute of Chemical Engineers*, 99:9–17.

Rasool, Ghulam, et al. (2021). Numerical scrutinization of Darcy-Forchheimer relation in convective magnetohydrodynamic nanofluid flow bounded by nonlinear stretching surface in the perspective of heat and mass transfer. *Micromachines*, 12(4):374.

Rasool, Ghulam, et al. (2022). Numerical investigation of EMHD nanofluid flows over a convectively heated riga pattern positioned horizontally in a Darcy-Forchheimer porous medium: Application of passive control strategy and generalized transfer laws. *Waves in Random and Complex Media*, pages 1–20.

Rasool, G. and Zhang, T. (2019). Darcy-Forchheimer nanofluidic flow manifested with Cattaneo-Christov theory of heat and mass flux over non-linearly stretching surface. *PLoS One*, 14(8):e0221302.

Reddy, Sudarsana, P., et al. (2022). Heat and mass transfer analysis of nanofluid flow over swirling cylinder with Cattaneo–Christov heat flux. *Journal of Thermal Analysis and Calorimetry*, 147(4):3453–3468.

Reddy, M. G. (2014). Unsteady heat and mass transfer MHD flow of a chemically reacting fluid past an impulsively started vertical plate with radiation. *Journal of Engineering Physics and Thermophysics*, 87(5):1233–1240.

Rehman, Sohail, et al. (2024). Role of nanomaterial on irreversibility and heat transport due to stretching surface driven blood flow in the view of buongiorno and tiwari-das models. *Ain Shams Engineering Journal*, 15(6):102747.

Riasat, Saima, et al. (2021). Comparative analysis of Yamada-Ota and Xue models for hybrid nanofluid flow amid two concentric spinning disks with variable thermophysical characteristics. *Case Studies in Thermal Engineering*, 26:101039.

Roberts, S. and Shipman, J. (1967). Continuation in shooting methods for two-point boundary value problems. *Journal of mathematical analysis and applications*, 18(1):45–58.

Rudraswamy, NG, et al. (2017). Numerical analysis of MHD three-dimensional Carreau nanoliquid flow over bidirectionally moving surface. *Journal of the Brazilian Society of Mechanical Sciences and Engineering*, 39:5037–5047.

Sadiq, Naeem, et al. (2024). Comparative analysis of non-newtonian and newtonian fluid flow with dual slip in the presence of motile microorganisms and nanoparticles. *BioNanoScience*, 14(2):1504–1519.

Saeed, Anwar, et al. (2021). Hybrid nanofluid flow through a spinning Darcy–Forchheimer porous space with thermal radiation. *Scientific reports*, 11(1):16708.

Saidur, Rahman, et al. (2011). A review on applications and challenges of nanofluids. *Renewable and sustainable energy reviews*, 15(3):1646–1668.

Sakiadis, B. C. (1961). Boundary-layer behavior on continuous solid surfaces: I. Boundary-layer equations for two-dimensional and axisymmetric flow. *AIChE Journal*, 7(1):26–28.

Salahuddin, T, et al. (2022). A significant study on flow analysis of viscoelastic fluid with variable thermo-physical properties. *Mathematics and Computers in Simulation*, 194:416–429.

Saleem, M. and Hussain, M. (2023). Impression of nonlinear radiation and Stefan blowing on the magneto cross nano-Williamson fluid above exponentially stretching sheet. *Results in Engineering*, 17:100864.

Schlichting, H. and Gersten, K. (2016). *Boundary-layer theory*. springer.

Sedki, A. M. (2022). Effect of thermal radiation and chemical reaction on MHD mixed convective heat and mass transfer in nanofluid flow due to nonlinear stretching surface through porous medium. *Results in Materials*, 16:100334.

Serrano, Elena, et al. (2009). Nanotechnology for sustainable energy. *Renewable and Sustainable Energy Reviews*, 13(9):2373–2384.

Shah, Zahir, et al. (2019). Radiative heat and mass transfer analysis of micropolar nanofluid flow of Casson fluid between two rotating parallel plates with effects of Hall current. *Journal of Heat Transfer*, 141(2):022401.

Shahid, A, et al. (2022). Numerical experiment to examine activation energy and bi-convection Carreau nanofluid flow on an upper paraboloid porous surface: Application in solar energy. *Sustainable Energy Technologies and Assessments*, 52:102029.

Shahid, A. et al. (2021). Numerical analysis of activation energy on MHD nanofluid flow with exponential temperature-dependent viscosity past a porous plate. *Journal of Thermal Analysis and Calorimetry*, 143:2585–2596.

Shahsavar, A, et al. (2015). An experimental study on the effect of ultrasonication on thermal conductivity of ferrofluid loaded with carbon nanotubes. *Thermochimica Acta*, 617:102–110.

Shaw, S, et al. (2022). Hydromagnetic flow and thermal interpretations of cross hybrid nanofluid influenced by linear, nonlinear and quadratic thermal radiations for any Prandtl number. *International Communications in Heat and Mass Transfer*, 130:105816.

Shaw, Sachin, et al. (2013). Homogeneous-heterogeneous reactions in micropolar fluid flow from a permeable stretching or shrinking sheet in a porous medium. *Boundary Value Problems*, 2013:1–10.

Shawky, M, H., et al. (2019). MHD flow with heat and mass transfer of Williamson nanofluid over stretching sheet through porous medium. *Microsystem technologies*, 25:1155–1169.

Sheikholeslami, M. and Ganji, D. D. (2015). Entropy generation of nanofluid in presence of magnetic field using Lattice Boltzmann method. *Physica A: Statistical Mechanics and its Applications*, 417:273–286.

Sheremet, M. A. and Pop, I. (2014). Thermo-bioconvection in a square porous cavity filled by oxytactic microorganisms. *Transport in Porous Media*, 103:191–205.

Shevchuk, I. V. (2009). *Convective heat and mass transfer in rotating disk systems*, volume 45. Springer.

Shizgal, B. (2015). Spectral methods in chemistry and physics. *Scientific Computation. Springer*.

Siddiq, MK, et al. (2021). MHD thermally radiative flow of Carreau fluid subjected to the stretching sheet by considering non-Darcy Forchheimer law. *Pramana*, 95:1–9.

Singh, Pratap, S., et al. (2024). Flow and heat transfer assessment in magnetized Darcy-Forchheimer flow of Casson hybrid nanofluid through cone, wedge, and plate. *BioNanoScience*, 14(1):395–408.

Singh, S. P. et al. (2023). Ternary hybrid nanofluid ($\mathrm{TiO_2}$- $\mathrm{SiO_2}$- $\mathrm{MoS_2}$/kerosene oil) flow over a rotating disk with quadratic thermal radiation and Cattaneo-Christov model. *Journal of Central South University*, 30(4):1262–1278.

Sobieski, W. and Trykozko, A. (2014). Darcy's and Forchheimer's laws in practice. Part 1. The experiment. *Technical Sciences/University of Warmia and Mazury in Olsztyn*.

Sohail, Muhammad, et al. (2022). Galerkin finite element analysis for the augmentation in thermal transport of ternary-hybrid nanoparticles by engaging non-Fourier's law. *Scientific Reports*, 12(1):13497.

Song, Ying-Qing, et al. (2021). Bioconvection analysis for Sutterby nanofluid over an axially stretched cylinder with melting heat transfer and variable thermal features: A Marangoni and solutal model. *Alexandria Engineering Journal*, 60(5):4663–4675.

Subhas, A. and Veena, P. (1998). Visco-elastic fluid flow and heat transfer in a porous medium over a stretching sheet. *International journal of non-linear mechanics*, 33(3):531–540.

Sulochana, C, et al. (2020). Magnetohydrodynamic MgO/CuO-water hybrid nanofluid flow driven by two distinct geometries. *Heat Transfer*, 49(6):3663–3682.

Suresh, Sivan, et al. (2012). Effect of Al_2O_3–Cu/water hybrid nanofluid in heat transfer. *Experimental Thermal and Fluid Science*, 38:54–60.

Tahmasebi-Boldaji, Ramin, et al. (2023). Experimental investigation of ultrasonic cycle/magnetic stirrer (UC/MS) effect on water/α-Al_2O_3 nanofluid stability and thermal conductivity and its ANFIS/PSO modeling. *Results in Engineering*, 19:101284.

Thakur, Archie, et al. (2023). Mixed convective flow of tri-hybrid nanofluid TiO_2–Al_2O_3–SiO_2/H_2O past a variably thicked stretching sheet with Newtonian heating. *Journal of Nanofluids*, 12(7):1782–1793.

Timofeeva, V, E., et al. (2011). Base fluid and temperature effects on the heat transfer characteristics of SiC in ethylene glycol/H_2O and H_2O nanofluids. *Journal of Applied Physics*, 109(1).

Tiwari, R. K. and Das, M. K. (2007). Heat transfer augmentation in a two-sided lid-driven differentially heated square cavity utilizing nanofluids. *International Journal of heat and Mass transfer*, 50(9-10):2002–2018.

Trefethen, L. N. (2000). *Spectral methods in MATLAB*. SIAM.

Truesdell, C. (2012). *Essays in the History of Mechanics*. Springer Science & Business Media.

Tsou, F., Sparrow, E. M., and Goldstein, R. J. (1967). Flow and heat transfer in the boundary layer on a continuous moving surface. *International Journal of Heat and Mass Transfer*, 10(2):219–235.

Verma, Kumar, A., et al. (2021). Boundary layer flow of non-Newtonian Eyring–Powell nanofluid over a moving flat plate in Darcy porous medium with a parallel free-stream: Multiple solutions and stability analysis. *Pramana*, 95(4):173.

Waqas, M. (2021). A study on magneto-hydrodynamic non-Newtonian thermally radiative fluid considering mixed convection impact towards convective stratified surface. *International Communications in Heat and Mass Transfer*, 126:105262.

Xu, H. and Liao, S.-J. (2009). Laminar flow and heat transfer in the boundary-layer of non-Newtonian fluids over a stretching flat sheet. *Computers & Mathematics with Applications*, 57(9):1425–1431.

Xuan, Y. and Li, Q. (2000). Heat transfer enhancement of nanofluids. *International Journal of heat and fluid flow*, 21(1):58–64.

Yaseen, Moh, et al. (2022). Cattaneo–Christov heat flux model in Darcy–Forchheimer radiative flow of MoS_2–SiO_2/kerosene oil between two parallel rotating disks. *Journal of Thermal Analysis and Calorimetry*, 147(19):10865–10887.

Zeeshan, Ahmad, et al. (2018). Hydromagnetic nanofluid flow past a stretching cylinder embedded in non-Darcian Forchheimer porous media. *Neural Computing and Applications*, 30:3479–3489.

Zhang, Jing-Kui, et al. (2017). Analysis of magnetohydrodynamics (MHD) natural convection in 2D cavity and 3D cavity with thermal radiation effects. *International Journal of Heat and Mass Transfer*, 112:216–223.

Zhang, Xiaolei, et al. (2011). Synthesis of nanoparticles by microorganisms and their application in enhancing microbiological reaction rates. *Chemosphere*, 82(4):489–494.

Zhou, Shuang-Shuang, et al. (2021). Numerical analysis of thermal radiative maxwell nanofluid flow over-stretching porous rotating disk. *Micromachines*, 12(5):540.

APPENDICES

A. Flow types, Definitions and Theorems

A.1 Types of Flow

Uniform vs. Nonuniform Flow

- **Uniform Flow**: A flow is uniform if its velocity and other properties remain constant along the flow direction at a given instant, i.e.,
$$\frac{\partial}{\partial x} = 0. \tag{0.0.1}$$
- **Nonuniform Flow**: A flow is nonuniform if its velocity and other characteristics change along the spatial coordinates, i.e.,
$$\frac{\partial}{\partial x} \neq 0. \tag{0.0.2}$$
Most real-world flows exhibit nonuniformity due to boundary effects and external forces.

Steady vs. Unsteady Flow

- **Steady Flow**: A fluid flow is considered steady if its velocity, pressure, and other properties at any fixed spatial point remain invariant over time, i.e.,
$$\frac{\partial}{\partial t} = 0. \tag{0.0.3}$$
- **Unsteady Flow**: A flow is unsteady if its properties vary with time at a fixed location, implying
$$\frac{\partial}{\partial t} \neq 0. \tag{0.0.4}$$
Unsteady flows may be periodic or random, depending on their temporal variations.

Rotational vs. Irrotational Flow

- **Rotational Flow**: A flow is rotational if its vorticity is nonzero, indicating the presence of local angular momentum within the fluid elements:
$$\boldsymbol{\omega} = \nabla \times \mathbf{V} \neq 0. \tag{0.0.5}$$
This occurs in shear-dominated and vortex-dominated regions.
- **Irrotational Flow**: A flow is irrotational if its vorticity vanishes everywhere:
$$\nabla \times \mathbf{V} = 0. \tag{0.0.6}$$
Irrotational flows are often modeled using potential flow theory.

Laminar vs. Turbulent Flow

- **Laminar Flow**: A flow is laminar if it is smooth and orderly, characterized by parallel streamlines with minimal mixing. It occurs at low Reynolds numbers ($\mathrm{Re} < \mathrm{Re}_{\mathrm{crit}}$) and is dominated by viscous forces.

- **Turbulent Flow**: A flow is turbulent if it exhibits chaotic, irregular motion with vortices, eddies, and significant mixing. It occurs at high Reynolds numbers ($\mathrm{Re} > \mathrm{Re}_{\mathrm{crit}}$), where inertial forces dominate over viscous effects.

Axisymmetric Flow

It refers to a fluid motion where all relevant properties (e.g., velocity field) remain unchanged when rotated about a central axis. Mathematically,

$$\frac{\partial \phi}{\partial \theta} = 0. \tag{0.0.7}$$

where, ϕ is fluid property and θ is azimuthal direction in cylindrical coordinate.

A.2 Definitions

Definition 1. The *Boussinesq approximation* is a mathematical simplification applied to the governing equations of fluid motion, where variations in fluid density are considered negligible except in the *buoyancy (body force) term* of the momentum equation.

For a fluid in which buoyancy arises due to gradients in **temperature** (T), **solute concentration** (C), and **microorganism density** (N), the fluid density ρ is approximated as a linear function of T, C, and N around a reference state as:

$$\rho(T,C,N) \approx \rho_0 \left[1 - \beta_T(T - T_\infty) - \beta_C(C - C_\infty) - \beta_N(N - N_\infty)\right] \tag{0.0.8}$$

where:

- ρ_0 is the reference fluid density,
- T_∞, C_∞, N_∞ are the ambient temperature, concentration, and microorganism density,
- β_T, β_C, and β_N are the thermal, solutal, and microbial expansion coefficients, respectively.

Under this approximation, the modified incompressible Navier–Stokes momentum equation becomes:

$$\rho_0 \left(\frac{\partial \mathbf{u}}{\partial t} + \mathbf{u} \cdot \nabla \mathbf{u} \right) = -\nabla p^* + \mu \nabla^2 \mathbf{u} - \rho_0 \mathbf{g} \left[\beta_T(T - T_\infty) + \beta_C(C - C_\infty) + \beta_N(N - N_\infty)\right] \tag{0.0.9}$$

This formulation accounts for the combined effects of thermal, solutal, and microbial buoyancy driven flows.

Definition 2. Let $f(x)$ and $g(x)$ be arbitrary functions. The inner product of $f(x)$ with $g(x)$ with respect to the weight function $\omega(x)$ on the interval [a,b] is defined by

$$(f,g) := \int_a^b f(x)g(x)\omega(x)dx$$

Definition 3. A set of basis function $\phi_n(x)$ is said to be orthogonal with respect to a given inner product if

$$(\phi_m, \phi_n) = \delta_{mn}\nu^2,$$

where δ_{mn} is the kronecker delta function defined by

$$\delta_{mn} = \begin{cases} 1, \; m = n \\ 0, \; m \neq n \end{cases}$$

and where the constants ν_n are called normalization constants.

Definition 4. The Jacobi polynomials $p_n^{\alpha,\beta}(x)$ of degree n are polynomials that depend on α and β (both > -1) satisfy the orthogonality relation:

$$\int_{-1}^{1} p_n^{\alpha,\beta}(x) p_m^{\alpha,\beta}(x)(1-x)^{\alpha}(1+x)^{\beta} dx = 0, \text{ for } m \neq n$$

The two most important special cases of Jacobi polynomials are Legendre and Chebyshev polynomials, obtained respectively by setting $\alpha, \; \beta = 0$, and $\alpha, \; \beta = \frac{-1}{2}$.

Definition 5. Chebyshev polynomials (of the first kind) are special case of the Jacobi polynomials with $(\alpha, \beta) = (-1/2, -1/2)$ and are orthogonal with respect to the weight function $\omega(x) = (1-x^2)^{-1/2}$. The three-term recurrence relation for the Chebyshev polynomials reads:

$$T_{n+1}(x) = 2xT_n(x) - T_{n-1}(x), \; n \geq 1$$

with $T_0(x) = 1$, and $T_1(x) = x$. It is more convenient to explore the relation between Chebyshev polynomials and trigonometric functions and is defined as

$$T_n(x) = \cos(n\theta), \; \theta = \arccos x, \; n \geq 1, x \in I$$

A.3 Theorems

Gauss's Divergence Theorem

Let **F** be a vector field defined throughout a volume V enclosed within a piecewise smooth surface S on which the outward drawn unit normal is **n**. Then, if the components of **F** and its first order partial derivatives are continuous throughout V and on S, dV is an element of volume of V, and dS is an element of area of S, then

$$\iiint_V \nabla \cdot \mathbf{F} dV = \iint_S \mathbf{F} \cdot \mathbf{n} dS, \tag{0.0.10}$$

where $\nabla = \left(\frac{\partial}{\partial x}, \frac{\partial}{\partial y}, \frac{\partial}{\partial z}\right)$ and $\mathbf{F} = \left(F_1, F_2, F_3\right)$.

Reynolds transport theorem

Let E be any property of the fluid (mass, momentum, energy, etc) and let $\epsilon = \dfrac{dE}{dm}$ be the intensive value of E (amount of E per unit mass) in any small element of the fluid. The theorem states for the arbitrary moving and formidable control volume CV, the instantaneous total change of E in the material volume (MV) is equal to the instantaneous total change of E with in the CV plus the net flow of E into and out of the CV through its control surface (S), mathematically expressed as,

$$\left(\frac{dE}{dt}\right)_{MV} = \int_{CV} \frac{\partial(\rho\epsilon)}{\partial t} dV + \int_S \rho\epsilon(\boldsymbol{v}.\boldsymbol{n}) dS, \tag{0.0.11}$$

where, $\boldsymbol{v}(t, \boldsymbol{x})$ is the velocity of the fluid, $\boldsymbol{n}$ is the outward unit normal to the control volume surface, ρ is the density of the fluid.

Stokes' Theorem

Let S be an open piecewise smooth orientable surface bounded by a closed space curve Γ around which a sense of direction is specified. At every point of the surface, let the unit normal **n** to S point in the direction specified for orientable surfaces relative to the sense around Γ. Then, if **F** is a differentiable vector function over the surface S,

$$\int_\Gamma \mathbf{F} \cdot d\mathbf{r} = \iint_S (\nabla \times \mathbf{F}) \cdot d\mathbf{S}, \tag{0.0.12}$$

where **r** is the position vector of a general point on Γ and $d\boldsymbol{S} = \boldsymbol{n} dS$. This theorem is fundamental in electromagnetism, particularly in Maxwell's equations.

B. MATLAB Code: SQLM

```
%% Chebsheve Differentiation matrix
N=80;
[D,x]=cheb(N);
%% Costants
%%  La1= relaxation time, M= magnetic para, La= porosity par, F = inertial coeff,tr= temperature ratio,
% La2= mixed convec para, Rd= radiation par, Pr= prandtle num, Ec= Eckert
% numb, La3= Thermal relaxation para, Q0=heat source/sink,b0= Stretching ratio, bw=
% suction/injection para, bi = Biot number,b2= velocity slip para,b3= thermal slip parameter, v1,v2,v2= volume
% fraction of nanoparticle 1,2,3 respe
% Default values:M=3; La1=1.2;F= 3.5;Pr=8; La=1.5;La2=2;La3=0.5; Rd=4.5;xx=0.15;La3=0.5;
%Ec= 0.3; Q0=0.05;v1= 0.04 ; v2=0.04  ; v3=0.04
% bw=0.4;b0=0.15;;b2=0.05;b3=1.2; Br=0.4; alpha_bar=xx; gamma_bar =0.6;
% Re=0.5;
```

```
%% Here,  simple nanofluid is made from Fe3O4 + Sodium alginate
%Hybrid nanofluid is made from CuO + Fe3O4 + Sodium alginat
% Ternay hybrid nanofluid made from     CuO + Fe3O4 + MoS2 + Sodium alginat
% Thefore f is subscript for SA, 1 subscripts for Fe3O4, 2 subscript for CuO, 3 is subscript for MoS2
% with the respective volume fractions of nanoparticle v1, v2, v3
%% The defualt volume fractions are v1=v2=v3=0.04
M=3;F= 3.5;Ec=0.3;Rd=4.5;Pr=8;La1=1.2;La2=2;La3=0.5;Q0=0.05;xx=0.05;bi=0.3;b0=0.15;b2=0.05;b3=1.2;bw=0.4;
Br=0.4;alpha_bar=xx;  gamma_bar=0.6;Re=5;
v1= 0.04 ; v2=0.04 ; v3=0.04;
rof=989;ro3=5180;ro2=6320;ro1=5060;kf=0.6376;k3=9.7;k2=76.5;k1=34.5;ef=2.6*1e-4; e3=2.5*1e-4;e2=6.9*1e-2;e1=2.09*1e-5; spf=4175;sp3=670; sp2=531.8; sp1=397.746;  exf=99*1e-5; ex3=1.3*1e-5; ex2=1.8*1e-5;ex1=2.8424*1e-5;
%%
Linf=6;
%%
% Note: SA = f, FeO4=1, CuO=2, Mo2=3
% We consider Fe3O4,CuO and MO2 nanoparticles + Sodium alginate base fluid
%                 Sodium alginate   Fe3O4      CuO      MO2
% rho(Kg/m^3)       989              5180      6320      5060
% k(W/(mK))         0.6376           9.7       76.5     34.5
% Delta(S/m)       2.6*1e-4      2.5*1e-4   2.7*1e-8   2.09*1e-5
% Cp(J/0.5(kgK))    4175             670       531.8     397.746
% beta/1e-5(1/K)    99               1.3       18         2.8424

%% Dynmic viscosity w1= mu_thn/mu_f:ternayhybrid nanofluid
w1= 1/((1-v1)^2.5*(1-v2)^2.5*(1-v3)^2.5);
%% Dynmic viscosity w12= mu_hnf/mu_f   :hybrid-nanofluid
%w12= 1/((1-v1)^2.5*(1-v2)^2.5);
%% Dynmic viscosity w13= mu_nf/mu_f    :nanofluid
%w13= 1/((1-v1)^2.5);
%% Density w2= rho_thn/rho_f         :ternayhybrid-nanofluid
w2= (1-v1)*((1-v2)*((1-v3)+v3*(ro3/rof))+v2*(ro2/rof))+v1*(ro1/rof);
%% Density w22= rho_hn/rho_f              :hybrid-nanofluid
%w22= (1-v1)*((1-v2)*v2*(ro2/rof))+v1*(ro1/rof);
%% Density w23= rho_n/rho_f               :nanofluid
% w23= (1-v1)+v1*(ro1/rof);
%%  electrical conductivity w3=e_thnf/e_f :ternayhybrid-nanofluid
```

```
        enf=ef*(1+3*(e3/ef-1)*v3/((e3/ef+2)-(e3/ef-1)*v3));
        ehnf=enf*(1+3*(e2/enf-1)*v2/((e2/enf+2)-(e2/enf-1)*v2));
        ethnf=ehnf*(1+3*(e1/ehnf-1)*v1/((e1/ehnf+2)-(e1/ehnf-1)*v1));
        w3= ethnf/ef;
        %%  electrical conductivity w32=e_hnf/e_f;   :hybrid-nanofluid
        % w32= ehnf/ef;
        %%  electrical conductivity w32=e_nf/e_f;     :nanofluid
        % w33= enf/ef;

        %% Thermal expansion w4= ex_thnf/ex_f:ternary hybrid nanofluid
        roex_thnf=rof*exf*(v1*ro1*ex1/(rof*exf)+(1-v1)*((1-v2)*((1-v3)+v3*ro3*ex3/(rof*exf))+v2*ro2*ex2/(rof*exf)));
        w4=roex_thnf/(rof*exf);
        %% Thermal expansion w42= ex_hnf/ex_f :hybrid-nanofluid
        % roex_hnf=rof*exf*(v1*ro1*ex1/(rof*exf)+(1-v1)*((1-v2) + v2*ro2*ex2/(rof*exf)));
        % w42=roex_hnf/(rof*exf);
        %% Thermal expansion w43= ex_hnf/ex_f :nanofluid
        % roex_nf=rof*exf*(v1*ro1*ex1/(rof*exf)+(1-v1);  w43=roex_hnf/(rof*exf);
        %% Specfic heat w5=sp_thnf/sp_f:ternay-hybrid nanofluid
        rosp_thnf=rof*spf*(v1*ro1*sp1/(rof*spf)+(1-v1)*((1-v2)*((1-v3)+v3*ro3*sp3/(rof*spf))+v2*ro2*sp2/(rof*spf)));
        w5=rosp_thnf/(rof*spf);
        %% Specfic heat w52=sp_hnf/sp_f:hybrid-nanofluid
        % rosp_hnf=rof*spf*(v1*ro1*sp1/(rof*spf)+(1-v1)*((1-v2)+v2*ro2*sp2/(rof*spf)));
        % w52=rosp_hnf/(rof*spf);
        %% Specfic heat w52=sp_nf/sp_f  :nanofluid
        % rosp_nf=rof*spf*(v1*ro1*sp1/(rof*spf)+(1-v1);  w53=rosp_nf/(rof*spf);
        %% Thermal conductivity w6= kthnf/kf:ternayhybrid nanofluid
        knf= kf*((k3+2*kf-2*v3*(kf-k3))/(k3+2*kf+v3*(kf-k3)));
        khnf=knf*((k2+2*knf-2*v2*(knf-k2))/(k2+2*knf+v2*(knf-k2)));
        kthnf=khnf*((k1+2*khnf-2*v1*(khnf-k1))/(k1+2*khnf+v1*(khnf-k1)));
        w6=kthnf/kf;
        %% Thermal conductivity w62= khnf/kf:hybrid-nanofluid
        % w62= khnf/kf;
        %% Thermal conductivity w62= knf/kf:nanofluid
        % w63= knf/kf;
        %%  Physical domain to computational domain
        y=(Linf/2)*(1+x(1:N+1)); I=eye(N+1);
        for i=1:4
        La =[1 2 3 4];
        k = La(i);
        %% Initial solutions satisfying boundary conditions
```

```matlab
        fr=bw*ones(N+1,1);% +(A/(1+B0))*(1-exp(-y(1:N+1)));   % Or you may use : fr=S+1-exp(-y(1:N+1))%;
        gr=(1/(1+b2))*exp(-y(1:N+1));
        thr=(bi/(w6+bi))*exp(-y(1:N+1));
        U00=[fr; gr; thr];
        %% Differentiation matrix to fit Physical domain
        Dr=2/Linf*D; Dr2=Dr^2;Dr3=Dr^3;Tol=1e-9;n=100; it =0;
        %% IterationsF= 3.5;Rd=4.5;Ec=0.3;Pr=6;La=1.5;La1=1.2;La2=2;La3=0.5;Q0=0.05;xx=0.05;bi=0.3;b0=0.15;b2=0.05;b3=1.2;bw=0.4;
        change=1;
        while (change <= n)
        %% Known values at previous iteration
        grr=Dr*gr;grrr=Dr2*gr; frr=Dr*fr; frrr=Dr2*fr;thrr=Dr*thr;thrrr=Dr2*thr; frrrr=Dr3*fr;
        %% Coefficients of the first equation
        a3r=2*La1*w2*fr.^2-2*w1;
        a2r=2*w2*fr+2*La1*w2*fr.*frr+La1*w3*M*fr;
        a1r=-2*La1*w2*fr.*frrr+2*w2*frr+w3*M+w1*k+2*w2*F*frr;
        a0r=4*La1*w2*fr.*frrrr-2*w2*frrr-2*La1*w2*frr.*frrr-La1*w3*M*frrr+2*w2*La1*gr.*grr;
        b1r= 2*w2*La1*gr.*fr;
        b0r=2*w2*La1*grr.*fr-2*w2*gr;
        c0r=-w4*La3;
        %% Residual of the first equation R1r
        d11=-2*La1*w2*fr.*frr.*frrr+w2*frr.^2+w2*F*frr.^2+4*La1*w2*fr.^2.*frrrr-2*w2*fr.*frrr-...
        2*La1*w2*fr.*frr.*frrr-La1*w3*M*fr.*frrr+4*w2*La1*gr.*fr.*grr-w2*gr.^2;
        %% Coefficients of the second equation
        e2r=-2*w2*La1*fr.*gr;
        e1r=-2*La1*w2*fr.*grr+2*w2*gr;
        e0r= 4*La1*w2*grrr.*fr-2*w2*grr-2*La1*w2*frr.*grr-w3*M*La1*grr-2*w2*La1*frrr.*gr;
        h2r=-2*w1+2*La1*w2*fr.^2;
        h1r=2*w2*fr+2*La1*w2*fr.*frr+w3*M*La1*fr;
        h0r=w1*k+w3*M+2*w2*F*gr-2*w2*La1*fr.*frrr+2*w2*frr;
        %% Residual of the second equation R2r; b4r
        d21=-2*w2*La1*fr.*frrr.*gr-2*La1*w2*fr.*frr.*grr+2*w2*gr.*frr+4*La1*w2*grrr.*fr.^2-2*w2*grr.*fr-...
        2*La1*w2*frr.*fr.*grr-w3*M*La1*grr.*fr-2*w2*La1*fr.*frrr.*gr+w2*F*gr.^2;
        %% Coefficients of the third equation
        l2r=2*w1*Ec*Pr*frrr;
        l1r=w3*M*Ec*Pr*frr-w5*La2*Pr*fr.*thrr;
        l0r=-2*w5*La2*Pr*thrrr.*fr+w5*Pr*thrr-w5*La2*Pr*frr.*thrr;
        n1r=2*w1*Ec*Pr*grr;
```

```
n0r=w3*M*Ec*Pr*gr;
m2r=w6+Rd*(1+xx*thr).^3-w5*La2*Pr*fr.^2;
m1r=6*Rd*xx*(1+xx*thr).^2.*thrr+w5*Pr*fr-w5*La2*Pr*fr.*frr;
m0r=3*Rd*xx*(1+xx*thr).^2.*thrrr+6*Rd*xx^2*(1+xx*thr).*thrr.^2+Q0*Pr;
%% Residual of the third equation R3r; c4r
d31=w1*Ec*Pr*frrr.^2+0.5*w3*M*Ec*Pr*frr.^2-w5*La2*Pr*fr.*frr.*thrr-2*w5*La2*Pr*thrrr.*fr.^2+w5*Pr*thrr.*fr-...
w5*La2*Pr*fr.*frr.*thrr+w1*Ec*Pr*grr.^2+0.5*w3*M*Ec*Pr*gr.^2+3*Rd*xx*(1+xx*thr).^2.*thrr.^2+...
3*Rd*xx*(1+xx*thr).^2.*thr.*thrrr+6*Rd*xx^2*(1+xx*thr).*thr.*thrr.^2;
%% Block matrix
A11=diag(a3r)*Dr3-diag(a2r)*Dr2+diag(a1r)*Dr+diag(a0r)*I;
A11(1,:)=Dr(1,:); A11(N,:)=Dr(N+1,:)-b2*Dr2(N+1,:);
A11(N+1,:)=0;             A11(N+1,N+1)=1;
A12=diag(b1r)*Dr+diag(b0r)*I; A12(1,:)=0;A12(N,:)=0;A12(N+1,:)=0;
A13=diag(c0r)*I; A13(1,:)=0;  A13(N,:)=0; A13(N+1,:)=0;
A21= diag(e2r)*Dr2+diag(e1r)*D+diag(e0r)*I;
A21(1,:)=0; A21(N+1,:)=0;
A22 =diag(h2r)*Dr2-diag(h1r)*Dr+ diag(h0r)*I;
A22(1,:)=0; A22(1,1)=1;
A22(N+1,:)=I(N+1,:)-b2*Dr(N+1,:);
A23=zeros(N+1,N+1); A23(1,:)=0;    A23(N+1,:)=0;
A31= diag(l2r)*Dr2+diag(l1r)*Dr+diag(l0r)*I;
A31(1,:)=0;    A31(N+1,:)=0;
A32=diag(n1r)*Dr+diag(n0r)*I;
A32(1,:)=0;    A32(N+1,:)=0;
A33=diag(m2r)*Dr2+diag(m1r)*Dr+ diag(m0r)*I;
A33(1,:)=0;    A33(1,1)=1;
A33(N+1,:)=(w6-b3)*Dr(N+1,:)-bi*I(N+1,:);
%%
R1r=d11;R2r=d21;R3r=d31;R1r(1)=0 ; R1r(N)=b0;R1r(N+1)=bw;
R2r(1)=0; R2r(N+1)=1;R3r(1)=0; R3r(N+1)=-bi;
Arr=[A11 A12 A13; A21 A22 A23;A31 A32 A33];
%% Residual
Rrr=[R1r;R2r;R3r];
%% Iterations
U00new=Arr\Rrr;
if norm(U00new(1:N+1)-U00(1:N+1),inf)<Tol && norm(U00new(N+2:2*N+2)-U00(N+2:2*N+2),inf)<Tol &&...
norm(U00new(2*N+3:3*N+3)-U00(2*N+3:3*N+3), inf)<Tol
U00new;
break
else
change=change+1; U00=U00new;
```

```
fr=U00(1:N+1);gr=U00(N+2:2*N+2); thr=U00(2*N+3:3*N+3);
end
[fr gr thr];
end
if (change>n)
disp('Method failed to converge')
end
% Entropy and Bejan number analysis
Ng=w6*alpha_bar*(1+(Rd/w6)*(1+xx*thr).^3).*Dr*thr.*Dr*thr+w1*Br*(6/Re*(Dr*fr.*Dr*fr)+gamma_bar^2*...
Dr2*fr.*Dr2*fr+gamma_bar^2*Dr*gr.*Dr*gr)+w1/2*Br*k*gamma_bar^2*(Dr*fr.*Dr*fr+gr.*gr)+w2/2*Br*F*...
gamma_bar^3*(Dr*fr.*Dr*fr.*Dr*fr+gr.*gr.*gr)+w3*M/2*Br*gamma_bar^2*(Dr*fr.*Dr*fr+gr.*gr);
Be= (w6*alpha_bar*(1+(Rd/w6)*(1+xx*thr).^3).*Dr*thr.*Dr*thr)./Ng;
%% Results
% Radial and tangential Skin friction Re^1/2*C_fr=Cfr and Re^1/2*C_gphi=Cgp
Cfr=2*sqrt(2)*(w1/w2)*Dr2*fr;Cgp=2*sqrt(2)*(w1/w2)*Dr*gr; Cfg=2*sqrt(2)*(w1/w2)*sqrt(Dr2*fr.*Dr2*fr+Dr*gr.*Dr*gr);
[Cfr(N+1) Cgp(N+1)];% Cfg(N+1)]
% Local heat transfer rate Re^{-1/2}*Nu_w
Nuw=-sqrt(2)*(w6+Rd*(1+xx*thr).^3).*Dr*thr;
Nuw(N+1); kk=Dr*fr; kk_rate= Dr*thr;kk_rate(N+1); Cf= w1/w2*Dr2*fr;Cf(N+1);
kkk3= Dr*thr;kkk1= Dr*fr;kkk1(N+1); [kkk1(N+1) kkk3(N+1)];
[fr gr thr];
%% Graph plots
if k== La(1)
plot(y,kk, 'k', 'linewidth',1);
hold on
elseif k== La(2)
plot(y,kk,'r', 'linewidth',1);
hold on
elseif k == La(3)
plot(y,kk,'b', 'linewidth',1);
hold on
elseif k == La(4)
plot(y,kk,'m', 'linewidth',1);
hold on
end
end
set(gcf, 'Position', [100, 100, 600, 800]);% figure will have a width of 800
% pixels and a height of 600 pixels
title(sprintf('no.Iter=%d',change))
```

```
        xlabel('\eta'); ylabel('f''(\eta)');
        t1=['\rm{=Fe_3O_4+CuO+MoS_2/SA}'];
        gtext(t1);
        t5=('\rm{\lambda=1,2,3,4}');
        gtext(t5);
```